AD_____

Award Number: DAMD17-99-1-9226


TITLE: New Transfer Theory Relationships for Signal and Noise
Analyses of X-Ray Detectors


PRINCIPAL INVESTIGATOR: Ian A. Cunningham, Ph.D.


CONTRACTING ORGANIZATION: The John P. Roberts Research Institute
London, Ontario N6A 5K8
Canada

REPORT DATE: October 2002


TYPE OF REPORT: Final


PREPARED FOR: U.S. Army Medical Research and Materiel Command
Fort Detrick, Maryland 21702-5012


DISTRIBUTION STATEMENT: Approved for Public Release;
Distribution Unlimited


The views, opinions and/or findings contained in this report are
those of the author(s) and should not be construed as an official
Department of the Army position, policy or decision unless so
designated by other documentation.

20050727 086

# REPORT DOCUMENTATION PAGE

Form Approved
OMB No. 0704-0188

Public reporting burden for this collection of information is estimated to average 1 hour per response, including the time for reviewing instructions, searching existing data sources, gathering and maintaining the data needed, and completing and reviewing this collection of information. Send comments regarding this burden estimate or any other aspect of this collection of information, including suggestions for reducing this burden to Department of Defense, Washington Headquarters Services, Directorate for Information Operations and Reports (0704-0188), 1215 Jefferson Davis Highway, Suite 1204, Arlington, VA 22202-4302. Respondents should be aware that notwithstanding any other provision of law, no person shall be subject to any penalty for failing to comply with a collection of information if it does not display a currently valid OMB control number. **PLEASE DO NOT RETURN YOUR FORM TO THE ABOVE ADDRESS.**

| 1. REPORT DATE (DD-MM-YYYY) | 2. REPORT TYPE | 3. DATES COVERED (From - To) |
|---|---|---|
| 01-10-2002 | Final | 1 Oct 1999 - 30 Sep 2002 |

**4. TITLE AND SUBTITLE**
The Role of Neuropilin in Breast Cancer Metastasis

**5a. CONTRACT NUMBER**

**5b. GRANT NUMBER**
DAMD17-99-1-9226

**5c. PROGRAM ELEMENT NUMBER**

**6. AUTHOR(S)**
Ian A. Cunningham, Ph.D.

E-Mail: icunning@imaging.robarts.ca

**5d. PROJECT NUMBER**

**5e. TASK NUMBER**

**5f. WORK UNIT NUMBER**

**7. PERFORMING ORGANIZATION NAME(S) AND ADDRESS(ES)**
The John P. Roberts Research Institute
London, Ontario N6A 5K8
Canada

**8. PERFORMING ORGANIZATION REPORT NUMBER**

**9. SPONSORING / MONITORING AGENCY NAME(S) AND ADDRESS(ES)**
U.S. Army Medical Research and Materiel Command
Fort Detrick, Maryland 21702-5012

**10. SPONSOR/MONITOR'S ACRONYM(S)**

**11. SPONSOR/MONITOR'S REPORT NUMBER(S)**

**12. DISTRIBUTION / AVAILABILITY STATEMENT**
Approved for Public Release; Distribution Unlimited

**13. SUPPLEMENTARY NOTES**

**14. ABSTRACT**
Abstract follows.

**15. SUBJECT TERMS**
No subject terms provided.

| 16. SECURITY CLASSIFICATION OF: | | | 17. LIMITATION OF ABSTRACT | 18. NUMBER OF PAGES | 19a. NAME OF RESPONSIBLE PERSON |
|---|---|---|---|---|---|
| a. REPORT U | b. ABSTRACT U | c. THIS PAGE U | UU | 45 | 19b. TELEPHONE NUMBER (include area code) |

Standard Form 298 (Rev. 8-98)
Prescribed by ANSI Std. Z39.18

# ABSTRACT

X-ray mammography is the most reliable method available at present for the detection of breast cancer in screening programs. Unfortunately, it still misses many cancers, particularly in the radiographically dense breast more common in younger populations where the benefits of mammography screening are more controversial. Digital mammography holds the promise of improved specificity and sensitivity for the detection of small cancers. However, superior image quality can only be achieved if these digital systems are optimally designed to extract all information possible from the x-ray beam.

The metric most generally accepted to describe signal and noise performance of detectors is the detective quantum efficiency (DQE), and theoretical methods for predicting the DQE are essential for the optimal design of new systems. Current methods using "cascaded-systems" analyses are simplistic and do not agree very well with measurements. In this research, we introduced the idea of "parallel cascades" as a means of developing comprehensive models of x-ray detectors that accurately describe the DQE of many x-ray systems. We discovered a mathematical description of the required cross-spectral noise-power density and showed that this approach gives an accurate estimate of the DQE based on design parameters. The results of this research are now used routines in the design and assessment of new x-ray systems by scientists and engineers in both academic and industrial laboratories around the world.

# Table of Contents

# Introduction

X-ray imaging is the mainstay of diagnostic radiology. Although x-ray technologies have been under development for over 100 years, their cost, use and potential for diagnosis continue to accelerate. Due to the health risks associated with exposure to radiation and the risks from inconclusive or misleading diagnoses, technical excellence in medical imaging systems is critical to high-quality medical care.

In radiology, image quality is a balance between system performance and patient radiation dose. This balance is particularly important for difficult diagnostic tasks such as mammographic screening, where large numbers of patients are exposed to radiation and high-quality images are essential to enable early detection when the disease is still *in situ* or minimally invasive.(Tabar et al., 1995;Hendrick et al., 1997;Heine and Malhotra, 2002a;Heine and Malhotra, 2002b) While film-screen mammography has been the most reliable method available for the detection of breast cancer in screening programs in the past,(Zhou and Gordon, 1989;Hurley and Kaldor, 1992) new digital technologies under development are expected to have improved sensitivity and specificity.(Baines et al., 1990;Yaffe, 1992;Feig and Yaffe, 1998) This is particularly important for examinations of the radiographically-dense breast,(Boyd et al., 1998;Heine and Malhotra, 2002a;Heine and Malhotra, 2002b) found more often in younger populations where the benefits of screening mammography remain controversial.(Kerlikowske et al., 1996a;Kerlikowske et al., 1996b)

The scientific community has generally accepted the modulation transfer function (MTF) and detective quantum efficiency (DQE) as the most important metrics describing system imaging performance.(Metz et al., 1995) The MTF describes spatial resolution (as a function of spatial frequency) - essential for imaging small detail such as breast microcalcifications. The DQE describes the ability of a system to capture the signal-to-noise ratio available in a radiation beam and is a fundamental measure of system "radiation dose efficiency."

Theoretical models of the DQE are essential for the optimal design of high-quality imaging systems. An approach called "cascaded-systems analysis" has gained recent popularity as a method of understanding the general behavior of the DQE of many existing detectors. However, this approach has been too simplistic to be of much practical value for developing comprehensive models of the DQE.

The overall goal of this research was to develop the theoretical basis of a sophisticated cascaded-systems method, and to evaluate this method by generating comprehensive DQE models of real systems and comparing these with Monte Carlo and experimental results. These models are then used to develop an understanding of the physical factors that limit performance - factors that must be addressed in the optimal design of new "next-generation" detectors.

# Body

This research has lead directly to the development and use of cascaded-systems analysis as a generalized method for developing comprehensive models of signal and noise transfer in x-ray imaging systems. It

has made possible the development of cascaded models of the DQE that accurately describe system performance and can be validated directly by experimental measurements and Monte Carlo calculations.

# Key Research Accomplishments

Our primary accomplishment was development of what we call "parallel cascades." This is a method of reducing complex physical processes involved in the generation of an x-ray image into a number of simpler processes. These simple processes have well defined (and understood) signal and noise-transfer properties, and can be combined arbitrarily to represent the actual complex processes. The concepts that make parallel cascades possible were developed in the first year of the grant. In the second and third years, these concepts were further refined, validated and published. We used this approach to study a CsI-based flat panel detector and determine what physical properties were responsible for limiting the performance of this detector, and therefore what parameters must be addressed before improvements in detector performance are possible.

Details of our scientific contributions are described in the attached publications. In this section, each accomplishment is summarized in terms of the specific tasks and goals of the grant.

*Year I:*
I-1) Develop expertise in statistical point-process theory
I-2) Develop expertise in moment generating functions theory
I-3) Develop general expression for generalized cross-spectral density term required for parallel cascades
I-4) Design and construct x-ray system for production of mono-energetic x rays using a secondary target

Our primary accomplishment was to develop the concept of the cross spectral density of amplified point processes. This was the missing link preventing use of the cascaded-systems approach for high-accuracy, comprehensive models of the DQE in the past, and was completed using the random point-process approach. A manuscript was submitted for publication in Medical Physics (Publication 1: *Parallel cascades: New ways to describe noise transfer in medical imaging systems*). The final result of this work can be expressed as a single equation: the general expression for the cross covariance of amplified point processes and an expression for the cross spectral density for wide-sense stationary conditions is given by Eq. 81 in Publication 1. The fact that a highly sophisticated theoretical development reduces to this simple and easy-to-apply result is likely the reason that parallel cascades are now widely used by scientists and engineers. It means that the mathematical sophistication is "concealed" from the user, making the use of cascaded DQE models more accessible to a wider audience.

These results extend the generalized transfer-theory approach to include the description of more complex image-forming processes involving parallel cascades of quantum amplification processes. This parallel-cascade approach has been used to develop a theoretical expression for noise-power transfer in a simple radiographic screen that includes the effect of characteristic x-ray reabsorption. The result confirms earlier work by Metz and Vyborny(Metz and Vyborny, 1983) who showed that reabsorption increases image noise and decreases the detective quantum efficiency (DQE) at some spatial frequencies. Use of the transfer-theory approach facilitates a straightforward generalization to many new digital imaging systems including conventional angiographic and active-matrix flat-panel systems.

Task I-4 was the development of a mono-energetic x-ray source based on a secondary lanthanum target for experimental validation of the parallel cascades concept. Figure 1 shows a photograph of the mono-energetic source and Fig. 2 shows a schematic drawing of the design.

***Year II:***
II-1) Identify other transfer relationships as described in proposal
II-2) Develop expressions for signal and noise transfer through each relationship
II-3) Perform Monte Carlo verification study of parallel cascade results
II-4) Perform experiments using mono-energetic x rays to confirm NPS and DQE degradation due to reabsorption of K x rays in radiograhic screen using CCD camera (equipment
II-5) Write paper describing generalized cross-spectral density term and comparison of resulting theoretical prediction of NPS and DQE degradation due to reabsorption with mono-energetic experiment

X ray images are generated when an x-ray beam deposits energy into the detector, primarily by photo-electric and Compton interactions. Image noise is directly related to the number of interacting x-ray quanta and to details of how the energy is absorbed. The most important outcome from our work in year II was to recognize that both photo-electric and Compton interactions, should be - and can be - represented as linear and shift-invariant random point processes. This was important because it meant these fundamental processes can be described as Fourier-based transfer functions in terms of parallel cascaded processes.

This Fourier representation of x-ray physics was a critical step towards a comprehensive theoretical framework for optimizing detector design and exposure techniques on the MTF and DQE. It was made possible by our development of parallel cascades in year I. In year II we extended this approach to represent Compton scatter (Publication 2: *Compton scatter in frequency space: a theoretical study*). It is limited at present to "thin" detectors where multiple scatter can be ignored, but is applicable to most detectors used for mammography.

A number of other key transfer relationships were identified and used to study the transfer of signal and
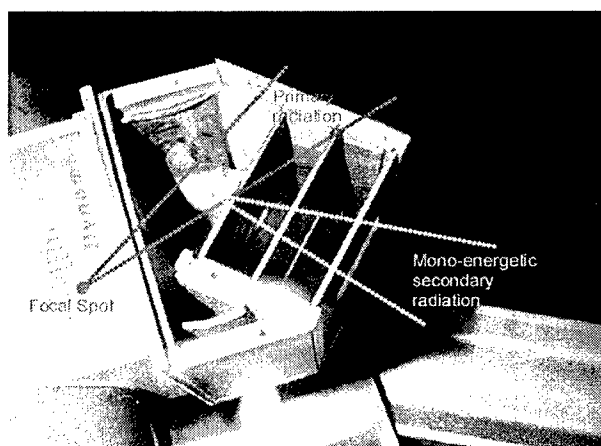


**Figure 1.** Photograph of mono-energetic x-ray source with top removed.
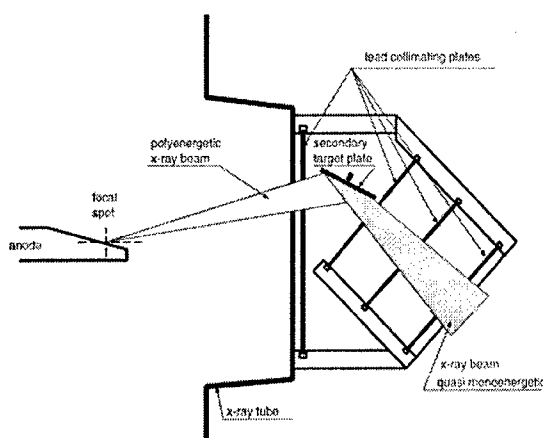


**Figure 2.** Schematic illustration of mono-energetic x-ray source.

noise in a CsI-based flat panel detector (Publication 3: *Cascaded models and the DQE of flat-panel imagers: noise aliasing, secondary quantum noise and reabsorption*). In addition, this investigator was invited to contribute a chapter on the use of cascaded-systems in detector design for The Handbook of Medical Imaging published by the Society for Optical Engineering[Cunningham 2000 6817 /id] (Publication 4) and now teaches an annual course on cascaded systems in medical imaging for this society based on this chapter.

*Year III:*
1) Perform Monte Carlo verification study of all digital-system relationships
2) Write paper describing all transfer relationships

The parallel cascaded-systems approach has now been validated by both Monte Carlo and experimental measurements of the DQE on several systems, both by this investigator and others. In year III and subsequent years several more publications have been completed, either fully or partially funded by this award (Publications 5-11: *A framework for noise-power spectrum analysis of multidimensional images, Fundamental limitations imposed by x-ray interactions on the modulation transfer function of existing x-ray detectors: a Monte Carlo study, Can a Fourier-based cascaded-systems analysis describe noise in complex shift-variant spatially sampled detectors?, Validation of complex cascaded models of medical imaging systems by Monte Carlo, Penalty on the detective quantum efficiency from off-axis incident x rays, Computational engine for development of complex cascaded models of signal and noise in x-ray imaging systems,* and *Signal and noise transfer properties of photoelectric interactions in diagnostic-imaging detectors*).

# Reportable Outcomes

## Publications

1.      J. Yao and I.A. Cunningham. Parallel cascades: New ways to describe noise transfer in medical imaging systems, Medical Physics 28(10): 2020-38 (2001).

2.      J. Yao and I.A. Cunningham. "Compton scatter in frequency space: a theoretical study" in *Medical Imaging 2002: Physics of Medical Imaging*, L. Antonuk and M. Yaffe Editors, Proc. SPIE 4682: 479-490 (2002).

3.      I.A. Cunningham. "Cascaded models and the DQE of flat-penel imagers: noise aliasing, secondary quantum noise and reabsorption" in *Medical Imaging 2002: Physics of Medical Imaging*, L. Antonuk and M. Yaffe Editors, Proc. SPIE 4682: 61-72 (2002).

4.      I.A. Cunningham. Applied linear-systems theory, Chapter 2, Handbook of Medical Imaging, Vol 1. Physics and Psychophysics, Eds. J. Beutel, H.L. Kundel and R.L. Van Metter, pp. 79-159 (The International Society for Optical Engineering, Bellingham, Washington, 2000).

5.	J.H. Siewerdsen, I.A. Cunningham and D.A. Jaffray.  A framework for noise-power spectrum analysis of multidimensional images, Medical Physics 29(11): 2655-71 (2002). This paper was awarded the 2003 COMP Sylvia Fedoruk Prize in Medical Physics (best paper of the year).

6.	G. Hajdok and I.A. Cunningham, "Fundamental limitations imposed by x-ray interactions on the modulation transfer function of existing x-ray detectors: a Monte Carlo study" in *Medical Imaging 2003: Physics of Medical Imaging,* M.J. Yaffe and L. Antonuk Editors, Proc. SPIE **5030** (2003).

7.	I.A. Cunningham, M. Sattarivand, G. Hajdok and J. Yao, "Can a Fourier-based cascaded-systems analysis describe noise in complex shift-variant spatially sampled detectors?," *Medical Imaging 2004: Physics of Medical Imaging,* Eds Yaffe and Flynn, Proc SPIE **5368** 79-88 (2004).

8.	M. Sattarivand and I.A. Cunningham, "Validation of complex cascaded models of medical imaging systems by Monte Carlo," *Medical Imaging 2004: Physics of Medical Imaging,* Eds Yaffe and Flynn, Proc SPIE **5368** 98-108 (2004).

9.	G. Hajdok and I.A. Cunningham, "Penalty on the detective quantum efficiency from off-axis incident x rays," *Medical Imaging 2004: Physics of Medical Imaging,* Eds Yaffe and Flynn, Proc SPIE **5368** 109-118 (2004).

10.	M. Satarivand, G. Hajdok and I.A. Cunningham, Computational engine for development of complex cascaded models of signal and noise in x-ray imaging systems, IEEE Transactions on Medical Imaging, 24: 211-22 (2005).

11.	J. Yao, G. Hajdok and I.A. Cunningham, Signal and noise transfer properties of photoelectric interactions in diagnostic-imaging detectors, Medical Physics (2005) [accepted].

## Invited Presentations
*The following presentations were based in whole or in part on research completed for this research award.*
1.	X-ray detector performance: principles and measurements using a linear systems approach, SPIE Course, San Diego, February 12 2005.
2.	X-ray detector performance: principles and measurements using a linear systems approach, SPIE Course, San Diego, February 14 2004.
3.	Understanding radiologic image quality: A linear-systems approach, SPIE Course, San Diego, February 2002.
4.	Fundamental Limits of Image Quality in Diagnostic and Therapeutic Imaging Systems, Great Lakes Chapter of the AAPM, Michigan, January 19 2002.
5.	Digital Image Quality, Invited address to the ACMP annual symposium "Digital Radiography: Clinical State of the Art", Hershey, PA, June 4-5 2001.
6.	Understanding radiologic image quality: A linear-systems approach, SPIE Short Course, San Diego, February 2001.
7.	The DQE of fluoroscopic systems: Does the ideal observer have infinite patience? William Beaumont Hospital, Department of Radiation Oncology, November 20, 2000.

8.    The detective quantum efficiency of fluoroscopic systems: A spatial-temporal approach. University of Michigan Medical Center, September 2000.
9.    Understanding radiologic image quality: From basic concepts to a practical tool-kit for scientists and engineers, American Association of Physicists in Medicine, Chicago, July 2000.

## Abstracts and Presentations

10.   I.A. Cunningham, M. Sattarivand, !G. Hajdok and !J. Yao, "Can a Fourier-based cascaded-systems analysis describe noise in complex shift-variant spatially sampled detectors?," Medical Imaging 2004: Physics of Medical Imaging, Eds Yaffe and Flynn, Proc SPIE 5368 2004.
11.   M. Sattarivand and I.A. Cunningham, "Validation of complex cascaded models of medical imaging systems by Monte Carlo," Medical Imaging 2004: Physics of Medical Imaging, Eds Yaffe and Flynn, Proc SPIE 5368 2004.
12.   G. Hajdok and I.A. Cunningham, "Penalty on the detective quantum efficiency from off-axis incident x-rays," Medical Imaging 2004: Physics of Medical Imaging, Eds Yaffe and Flynn, Proc SPIE 5368 2004.
13.   M. Sattarivand and I.A. Cunningham, "Development of a graphical programming environment for the design of cascaded quantum imaging systems," COMP 2003, Edmonton.
14.   G. Hajdok and I.A. Cunningham, "Fundamental spatial resolution limits in existing diagnostic x-ray detectors," COMP 2003, Edmonton.
15.   G. Hajdok and I.A. Cunningham, "Fundamental limitations imposed by x-ray interactions on the modulation transfer function of existing x-ray detectors: a Monte Carlo study" Medical Imaging 2003: Physics of Medical Imaging, San Diego SPIE 5030: Feb. 2003.
16.   I.A. Cunningham, "New Transfer Theory Relationships for Signal and Noise Analysis of X-Ray Detectors", U.S. Army, Era of Hope Breasth Cancer Research Meeting, Orlando, Florida, September 25-28, 2002.
17.   J. Yao and I.A. Cunningham, "Model of Compton Scatter on Signal and Noise Transfer in Medical Imaging Systems," COMP/AAPM July 2002, Montreal, Med Phys 29: 1344 (2002).
18.   Yao and I.A. Cunningham. "Compton scatter in a thin detector: Theoretical signal and noise transfer in the Fourier domain" in Medical Imaging 2002: Physics of Medical Imaging, San Diego SPIE 4682 Feb 2002.
19.   I.A. Cunningham. "Cascaded models and the DQE of flat-penel imagers: noise aliasing, secondary quantum noise and reabsorption" in Medical Imaging 2002: Physics of Medical Imaging, SPIE 4682: Feb 2002
20.   J. Yao and I.A. Cunningham, "Influence of Energy Deposited by Compton Scatter on Imaging System MTF and DQE", RSNA, Chicago, November 2001.
21.   J. Yao and I.A. Cunningham, "Influence of Energy Deposited by Compton Scatter on Imaging System MTF and DQE", COMP, Killowna BC, July 2001.
22.   J. Yao, !T. Moschandreou and I.A. Cunningham, Cross Covariance of Correlated Point Processes for use in Linear Systems Theory, World Congress of Medical Physics and Biomedical Engineering, Chicago, July 2000.
23.   T. Moschandreou, J. Yao and I.A. Cunningham, Use of the Cross Covariance in Linear Systems Theory to Model the DQE of Detectors with Fluorescence Reabsorption, World Congress of Medical Physics and Biomedical Engineering, Chicago, July 2000.

# Conclusions

This research award funded the development of what we have called the "parallel cascaded-systems" method of calculating signal and noise-transfer properties of detectors used for x-ray mammography. This method is now routinely used by scientists and engineers in laboratories around the world to generate theoretical models of the DQE (detective quantum efficiency) of new and old x-ray detectors based on physical design parameters. These models are critical for understanding how well a detector is performing, relative to expected performance, and to develop new detectors optimized to produce the best possible image quality. This award funded five publications directly and much of the science for an additional six.

I am also pleased to report that this award was a turning point both in the development of new models for understanding the signal and noise performance of new detector designs, and in terms of the research program of this investigator. Based on results obtained during the tenure of this award, this investigator has started a new major research program on theoretical methods for the optimized design of new detector systems. At present, this investigator holds a new major five-year award from the Canadian Institutes of Health Research (the Canadian equivalent of the NIH) plus new research funding from General Electric Medical Systems and the Ontario Research Development and Challenge Fund totaling over US$1,200,000. This funding can be attributed in great part to the initial funding provided by the US Army Medical Research program.

# References

Baines, C. J., A. B. Miller, D. B. Kopans, M. Moskowitz, D. E. Sanders, E. A. Sickles, T. To, and C. Wall, 1990, Canadian national breast screening study: assessment of technical quality by external review: American Journal of Roentgenology, v. 155, p. 743-747.

Boyd, N. F., G. A. Lockwood, J. W. Byng, D. L. Tritchler, and M. J. Yaffe, 1998, Mammographic densities and breast cancer risk: Cancer Epidemiol.Biomarkers Prev., v. 7, no. 12, p. 1133-1144.

Feig, S. A., and M. J. Yaffe, 1998, Digital mammography: Radiographics, v. 18, no. 4, p. 893-901.

Heine, J. J., and P. Malhotra, 2002a, Mammographic tissue, breast cancer risk, serial image analysis, and digital mammography. Part 1. Tissue and related risk factors: Acad.Radiol., v. 9, no. 3, p. 298-316.

Heine, J. J., and P. Malhotra, 2002b, Mammographic tissue, breast cancer risk, serial image analysis, and digital mammography. Part 2. Serial breast tissue change and related temporal influences: Acad.Radiol., v. 9, no. 3, p. 317-335.

Hendrick, R. E., R. A. Smith, J. H. Rutledge, III, and C. R. Smart, 1997, Benefit of screening mammography in women aged 40-49: a new meta- analysis of randomized controlled trials: J.Natl.Cancer Inst.Monogr, no. 22, p. 87-92.

Hurley, S. F., and J. M. Kaldor, 1992, The benefits and risks of mammographic screening for breast cancer: Epidemiol Rev, v. 14, p. 101-130.

Kerlikowske, K., D. Grady, J. Barclay, E. A. Sickles, and V. Ernster, 1996a, Effect of age, breast density, and family history on the sensitivity of first screening mammography: JAMA, v. 276, no. 1, p. 33-38.

Kerlikowske, K., D. Grady, J. Barclay, E. A. Sickles, and V. Ernster, 1996b, Likelihood ratios for modern screening mammography. Risk of breast cancer based on age and mammographic interpretation: JAMA, v. 276, no. 1, p. 39-43.

Metz, C. E., and C. J. Vyborny, 1983, Wiener spectral effects of spatial correlation between the sites of characteristic x-ray emission and reabsorption in radiographic screen-film systems: Physics in Medicine & Biology, v. 28, p. 547-564.

Metz, C. E., R. F. Wagner, K. Doi, D. G. Brown, R. M. Nishikawa, and K. J. Myers, 1995, Toward consensus on quantitative assessment of medical imaging systems. [Review]: Medical Physics, v. 22, p. 1057-1061.

Tabar, L., G. Fagerberg, H. H. Chen, S. W. Duffy, C. R. Smart, A. Gad, and R. A. Smith, 1995, Efficacy of breast cancer screening by age. New results from the Swedish Two-County Trial: Cancer, v. 75, no. 10, p. 2507-2517.

Yaffe, M. J., 1992, Digital Mammography, in AG Haus and MJ Yaffe eds., Syllabus: A Categorical Course in Physics Technical Aspects of Breast Imaging: Oak Brook, Il, Radiological Society of North America, p. 245-255.

Zhou, X., and R. Gordon, 1989, Detection of early breast cancer: an overview and future prospects: Crit Rev Biomed Eng, v. 17, p. 203-255.

# Parallel cascades: New ways to describe noise transfer in medical imaging systems

J. Yao[a)]
*Imaging Research Laboratories, The John P. Robarts Research Institute, P.O. Box 5015, 100 Perth Drive, London, Ontario N6A 5K8, Canada*

I. A. Cunningham
*Imaging Research Laboratories, The John P. Robarts Research Institute, P.O. Box 5015, 100 Perth Drive, London, Ontario N6A 5K8,*
*Canada and Department of Diagnostic Radiology, London Health Sciences Center*
*and The University of Western Ontario, London, Ontario, Canada*

A generalized approach to describing transfer of the noise power spectrum through medical imaging systems has been developed over the past several years in which image-forming processes are represented in terms of a cascade of amplified point processes. Until recently, this approach has been restricted to serial cascades only. Here we develop a generalized expression for the cross covariance of amplified point processes and an expression for the cross spectral density for wide-sense stationary conditions. These results extend the generalized transfer-theory approach to include the description of more complex image-forming processes involving *parallel* cascades of quantum amplification processes. This parallel-cascade approach is used to develop a theoretical expression for noise-power transfer in a simple radiographic screen that includes the effect of characteristic x-ray reabsorption. The result confirms earlier work by Metz and Vyborny, who showed that reabsorption increases image noise and decreases the detective quantum efficiency at low spatial frequencies. Use of the transfer-theory approach facilitates a straightforward generalization to many new digital imaging systems including conventional angiographic and active-matrix flat-panel systems. © *2001 American Association of Physicists in Medicine.* [DOI: 10.1118/1.1405842]

Key words: random point processes, amplified point processes, cross covariance, cross spectral density, noise power spectrum, transfer theory

## I. INTRODUCTION

Medical x-ray imaging systems must be designed to ensure that maximum image quality is obtained for a specified radiation dose to the patient. While there are many aspects to "image quality," one important consideration is image noise as described by the Wiener spectrum, or noise power spectrum (NPS).[1–3] The NPS describes the spectral decomposition of second-moment statistics in terms of spatial frequencies under wide-sense stationary (WSS) conditions.[2,3] It is required for the determination of other image-quality metrics used to quantify image quality and system performance including the noise-equivalent number of quanta (NEQ),[1,4,5] which describes an equivalent number of quanta forming an image, and the detective quantum efficiency (DQE),[4–9] which describes the ability of an imaging system to make efficient use of the incident image quanta.

Over the past several years, a generalized transfer-theory approach[10–12] has been developed to describe how the NPS is transferred from the input of an imaging system to the output image.[13–18] Of particular significance in this development was a description of how the NPS is transferred through quantum gain and quantum scattering stages by Rabbani, Shaw, and Van Metter[13] and by Barrett, Wagner, and Myers.[19,20] This generalized description of image noise has resulted in a comprehensive framework for the understanding of system performance built upon a communication-theory-based approach.

Using this method, many imaging systems can be represented in terms of serial cascades of three elementary processes: (i) quantum gain; (ii) quantum scattering; and, (iii) linear filters. Transfer of signal and noise through these models can be described by cascading transfer relationships for each process. In Appendix A, transfer properties of these three elementary processes are summarized. This approach has been used recently to describe signal and noise transfer and the DQE of a number of x-ray medical imaging systems, including film screen systems,[21–23] active-matrix flat-panel systems for digital radiography,[24–26] video-based systems for portal imaging and radiation therapy verification,[27,28] and other new system designs.[29–32]

Transfer theory is sometimes viewed as being simplistic, providing limited new insight into system performance. However, this need not be the case, and we are developing a number of new transfer-theory relationships to describe noise transfer through processes where existing relationships are inadequate. These relationships form the basis of theoretical "tools" that can be used by scientists and engineers developing or assessing new system designs. Of particular practical importance is the spatial-frequency-dependent form of these tools for WSS conditions. They can be used to make a

theoretical prediction of the NEQ or DQE of a particular system design.

One such current limitation of the transfer-theory approach is that it has been restricted to *serial* cascades of the elementary processes. This excludes the situation where more than one image-forming process must be summed to form an image.[16] For example, most of the energy deposited in a radiographic screen by diagnostic x rays is through the photoelectric interaction. This process often results in the emission of a characteristic x ray that may be reabsorbed elsewhere in the screen. Light is generated at both the primary-interaction and reabsorption sites, but with different intensities. In addition, the reabsorption site is randomly located but spatially correlated with the primary-interaction site. Light from both sites contribute to the final radiographic image recorded on film. However, it is not possible to describe image noise as the sum of these correlated image-forming processes using a simple serial cascade, and hence the effect of reabsorption has not been included in any transfer-theory analysis. By extending the transfer-theory approach to include reabsorption, analytic models can be developed for many particular systems that specifically describe degradation of the DQE due to this effect. This is important to scientists and engineers who are concerned with improving existing systems or developing new systems with improved image quality.

In this article, we extend the capabilities of the transfer-theory approach so that more complex systems requiring both serial and parallel cascades of these elementary processes can be represented. This is accomplished by developing a general expression for the cross covariance and cross spectral density of noise processes that can be incorporated into the transfer-theory analysis (see Appendix B). Use is made of random point process theory, where a quantum image is represented as a two-dimensional spatial point process in which each quantum is represented as a point impulse.[19,20,33] A general expression is derived for the cross covariance of two correlated random point processes. This is then simplified for the special case of wide-sense stationary random point processes where the cross spectral density function is derived.

Of practical importance for applications in medical imaging is the special case where each point process represents a subset of a common input point distribution. The cross covariance of these two subsets is derived, and then generalized to describe the cross covariance of the two distributions after they subsequently undergo an arbitrary cascade of quantum amplification and scattering processes. It is shown that a very simple closed-form expression for the cross covariance and cross spectral density exists under WSS conditions, where the cross spectral density is the Fourier transform of the cross covariance. Use of the cross spectral density is then demonstrated in an analysis of noise in a radiographic screen with reabsorption. This problem was first solved by Metz and Vyborny[34] using a very different type of statistical analysis. Our work confirms their result, and is of a more general nature that is readily extended to describe reabsorption in

other imaging systems including digital flat-panel radiographic systems.

Throughout the following description, we use notation where the tilde (e.g., $\tilde{N}$) indicates a random variable, overline (e.g., $\overline{q}$) indicates a mean value and boldface (e.g., $\mathbf{r}$) indicates a vector. A table of symbols and definitions used is given in Appendix C.

## II. THEORY

The framework of this analysis is based in part on earlier works by Barrett *et al.*,[19,20] who developed the use of random point process theory for studying noise in imaging systems. A random point process is any random process for which all sample functions can be represented as a distribution of points, and we will represent each point as a spatial Dirac $\delta$ function. For instance, a quantum image is described as a spatial distribution of $\delta$ functions. However, these points may also represent a spatial distribution of certain events, such as a distribution of photoelectric events, or a distribution of photoelectric events when a $K$ x ray is reabsorbed.

A random point process is associated with two important quantities: the location of points in space where events occur and the number of such points.[33] The mathematical realization of a spatial point process can be expressed as a sequence of random impulses, given by

$$\tilde{q}(\mathbf{r}) = \sum_{n=1}^{\tilde{N}} \delta(\mathbf{r} - \tilde{\mathbf{r}}_n), \qquad (1)$$

where $\mathbf{r}$ is a multidimensional spatial coordinate vector in space $S$ where the point process is defined, $\tilde{\mathbf{r}}_n$ is a continuous random vector describing the location of the $n$th point falling in $S$, and $\tilde{N}$ is a random variable describing the number of points. The random vector ensemble describing the positions of all $\tilde{N}$ points is $\{\tilde{\mathbf{r}}_n : n = 1, 2, \dots, \tilde{N}\}$. In this section, we derive a general expression for the cross covariance of two correlated point processes drawing on previous work by Barrett *et al.*[19,20]

A quantum image is represented as a sample $q(\mathbf{r})$ of the random point process given by Eq. (1), where the space $S$ of points denotes the two-dimensional image area. Our analysis is also applicable to higher dimensional space. Although the size of $S$ is arbitrary, an infinite size is required for the analysis under WSS conditions, and hence we consider $S$ to be infinite in size.

### A. Cross covariance of point processes

For the general case, we consider two random spatial point processes (quantum images),

$$\tilde{q}_A(\mathbf{r}) = \sum_{n=1}^{\tilde{N}^A} \delta(\mathbf{r} - \tilde{\mathbf{r}}_n^A), \qquad (2)$$

and

$$\tilde{q}_B(\mathbf{r}) = \sum_{j=1}^{\tilde{N}^B} \delta(\mathbf{r} - \tilde{\mathbf{r}}_j^B), \qquad (3)$$

which may or may not be statistically correlated. The cross correlation of $\tilde{q}_A(\mathbf{r})$ and $\tilde{q}_B(\mathbf{r})$ is the mean of the product $q_A(\mathbf{r})q_B^*(\mathbf{r}')$,[2] i.e.,

$$R_{AB}(\mathbf{r},\mathbf{r}') = \langle \tilde{q}_A(\mathbf{r})\tilde{q}_B^*(\mathbf{r}') \rangle, \tag{4}$$

where an asterisk denotes a complex conjugate and angular brackets represents an expectation operator. The cross covariance of $\tilde{q}_A(\mathbf{r})$ and $\tilde{q}_B(\mathbf{r})$ is given by

$$K_{AB}(\mathbf{r},\mathbf{r}') = R_{AB}(\mathbf{r},\mathbf{r}') - \langle \tilde{q}_A(\mathbf{r})\rangle\langle \tilde{q}_B^*(\mathbf{r}')\rangle. \tag{5}$$

Barrett et al.[19,20] have shown that the mean of $\tilde{q}_A(\mathbf{r})$ in Eq. (2) is given by

$$\overline{q}_A(\mathbf{r}) = \langle \tilde{q}_A(\mathbf{r})\rangle = \left\langle \sum_{n=1}^{\tilde{N}^A} \mathrm{pr}_{\tilde{\mathbf{r}}_n^A}(\mathbf{r}|N^A) \right\rangle_{\tilde{N}^A}, \tag{6}$$

where $\mathrm{pr}_{\tilde{\mathbf{r}}_n^A}(\mathbf{r}|N^A)$ is the conditional probability density function of the process $\tilde{q}_A(\mathbf{r})$ describing the mean probability of finding the $n$th quantum at $\mathbf{r}_n = \mathbf{r}$ for a specified value of $N^A$, and we denote by $\langle\ \rangle_{\tilde{N}^A}$ the average over $\tilde{N}^A$. Similarly,

$$\overline{q}_B(\mathbf{r}) = \langle \tilde{q}_B(\mathbf{r})\rangle = \left\langle \sum_{j=1}^{\tilde{N}^B} \mathrm{pr}_{\tilde{\mathbf{r}}_j^B}(\mathbf{r}|N^B) \right\rangle_{\tilde{N}^B}. \tag{7}$$

If $\tilde{q}_A(\mathbf{r})$ is statistically independent of $\tilde{q}_B(\mathbf{r})$, the cross correlation $R_{AB}(\mathbf{r},\mathbf{r}')$ is equal to the product of their means, and the cross covariance $K_{AB}(\mathbf{r},\mathbf{r}')$ in Eq. (5) becomes zero. Spatial point processes $\tilde{q}_A(\mathbf{r})$ and $\tilde{q}_B(\mathbf{r})$ are then called uncorrelated.

In order to calculate the mean of the product $\tilde{q}_A(\mathbf{r})\tilde{q}_B^*(\mathbf{r}')$ in Eq. (4) where $\tilde{q}_A(\mathbf{r})$ and $\tilde{q}_B(\mathbf{r})$ may be statistically correlated, we must average over all random quantities $\{\tilde{\mathbf{r}}_n^A\}$, $\{\tilde{\mathbf{r}}_j^B\}$, $\tilde{N}^A$ and $\tilde{N}^B$ in processes $\tilde{q}_A(\mathbf{r})$ and $\tilde{q}_B(\mathbf{r}')$. The procedure is divided into two steps.[19] The first one is to take the conditional expectation of the continuous random quantities $\{\tilde{\mathbf{r}}_n^A\}$ and $\{\tilde{\mathbf{r}}_j^B\}$ for fixed $N^A$ and $N^B$. By definition of the statistical average over a continuous random variable, shown in Appendix D, we have

$$E\{\tilde{q}_A(\mathbf{r})\tilde{q}_B^*(\mathbf{r}')|N^A,N^B\}$$

$$= \int_\infty d\mathbf{r}_1^A \cdots \int_\infty d\mathbf{r}_{N^B}^B \left\{ \sum_{n=1}^{N^A} \delta(\mathbf{r}-\mathbf{r}_n^A)\sum_{j=1}^{N^B} \delta(\mathbf{r}'-\mathbf{r}_j^B) \right.$$

$$\left. \times \mathrm{pr}(\{\mathbf{r}_n^A\},\{\mathbf{r}_j^B\}|N^A,N^B) \right\}$$

$$= \sum_{n=1}^{N^A} \sum_{j=1}^{N^B} \int_\infty d\mathbf{r}_1^A \cdots \int_\infty d\mathbf{r}_{N^B}^B \{ \delta(\mathbf{r}-\mathbf{r}_n^A)\delta(\mathbf{r}'-\mathbf{r}_j^B)$$

$$\times \mathrm{pr}(\{\mathbf{r}_n^A\},\{\mathbf{r}_j^B\}|N^A,N^B) \}, \tag{8}$$

where $\mathrm{pr}(\{\mathbf{r}_n^A\},\{\mathbf{r}_j^B\}|N^A,N^B)$ is the conditional joint density function of random variables $\{\tilde{\mathbf{r}}_n^A\}$ and $\{\tilde{\mathbf{r}}_j^B\}$ given $N^A$ and $N^B$, and we use the symbol $\int_\infty$ to denote a multidimensional integral over all $S$. Using the property of marginal densities, shown in Appendix D, we obtain

$$E\{\tilde{q}_A(\mathbf{r})\tilde{q}_B^*(\mathbf{r}')|N^A,N^B\}$$

$$= \sum_{n=1}^{N^A} \sum_{j=1}^{N^B} \int_\infty d\mathbf{r}_n^A \int_\infty d\mathbf{r}_j^B \{ \delta(\mathbf{r}-\mathbf{r}_n^A)\delta(\mathbf{r}'-\mathbf{r}_j^B)$$

$$\times \mathrm{pr}_{\tilde{\mathbf{r}}_n^A,\tilde{\mathbf{r}}_j^B}(\mathbf{r}_n^A,\mathbf{r}_j^B|N^A,N^B) \}. \tag{9}$$

It follows from the sifting property of delta functions that

$$E\{\tilde{q}_A(\mathbf{r})\tilde{q}_B^*(\mathbf{r}')|N^A,N^B\}$$

$$= \sum_{n=1}^{N^A} \sum_{j=1}^{N^B} \mathrm{pr}_{\tilde{\mathbf{r}}_n^A,\tilde{\mathbf{r}}_j^B}(\mathbf{r},\mathbf{r}'|N^A,N^B), \tag{10}$$

where $\mathrm{pr}_{\tilde{\mathbf{r}}_n^A,\tilde{\mathbf{r}}_j^B}(\mathbf{r},\mathbf{r}'|N^A,N^B)$ is the conditional joint density function of $\tilde{\mathbf{r}}_n^A$ and $\tilde{\mathbf{r}}_j^B$ for fixed $N^A$ and $N^B$, evaluated at $\mathbf{r}_n^A = \mathbf{r}$ and $\mathbf{r}_j^B = \mathbf{r}'$. Next, by averaging Eq. (10) over $\tilde{N}^A$ and $\tilde{N}^B$, we obtain the cross correlation of $\tilde{q}_A(\mathbf{r})$ and $\tilde{q}_B(\mathbf{r})$ given by

$$R_{AB}(\mathbf{r},\mathbf{r}') = \left\langle \sum_{n=1}^{\tilde{N}^A} \sum_{j=1}^{\tilde{N}^B} \mathrm{pr}_{\tilde{\mathbf{r}}_n^A,\tilde{\mathbf{r}}_j^B}(\mathbf{r},\mathbf{r}'|N^A,N^B) \right\rangle_{\tilde{N}^A,\tilde{N}^B}. \tag{11}$$

From Eqs. (5) to (7) and (11), therefore, the cross covariance of $\tilde{q}_A(\mathbf{r})$ and $\tilde{q}_B(\mathbf{r})$ is given by

$$K_{AB}(\mathbf{r},\mathbf{r}') = \left\langle \sum_{n=1}^{\tilde{N}^A} \sum_{j=1}^{\tilde{N}^B} \mathrm{pr}_{\tilde{\mathbf{r}}_n^A,\tilde{\mathbf{r}}_j^B}(\mathbf{r},\mathbf{r}'|N^A,N^B) \right\rangle_{\tilde{N}^A,\tilde{N}^B}$$

$$- \left\langle \sum_{n=1}^{\tilde{N}^A} \mathrm{pr}_{\tilde{\mathbf{r}}_n^A}(\mathbf{r}|N^A) \right\rangle_{\tilde{N}^A} \left\langle \sum_{j=1}^{\tilde{N}^B} \mathrm{pr}_{\tilde{\mathbf{r}}_j^B}(\mathbf{r}'|N^B) \right\rangle_{\tilde{N}^B}. \tag{12}$$

Without loss of generality we assume that each point has the same conditional probability density function for given $N^A$ or $N^B$. The probability density functions are therefore independent of the indices $n$ and $j$ and we simplify our notation by using $\tilde{\mathbf{r}}^A$ and $\tilde{\mathbf{r}}^B$ instead of $\tilde{\mathbf{r}}_n^A$ and $\tilde{\mathbf{r}}_j^B$. Thus, Eq. (12) becomes

$$K_{AB}(\mathbf{r},\mathbf{r}') = \langle \tilde{N}^A\tilde{N}^B \mathrm{pr}_{\tilde{\mathbf{r}}^A,\tilde{\mathbf{r}}^B}(\mathbf{r},\mathbf{r}'|N^A,N^B)\rangle_{\tilde{N}^A,\tilde{N}^B}$$

$$- \langle \tilde{N}^A \mathrm{pr}_{\tilde{\mathbf{r}}^A}(\mathbf{r}|N^A)\rangle_{\tilde{N}^A}\langle \tilde{N}^B \mathrm{pr}_{\tilde{\mathbf{r}}^B}(\mathbf{r}'|N^B)\rangle_{\tilde{N}^B}, \tag{13}$$

where the $\tilde{N}^A \times \tilde{N}^B$ terms in the double sum over $n$ and $j$ are identical.

Equation (13) is a general expression for the cross covariance of two random point processes under both stationary and nonstationary conditions. For imaging applications where, in general, $\tilde{N}^A, \tilde{N}^B \gg 1$ and the probability density and the joint density functions are independent of $N^A$ and $N^B$, the statistical nature of $\tilde{N}^A$ and $\tilde{N}^B$ can often be ignored and the cross covariance of two quantum images is then given by

$$K_{AB}(\mathbf{r},\mathbf{r}') \approx N^A N^B[\mathrm{pr}_{\tilde{\mathbf{r}}^A,\tilde{\mathbf{r}}^B}(\mathbf{r},\mathbf{r}') - \mathrm{pr}_{\tilde{\mathbf{r}}^A}(\mathbf{r})\mathrm{pr}_{\tilde{\mathbf{r}}^B}(\mathbf{r}')]. \tag{14}$$

## B. Cross covariance of random subsets of a random point process

If the quanta in two images are independent of each other, the cross covariance of the two images will be zero. This is certainly the case when two images are acquired independently of each other. However, we are interested in the special case where two point distributions (images) are not independent, but are each random subsets of a common input point distribution or image. If quanta in the input image are statistically correlated, there will in general be a nonzero cross covariance between the two subsets.

The process of randomly selecting points from a distribution is illustrated in Fig. 1. This random process represents a sequence of independent trials in which each trial makes a random determination for each point in the input distribution. The point is selected to path $A$ with probability $\overline{\xi}$, and path $B$ with probability $\overline{\zeta}$. That is, each trial is described in terms of two binomial random variables, denoted by $\widetilde{\xi}_n$ and $\widetilde{\zeta}_n$ for the $n$th trial, where each random variable can have a value of 0 or 1 only. Each trial is independent of all others, but we will allow statistical relationships between variables $\widetilde{\xi}_n$ and $\widetilde{\zeta}_n$ for a given trial $n$. For $N$ trials, the set of random variables $\widetilde{\xi}_n$ and $\widetilde{\zeta}_n$ required to describe a single image is given by $\{\widetilde{\xi}_n, \widetilde{\zeta}_n : n=1,2,\ldots,N\}$.

Similar to Eq. (1), the input is a general spatial point process rewritten as

$$\widetilde{q}_{\text{in}}(\mathbf{r}) = \sum_{n=1}^{\widetilde{N}} \delta(\mathbf{r} - \widetilde{\mathbf{R}}_n), \tag{15}$$

where $\widetilde{\mathbf{R}}_n$ is a random vector describing the position of the $n$th quantum in the input image. The point selection process is assumed to be independent of $\widetilde{q}_{\text{in}}(\mathbf{r})$. The outputs $\widetilde{q}_A(\mathbf{r})$ and $\widetilde{q}_B(\mathbf{r})$ can therefore be written in terms of the random variables $\widetilde{\xi}_n$ and $\widetilde{\zeta}_n$ as

$$\widetilde{q}_A(\mathbf{r}) = \sum_{n=1}^{\widetilde{N}} \widetilde{\xi}_n \, \delta(\mathbf{r} - \widetilde{\mathbf{R}}_n),$$

$$\tag{16}$$

$$\widetilde{q}_B(\mathbf{r}) = \sum_{n=1}^{\widetilde{N}} \widetilde{\zeta}_n \, \delta(\mathbf{r} - \widetilde{\mathbf{R}}_n).$$
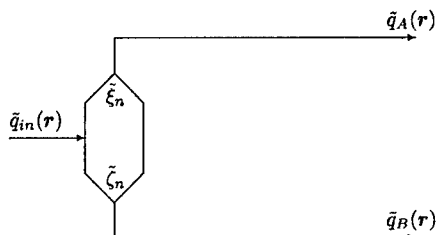


FIG. 1. Illustration of randomly selecting points from a random point process. Both $\widetilde{q}_A(\mathbf{r})$ and $\widetilde{q}_B(\mathbf{r})$ represent randomly selected subsets of the input point process $\widetilde{q}_{\text{in}}(\mathbf{r})$.

In Eq. (16), the point processes $\widetilde{q}_A(\mathbf{r})$ and $\widetilde{q}_B(\mathbf{r})$ are random subsets of $\widetilde{q}_{\text{in}}(\mathbf{r})$. We are interested in the cross covariance of $\widetilde{q}_A(\mathbf{r})$ and $\widetilde{q}_B(\mathbf{r})$. In the following, we examine both first-order and second-order statistics.

### 1. Mean

We calculate the mean of $\widetilde{q}_A(\mathbf{r})$ in Eq. (16) in two steps. The first step is to take the conditional expectation of $\widetilde{q}_A(\mathbf{r})$ for fixed $\{\mathbf{R}_n\}$ and $N$, i.e., for fixed $q_{\text{in}}(\mathbf{r})$ refering to the sample space of $\widetilde{q}_{\text{in}}(\mathbf{r})$, and then to average over $\widetilde{q}_{\text{in}}(\mathbf{r})$. Thus, we have

$$E\{\widetilde{q}_A(\mathbf{r})|q_{\text{in}}(\mathbf{r})\} = \left\langle \sum_{n=1}^{\widetilde{N}} \widetilde{\xi}_n \delta(\mathbf{r} - \widetilde{\mathbf{R}}_n) \middle| q_{\text{in}}(\mathbf{r}) \right\rangle_{\widetilde{\xi}_n}$$

$$= \sum_{n=1}^{N} E\{\widetilde{\xi}_n\} \delta(\mathbf{r} - \mathbf{R}_n)|_{q_{\text{in}}(\mathbf{r})}$$

$$= \overline{\xi} \sum_{n=1}^{N} \delta(\mathbf{r} - \mathbf{R}_n) = \overline{\xi} \, q_{\text{in}}(\mathbf{r}), \tag{17}$$

where $\widetilde{\xi}_n$ has the same mean value for all $n$, given by $\overline{\xi}$, and we use the symbol $|_{q_{\text{in}}(\mathbf{r})}$ to denote the computation condition, i.e., for fixed $q_{\text{in}}(\mathbf{r})$. Next, by averaging over $\widetilde{q}_{\text{in}}(\mathbf{r})$, we obtain the mean of $\widetilde{q}_A(\mathbf{r})$ given by

$$\overline{q}_A(\mathbf{r}) = E\{\widetilde{q}_A(\mathbf{r})\} = \overline{\xi} \, \overline{q}_{\text{in}}(\mathbf{r}). \tag{18}$$

Similarly,

$$\overline{q}_B(\mathbf{r}) = E\{\widetilde{q}_B(\mathbf{r})\} = \overline{\zeta} \, \overline{q}_{\text{in}}(\mathbf{r}). \tag{19}$$

### 2. Cross correlation and cross covariance

The cross correlation of $\widetilde{q}_A(\mathbf{r})$ and $\widetilde{q}_B(\mathbf{r})$, $R_{AB}(\mathbf{r},\mathbf{r}')$, is the mean of the product $\widetilde{q}_A(\mathbf{r})\widetilde{q}_B^*(\mathbf{r}')$, i.e.,

$$R_{AB}(\mathbf{r},\mathbf{r}') = E\{\widetilde{q}_A(\mathbf{r})\widetilde{q}_B^*(\mathbf{r}')\}$$

$$= \left\langle \sum_{n=1}^{\widetilde{N}} \widetilde{\xi}_n \, \delta(\mathbf{r} - \widetilde{\mathbf{R}}_n) \sum_{j=1}^{\widetilde{N}} \widetilde{\zeta}_j \, \delta(\mathbf{r}' - \widetilde{\mathbf{R}}_j) \right\rangle. \tag{20}$$

Again, using an approach similar to Barrett et al.,[19] computation of the expectation in Eq. (20) is divided into two steps. That is, the first one is to average over $\{\widetilde{\xi}_n\}$ and $\{\widetilde{\zeta}_n\}$ for fixed input $q_{\text{in}}(\mathbf{r})$, and then average over $\widetilde{q}_{\text{in}}(\mathbf{r})$. There are two cases to be considered in Eq. (20), corresponding to $n = j$ and $n \neq j$. When $n = j$, which has $N$ terms,

$$E\{\widetilde{q}_A(\mathbf{r})\widetilde{q}_B^*(\mathbf{r}')|q_{\text{in}}(\mathbf{r})\}|_{n=j}$$

$$= \left\langle \sum_{n=1}^{\widetilde{N}} \widetilde{\xi}_n \widetilde{\zeta}_n \, \delta(\mathbf{r} - \widetilde{\mathbf{R}}_n) \delta(\mathbf{r}' - \widetilde{\mathbf{R}}_n)|q_{\text{in}}(\mathbf{r}) \right\rangle_{\widetilde{\xi}_n,\widetilde{\zeta}_n}\Bigg|_{n=j}.$$

$$\tag{21}$$

It is convenient to denote the cross correlation of $\widetilde{\xi}_n$ and $\widetilde{\zeta}_n$ for $n=1,2,\ldots,N$ as $R_{\xi\zeta} = E\{\widetilde{\xi}_n\widetilde{\zeta}_n\}$. It is nonzero when the two random variables are nonorthogonal. For instance, if the two images $A$ and $B$ represent identical subsets of the input

distribution, where $\tilde{\zeta}_n = \tilde{\xi}_n$, they are correlated and the cross correlation of $\tilde{\xi}_n$ and $\tilde{\zeta}_n$ is $R_{\xi\zeta}$. If the two images represent complementary subsets, where there are no common points in $A$ and $B$, then $\tilde{\zeta}_n$ is orthogonal with $\tilde{\xi}_n$, i.e., $\tilde{\zeta}_n = (1 - \tilde{\xi}_n)$ and $R_{\xi\zeta} = 0$. With this notation, we have

$$E\{\tilde{q}_A(\mathbf{r})\tilde{q}_B^*(\mathbf{r}')|q_{in}(\mathbf{r})\}|_{n=j}$$

$$= R_{\xi\zeta}\sum_{n=1}^{N} \delta(\mathbf{r}-\mathbf{R}_n)\delta(\mathbf{r}'-\mathbf{R}_n)|_{n=j}$$

$$= R_{\xi\zeta}\, q_{in}(\mathbf{r})q_{in}(\mathbf{r}')|_{n=j}. \tag{22}$$

When $n \neq j$, the random variable $\tilde{\xi}_n$ is independent of $\tilde{\zeta}_j$ and $E\{\tilde{\xi}_n\tilde{\zeta}_j\} = \bar{\xi}\bar{\zeta}$. In this case, we have

$$E\{\tilde{q}_A(\mathbf{r})\tilde{q}_B^*(\mathbf{r}')|q_{in}(\mathbf{r})\}|_{n \neq j}$$

$$= \left\langle \sum_{n=1}^{\tilde{N}} \sum_{j=1}^{\tilde{N}} \tilde{\xi}_n\tilde{\zeta}_j\, \delta(\mathbf{r}-\tilde{\mathbf{R}}_n)\delta(\mathbf{r}'-\tilde{\mathbf{R}}_j)|q_{in}(\mathbf{r}) \right\rangle_{\tilde{\xi}_n,\tilde{\zeta}_j}\Bigg|_{n \neq j}$$

$$= \bar{\xi}\bar{\zeta}\sum_{n=1}^{N} \sum_{j=1}^{N} \delta(\mathbf{r}-\mathbf{R}_n)\delta(\mathbf{r}'-\mathbf{R}_j)|_{n \neq j}$$

$$= \bar{\xi}\bar{\zeta}\, q_{in}(\mathbf{r})q_{in}(\mathbf{r}')|_{n \neq j}. \tag{23}$$

Adding Eqs. (22) and (23), the conditional expectation of the product $\tilde{q}_A(\mathbf{r})\tilde{q}_B^*(\mathbf{r}')$ is given by

$$E\{\tilde{q}_A(\mathbf{r})\tilde{q}_B^*(\mathbf{r}')|q_{in}(\mathbf{r})\}$$

$$= R_{\xi\zeta}\, q_{in}(\mathbf{r})q_{in}(\mathbf{r}')|_{n=j} + \bar{\xi}\bar{\zeta}\, q_{in}(\mathbf{r})q_{in}(\mathbf{r}')|_{n \neq j}, \tag{24}$$

which after averaging over $\tilde{q}_{in}(\mathbf{r})$ yields

$$R_{AB}(\mathbf{r},\mathbf{r}') = R_{\xi\zeta}R_{in}(\mathbf{r},\mathbf{r}')|_{n=j} + \bar{\xi}\bar{\zeta}R_{in}(\mathbf{r},\mathbf{r}')|_{n \neq j}, \tag{25}$$

where $R_{in}(\mathbf{r},\mathbf{r}') = E\{\tilde{q}_{in}(\mathbf{r})\tilde{q}_{in}^*(\mathbf{r}')\}$ is the autocorrelation of $\tilde{q}_{in}(\mathbf{r})$ and can be expressed as

$$R_{in}(\mathbf{r},\mathbf{r}') = R_{in}(\mathbf{r},\mathbf{r}')|_{n=j} + R_{in}(\mathbf{r},\mathbf{r}')|_{n \neq j}. \tag{26}$$
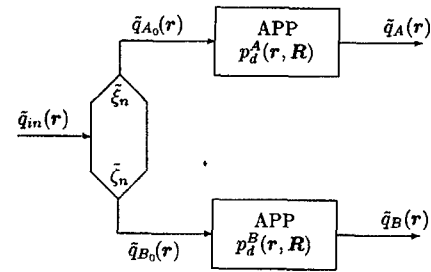
Equation (25) can be further simplified by noting that for a general point process as in Eq. (15), we have[19,20]

$$R_{in}(\mathbf{r},\mathbf{r}')|_{n=j} = \bar{q}_{in}(\mathbf{r})\delta(\mathbf{r}-\mathbf{r}'). \tag{27}$$

From Eqs. (25) to (27), therefore, the cross correlation of $\tilde{q}_A(\mathbf{r})$ and $\tilde{q}_B(\mathbf{r})$ becomes

$$R_{AB}(\mathbf{r},\mathbf{r}')$$

$$= R_{\xi\zeta}R_{in}(\mathbf{r},\mathbf{r}')|_{n=j} + \bar{\xi}\bar{\zeta}[R_{in}(\mathbf{r},\mathbf{r}') - R_{in}(\mathbf{r},\mathbf{r}')|_{n=j}]$$

$$= (R_{\xi\zeta} - \bar{\xi}\bar{\zeta})R_{in}(\mathbf{r},\mathbf{r}')|_{n=j} + \bar{\xi}\bar{\zeta}R_{in}(\mathbf{r},\mathbf{r}')$$

$$= (R_{\xi\zeta} - \bar{\xi}\bar{\zeta})\bar{q}_{in}(\mathbf{r})\delta(\mathbf{r}-\mathbf{r}') + \bar{\xi}\bar{\zeta}R_{in}(\mathbf{r},\mathbf{r}')$$

$$= K_{\xi\zeta}\bar{q}_{in}(\mathbf{r})\delta(\mathbf{r}-\mathbf{r}') + \bar{\xi}\bar{\zeta}R_{in}(\mathbf{r},\mathbf{r}'), \tag{28}$$

where $K_{\xi\zeta}$ is the cross covariance of random variables $\tilde{\xi}_n$ and $\tilde{\zeta}_n$, given by $K_{\xi\zeta} = R_{\xi\zeta} - \bar{\xi}\bar{\zeta}$.



†APP: Amplified Point Process

Fig. 2. Schematic illustration of two parallel amplified point processes. Building on Fig. 1, $\tilde{q}_{A_0}(\mathbf{r})$ and $\tilde{q}_{B_0}(\mathbf{r})$ represent random subsets of an input point process $\tilde{q}_{in}(\mathbf{r})$, that each subsequently undergo an amplified point process.

Finally, the cross covariance of $\tilde{q}_A(\mathbf{r})$ and $\tilde{q}_B(\mathbf{r})$ is given by

$$K_{AB}(\mathbf{r},\mathbf{r}') = R_{AB}(\mathbf{r},\mathbf{r}') - \bar{q}_A(\mathbf{r})\bar{q}_B(\mathbf{r}')$$

$$= K_{\xi\zeta}\bar{q}_{in}(\mathbf{r})\delta(\mathbf{r}-\mathbf{r}') + \bar{\xi}\bar{\zeta}R_{in}(\mathbf{r},\mathbf{r}')$$

$$- \bar{q}_A(\mathbf{r})\bar{q}_B(\mathbf{r}'). \tag{29}$$

Combining this result with Eqs. (18) and (19) gives

$$K_{AB}(\mathbf{r},\mathbf{r}') = K_{\xi\zeta}\bar{q}_{in}(\mathbf{r})\delta(\mathbf{r}-\mathbf{r}') + \bar{\xi}\bar{\zeta}K_{in}(\mathbf{r},\mathbf{r}'), \tag{30}$$

where $K_{in}(\mathbf{r},\mathbf{r}')$ is the autocovariance of the input point process $\tilde{q}_{in}(\mathbf{r})$.

Equation (30) is a general expression for the cross covariance of $\tilde{q}_A(\mathbf{r})$ and $\tilde{q}_B(\mathbf{r})$, where each is a random subset of the input point process. It consists of two components. The first represents uncorrelated noise given as a $\delta$ function scaled by the cross covariance $K_{\xi\zeta}$ of the two binomial random variables and the mean number $\bar{q}_{in}(\mathbf{r})$ of quanta per unit area in the input. This component is zero when $A$ and $B$ represent independent subsets of the input, and nonzero otherwise. The second component represents correlated noise and is proportional to the cross covariance of the input point process, $K_{in}(\mathbf{r},\mathbf{r}')$.

## C. Cross covariance following an amplified point process

A more general case involves the cross covariance of two point processes that undergo point amplification subsequent to selection as illustrated in Fig. 2. In Fig. 2, $\tilde{q}_{A_0}(\mathbf{r})$ and $\tilde{q}_{B_0}(\mathbf{r})$ each represent subsets of the input point process $\tilde{q}_{in}(\mathbf{r})$. The distributions $\tilde{q}_A(\mathbf{r})$ and $\tilde{q}_B(\mathbf{r})$ represent the results of each subset undergoing a subsequent independent amplified point process. Following the work of Rabbani, Shaw, and Van Metter,[13] and Barrett et al.,[19,20] an amplified point process is considered to be a random point process where each point is converted into a random "cluster" of $\tilde{k}_n$ secondary points distributed by the random vectors $\{\tilde{\boldsymbol{\Delta}}_{nk}: k = 1,2,...,\tilde{k}_n\}$. This can be expressed as a cascade of the elementary processes quantum gain and quantum scatter, de-

scribed in Appendix A. If each amplification process is independent of all others, the point processes $\tilde{q}_A(\mathbf{r})$ and $\tilde{q}_B(\mathbf{r})$ in Fig. 2 can be written as

$$\tilde{q}_A(\mathbf{r}) = \sum_{n=1}^{\tilde{N}} \tilde{\xi}_n \sum_{k=1}^{\tilde{k}_n^A} \delta(\mathbf{r} - \tilde{\mathbf{R}}_n - \tilde{\mathbf{\Delta}}_{nk}^A),$$

$$\tilde{q}_B(\mathbf{r}) = \sum_{n=1}^{\tilde{N}} \tilde{\zeta}_n \sum_{k=1}^{\tilde{k}_n^B} \delta(\mathbf{r} - \tilde{\mathbf{R}}_n - \tilde{\mathbf{\Delta}}_{nk}^B),$$

(31)

where the $n$th input quantum randomly located at $\tilde{\mathbf{R}}_n$, if passed to paths $A$ and $B$ produce $\tilde{k}_n^A$ and $\tilde{k}_n^B$ quanta, respectively, and

$$\tilde{\mathbf{r}}_{nk}^A \triangleq \tilde{\mathbf{R}}_n + \tilde{\mathbf{\Delta}}_{nk}^A$$

and

$$\tilde{\mathbf{r}}_{nk}^B \triangleq \tilde{\mathbf{R}}_n + \tilde{\mathbf{\Delta}}_{nk}^B$$

are random vectors describing the positions of the $k$th quantum produced by the $n$th primary in the image plane for each path. As assumed by Barrett et al.,[19,20] we assume the random displacements $\tilde{\mathbf{\Delta}}_{nk}^A$ and $\tilde{\mathbf{\Delta}}_{nk}^B$ are independent of all others, possibly depending on the position of the primary for nonstationary processes.

Denote by $\mathrm{pr}_\Delta^A(\mathbf{\Delta}_{nk}^A|\mathbf{R}_n)$ the univariate probability density function of

$$\{\tilde{\mathbf{\Delta}}_{nk}^A : k = 1, 2, \ldots, \tilde{k}_n; n = 1, 2, \ldots, \tilde{N}\}$$

given the primary $\mathbf{R}_n$. The following relationship is then known:[19,20]

$$\mathrm{pr}_\Delta^A(\mathbf{\Delta}_{nk}^A|\mathbf{R}_n) = [\overline{k}_n^A(\mathbf{R}_n)]^{-1} p_d^A(\mathbf{\Delta}_{nk}^A + \mathbf{R}_n, \mathbf{R}_n),$$

(32)

where the mean number $\overline{k}_n^A(\mathbf{R}_n)$ of secondaries resulting from primary $\mathbf{R}_n$ in path $A$ is

$$\overline{k}_n^A(\mathbf{R}_n) = \int_\infty d\mathbf{r}\, p_d^A(\mathbf{r}, \mathbf{R}_n),$$

(33)

and $p_d^A(\mathbf{r}, \mathbf{R}_n)$, for path $A$, is defined as the mean distribution of secondaries at $\mathbf{r}$ when a primary is absorbed at $\mathbf{R}_n$. Similarly for path $B$, we have

$$\mathrm{pr}_\Delta^B(\mathbf{\Delta}_{nk}^B|\mathbf{R}_n) = [\overline{k}_n^B(\mathbf{R}_n)]^{-1} p_d^B(\mathbf{\Delta}_{nk}^B + \mathbf{R}_n, \mathbf{R}_n),$$

(34)

where $\mathrm{pr}_\Delta^B(\mathbf{\Delta}_{nk}^B|\mathbf{R}_n)$ is the univariate probability density function of $\{\tilde{\mathbf{\Delta}}_{nk}^B\}$ given $\mathbf{R}_n$, and

$$\overline{k}_n^B(\mathbf{R}_n) = \int_\infty d\mathbf{r}\, p_d^B(\mathbf{r}, \mathbf{R}_n).$$

(35)

We now examine the means and cross covariance of $\tilde{q}_A(\mathbf{r})$ and $\tilde{q}_B(\mathbf{r})$ for these amplification processes.

### 1. Mean

The mean of the point processes $\tilde{q}_A(\mathbf{r})$ and $\tilde{q}_B(\mathbf{r})$ are calculated using an approach similar to that described by Barrett et al.[19] For path $A$, the procedure is as follows:

(a)   average over displacements $\{\tilde{\mathbf{\Delta}}_{nk}^A\}$ for fixed $\mathbf{R}_n$,

(b)   average over number $\tilde{k}_n^A$ of secondaries for fixed $\mathbf{R}_n$,

(c)   average over binomial random variables $\tilde{\xi}_n$ for fixed $q_{\mathrm{in}}(\mathbf{r})$,

(d)   average over positions $\{\tilde{\mathbf{R}}_n\}$ of input quanta for fixed $N$, and

(e)   average over total number $\tilde{N}$ of input quanta to get the result $E\{\tilde{q}_A(\mathbf{r})\}$.

Steps (a) and (b) calculate the conditional expectation of secondary points given a primary. Step (c) averages over the selection of quanta entering path $A$ for fixed input. An average over the input point process is obtained in steps (d) and (e). In an attempt to simplify the notation, we will use the step label as a subscript to express the result of a step (a)–(e). For example, denote by $E_{(a)}\{\tilde{q}_A(\mathbf{r})\}$ the result of step (a).

Step (a) is the statistical average over the continuous random vectors $\{\mathbf{\Delta}_{nk}^A\}$ given $\mathbf{R}_n$. In a similar way to Eqs. (8)–(10), we can obtain

$$E_{(a)}\{\tilde{q}_A(\mathbf{r})\} = \sum_{n=1}^{N} \xi_n \sum_{k=1}^{k_n^A} [\overline{k}_n^A(\mathbf{R}_n)]^{-1} p_d^A(\mathbf{r}, \mathbf{R}_n),$$

(36)

where the probability density function $\mathrm{pr}_\Delta^A(\mathbf{\Delta}_{nk}^A|\mathbf{R}_n)$ has been expressed in terms of $p_d^A(\mathbf{r}, \mathbf{R}_n)$ from Eq. (32). We can simplify Eq. (36) into

$$E_{(a)}\{\tilde{q}_A(\mathbf{r})\} = \sum_{n=1}^{N} \xi_n k_n^A [\overline{k}_n^A(\mathbf{R}_n)]^{-1} p_d^A(\mathbf{r}, \mathbf{R}_n),$$

(37)

since the kernel in the sum over $k$ is independent of $k$.

Step (b) requires the average of Eq. (37) over discrete value $\tilde{k}_n^A$ given $\mathbf{R}_n$. This leads to cancellation of $[\overline{k}_n^A(\mathbf{R}_n)]^{-1}$ in Eq. (37) because of the conditional expectation of $\tilde{k}_n^A$ given $\mathbf{R}_n$ as shown by $E_{(b)}\{\tilde{k}_n^A\} = \overline{k}_n^A(\mathbf{R}_n)$. Thus

$$E_{(b)}\{\tilde{q}_A(\mathbf{r})\} = E_{(b)}\{E_{(a)}\{\tilde{q}_A(\mathbf{r})\}\} = \sum_{n=1}^{N} \xi_n p_d^A(\mathbf{r}, \mathbf{R}_n).$$

(38)

Step (c) can be obtained simply by replacing $\xi_n$ in Eq. (38) with $\overline{\xi}$ since $\tilde{\xi}_n$ is independent of all other terms for given $\mathbf{R}_n$, i.e.,

$$E_{(c)}\{\tilde{q}_A(\mathbf{r})\} = E_{(c)}\{E_{(b)}\{\tilde{q}_A(\mathbf{r})\}\} = \sum_{n=1}^{N} \overline{\xi} p_d^A(\mathbf{r}, \mathbf{R}_n).$$

(39)

Step (d), averaging over the positions $\{\tilde{\mathbf{R}}_n\}$ of input quanta, is obtained by using Eq. (D6), giving

$$E_{(d)}\{\tilde{q}_A(\mathbf{r})\}$$

$$= \int_\infty d\mathbf{R}_1 \cdots \int_\infty d\mathbf{R}_N \sum_{n=1}^{N} \overline{\xi} p_d^A(\mathbf{r}, \mathbf{R}_n) \mathrm{pr}_{\{\tilde{\mathbf{R}}_n\}}(\{\mathbf{R}_n\}|N)$$

$$= \sum_{n=1}^{N} \overline{\xi} \int_\infty d\mathbf{R}_1 \cdots \int_\infty d\mathbf{R}_N\, p_d^A(\mathbf{r}, \mathbf{R}_n) \mathrm{pr}_{\{\tilde{\mathbf{R}}_n\}}(\{\mathbf{R}_n\}|N).$$

(40)

The nested integrals of the joint density function over $\{\widetilde{\mathbf{R}}_n\}$ except the one with $n$ is represented as the marginal density $\mathrm{pr}_{\bar{\mathbf{R}}_n}(\mathbf{R}_n|N)$ using the property of marginal density as described by Eq. (D5). Thus,

$$E_{(d)}\{\widetilde{q}_A(\mathbf{r})\} = \sum_{n=1}^{N} \overline{\xi} \int_{\infty} d\mathbf{R}_n\, p_d^A(\mathbf{r},\mathbf{R}_n)\mathrm{pr}_{\bar{\mathbf{R}}_n}(\mathbf{R}_n|N)$$

$$= \sum_{n=1}^{N} \overline{\xi} \int_{\infty} d\mathbf{R}\, p_d^A(\mathbf{r},\mathbf{R})\mathrm{pr}_{\bar{\mathbf{R}}_n}(\mathbf{R}|N), \qquad (41)$$

where the integration variable $\mathbf{R}_n$ is renamed $\mathbf{R}$ in the last line. Since the conditional expectation of $\widetilde{q}_{\mathrm{in}}(\mathbf{r})$ for fixed $N$ is given by [see Eq. (6)]

$$E\{\widetilde{q}_{\mathrm{in}}(\mathbf{r})|N\} = \sum_{n=1}^{N} \mathrm{pr}_{\bar{\mathbf{R}}_n}(\mathbf{r}|N), \qquad (42)$$

then Eq. (41) becomes

$$E_{(d)}\{\widetilde{q}_A(\mathbf{r})\} = \overline{\xi} \int_{\infty} d\mathbf{R}\, p_d^A(\mathbf{r},\mathbf{R}) E\{\widetilde{q}_{\mathrm{in}}(\mathbf{R})|N\}. \qquad (43)$$

Step (e), the average of Eq. (43) over $\widetilde{N}$, yields

$$\overline{q}_A(\mathbf{r}) = \overline{\xi} \int_{\infty} d\mathbf{R}\, p_d^A(\mathbf{r},\mathbf{R})\overline{q}_{\mathrm{in}}(\mathbf{R}), \qquad (44)$$

where $\overline{q}_{(\mathrm{in})}(\mathbf{R})$ was obtained by averaging $E\{\widetilde{q}_{\mathrm{in}}(\mathbf{R})|N\}$ over $\widetilde{N}$. Since $\overline{q}_{A_0}(\mathbf{r}) = \overline{\xi}\,\overline{q}_{\mathrm{in}}(\mathbf{r})$, where point process $\widetilde{q}_{A_0}(\mathbf{r})$ is the output of the point-selection process for path $A$ (see Fig. 2), we obtain

$$\overline{q}_A(\mathbf{r}) = \int_{\infty} d\mathbf{R}\, p_d^A(\mathbf{r},\mathbf{R})\overline{q}_{A_0}(\mathbf{R}). \qquad (45)$$

Equations (44) and (45) are general expressions for the mean of an amplified point process. Similarly, the mean of $\widetilde{q}_B(\mathbf{r})$ is given by

$$\overline{q}_B(\mathbf{r}) = \overline{\zeta} \int_{\infty} d\mathbf{R}\, p_d^B(\mathbf{r},\mathbf{R})\overline{q}_{\mathrm{in}}(\mathbf{R})$$

$$= \int_{\infty} d\mathbf{R}\, p_d^B(\mathbf{r},\mathbf{R})\overline{q}_{B_0}(\mathbf{R}). \qquad (46)$$

### 2. Cross correlation and cross covariance

We now calculate the cross correlation for the output point processes $\widetilde{q}_A(\mathbf{r})$ and $\widetilde{q}_B(\mathbf{r})$. By definition, $R_{AB}(\mathbf{r},\mathbf{r}')$ is given by

$$R_{AB}(\mathbf{r},\mathbf{r}') = E\{\widetilde{q}_A(\mathbf{r})\widetilde{q}_B^*(\mathbf{r}')\}$$

$$= \left\langle \sum_{n=1}^{\widetilde{N}} \widetilde{\xi}_n \sum_{k=1}^{\widetilde{k}_n^A} \delta(\mathbf{r}-\widetilde{\mathbf{R}}_n-\widetilde{\mathbf{\Delta}}_{nk}^A)\sum_{n=1}^{\widetilde{N}} \widetilde{\zeta}_n \right.$$

$$\left. \times \sum_{k=1}^{\widetilde{k}_n^B} \delta(\mathbf{r}'-\widetilde{\mathbf{R}}_n-\widetilde{\mathbf{\Delta}}_{nk}^B) \right\rangle. \qquad (47)$$

Similar to the computation of the mean of $\widetilde{q}_A(\mathbf{r})$, we calculate the expectation in Eq. (47) by the five steps (a)–(e)

shown previously. Step (a) is to average over displacements $\{\widetilde{\mathbf{\Delta}}_{nk}^A\}$ in $\widetilde{q}_A(\mathbf{r})$ and $\{\widetilde{\mathbf{\Delta}}_{nk}^B\}$ in $\widetilde{q}_B(\mathbf{r})$ for fixed $\{\mathbf{R}_n\}$, denoted by $E_{(a)}\{\widetilde{q}_A(\mathbf{r})\widetilde{q}_B(\mathbf{r}')\}$. Step (b) is to average over $\widetilde{k}_n^A$ and $\widetilde{k}_n^B$ for fixed $\{\mathbf{R}_n\}$, denoted by $E_{(b)}\{\widetilde{q}_A(\mathbf{r})\widetilde{q}_B(\mathbf{r}')\}$. We assume the point amplification processes in paths $A$ and $B$ may depend on incident locations $\{\mathbf{R}_n\}$, but are independent of all other terms. That is, both the gain factors $\{\widetilde{k}_n^A\}$ and $\{\widetilde{k}_n^B\}$ are independent for all $n$ and the scatter vectors $\{\widetilde{\mathbf{\Delta}}_{nk}^A\}$ and $\{\widetilde{\mathbf{\Delta}}_{nk}^B\}$ are independent for all $n$ and $k$. Therefore, we can write down the results for steps (a) and (b) as

$$E_{(a)}\{\widetilde{q}_A(\mathbf{r})\widetilde{q}_B(\mathbf{r}')\} = E_{(a)}\{\widetilde{q}_A(\mathbf{r})\} E_{(a)}\{\widetilde{q}_B(\mathbf{r}')\} \qquad (48)$$

and

$$E_{(b)}\{\widetilde{q}_A(\mathbf{r})\widetilde{q}_B(\mathbf{r}')\} = E_{(b)}\{\widetilde{q}_A(\mathbf{r})\} E_{(b)}\{\widetilde{q}_B(\mathbf{r}')\}, \qquad (49)$$

respectively. From Eq. (38) and

$$E_{(b)}\{\widetilde{q}_B(\mathbf{r}')\} = \sum_{j=1}^{N} \zeta_j\, p_d^B(\mathbf{r}',\mathbf{R}_j), \qquad (50)$$

we can obtain the following result:

$$E_{(b)}\{\widetilde{q}_A(\mathbf{r})\widetilde{q}_B(\mathbf{r}')\} = \sum_{n=1}^{N}\sum_{j=1}^{N} \xi_n\zeta_j\, p_d^A(\mathbf{r},\mathbf{R}_n)p_d^B(\mathbf{r}',\mathbf{R}_j). \qquad (51)$$

In order to average over $\{\widetilde{\xi}_n\}$ and $\{\widetilde{\zeta}_j\}$ for fixed $q_{\mathrm{in}}(\mathbf{r})$ in step (c), we must consider two cases, denoted by $E_{(c)}\{\widetilde{q}_A(\mathbf{r})\widetilde{q}_B(\mathbf{r}')\}|_{n=j}$ when $n=j$ and by $E_{(c)}\{\widetilde{q}_A(\mathbf{r})\widetilde{q}_B(\mathbf{r}')\}|_{n\neq j}$ when $n\neq j$.

For the double sum over $n$ and $j$ in Eq. (51), there are $N$ terms with $n=j$. Averaging these $N$ terms in Eq. (51) yields

$$E_{(c)}\{\widetilde{q}_A(\mathbf{r})\widetilde{q}_B(\mathbf{r}')\}|_{n=j}$$

$$= \left\langle \sum_{n=1}^{\widetilde{N}} \widetilde{\xi}_n\widetilde{\zeta}_n\, p_d^A(\mathbf{r},\mathbf{R}_n)p_d^B(\mathbf{r}',\mathbf{R}_n) \right\rangle_{(c)}\Bigg|_{n=j}$$

$$= \sum_{n=1}^{N} E\{\widetilde{\xi}_n\widetilde{\zeta}_n\}p_d^A(\mathbf{r},\mathbf{R}_n)p_d^B(\mathbf{r}',\mathbf{R}_n)$$

$$= R_{\xi\zeta}\sum_{n=1}^{N} p_d^A(\mathbf{r},\mathbf{R}_n)p_d^B(\mathbf{r}',\mathbf{R}_n). \qquad (52)$$

The calculation for steps (d) and (e) on Eq. (52) is now similar to what was done in Eqs. (41)–(44). Thus, the result is given by

$$E_{(e)}\{\widetilde{q}_A(\mathbf{r})\widetilde{q}_B(\mathbf{r}')\}|_{n=j} = R_{\xi\zeta}\int_{\infty} d\mathbf{R}\, p_d^A(\mathbf{r},\mathbf{R})p_d^B(\mathbf{r}',\mathbf{R})\overline{q}_{\mathrm{in}}(\mathbf{R}). \qquad (53)$$

Next, consider the case of $n\neq j$ for step (c). From Eq. (51), we have

$E_{(c)}\{\tilde{q}_A(\mathbf{r})\tilde{q}_B(\mathbf{r}')\}|_{n\neq j}$

$$=\left\langle\sum_{n=1}^{\tilde{N}}\sum_{j=1}^{\tilde{N}}\tilde{\xi}_n\tilde{\zeta}_j p_d^A(\mathbf{r},\mathbf{R}_n)p_d^B(\mathbf{r}',\mathbf{R}_j)\right\rangle_{(c)}\Bigg|_{n\neq j}$$

$$=\sum_{n=1}^{N}\sum_{j=1}^{N}E\{\tilde{\xi}_n\tilde{\zeta}_j\}p_d^A(\mathbf{r},\mathbf{R}_n)p_d^B(\mathbf{r}',\mathbf{R}_j)|_{n\neq j}$$

$$=\overline{\xi}\,\overline{\zeta}\sum_{n=1}^{N}\sum_{j=1}^{N}p_d^A(\mathbf{r},\mathbf{R}_n)p_d^B(\mathbf{r}',\mathbf{R}_j)|_{n\neq j}.\qquad(54)$$

Again, similar to Eq. (41), step (d) applied to Eq. (54) now gives

$E_{(d)}\{\tilde{q}_A(\mathbf{r})\tilde{q}_B(\mathbf{r}')\}|_{n\neq j}$

$$=\overline{\xi}\,\overline{\zeta}\int_\infty d\mathbf{R}\int_\infty d\mathbf{R}'\left\{p_d^{(A)}(\mathbf{r},\mathbf{R})p_d^{(B)}(\mathbf{r}',\mathbf{R}')\right.$$

$$\left.\times\sum_{n=1}^{N}\sum_{j=1}^{N}\mathrm{pr}_{\tilde{\mathbf{R}}_n,\tilde{\mathbf{R}}_j}(\mathbf{R},\mathbf{R}'|N)\right\}\Bigg|_{n\neq j}.\qquad(55)$$

Based on the work by Barrett et al.[19] it can be shown that

$$E\{\tilde{q}_{in}(\mathbf{R})\tilde{q}_{in}(\mathbf{R}')|N\}|_{n\neq j}=\sum_{n=1}^{N}\sum_{j=1}^{N}\mathrm{pr}_{\tilde{\mathbf{R}}_n,\tilde{\mathbf{R}}_j}(\mathbf{R},\mathbf{R}'|N)|_{n\neq j}.$$
$$(56)$$

Substituting Eq. (56) into Eq. (55), we have

$E_{(d)}\{\tilde{q}_A(\mathbf{r})\tilde{q}_B(\mathbf{r}')\}|_{n\neq j}$

$$=\overline{\xi}\,\overline{\zeta}\int_\infty d\mathbf{R}\int_\infty d\mathbf{R}'\{p_d^A(\mathbf{r},\mathbf{R})p_d^B(\mathbf{r}',\mathbf{R}')$$

$$\times E\{\tilde{q}_{in}(\mathbf{R})\tilde{q}_{in}(\mathbf{R}')|N\}|_{n\neq j}\}.\qquad(57)$$

Now it is easily shown that step (e) applied to Eq. (57), to obtain the average over $\tilde{N}$, gives

$E_{(e)}\{\tilde{q}_A(\mathbf{r})\tilde{q}_B(\mathbf{r}')\}|_{n\neq j}$

$$=\overline{\xi}\,\overline{\zeta}\int_\infty d\mathbf{R}\int_\infty d\mathbf{R}'\,p_d^A(\mathbf{r},\mathbf{R})p_d^B(\mathbf{r}',\mathbf{R}')$$

$$\times E\{\tilde{q}_{in}(\mathbf{R})\tilde{q}_{in}(\mathbf{R}')\}|_{n\neq j}$$

$$=\overline{\xi}\,\overline{\zeta}\int_\infty d\mathbf{R}\int_\infty d\mathbf{R}'\,p_d^A(\mathbf{r},\mathbf{R})p_d^B(\mathbf{r}',\mathbf{R}')R_{in}(\mathbf{R},\mathbf{R}')|_{n\neq j}.$$
$$(58)$$

To replace $R_{in}(\mathbf{R},\mathbf{R}')|_{n\neq j}$ in Eq. (58) with $R_{in}(\mathbf{R},\mathbf{R}')$, we invoke Eqs. (26) and (27) again. Thus Eq. (58) becomes

$E_{(e)}\{\tilde{q}_A(\mathbf{r})\tilde{q}_B(\mathbf{r}')\}|_{n\neq j}$

$$=\overline{\xi}\,\overline{\zeta}\int_\infty d\mathbf{R}\int_\infty d\mathbf{R}'\,p_d^A(\mathbf{r},\mathbf{R})p_d^B(\mathbf{r}',\mathbf{R}')R_{in}(\mathbf{R},\mathbf{R}')$$

$$-\overline{\xi}\,\overline{\zeta}\int_\infty d\mathbf{R}\,p_d^A(\mathbf{r},\mathbf{R})p_d^B(\mathbf{r}',\mathbf{R})\,\overline{q}_{in}(\mathbf{R}).\qquad(59)$$
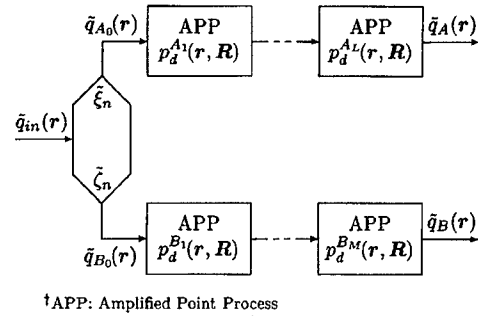
†APP: Amplified Point Process

FIG. 3. Schematic illustration of two parallel cascades of amplified point processes operating on randomly selected subsets of the input point process $\tilde{q}_{in}(\mathbf{r})$.

Adding Eqs. (53) and (59), the cross correlation of $\tilde{q}_A(\mathbf{r})$ and $\tilde{q}_B(\mathbf{r})$ is given by

$$R_{AB}(\mathbf{r},\mathbf{r}')=K_{\xi\zeta}\int_\infty d\mathbf{R}\,p_d^A(\mathbf{r},\mathbf{R})p_d^B(\mathbf{r}',\mathbf{R})\,\overline{q}_{in}(\mathbf{R})+\overline{\xi}\,\overline{\zeta}\int_\infty d\mathbf{R}$$

$$\times\int_\infty d\mathbf{R}'\,p_d^A(\mathbf{r},\mathbf{R})p_d^B(\mathbf{r}',\mathbf{R}')R_{in}(\mathbf{R},\mathbf{R}'),\qquad(60)$$

which is a general expression for the nonstationary cross correlation of two subsets of a point process each undergoing an amplified point process. The cross covariance of $\tilde{q}_A(\mathbf{r})$ and $\tilde{q}_B(\mathbf{r})$ is given by subtracting the product of means from the cross correlation. From Eqs. (44), (46), and (60), finally, we have

$$K_{AB}(\mathbf{r},\mathbf{r}')=K_{\xi\zeta}\int_\infty d\mathbf{R}\,p_d^A(\mathbf{r},\mathbf{R})p_d^B(\mathbf{r}',\mathbf{R})\,\overline{q}_{in}(\mathbf{R})+\overline{\xi}\,\overline{\zeta}\int_\infty d\mathbf{R}$$

$$\times\int_\infty d\mathbf{R}'\,p_d^A(\mathbf{r},\mathbf{R})p_d^B(\mathbf{r}',\mathbf{R}')K_{in}(\mathbf{R},\mathbf{R}'),\qquad(61)$$

which is the desired result. For the case illustrated in Fig. 2, the expressions given by Eqs. (60) and (61) show that: (a) the correlation in $\tilde{q}_A(\mathbf{r})$ and $\tilde{q}_B(\mathbf{r})$ is proportional to the cross correlation of the binomial random variables $\tilde{\xi}_n$ and $\tilde{\zeta}_n$ describing the point selection as given by the first term on the right-hand side of Eqs. (60) and (61), and (b) any correlation in the random source $\tilde{q}_{in}(\mathbf{r})$ is transferred to the outputs through paths $A$ and $B$ as shown by the second term.

## D. Cross covariance following multiple amplified point processes

We now generalize the results of Eqs. (60) and (61) derived previously to an arbitrary number of cascaded amplification stages in each of the two paths $A$ and $B$, as illustrated in Fig. 3. In Fig. 3, $\tilde{q}_{A_0}(\mathbf{r})$ and $\tilde{q}_{B_0}(\mathbf{r})$ are random subsets of the input point process $\tilde{q}_{in}(\mathbf{r})$ and undergo multiple amplified point processes resulting in $\tilde{q}_A(\mathbf{r})$ and $\tilde{q}_B(\mathbf{r})$ in paths $A$ and $B$, respectively. This analysis assumes that each amplification stage is an independent process.
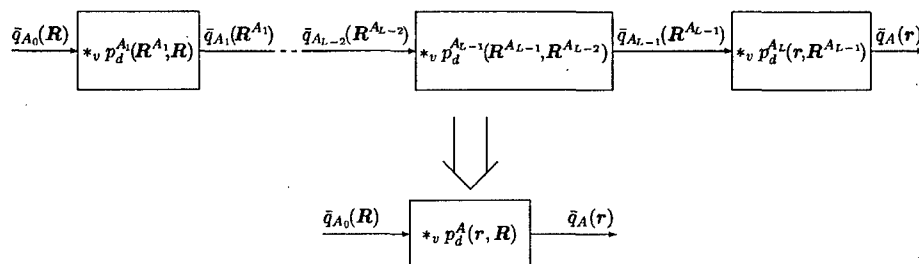
FIG. 4. Illustration of the transfer of mean for multiple amplified point processes.

Similar to the procedure discussed previously, we calculate the cross correlation of $\tilde{q}_A(\mathbf{r})$ and $\tilde{q}_B(\mathbf{r})$ in two steps: (a) average $\tilde{q}_A(\mathbf{r})$ and $\tilde{q}_B(\mathbf{r})$ for fixed $\tilde{q}_{A_0}(\mathbf{r})$ and $\tilde{q}_{B_0}(\mathbf{r})$; and (b) average over $\tilde{q}_{A_0}(\mathbf{r})$ and $\tilde{q}_{B_0}(\mathbf{r})$ to get the result. Under the condition of fixed $\tilde{q}_{A_0}(\mathbf{r})$ and $\tilde{q}_{B_0}(\mathbf{r})$, the point process $\tilde{q}_A(\mathbf{r})$ is independent of $\tilde{q}_B(\mathbf{r})$ due to the independence of each amplification stage in Fig. 3. Thus, from Eq. (4),

$$R_{AB}(\mathbf{r},\mathbf{r}')\big|_{\substack{q_{A_0}(\mathbf{r})\\q_{B_0}(\mathbf{r})}}=E\{\tilde{q}_A(\mathbf{r})\tilde{q}_B(\mathbf{r}')\}\big|_{\substack{q_{A_0}(\mathbf{r})\\q_{B_0}(\mathbf{r})}}$$

$$=\overline{q}_A(\mathbf{r})\overline{q}_B(\mathbf{r}')\big|_{\substack{q_{A_0}(\mathbf{r})\\q_{B_0}(\mathbf{r})}}, \tag{62}$$

which shows that the conditional cross correlation of $\tilde{q}_A(\mathbf{r})$ and $\tilde{q}_B(\mathbf{r})$ is the product of their means for fixed $\tilde{q}_{A_0}(\mathbf{r})$ and $\tilde{q}_{B_0}(\mathbf{r})$. Therefore, it is useful to first derive expressions for the mean values of $\tilde{q}_A(\mathbf{r})$ and $\tilde{q}_B(\mathbf{r})$.

We define the integral operator $H(\cdot)$ as a mapping from the mean input $\overline{q}(\mathbf{R})$ of an amplification stage at $\mathbf{R}$ to the output at $\mathbf{r}$, where $\tilde{q}(\mathbf{R})$ is a point process. Thus, in terms of Eq. (45),

$$H(\overline{q}(\mathbf{R}))=\int_\infty d\mathbf{R}\,p_d(\mathbf{r},\mathbf{R})\,\overline{q}(\mathbf{R}), \tag{63}$$

which is written in short form as

$$H(\overline{q}(\mathbf{R}))=p_d(\mathbf{r},\mathbf{R})*_v\overline{q}(\mathbf{R}), \tag{64}$$

where $*_v$ represents a superposition integral operator. For a single amplification stage, the mean distribution of secondary points is given by the scatter point spread function scaled by the amplification factor. Therefore, from Eq. (32), we have

$$p_d(\mathbf{r},\mathbf{R})=\overline{k}_n(\mathbf{R})\,\mathrm{pr}\,_{\tilde{A}}(\mathbf{r}-\mathbf{R}|\mathbf{R}) \tag{65}$$

for each stage, and it follows that

$$H(\overline{q}(\mathbf{R}))=\int_\infty d\mathbf{R}\,\mathrm{pr}\,_{\tilde{A}}(\mathbf{r}-\mathbf{R}|\mathbf{R})\,\overline{k}_n(\mathbf{R})\,\overline{q}(\mathbf{R}), \tag{66}$$

which is equivalent to Eq. (63). This result can be found in Ref. 13, developed by Rabbani *et al.* from the view of multivariate moment-generating functions. If the amplified point process is shift invariant, then the mean gain and density function are independent of position $\mathbf{R}$, where $\overline{k}_n(\mathbf{R})=\overline{k}$ and $\mathrm{pr}\,_{\tilde{A}}(\mathbf{r}-\mathbf{R}|\mathbf{R})=\mathrm{pr}\,_{\tilde{A}}(\mathbf{r}-\mathbf{R})$. In this case, Eq. (66) becomes the convolution integral, i.e.,

$$H(\overline{q}(\mathbf{R}))=\int_\infty d\mathbf{R}\,\mathrm{pr}\,_{\tilde{A}}(\mathbf{r}-\mathbf{R})\,\overline{k}\overline{q}(\mathbf{R})$$

$$=\overline{k}\,\mathrm{pr}\,_{\tilde{A}}(\mathbf{r})*\overline{q}(\mathbf{r}). \tag{67}$$

We now consider the means of $\tilde{q}_A(\mathbf{r})$ and $\tilde{q}_B(\mathbf{r})$ in Fig. 3. The mean of the output $\tilde{q}_A(\mathbf{r})$ may be obtained by cascading Eq. (64) with the $L$ amplification stages, as shown in Fig. 4. After the last amplification stage, the mean $\overline{q}_A(\mathbf{r})$ is given by Eq. (64) as

$$\overline{q}_A(\mathbf{r})=p_d^{A_L}(\mathbf{r},\mathbf{R}^{A_{L-1}})*_v\overline{q}_{A_{L-1}}(\mathbf{R}^{A_{L-1}}), \tag{68}$$

and after $L$ amplification stages as

$$\overline{q}_A(\mathbf{r})=p_d^{A_L}(\mathbf{r},\mathbf{R}^{A_{L-1}})*_v\cdots*_v p_d^{A_1}(\mathbf{R}^{A_1},\mathbf{R})*_v\overline{q}_{A_0}(\mathbf{R}). \tag{69}$$

Similar to the associative property of the convolution integral,[35] the superposition integral operator is associative and we can combine the $p_d(\ )$ terms resulting in

$$\overline{q}_A(\mathbf{r})=p_d^A(\mathbf{r},\mathbf{R})*_v\overline{q}_{A_0}(\mathbf{R})=\int_\infty d\mathbf{R}\,p_d^A(\mathbf{r},\mathbf{R})\,\overline{q}_{A_0}(\mathbf{R}), \tag{70}$$

where we have defined $p_d^A(\mathbf{r},\mathbf{R})$ as

$$p_d^A(\mathbf{r},\mathbf{R})\triangleq p_d^{A_L}(\mathbf{r},\mathbf{R}^{A_{L-1}})*_v\cdots*_v p_d^{A_1}(\mathbf{R}^{A_1},\mathbf{R}). \tag{71}$$

Similarly, for path $B$, we obtain the mean of $\tilde{q}_B(\mathbf{r})$ as

$$\overline{q}_B(\mathbf{r})=p_d^B(\mathbf{r},\mathbf{R})*_v\overline{q}_{B_0}(\mathbf{R})=\int_\infty d\mathbf{R}\,p_d^B(\mathbf{r},\mathbf{R})\,\overline{q}_{B_0}(\mathbf{R}), \tag{72}$$

where

$$p_d^B(\mathbf{r},\mathbf{R})\triangleq p_d^{B_M}(\mathbf{r},\mathbf{R}^{B_{M-1}})*_v\cdots*_v p_d^{B_1}(\mathbf{R}^{B_1},\mathbf{R}). \tag{73}$$

These results show that for the purpose of describing transfer of the mean value, cascaded multiple amplified point processes can be described as a single amplification stage. Since $\overline{q}_{A_0}(\mathbf{R})=\overline{\xi}\,\overline{q}_{\mathrm{in}}(\mathbf{R})$ and $\overline{q}_{B_0}(\mathbf{R})=\overline{\zeta}\,\overline{q}_{\mathrm{in}}(\mathbf{R})$, Eqs. (70) and (72) may be written as

$$\bar{q}_A(\mathbf{r}) = \bar{\xi} \int_\infty d\mathbf{R}\, p_d^A(\mathbf{r},\mathbf{R}) \bar{q}_{\text{in}}(\mathbf{R}), \qquad (74)$$

$$\bar{q}_B(\mathbf{r}) = \bar{\zeta} \int_\infty d\mathbf{R}\, p_d^B(\mathbf{r},\mathbf{R}) \bar{q}_{\text{in}}(\mathbf{R}), \qquad (75)$$

which are the generalization of Eqs. (44) and (46) for cascaded multiple amplification stages. Note that for fixed $q_{A_0}(\mathbf{r})$ and $q_{B_0}(\mathbf{r})$, Eqs. (70) and (72) become

$$\bar{q}_A(\mathbf{r})\big|_{q_{A_0}(\mathbf{r})} = \int_\infty d\mathbf{R}\, p_d^A(\mathbf{r},\mathbf{R}) q_{A_0}(\mathbf{R}), \qquad (76)$$

$$\bar{q}_B(\mathbf{r})\big|_{q_{B_0}(\mathbf{r})} = \int_\infty d\mathbf{R}\, p_d^B(\mathbf{r},\mathbf{R}) q_{B_0}(\mathbf{R}). \qquad (77)$$

Combining Eqs. (76) and (77) with Eq. (62) gives

$$R_{AB}(\mathbf{r},\mathbf{r}')\big|_{\substack{q_{A_0}(\mathbf{r}) \\ q_{B_0}(\mathbf{r})}}$$

$$= \int_\infty d\mathbf{R} \int_\infty d\mathbf{R}'\, p_d^A(\mathbf{r},\mathbf{R})\, p_d^B(\mathbf{r},\mathbf{R}')\, q_{A_0}(\mathbf{R})\, q_{B_0}(\mathbf{R}'). \qquad (78)$$

The second step is to average Eq. (78) over random subsets $\tilde{q}_{A_0}(\mathbf{r})$ and $\tilde{q}_{B_0}(\mathbf{r})$ of the input point process $\tilde{q}_{\text{in}}(\mathbf{r})$, giving

$$R_{AB}(\mathbf{r},\mathbf{r}')$$

$$= \int_\infty d\mathbf{R} \int_\infty d\mathbf{R}'\, p_d^A(\mathbf{r},\mathbf{R})\, p_d^B(\mathbf{r},\mathbf{R}')\, E\{q_{A_0}(\mathbf{R})\, q_{B_0}(\mathbf{R}')\}$$

$$= \int_\infty d\mathbf{R} \int_\infty d\mathbf{R}'\, p_d^A(\mathbf{r},\mathbf{R})\, p_d^B(\mathbf{r},\mathbf{R}')\, R_{A_0 B_0}(\mathbf{R},\mathbf{R}'). \qquad (79)$$

In Sec. II B 2, we derived the cross correlation for random subsets of a random point process, given by Eq. (28). Combining Eq. (79) with Eq. (28) gives

$$R_{AB}(\mathbf{r},\mathbf{r}') = K_{\xi\zeta} \int_\infty d\mathbf{R}\, p_d^A(\mathbf{r},\mathbf{R}) p_d^B(\mathbf{r}',\mathbf{R})\, \bar{q}_{\text{in}}(\mathbf{R}) + \overline{\xi}\,\overline{\zeta} \int_\infty d\mathbf{R}$$

$$\times \int_\infty d\mathbf{R}'\, p_d^A(\mathbf{r},\mathbf{R}) p_d^B(\mathbf{r}',\mathbf{R}') R_{\text{in}}(\mathbf{R},\mathbf{R}'), \qquad (80)$$

which has the same form as Eq. (60) for a single amplification stage. Subtracting the product of $\bar{q}_A(\mathbf{R})$ and $\bar{q}_B(\mathbf{R})$, given by Eqs. (74) and (75), from the cross correlation in Eq. (80), we conclude that the cross covariance $K_{AB}(\mathbf{r},\mathbf{r}')$ is also given by Eq. (61), where $p_d^A(\mathbf{r},\mathbf{R})$ is described by Eq. (71) and $p_d^B(\mathbf{r},\mathbf{R})$ by Eq. (73).

## E. Important special cases

### 1. Doubly stochastic poisson impulses source

In medical imaging systems, x rays incident on a detector form a quantum image that can be expressed as a sample function of a spatial point process $\tilde{q}_{\text{in}}(\mathbf{r})$ as in Eq. (15). Barrett et al.[19] have shown that such a point process may be described in terms of doubly stochastic Poisson impulses
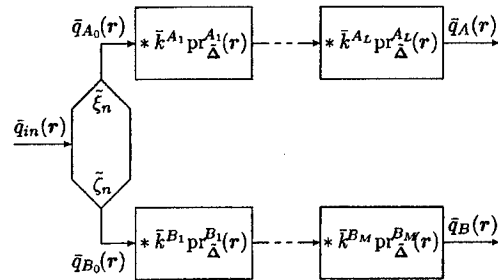


FIG. 5. Schematic illustration of shift-invariant system with two parallel cascades of multiple amplified point processes.

with intensity process $\tilde{b}(\mathbf{r})$, which they call the random input fluence. In x-ray imaging, for instance, the random nature of quanta arriving from a radiation source makes $b(\mathbf{r})$ spatially random.

For the input point process $\tilde{q}_{\text{in}}(\mathbf{r})$ of doubly stochastic Poisson impulses, Barrett et al. show that the mean is given by

$$\bar{q}_{\text{in}}(\mathbf{r}) = \bar{b}(\mathbf{r}) \qquad (81)$$

and the autocovariance is

$$K_{\text{in}}(\mathbf{r},\mathbf{r}') = \bar{b}(\mathbf{r}) \delta(\mathbf{r}-\mathbf{r}') + K_b(\mathbf{r},\mathbf{r}'), \qquad (82)$$

where $K_b(\mathbf{r},\mathbf{r}')$ is the autocovariance of $\tilde{b}(\mathbf{r})$. Substituting Eqs. (81) and (82) into Eq. (30), we obtain (see Fig. 1)

$$K_{AB}(\mathbf{r},\mathbf{r}') = R_{\xi\zeta}\, \bar{b}(\mathbf{r}) \delta(\mathbf{r}-\mathbf{r}') + \overline{\xi}\,\overline{\zeta}\, K_b(\mathbf{r},\mathbf{r}'), \qquad (83)$$

where $R_{\xi\zeta} = K_{\xi\zeta} + \overline{\xi}\,\overline{\zeta}$ is the cross correlation of random binomial variables $\tilde{\xi}_n$ and $\tilde{\zeta}_n$. Similarly, substituting Eqs. (81) and (82) into Eq. (61), after some algebraic manipulations, the cross covariance becomes

$$K_{AB}(\mathbf{r},\mathbf{r}') = R_{\xi\zeta} \int_\infty d\mathbf{R}\, p_d^A(\mathbf{r},\mathbf{R}) p_d^B(\mathbf{r}',\mathbf{R})\, \bar{b}(\mathbf{R}) + \overline{\xi}\,\overline{\zeta} \int_\infty d\mathbf{R}$$

$$\times \int_\infty d\mathbf{R}'\, p_d^A(\mathbf{r},\mathbf{R}) p_d^B(\mathbf{r}',\mathbf{R}') K_b(\mathbf{R},\mathbf{R}'), \qquad (84)$$

which is the result of Fig. 2 for the input process of doubly stochastic Poisson impulses. Equations (83) and (84) are given to show the relationship to Barrett's work, but are not required to obtain the following special cases.

### 2. Shift-invariant system with multiple amplified point processes

If the system shown in Fig. 3 is shift invariant, which requires that the mean gain and the probability density function for each amplification stage be independent of position, then the propagation of the mean of the input point process is shown in Fig. 5. From Fig. 5 and Eq. (67), it is easily shown that

$$\overline{q}_A(\mathbf{r}) = \overline{k}^A \operatorname{pr}_\Delta^A(\mathbf{r}) * \overline{q}_{A_0}(\mathbf{r}),$$

$$\overline{q}_B(\mathbf{r}) = \overline{k}^B \operatorname{pr}_\Delta^B(\mathbf{r}) * \overline{q}_{B_0}(\mathbf{r}),\tag{85}$$

where the probability density functions $\operatorname{pr}_\Delta^A(\mathbf{r})$ and $\operatorname{pr}_\Delta^B(\mathbf{r})$ for the entire amplified point processes along paths $A$ and $B$, respectively, are expressed as convolutions of the density functions of substages in each path, i.e.,

$$\operatorname{pr}_\Delta^A(\mathbf{r}) = \operatorname{pr}_\Delta^{A_L}(\mathbf{r}) * \operatorname{pr}_\Delta^{A_{L-1}}(\mathbf{r}) * \cdots * \operatorname{pr}_\Delta^{A_1}(\mathbf{r}),$$

$$\operatorname{pr}_\Delta^B(\mathbf{r}) = \operatorname{pr}_\Delta^{B_M}(\mathbf{r}) * \operatorname{pr}_\Delta^{B_{M-1}}(\mathbf{r}) * \cdots * \operatorname{pr}_\Delta^{B_1}(\mathbf{r}),\tag{86}$$

and the mean gains $\overline{k}^A$ and $\overline{k}^B$ for the entire amplified point processes of paths $A$ and $B$, respectively, are given by

$$\overline{k}^A = \prod_{i=1}^L \overline{k}^{A_i}, \quad \overline{k}^B = \prod_{j=1}^M \overline{k}^{B_j}.\tag{87}$$

From Eq. (32), we obtain the function $p_d^A(\mathbf{r},\mathbf{R})$ for the entire amplified point process of path $A$, i.e.,

$$p_d^A(\mathbf{r},\mathbf{R}) = \overline{k}^A \operatorname{pr}_\Delta^A(\mathbf{r}-\mathbf{R}).\tag{88}$$

Similarly, we have

$$p_d^B(\mathbf{r},\mathbf{R}) = \overline{k}^B \operatorname{pr}_\Delta^B(\mathbf{r}-\mathbf{R}).\tag{89}$$

Substituting Eqs. (88) and (89) into Eq. (61), the cross covariance function of $\widetilde{q}_A(\mathbf{r})$ and $\widetilde{q}_B(\mathbf{r})$ is given by

$$K_{AB}(\mathbf{r},\mathbf{r}') = K_{\xi\zeta}\overline{k}^A\overline{k}^B \int_\infty d\mathbf{R}\, \operatorname{pr}_\Delta^A(\mathbf{r}-\mathbf{R})\, \operatorname{pr}_\Delta^B(\mathbf{r}'-\mathbf{R})\, \overline{q}_{in}(\mathbf{R})$$

$$+ \overline{\xi}\,\overline{\zeta}\,k^A k^B \int_\infty d\mathbf{R} \int_\infty d\mathbf{R}'\, \operatorname{pr}_\Delta^A(\mathbf{r}-\mathbf{R})$$

$$\times \operatorname{pr}_\Delta^B(\mathbf{r}'-\mathbf{R}')K_{in}(\mathbf{R},\mathbf{R}'),\tag{90}$$

which is the desired result for the case when the system is shift invariant.

## 3. Cross covariance and cross spectral density under WSS conditions

If the output point processes $\widetilde{q}_A(\mathbf{r})$ and $\widetilde{q}_B(\mathbf{r})$ in Fig. 2 are wide-sense stationary (WSS), we can describe the correlation between two paths $A$ and $B$ in the frequency domain by their cross spectral density[3] which is equal to the Fourier transform of the cross covariance $K_{AB}(\mathbf{r},\mathbf{r}')$. For the wide-sense stationary conditions, the input process must be stationary in the wide sense and the amplification processes must be shift invariant with uniform mean gains of quanta in an infinite imaging plane. Thus, $\overline{q}_{in}(\mathbf{R}) = \overline{q}_{in}$ and $K_{in}(\mathbf{R},\mathbf{R}') = K_{in}(\mathbf{R}-\mathbf{R}')$. Moreover, the functions $p_d^A(\mathbf{r},\mathbf{R})$ and $p_d^B(\mathbf{r}',\mathbf{R}')$ in Eq. (61) are replaced with the products of their corresponding constant mean gains and shift-invariant density functions as in Eqs. (88) and (89), respectively. We obtain

$$K_{AB}(\mathbf{r},\mathbf{r}') = K_{AB}(\mathbf{r}-\mathbf{r}')$$

$$= K_{\xi\zeta}\overline{k}^A\overline{k}^B\, \overline{q}_{in} \int_\infty d\mathbf{R}\, \operatorname{pr}_\Delta^A(\mathbf{r}-\mathbf{R})\, \operatorname{pr}_\Delta^B(\mathbf{r}'-\mathbf{R})$$

$$+ \overline{\xi}\,\overline{\zeta}\,k^A k^B \int_\infty d\mathbf{R} \int_\infty d\mathbf{R}'\, \operatorname{pr}_\Delta^A(\mathbf{r}-\mathbf{R})$$

$$\times \operatorname{pr}_\Delta^B(\mathbf{r}'-\mathbf{R}')K_{in}(\mathbf{R}-\mathbf{R}').\tag{91}$$

By changing the integral variable $\mathbf{R}$ such that $\boldsymbol\tau' = \mathbf{r}' - \mathbf{R}$, the integral of the first term in Eq. (91) can be rewritten as

$$\int_\infty d\boldsymbol\tau'\, \operatorname{pr}_\Delta^A(\mathbf{r}-\mathbf{r}'+\boldsymbol\tau')\, \operatorname{pr}_\Delta^B(\boldsymbol\tau'),$$

which is the correlation integral of two functions $\operatorname{pr}_\Delta^A(\boldsymbol\tau)$ and $\operatorname{pr}_\Delta^B(\boldsymbol\tau)$ over $\boldsymbol\tau'$, denoted in short form by $\operatorname{pr}_\Delta^A(\boldsymbol\tau)\star\operatorname{pr}_\Delta^B(\boldsymbol\tau)$, where $\boldsymbol\tau = \mathbf{r}-\mathbf{r}'$. Moreover, for the double integral of the second term in Eq. (91), we perform the changes of $\boldsymbol\tau'' = \mathbf{r}' - \mathbf{R}'$ in the $\mathbf{R}'$ integral and $\boldsymbol\tau''' + \boldsymbol\tau'' = \mathbf{r}-\mathbf{R}$ in the $\mathbf{R}$ integral, yielding

$$\int_\infty d\boldsymbol\tau''' \left[ \int_\infty d\boldsymbol\tau''\, \operatorname{pr}_\Delta^A(\boldsymbol\tau''' + \boldsymbol\tau'')\, \operatorname{pr}_\Delta^B(\boldsymbol\tau'') \right] K_{in}(\mathbf{r}-\mathbf{r}'-\boldsymbol\tau''').$$

The integral over $\boldsymbol\tau''$ is the correlation integral of $\operatorname{pr}_\Delta^A(\boldsymbol\tau''')$ and $\operatorname{pr}_\Delta^B(\boldsymbol\tau''')$, and the integral over $\boldsymbol\tau'''$ is the convolution integral of the correlation integral and $K_{in}(\boldsymbol\tau)$. At this point we simplify our notation and let $\operatorname{pr}(\boldsymbol\tau) = \operatorname{pr}_\Delta(\boldsymbol\tau)$. Therefore, Eq. (91) becomes

$$K_{AB}(\boldsymbol\tau) = K_{\xi\zeta}\overline{k}^A\overline{k}^B\overline{q}_{in}\operatorname{pr}^A(\boldsymbol\tau)\star\operatorname{pr}^B(\boldsymbol\tau)$$

$$+ \overline{\xi}\,\overline{\zeta}\,k^A k^B [\operatorname{pr}^A(\boldsymbol\tau)\star\operatorname{pr}^B(\boldsymbol\tau)]*K_{in}(\boldsymbol\tau),\tag{92}$$

which is the desired expression of the cross covariance for wide-sense stationary $\widetilde{q}_A(\mathbf{r})$ and $\widetilde{q}_B(\mathbf{r})$.

The cross spectral density for paths $A$ and $B$ is defined as the Fourier transform of the cross covariance $K_{AB}(\boldsymbol\tau)$, given by

$$\operatorname{NPS}_{AB}(\boldsymbol\nu) = \mathcal{F}\{K_{AB}(\boldsymbol\tau)\}$$

$$= K_{\xi\zeta}\overline{k}^A\overline{k}^B\overline{q}_{in}\, \mathcal{F}\{\operatorname{pr}^A(\boldsymbol\tau)\star\operatorname{pr}^B(\boldsymbol\tau)\}$$

$$+ \overline{\xi}\,\overline{\zeta}\,k^A k^B \mathcal{F}\{[\operatorname{pr}^A(\boldsymbol\tau)\star\operatorname{pr}^B(\boldsymbol\tau)]*K_{in}(\boldsymbol\tau)\}.\tag{93}$$

Then the final result for the cross spectral density under WSS conditions is

$$\operatorname{NPS}_{AB}(\boldsymbol\nu) = \overline{k}^A\overline{k}^B\, T^A(\boldsymbol\nu)T^{B*}(\boldsymbol\nu)[\overline{\xi}\,\overline{\zeta}\operatorname{NPS}_{in}(\boldsymbol\nu) + K_{\xi\zeta}\overline{q}_{in}],\tag{94}$$

where $\operatorname{NPS}_{in}(\boldsymbol\nu)$ is the NPS of the input point process [the Fourier transform of $K_{in}(\boldsymbol\tau)$], $T^A(\boldsymbol\nu)$ and $T^B(\boldsymbol\nu)$ are Fourier transforms of $\operatorname{pr}^A(\boldsymbol\tau)$ and $\operatorname{pr}^B(\boldsymbol\tau)$, respectively. When paths $A$ and $B$ represent a cascade of multiple amplified point processes, the mean gains $\overline{k}^A$ and $\overline{k}^B$ are the product of mean
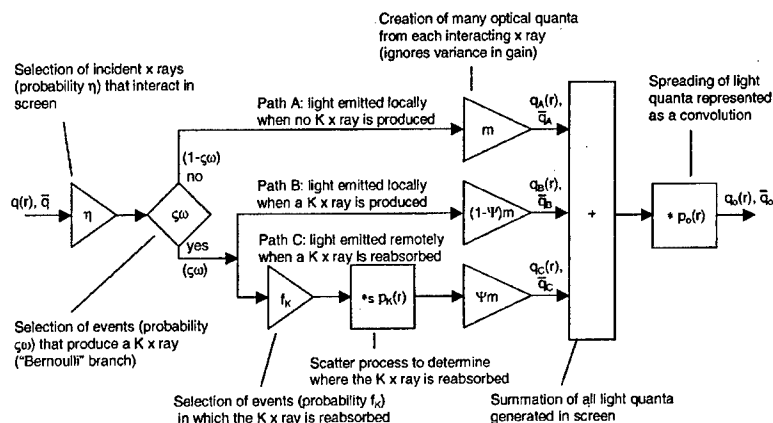
FIG. 6. Schematic of the parallel cascade model used to determine the reabsorption of characteristic $K$ x rays in a radiographic screen. Variance in the gain $m$ describing light generation is ignored to allow comparison with the results of Metz and Vyborny.

gains along each path as given by Eq. (87), and $\mathrm{pr}^A(\tau)$ and $\mathrm{pr}^B(\tau)$ represent the cascaded probability density functions for each path as given by Eq. (86). Taking the Fourier transform of both sides of Eq. (86) shows that $T^A(\nu)$ and $T^B(\nu)$ represent the product of all scatter transfer functions along each path, as given by

$$T^A(\nu)=\prod_{i=1}^{L} T^{Ai}(\nu),$$

$$T^B(\nu)=\prod_{j=1}^{M} T^{Bj}(\nu),$$

(95)

where $T^{Ai}(\nu)$ is the Fourier transform of the probability density function of the $i$th substage in path $A$. The probability density functions always have unity area, and hence the transfer functions $T^A(\nu)$ and $T^B(\nu)$ always have a value of unity at $\nu=0$.

The transfer functions will be complex if $\mathrm{pr}^A(\tau)$ or $\mathrm{pr}^B(\tau)$ is asymmetric in $\tau$. For this reason, the complex form of $\mathrm{NPS}_{AB}(\nu)$ must be maintained. However, as shown in Appendix B, the sum of any cross term pair, $\mathrm{NPS}_{AB}(\nu)+\mathrm{NPS}_{BA}(\nu)$, will always be real only, and hence the resulting NPS will always be real only.

## III. APPLICATION: REABSORPTION OF CHARACTERISTIC X RAYS IN A RADIOGRAPHIC SCREEN

Equation (94) is the general expression for the WSS cross spectral density of two parallel cascaded amplified point processes descending from a single input point process. In the following, this result is used in a description of characteristic reabsorption in a radiographic screen.

### A. Parallel cascade model of $K$ fluorescence in a radiographic screen

We examine here the effects on image noise of fluorescence reabsorption in a radiographic screen, where light is emitted at both the primary photoelectric interaction site and at the reabsorption site. This problem was studied previously

by Metz and Vyborny[34] using a relatively sophisticated statistical analysis. We show that the same result can be obtained using a simpler linear transfer-theory model that includes parallel cascades and the cross spectral density derived in Sec. II.

Figure 6 illustrates a "flow diagram" showing the sequence of events leading to light production in the Metz–Vyborny model. WSS conditions are assumed throughout so that each position in this diagram represents an intermediate step between input and output, characterized in terms of a two-dimensional distribution of quanta (points) $q(\mathbf{r})$. The processes included in Fig. 6 are based on three "elementary processes" (see Appendix A) in the serial cascades plus branch points that give rise to the parallel cascades.

Several simplifying assumptions are made in order to be consistent with Metz and Vyborny[34] and with earlier work by Rossmann.[36,37] They include the following: (a) incident x rays are assumed monoenergetic; (b) differences in light emission due to different x ray interaction depths are ignored; and (c) only photoelectric interactions are considered and it is assumed all absorbed energy is absorbed at the point of interaction. Metz and Vyborny also ignored the statistical nature of light generation in the screen.

At the input to the model in Fig. 6, a uniform x-ray distribution consisting of $\bar{q}$ quanta/mm$^2$, each with energy $E_x$, is incident on the radiographic screen. These quanta are Poisson distributed, and hence have an associated NPS given by $\mathrm{NPS}(\nu)=\bar{q}$.[38] A fraction $\eta$ of these incident quanta will result in a photoelectric interaction in the screen. Selection of these events is represented as a stochastic selection (binary gain) stage, where gain is represented by a random variable $\tilde{\eta}$ that can have a value of 0 or 1 only and mean of $\eta$. The output from this gain stage is a two-dimensional distribution of photoelectric events in the screen.

As described by Metz and Vyborny, there are three possible sequences of events whereby light can be generated for each photoelectric interaction: (1) absorption of the primary x-ray photon at the primary interaction site without emission of a characteristic $K$ x ray; (2) absorption of the primary x ray accompanied by emission of a $K$ x ray; and (3) reabsorption of the $K$ x ray at a remote location. These three se-
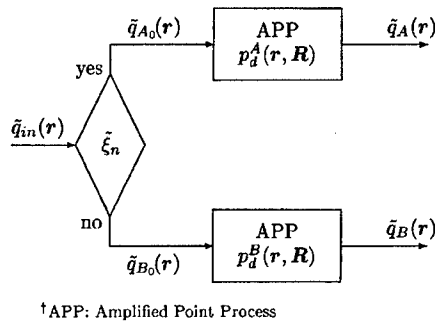
†APP: Amplified Point Process

FIG. 7. The Bernoulli branch with amplified point processes.

quences correspond to paths A, B, and C in Fig. 6.

Path A describes the emission of light at the primary interaction location when no $K$ x ray is produced. For each photoelectric interaction, there is a probability $\varsigma\omega$ that a $K$ x ray will be generated, and therefore a probability $(1-\varsigma\omega)$ that a $K$ x ray is not generated where $\varsigma$ is the probability that, when an incident photon interacts in the screen, it undergoes a $K$-shell interaction, and $\omega$ is the fluorescent yield of $K$-shell photoelectric interactions. This branching is represented in Fig. 6 as the diamond-shaped "Bernoulli branch." It is to be interpreted as a Bernoulli trial[2,38] that, for each interaction, determines the outcome "yes" or "no," where "yes" is obtained randomly with a probability $\varsigma\omega$, and "no" otherwise. If a $K$ x ray is not produced, corresponding to path $A$ in Fig. 6, it is assumed that the incident x-ray energy $E_x$ is absorbed locally producing the number $m$ optical quanta (the gain factor $m$ is assumed to be proportional to the absorbed energy) which will be emitted from the screen. Metz and Vyborny ignore the statistical nature of light emission. We therefore represent $m$ as a deterministic gain factor with variance $\sigma_m^2=0$. This is done to allow comparison of our results with Metz and Vyborny, and to focus attention on the parallel aspects of the model. For this reason, Swank noise and other conversion noise does not appear in the model. Note also that the gain factor $m$ only describes generation of the number of light quanta that are *emitted* from the screen.

Path $B$ describes light emission at the site of the photoelectric interaction when a $K$ x ray *is* emitted (which may or may not be reabsorbed). In this case, the energy $E_K=\psi E_x$ is carried away in the $K$ x ray, and the remaining energy $E_x-E_K$ is deposited at the primary interaction site. Thus, $(1-\psi)m$ optical quanta are emitted at the primary interaction site for each photoelectric interaction where $\psi=E_K/E_x$ and $E_K\approx59.3$ keV for tungsten in the calcium tungstate screen.

Path $C$ describes the light emitted from the screen at a remote site due to reabsorption of the $K$ x ray, where $f_K$ is the probability of reabsorption somewhere in the screen for each photoelectric interaction producing a $K$ x ray. The location of reabsorption is random, but the point-spread function $p_K(\mathbf{r})$, which has unity area, describes the probability density that the $K$ x ray is reabsorbed at a distance $\mathbf{r}$ from the photoelectric interaction site. The process representing this

random relocation of the $K$ x ray is a quantum scatter stage as described in Appendix A. At the reabsorption site, the $K$ x ray is converted to optical quanta with a conversion factor $\psi m$. Events are selected for both paths $B$ and $C$ for every "no" event in the Bernoulli branch. We call the point of separation of paths $B$ and $C$ a "cascade fork."

Due to geometrical spread and possibly light scatter in the screen, optical quanta are distributed spatially with a normalized point-spread function (PSF) given by $p_o(\mathbf{r})$. To be consistent with Metz and Vyborny, who ignore the statistical nature of light scatter, this redistribution of light is represented as a linear filter (convolution) with a kernel $p_o(\mathbf{r})$.

The total light emitted from the screen is therefore the sum of contributions from each path, resulting in

$$\overline{q_o}=\overline{q_A}+\overline{q_B}+\overline{q_C} \tag{96}$$

quanta per unit area, where we have used Eq. (A11) and $T_o(0)=1$ for the output linear filter in Fig. 6, and $T_o(\boldsymbol{\nu})$ is the Fourier transform of $p_o(\mathbf{r})$. The contributions from each path can be obtained by cascading the elementary processes (see Appendix A) included in each path and considering the outcome probability of the Bernoulli branch. Then, we have

$$\overline{q_A}=m(1-\varsigma\omega)\,\eta\,\overline{q}, \tag{97}$$

$$\overline{q_B}=(1-\psi)m\varsigma\omega\,\eta\,\overline{q}, \tag{98}$$

$$\overline{q_C}=\psi m f_K\varsigma\omega\,\eta\,\overline{q}. \tag{99}$$

Substituting Eqs. (97)–(99) into Eq. (96), we can obtain

$$\overline{q_o}=\overline{q}\,\eta m[\,1-\varsigma\omega\psi(1-f_K)\,]. \tag{100}$$

The NPS of light emitted from the screen, denoted by $\mathrm{NPS}_o(\boldsymbol{\nu})$, is therefore given by (see Appendix B)

$$\mathrm{NPS}_o(\boldsymbol{\nu})=[\mathrm{NPS}_A(\boldsymbol{\nu})+\mathrm{NPS}_B(\boldsymbol{\nu})+\mathrm{NPS}_C(\boldsymbol{\nu})+\mathrm{NPS}_{AB}(\boldsymbol{\nu})$$
$$+\mathrm{NPS}_{BA}(\boldsymbol{\nu})+\mathrm{NPS}_{AC}(\boldsymbol{\nu})+\mathrm{NPS}_{CA}(\boldsymbol{\nu})$$
$$+\mathrm{NPS}_{BC}(\boldsymbol{\nu})+\mathrm{NPS}_{CB}(\boldsymbol{\nu})]|T_o(\boldsymbol{\nu})|^2 \tag{101}$$

consisting of the NPS from each of the paths $A$, $B$, and $C$ plus corresponding cross terms as described in the following for the parallel paths with "Bernoulli branch" and "cascade fork" selection processes.

### 1. Bernoulli branch

The Bernoulli branch with amplified point processes is illustrated in Fig. 7. Each quantum in the input point process is selected for path $A$, denoted by "yes," when $\tilde{\xi}_n=1$ and for path $B$, denoted by "no," when $\tilde{\xi}_n=0$. The Bernoulli branch is a special case of the point selection process described in Fig. 2 where the two binomial random variables are related by $\tilde{\zeta}=(1-\tilde{\xi})$. This results in the cross covariance of these random variables given by

$$K_{\xi\zeta}=E\{\tilde{\xi}_n\tilde{\zeta}_n\}-E\{\tilde{\xi}_n\}E\{\tilde{\zeta}_n\}=-\overline{\tilde{\xi}\tilde{\zeta}}=-\overline{\xi}(1-\overline{\xi}). \tag{102}$$
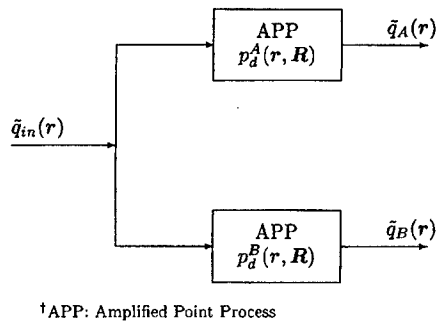
FIG. 8. The cascade fork with amplified point processes.



FIG. 9. Illustration of $T_K(\nu)$, the MTF corresponding to reabsorption in the film–screen system (adapted from Metz and Vyborny).

The cross spectral density following amplification is therefore given by Eq. (94) as

$$\mathrm{NPS}_{AB}(\nu)=\overline{\xi}(1-\overline{\xi})\overline{k}^A\overline{k}^B T^A(\nu)T^{B*}(\nu)[\mathrm{NPS}_{\mathrm{in}}(\nu)-\overline{q}_{\mathrm{in}}]$$

(103)

showing that there is correlation between paths $A$ and $B$ only if quanta in the input image are statistically correlated. That is, when $\mathrm{NPS}_{\mathrm{in}}(\nu)-\overline{q}_{\mathrm{in}}\neq 0$. If the quanta are uncorrelated and $\mathrm{NPS}_{\mathrm{in}}(\nu)=\overline{q}_{\mathrm{in}}$, the cross term is zero.

### 2. Cascade fork

The cascade fork with amplification is shown in Fig. 8 where every quantum in the input is selected for both paths $A$ and $B$. This again is a special case of the general point selection process described in Fig. 2 where $\widetilde{\xi}_n=\widetilde{\zeta}_n=1$, modeled as deterministic unit factors. The cross covariance of $\widetilde{\xi}_n$ and $\widetilde{\zeta}_n$ is therefore

$$K_{\xi\zeta}=E\{\widetilde{\xi}_n\widetilde{\zeta}_n\}-E\{\widetilde{\xi}_n\}E\{\widetilde{\zeta}_n\}=0,$$

(104)

and the cross spectral density term for the cascade fork based on Eq. (94) is given by

$$\mathrm{NPS}_{AB}(\nu)=\overline{k}^A\overline{k}^B T^A(\nu)T^{B*}(\nu)\mathrm{NPS}_{\mathrm{in}}(\nu),$$

(105)

which is always nonzero if the input is a random point process, and therefore there is always a cross term between paths $A$ and $B$.

### B. Degradation of the NPS due to reabsorption

The NPS in the distribution of optical quanta from each path in isolation is obtained by cascading appropriate combinations of the elementary processes described in Appendix A. We have

$$\mathrm{NPS}_A(\nu)=m^2(1-\mathrm{s}\omega)\,\eta\,\overline{q},$$

(106)

$$\mathrm{NPS}_B(\nu)=(1-\psi)^2 m^2\mathrm{s}\omega\,\eta\,\overline{q}.$$

(107)

An expression for $\mathrm{NPS}_C(\nu)$ is obtained by letting $\mathrm{NPS}'(\nu)=f_K\mathrm{s}\omega\,\eta\,\overline{q}=\overline{q}'$, where $\mathrm{NPS}'(\nu)$ denotes the NPS prior to the scatter process and $\overline{q}'$ is the mean density of Poisson quanta. Using Eq. (A9) gives

$$\mathrm{NPS}_C(\nu)=\psi^2 m^2\{[\mathrm{NPS}'(\nu)-\overline{q}']|T_K(\nu)|^2+\overline{q}'\}$$

$$=\psi^2 m^2\overline{q}'=\psi^2 m^2 f_K\mathrm{s}\omega\,\eta\,\overline{q},$$

(108)

where $T_K(\nu)$ is the characteristic transfer function describing the reabsorption probability density in terms of spatial frequencies and is equal to the Fourier transform of the reabsorption PSF, $p_K(\mathbf{r})$. Since quanta in the input image are statistically uncorrelated, the cross terms between paths separated by the Bernoulli branch are

$$\mathrm{NPS}_{AB}(\nu)=\mathrm{NPS}_{BA}(\nu)=0,$$

$$\mathrm{NPS}_{AC}(\nu)=\mathrm{NPS}_{CA}(\nu)=0.$$

Based on Eq. (105), the cross terms $\mathrm{NPS}_{BC}(\nu)$ and $\mathrm{NPS}_{CB}(\nu)$ can be derived. By noting that the mean gains $\overline{k}^B$ and $\overline{k}^C$ for paths $B$ and $C$ are $(1-\psi)m$ and $f_K\psi m$, respectively, and $T^B(\nu)=1$ and $T^C(\nu)=T_K(\nu)$, we have

$$\mathrm{NPS}_{BC}(\nu)=(1-\psi)\,\psi m^2 f_K T_K^*(\nu)\mathrm{s}\omega\,\eta\,\overline{q}$$

(109)

and

$$\mathrm{NPS}_{CB}(\nu)=(1-\psi)\,\psi m^2 f_K T_K(\nu)\mathrm{s}\omega\,\eta\,\overline{q}.$$

(110)

The sum of two complex conjugates is equal to two times their real part, giving

$$\mathrm{NPS}_{BC}(\nu)+\mathrm{NPS}_{CB}(\nu)=2\overline{q}\,\eta\mathrm{s}\omega(1-\psi)\,\psi m^2 f_K\,\mathrm{Re}\{T_K(\nu)\}.$$

(111)

Combining the above-mentioned results gives the NPS for the output optical image quanta, including the effect of the redistribution of light in the screen, as

$$\mathrm{NPS}_o(\nu)=\overline{q}\,\eta m^2[(1-\mathrm{s}\omega)+\mathrm{s}\omega(1-\psi)^2+\mathrm{s}\omega f_K\psi^2$$

$$+2\mathrm{s}\omega f_K\psi(1-\psi)\mathrm{Re}\{T_K(\nu)\}]|T_o(\nu)|^2,$$

(112)

which is the Metz–Vyborny result.

Assuming a constant film density (fixed light output $\overline{q}_o$), the effect of reabsorption is obtained by considering the NPS just above and below the $K$ edge. Above the $K$ edge, reabsorption takes place, the NPS and $\overline{q}_o$, denoted as $\mathrm{NPS}^+(\boldsymbol{\nu})$ and $\overline{q}_o^+$, are given by Eqs. (112) and (100), respectively. Below the $K$ edge, both the light output and NPS, denoted as $\overline{q}_o^-$ and $\mathrm{NPS}^-(\boldsymbol{\nu})$, are determined by setting $\varsigma\omega=0$. It follows that

$$\overline{q}_o^- = \overline{q}\,\eta m, \tag{113}$$

$$\mathrm{NPS}^-(\boldsymbol{\nu}) = \overline{q}\,\eta m^2 |T_o(\boldsymbol{\nu})|^2. \tag{114}$$

Therefore, the ratio of the NPS just above the $K$ edge to just below, normalized to fixed total light output, is given by $\Gamma(\boldsymbol{\nu})$ where

$$\Gamma(\boldsymbol{\nu}) = \frac{\mathrm{NPS}^+(\boldsymbol{\nu})/\overline{q}_o^+}{\mathrm{NPS}^-(\boldsymbol{\nu})/\overline{q}_o^-} = \frac{(1-\varsigma\omega)+\varsigma\omega(1-\psi)^2+\varsigma\omega f_K\psi^2+2\varsigma\omega f_K\psi(1-\psi)\mathrm{Re}\{T_K(\boldsymbol{\nu})\}}{1-\varsigma\omega\psi(1-f_K)}. \tag{115}$$

Figure 9 illustrates $T_K(\boldsymbol{\nu})$ as used by Metz and Vyborny for a Dupont Par Speed calcium tungstate screen. The corresponding degradation in the NPS for a constant light output, $\Gamma(\boldsymbol{\nu})$, is shown in Fig. 10 obtained using values listed in Table I. More x rays with energy above the tungsten $K$ edge interact than below due to an increased interaction coefficient. This results in a decrease in the NPS ratio at zero frequency by approximately 16% (1 to 0.84). At increasing frequencies, image noise is reduced further, asymptotically approaching the uncorrelated high frequency noise ratio of 0.76 due to reabsorption. Thus, reabsorption results in both a correlated and uncorrelated change in image noise. Reabsorption does not result in an improvement in image quality as the modulation transfer function (MTF) is also degraded. This effect is not discussed in detail in this article as these results are specific to a calcium tungstate screen which has limited use at present. Corresponding results for newer screens and other imaging systems can be obtained using the same formalism. The transfer-theory approach is sometimes more physically intuitive than a detailed statistical analysis, making an interpretation of the results more physically meaningful. For instance, it is clear from this analysis that the MTF describing reabsorption, $T_K(\boldsymbol{\nu})$, appears in the cross-spectral density term since light emitted remotely is correlated with light emitted locally when a $K$ x ray is produced. It appears in the first power since it appears in only one of two correlated paths.

## IV. CONCLUSIONS

The DQE is an important indicator of the performance of medical imaging systems. Recent developments in understanding noise transfer in medical imaging systems has resulted in a generalized transfer-theory approach that can be used to describe the DQE and other metrics of system performance for many imaging systems.

As part of a program developing new transfer-theory relationships, we describe how parallel cascades of image-forming processes (quantum gain and scatter) can be incorporated into the transfer-theory approach. Parallel cascades are required when more than one image-forming process combine to create the final image. It is shown that parallel cascades can be used with the introduction of the cross covariance between cascades. A general expression for the cross covariance of correlated point processes is developed, and in particular, the cross covariance of two amplified point processes descending from randomly selected quanta in a common input image is examined, which has particular importance for the analysis of medical imaging systems [Eq. (94) for WSS conditions].
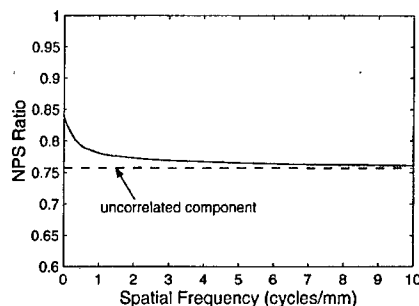
FIG. 10. Illustration of $\Gamma(\nu)$ from Eq. (115), consisting of both correlated and uncorrelated components (adapted from Metz and Vyborny).

TABLE I. Values used to determine $\Gamma(\nu)$ from Metz and Vyborny for a calcium tungstate screen.

| Variable | Value[a] | Physical meaning |
|---|---|---|
| $\varsigma$ | 0.85 | Probability that an interacting x ray undergoes a $K$-shell interaction |
| $\omega$ | 0.93 | Fluorescent yield of $K$-shell photoelectric interactions |
| $\psi$ | 0.866 | Fraction of incident x-ray energy transferred to $K$ x ray, $E_K/E_x$ |
| $f_K$ | 0.20 | Probability that a $K$ x ray is reabsorbed in the screen, depends on geometry |
| $E_K$ | 59.3 keV | Energy of $K$ x ray for tungsten |
| $E_x$ | 68.5 keV | Energy of incident x ray, assumed equal to the tungsten $K$ edge for comparison of results with Metz and Vyborny |

[a]See Ref. 34.

Under wide-sense stationary conditions, the Fourier transform of the cross covariance is the cross spectral density function. Using it, transfer-theory models can be developed to describe the noise power spectrum in imaging systems that require the use of parallel cascades of image-forming processes. One example is reabsorption of $K$ x rays in a radiographic screen. It is shown that the transfer-theory approach gives the same result obtained by Metz and Vyborny using a sophisticated statistical analysis when the same assumptions are made. The analytic model allows scientists and engineers to understand the importance of reabsorption on the DQE in the design of new systems.

Other examples requiring the use of parallel cascades include: (a) double-emulsion film–screen systems where light may cross from one emulsion to the other; (b) portal imaging systems where high-energy x rays may generate different kinds of secondary quanta in the detector such as electrons and light; and, (c) flat-panel active matrix detectors where scattered light may contribute a non-negligible fraction of the image signal. Extension of the transfer-theory approach to include parallel cascades increases the number of theoretical "tools" available to scientists and engineers in the transfer-theory "tool-box" for the analysis of new digital imaging systems.

## ACKNOWLEDGMENTS

## APPENDIX A: ELEMENTARY PROCESSES

Modeling of medical x-ray imaging systems requires the use of three elementary processes. Under wide-sense stationary (WSS) conditions, the elementary processes, and the transfer properties of signal and noise, are summarized in this Appendix.

### 1. Quantum gain and selection

Rabbani et al.[13] and Barrett et al.[19,20] described the transfer of signal and noise through a stochastic quantum gain stage, characterized by a random variable $\tilde{g}$, which has a mean value $\bar{g}$ and variance $\sigma_g^2$. They showed that the mean number of quanta per unit area and corresponding NPS are transferred according to

$$\bar{q}_{\text{out}} = \bar{g}\,\bar{q}_{\text{in}} \tag{A1}$$

and

$$\text{NPS}_{\text{out}}(\nu) = \bar{g}^2\,\text{NPS}_{\text{in}}(\nu) + \sigma_g^2\bar{q}_{\text{in}}, \tag{A2}$$

respectively. If $\tilde{g}$ is modeled as a deterministic gain factor, Eq. (A1) remains the same, but Eq. (A2) becomes

$$\text{NPS}_{\text{out}}(\nu) = \bar{g}^2\,\text{NPS}_{\text{in}}(\nu), \tag{A3}$$

which lacks the second term in Eq. (A2).

For the special case where $\tilde{g}$ represents a binary selection process such as the responsive quantum efficiency of the radiographic screen, $\tilde{g}$ can have a value of 0 or 1 only, $0 \leq \bar{g} \leq 1$, and $\sigma_g^2 = \bar{g}(1 - \bar{g})$. In this case, it is also possible to express signal transfer as

$$q_{\text{out}}(\mathbf{r}) = \tilde{g}\,q_{\text{in}}(\mathbf{r}), \tag{A4}$$

where $\tilde{g}$ is a random variable, $q_{\text{in}}(\mathbf{r})$ and $q_{\text{out}}(\mathbf{r})$ are sample functions of the input and output random point processes.

### 2. Quantum scatter (relocation)

Quantum scatter is a translated point process[33] whereby a quantum is randomly relocated by a random displacement vector.

The input to a scatter operation must be a point process, such as

$$\tilde{q}_{\text{in}}(\mathbf{r}) = \sum_{n=1}^{N} \delta(\mathbf{r} - \tilde{\mathbf{r}}_n), \tag{A5}$$

where each delta function represents one quantum at a position given by the random vector $\tilde{\mathbf{r}}_n$. The output from a scatter operation is given by

$$\tilde{q}_{\text{out}}(\mathbf{r}) = \sum_{n=1}^{N} \delta(\mathbf{r} - \tilde{\mathbf{r}}_n - \tilde{\boldsymbol{\Delta}}_n) \tag{A6}$$

where $\tilde{\boldsymbol{\Delta}}_n$ is a random vector describing the mislocation of the $n$th quantum. This scatter operation is represented as

$$q_{\text{out}}(\mathbf{r}) = p(\mathbf{r}) *_s q_{\text{in}}(\mathbf{r}), \tag{A7}$$

where $p(\mathbf{r})$ is a point-spread function (PSF) describing the distribution of $\tilde{\boldsymbol{\Delta}}_n$. The scatter operator neither creates nor destroys quanta and hence

$$\bar{q}_{\text{out}} = \bar{q}_{\text{in}}. \tag{A8}$$

The NPS transfer function through this scatter has been described by both Rabbani et al.[13] and Barrett et al.,[19,20] given by

$$\text{NPS}_{\text{out}}(\nu) = [\text{NPS}_{\text{in}}(\nu) - \bar{q}_{\text{in}}]|T(\nu)|^2 + \bar{q}_{\text{in}}, \tag{A9}$$

where $T(\nu)$ is the Fourier transform of $p(\mathbf{r})$.

### 3. Linear filter (convolution)

The transfer relationships through a linear shift-invariant filter are described by the convolution integral, given by[2]

$$d_{\text{out}}(\mathbf{r}) = p(\mathbf{r}) * q_{\text{in}}(\mathbf{r}), \tag{A10}$$

$$\bar{d}_{\text{out}} = \bar{q}_{\text{in}}, \tag{A11}$$

and

$$\text{NPS}_{\text{out}}(\nu) = \text{NPS}_{\text{in}}(\nu)|T(\nu)|^2, \tag{A12}$$

where an asterisk represents a convolution, $p(\mathbf{r})$ is the impulse response commonly referred to as the blur PSF normalized to unity area, and $T(\nu)$ is the characteristic transfer function of the filter, given by the Fourier transform of $p(\mathbf{r})$. Unlike the scattering process, the output $d_{\text{out}}(\mathbf{r})$ from a linear filter is not a point process.

## APPENDIX B: STATISTICS OF PARALLEL PROCESSES

When two random processes contribute to an output signal, the result is a random process that is the sum of two random processes. For example, consider a stochastic system described by $\tilde{c}(\mathbf{r}) = \tilde{a}(\mathbf{r}) + \tilde{b}(\mathbf{r})$. The autocorrelation of the sum process is[39]

$$
\begin{aligned}
R_c(\mathbf{r}, \mathbf{r}') &= E\{\tilde{c}(\mathbf{r})\tilde{c}^*(\mathbf{r}')\} \\
&= E\{[\tilde{a}(\mathbf{r}) + \tilde{b}(\mathbf{r})][\tilde{a}^*(\mathbf{r}') + \tilde{b}^*(\mathbf{r}')]\} \\
&= E\{\tilde{a}(\mathbf{r})\tilde{a}^*(\mathbf{r}')\} + E\{\tilde{b}(\mathbf{r})\tilde{b}^*(\mathbf{r}')\} \\
&\quad + E\{\tilde{a}(\mathbf{r})\tilde{b}^*(\mathbf{r}')\} + E\{\tilde{b}(\mathbf{r})\tilde{a}^*(\mathbf{r}')\} \\
&= R_a(\mathbf{r}, \mathbf{r}') + R_b(\mathbf{r}, \mathbf{r}') + R_{ab}(\mathbf{r}, \mathbf{r}') + R_{ba}(\mathbf{r}, \mathbf{r}'),
\end{aligned}
$$

$$(B1)$$

where an asterisk denotes a complex conjugate. When $\tilde{a}(\mathbf{r})$ and $\tilde{b}(\mathbf{r})$ are both wide-sense stationary (WSS), $\tilde{c}(\mathbf{r})$ is also WSS, and the autocorrelation of $\tilde{c}(\mathbf{r})$ in Eq. (B1) can be written as

$$
R_c(\tau) = R_a(\tau) + R_b(\tau) + R_{ab}(\tau) + R_{ba}(\tau), \tag{B2}
$$

where $\tau = \mathbf{r} - \mathbf{r}'$. Similar to above,

$$
K_c(\tau) = K_a(\tau) + K_b(\tau) + K_{ab}(\tau) + K_{ba}(\tau) \tag{B3}
$$

and the corresponding NPS of $\tilde{c}(\mathbf{r})$ is therefore

$$
\begin{aligned}
\text{NPS}_c(\nu) &= \mathcal{F}\{K_c(\tau)\} \\
&= \text{NPS}_a(\nu) + \text{NPS}_b(\nu) + \text{NPS}_{ab}(\nu) + \text{NPS}_{ba}(\nu),
\end{aligned}
$$

$$(B4)$$

where each term in Eq. (B4) is the Fourier transform of the corresponding term in Eq. (B3). The terms $\text{NPS}_{ab}(\nu)$ and $\text{NPS}_{ba}(\nu)$ are cross spectral densities and reflect the spatial-frequency dependence of the autocovariance.

By definition of the cross covariance for two random processes under WSS conditions, we have

$$
K_{ab}(\tau) = K_{ba}^*(-\tau). \tag{B5}
$$

The cross spectral density $\text{NPS}_{ab}(\nu)$ is the Fourier transform of $K_{ab}(\tau)$ given by

$$
\text{NPS}_{ab}(\nu) = \mathcal{F}\{K_{ab}(\tau)\} = \int_\infty K_{ab}(\tau)e^{-j2\pi\nu\tau}d\tau. \tag{B6}
$$

Substituting Eq. (B5) into Eq. (B6), we have

$$
\begin{aligned}
\text{NPS}_{ab}(\nu) &= \int_\infty K_{ba}^*(-\tau)e^{-j2\pi\nu\tau}d\tau \\
&= \int_\infty K_{ba}^*(\tau)e^{j2\pi\nu\tau}d\tau \\
&= \left\{ \int_\infty K_{ba}(\tau)e^{-j2\pi\nu\tau}d\tau \right\}^* \\
&= \{\mathcal{F}\{K_{ba}(\tau)\}\}^* = \text{NPS}_{ba}^*(\nu).
\end{aligned}
$$

$$(B7)$$

Thus, $\text{NPS}_{ab}(\nu)$ and $\text{NPS}_{ba}(\nu)$ are conjugate pairs and the sum of $\text{NPS}_{ab}(\nu) + \text{NPS}_{ba}(\nu)$ is always a real value, i.e.,

$$
\begin{aligned}
\text{NPS}_{ab}(\nu) + \text{NPS}_{ba}(\nu) &= 2\,\text{Re}\{\text{NPS}_{ab}(\nu)\} \\
&= 2\,\text{Re}\{\text{NPS}_{ba}(\nu)\},
\end{aligned}
$$

$$(B8)$$

where $\text{Re}\{\}$ denotes the real part of a complex quantity.

## APPENDIX C: LIST OF SYMBOLS

In this artcle, a tilde (e.g., $\tilde{N}$) indicates a random variable, both an overline (e.g., $\overline{q}$) and angle brackets (e.g., $\langle q \rangle$) indicate a mean value, boldface (e.g., $\mathbf{r}$) indicates a vector, and a superscript (e.g., [A]) identifies a particular process or path.

| Symbol | Definition |
| --- | --- |
| $d_{\text{out}}(\mathbf{r})$ | A function describing the output from a linear-filter process ($\text{mm}^{-2}$). It is a regular function, and hence a distinction must be made from $q(\mathbf{r})$, which is a generalized function describing a distribution of points (see the following). |
| $E\{\}$ or $\langle\rangle$ | An expectation (mean) value. |
| $\mathcal{F}\{\}$ | The Fourier transform operator. |
| $\tilde{k}_n^A, \tilde{k}_n^B$ | Random variables describing the number of secondary quanta produced by quantum amplification processes along paths $A$ or $B$. |
| $K_{AB}(\mathbf{r}, \mathbf{r}')$ | The cross covariance of random point processes $\tilde{q}_A(\mathbf{r})$ and $\tilde{q}_B(\mathbf{r})$ ($\text{mm}^{-4}$). |
| $\tilde{N}$ | A random variable describing the number of points in a random point process (number of quanta in an image). |
| $\text{NPS}_{AB}(\nu)$ | The cross spectral density of random point processes $\tilde{q}_A(\mathbf{r})$ and $\tilde{q}_B(\mathbf{r})$ ($\text{mm}^{-2}$). |
| $p_d(\mathbf{r}, \mathbf{R})$ | Mean distribution of secondary quanta at $\mathbf{r}$ when a primary quantum is absorbed at $\mathbf{R}$ ($\text{mm}^{-2}$). |
| $\text{pr}_{\tilde{r}_n}(\mathbf{r}|N)$ | The conditional probability density function of the $n$th quantum in an image, evaluated at $\mathbf{r}_n = \mathbf{r}$ for fixed value of $N$ ($\text{mm}^{-2}$). |
| $\text{pr}_{\{\tilde{R}_n\}}(\{\mathbf{R}_n\}|N)$ | The conditional joint probability density function of the ensemble of vectors $\{\tilde{\mathbf{R}}_n\}$ for fixed $N$, evaluated at $\{\tilde{\mathbf{R}}_n\} = \{\mathbf{R}_n\}$ ($\text{mm}^{-2}$). |

$\tilde{q}(\mathbf{r})$     A random point process, representing a random spatial distribution of quanta in an image ($mm^{-2}$). It is a generalized function consisting of the superposition of one $\delta$ function for each quantum.

$\tilde{q}_{A_0}(\mathbf{r}), \tilde{q}_{B_0}(\mathbf{r})$     Random subsets of $\tilde{q}_{in}(\mathbf{r})$. That is, an image consisting of randomly selected quanta from $\tilde{q}_{in}(\mathbf{r})$.

$\tilde{\mathbf{r}}_n$     A random vector describing the position of the $n$th quantum in an image (mm).

$\tilde{\mathbf{R}}_n$     A random vector describing the position of the $n$th quantum input to an amplified point process (mm).

$\{\tilde{\mathbf{r}}_n\}$     An ensemble of random vectors.

$R_{AB}(\mathbf{r},\mathbf{r}')$     The cross correlation of random point processes $\tilde{q}_A(\mathbf{r})$ and $\tilde{q}_B(\mathbf{r})$ ($mm^{-4}$).

$T(\boldsymbol{\nu})$     The Fourier transform of probability density function $pr(\tau)$ (unitless).

$\tilde{\boldsymbol{\Delta}}_{nk}$     A random vector describing the displacement of the $k$th secondary quantum produced by the $n$th primary in an amplified point process (mm).

$\tilde{\xi}, \tilde{\zeta}$     Binomial random variables (may take values of 0 or 1 only).

$*$     The convolution integral operator.

$*_s$     A random point process representing the random relocation (scatter) of individual quanta according to a specified PSF.

$*_v$     The superposition integral operator, may be shift invariant.

$\star$     The correlation integral operator.

$|_{q_{in}(\mathbf{r})}$     The computation condition for given $\tilde{q}_{in}(\mathbf{r})$.

## APPENDIX D: STATISTICAL AVERAGES AND MARGINAL PROBABILITY DENSITIES

The mean of a continuous random variable $\tilde{y}$, denoted by $\bar{y}$, is given by[2]

$$\bar{y} = E\{\tilde{y}\} = \int_\infty y \, pr_{\tilde{y}}(y) \, dy, \qquad (D1)$$

where $pr_{\tilde{y}}(y)$ is the probability density function of $\tilde{y}$. If $\tilde{y}$ can be written as a function of a continuous random variable $\tilde{x}$, denoted by $\tilde{y} = f(\tilde{x})$, with the probability density function $pr_{\tilde{x}}(x)$, and $f(x)$ is a single-valued function of $x$ mapping $\tilde{x}$ into $\tilde{y}$, then

$$\bar{y} = E\{\tilde{y}\} = E\{f(\tilde{x})\} = \int_\infty f(x) pr_{\tilde{x}}(x) dx, \qquad (D2)$$

which is the statistical average over random variable $\tilde{x}$. Equation (D1) refers to the sample space of $\tilde{y}$ and Eq. (D2) refers to the sample space of $\tilde{x}$.

When one is discussing multiple random variables, the statistics of each random variable taken in isolation are called marginal.[2] The combined statistics of more than one random variable are called joint. For example, if $pr_{\tilde{x}_1,\tilde{x}_2}(x_1,x_2)$ is a joint probability density function, it de-

scribes the distribution density of an event determined by both $x_1$ and $x_2$. The marginal probability density functions describe the distribution densities of each without regard to the other:

$$pr_{\tilde{x}_1}(x_1) = \int_\infty pr_{\tilde{x}_1,\tilde{x}_2}(x_1,x_2)dx_2 \qquad (D3)$$

and

$$pr_{\tilde{x}_2}(x_2) = \int_\infty pr_{\tilde{x}_1,\tilde{x}_2}(x_1,x_2)dx_1. \qquad (D4)$$

Equations (D3) and (D4) give the relationships between marginal and joint densities. Similarly, for a set of $N$ random variables, $\{\tilde{x}_n : n = 1,...,N\}$, the marginal density $pr_{\tilde{x}_n}(x_n)$ of $\tilde{x}_n$ ($n = 1,...,N$), may be obtained from the joint density $pr_{\{\tilde{x}_n\}}(x_1,...,x_N)$, as

$$pr_{\tilde{x}_n}(x_n) = \underbrace{\int_\infty dx_1 \cdots \int_\infty dx_i \cdots \int_\infty dx_N}_{i \neq n} pr_{\{\tilde{x}_n\}}(x_1,\cdots,x_N). \qquad (D5)$$

The property of marginal densities, Eq. (D5), allows one to express the marginal density function of one random variable, $pr_{\tilde{x}_n}(x_n)$, in terms of $N-1$ nested integrals of the joint probability density function involving all random variables.

Similar to Eq. (D2), if $\tilde{y} = f(\tilde{x}_1,\cdots,\tilde{x}_N)$, the mean of $\tilde{y}$ over all N random variables $\{\tilde{x}_n\}$ is given by

$$\bar{y} = E\{y\} = E\{f(\tilde{x})\}$$

$$= \int_\infty dx_1 \cdots \int_\infty dx_N f(x_1,\cdots,x_N) \, pr_{\{\tilde{x}_n\}}(x_1,\cdots,x_N). \qquad (D6)$$

[a]Electronic mail: jyao@irus.rri.on.ca

[1] J. C. Dainty and R. Shaw, Image Science (Academic, New York, 1974).

[2] A. Papoulis, Probability, Random Variables, and Stochastic Processes, 3rd ed. (McGraw–Hill, New York, 1991).

[3] G. M. Jenkins and D. G. Watts, Spectral Analysis and its Applications (Holden–Day, San Francisco, 1968).

[4] R. Shaw, "The equivalent quantum efficiency of the photographic process," J. Photogr. Sci. 11, 199–204 (1963).

[5] "Medical imaging—the assessment of image quality," ICRU Report No. 54 (International Commission of Radiation Units and Measurements, Bethesda, MD, 1995).

[6] R. Shaw, "Some fundamental properties of xeroradiographic images," Proc. SPIE 70, 359–363 (1975).

[7] R. F. Wagner and E. P. Muntz, "Detective quantum efficiency (DQE) analysis of electrostatic imaging and screen-film imaging in mammography," Proc. SPIE 173, 162–165 (1979).

[8] M. J. Tapiovaara and R. F. Wagner, "A generalized detective quantum efficiency (DQE) approach to the analysis of x-ray imaging," Proc. SPIE 454, 540–549 (1984).

[9] M. J. Tapiovaara and R. F. Wagner, "SNR and DQE analysis of broad spectrum x-ray imaging," Phys. Med. Biol. 30, 519–529 (1985).

[10] K. Rossmann, "Point spread-function, line spread-function, and modulation transfer function," Radiology 93, 257–272 (1969).

[11] C. E. Metz and K. Doi, "Transfer function analysis of radiographic imaging systems," Phys. Med. Biol. 24, 1079–1106 (1979).

[12] H. H. Barrett and W. Swindell, Radiological Imaging—The Theory of Image Formation, Detection, and Processing (Academic, New York, 1981).

[13] M. Rabbani, R. Shaw, and R. Van Metter, "Detective quantum efficiency of imaging systems with amplifying and scattering mechanisms," J. Opt. Soc. Am. A **4**, 895–901 (1987).

[14] M. Rabbani and R. Van Metter, "Analysis of signal and noise propagation for several imaging mechanisms," J. Opt. Soc. Am. A **7**, 1156–1164 (1989).

[15] P. L. Dillon, J. F. Hamilton, M. Rabbani, R. Shaw, and R. Van Metter, "Principles governing the transfer of signal modulation and photon noise by amplifying and scattering mechanisms," Proc. SPIE **535**, 130–139 (1985).

[16] I. A. Cunningham, "Linear-systems modeling of parallel cascaded stochastic processes: The NPS of radiographic screens with reabsorption of characteristic x radiation," Proc. SPIE **3336**, 220–230 (1998).

[17] I. A. Cunningham and R. Shaw, "Signal-to-noise optimization of medical imaging systems," J. Opt. Soc. Am. A **16**, 621–632 (1999).

[18] I. A. Cunningham, "Applied linear-systems theory," in *Handbook of Medical Imaging*, Physics and Psychophysics Vol. 1, edited by J. Beutel, H. L. Kundel, and R. Van Metter (SPIE, Bellingham, 2000), pp. 79–160.

[19] H. H. Barrett, R. F. Wagner, and K. J. Myers, "Correlated point processes in radiological imaging," Proc. SPIE **3032**, 110–125 (1997).

[20] H. H. Barrett and K. J. Myers, *Image Science: Mathematical and Statistical Foundations* (Wiley, New York, 2001).

[21] P. C. Bunch, K. E. Huff, and R. Van Metter, "Analysis of the detective quantum efficiency of a radiographic screen-film combination," J. Opt. Soc. Am. A **4**, 902–909 (1987).

[22] R. M. Nishikawa and M. J. Yaffe, "Effect of various noise sources on the detective quantum efficiency of phosphor screens," Med. Phys. **17**, 887–893 (1990).

[23] R. M. Nishikawa and M. J. Yaffe, "Model of the spatial-frequency-dependent detective quantum efficiency of phosphor screens," Med. Phys. **17**, 894–904 (1990).

[24] J. H. Siewerdsen, L. E. Anonuk, Y. El-Mohri, J. Yorkston, W. Huang, J. M. Boudry, and I. A. Cunningham, "Empirical and theoretical investigation of the noise performance of indirect detection, active matrix flat-panel imagers (AMFPIs) for diagnostic radiology," Med. Phys. **24**, 71–89 (1997).

[25] J. H. Siewerdsen, L. E. Anonuk, Y. El-Mohri, J. Yorkston, W. Huang, and I. A. Cunningham, "Signal, noise power spectrum and detective quantum efficiency of indirect-detection flat-panel imagers for diagnostic radiology," Med. Phys. **25**, 614–628 (1998).

[26] W. Zhao and J. A. Rowlands, "Digital radiology using active matrix readout of amorphous selenium: Theoretical analysis of detective quantum efficiency," Med. Phys. **24**, 1819–1833 (1997).

[27] J. P. Bissonnette, I. A. Cunningham, D. A. Jaffray, A. Fenster, and P. Munro, "A quantum accounting and detective quantum efficiency analysis for video-based portal imaging," Med. Phys. **24**, 815–826 (1997).

[28] T. Falco and B. G. Fallone, "Characteristics of metal-plate/film detectors at therapy energies. II. Detective quantum efficiency," Med. Phys. **25**, 2463–2468 (1998).

[29] R. N. Cahn, B. Cederstrom, M. Danielsson, A. Hall, M. Lundqvist, and D. Nygren, "Detective quantum efficiency dependence on x-ray energy weighting in mammography," Med. Phys. **26**, 2680–2683 (1999).

[30] H. Liu, L. L. Fajardo, and B. C. Penny, "Signal-to-noise ratio and detective quantum efficiency analysis of optically coupled CCD mammography imaging systems," Acad. Radiol. **3**, 799–805 (1996).

[31] D. Mah, J. A. Rawlinson, and J. A. Rowlands, "Detective quantum efficiency of an amorphous selenium detector to megavoltage radiation," Phys. Med. Biol. **44**, 1369–1384 (1999).

[32] M. B. Williams, P. U. Simoni, L. Smilowitz, M. Stanton, W. Phillips, and A. Stewart, "Analysis of the detective quantum efficiency of a developmental detector for digital mammography," Med. Phys. **26**, 2273–2285 (1999).

[33] D. L. Snyder and M. I. Miller, *Random Point Processes, in Time and Space* (Springer, New York, 1991).

[34] C. E. Metz and C. J. Vyborny, "Wiener spectral effects of spatial correlation between the sites of characteristic x-ray emission and reabsorption in radiographic screen-film systems," Phys. Med. Biol. **28**, 547–564 (1983).

[35] R. N. Bracewell, *The Fourier Transform and Its Applications*, 2nd ed. (McGraw–Hill, New York, 1986).

[36] K. Rossmann, "Measurement of the modulation transfer function of radiographic systems containing fluorescent screens," Phys. Med. Biol. **9**, 551–557 (1964).

[37] K. Rossmann, "The spatial frequency spectrum: A means for studying the quality of radiographic imaging systems," Radiology **90**, 1–13 (1968).

[38] F. A. Haight, *Handbook of the Poisson Distribution* (Wiley, New York, 1967).

[39] W. B. Davenport and W. L. Root, *Introduction to the Theory of Random Signals and Noise* (McGraw–Hill, New York, 1958).

# Compton scatter in frequency space: a theoretical study*

Jingwu Yao*[a] and Ian A. Cunningham**[a,b]

[a]Imaging Research Laboratories, The John P. Robarts Research Institute
[b]Dept. of Diagnostic Radiology, London Health Sciences Center

## ABSTRACT

For x-ray detectors, Compton interactions deposit photon energies along the paths of recoil electrons, which are not isotropic about the primary interaction sites. Light from each interacting x-ray is only generated near the path of a recoil electron. In this study, Compton scatter is modeled as an input-labeled cascade of the amplification and scattering processes to describe the transfer relationship of signal and noise in frequency space. The output of the model is the spatial distribution of secondary quanta generated by Compton recoil electrons. We determine the spatial dependence and statistical correlation of secondaries from the initial energy of the recoil electron and its range, resulting in the "Compton" modulation transfer function (MTF) and noise power spectrum (NPS), respectively. Then the "Compton" MTF and NPS are used to calculate the "Compton" detective quantum efficiency (DQE). The probability density function of scattering angle of Compton recoil electron is developed using the Klein-Nishina coefficients. Results are applied to the description of a portal imaging system at 6 MV where non-Compton interactions can be ignored. The MTF results are compared with a Monte Carlo calculation. This is the first model of how Compton interactions in the metal-plate/phosphor combination degrade image quality in terms of signal and noise. It is shown that Compton MTF depends on energy of x-ray photon in a complex way, and Compton scatter imposes a fundamental limitation on both the MTF and DQE of x-ray imaging system.

**Keywords:** Compton scatter, input-labeled model, modulation transfer function, noise power spectrum, detective quantum efficiency, portal imaging system

## 1. INTRODUCTION

The modulation transfer function (MTF) describes signal transfer in the Fourier domain, while the noise power spectrum (NPS) is an important measure of image noise.[1,2] Both the MTF and NPS are required to predict the detective quantum efficiency (DQE) and other metrics of system performance. Although calculations of the NPS and DQE based on experimental data are useful measures of image quality and system performance, theoretical models describing signal and noise transfer are required to identify key factors of system design that limit image quality. In addition, theoretical predictions of the DQE can be used as benchmarks for comparison with measured values to determine how well a particular system is performing.

In x-ray imaging, the spatial dependence and statistical correlation of how radiation energy is deposited have a strong influence on the MTF and NPS. This in turn depends on the physics of x-ray interactions. For instance, photoelectric interactions in a phosphor result in isotropic clusters of optical quanta centered at the interaction sites in the imaging, if the phosphor is considered to be homogeneous and reabsorption is ignored. Compton interactions differ as most photon energy is transferred to secondary electrons along the path of the Compton recoil electron, which is not isotropic about the primary interaction site. Thus, light from each interacting x-ray is generated near the path of a recoil electron. The asymmetric clusters of light quanta due to Compton scatters affect image quality. This is one of several reasons why therapy image quality, primarily due to Compton interactions, is poorer than diagnostic image quality.

The purpose of this article is to develop a Fourier model of the influence of Compton scatter on signal and noise transfer. We ignore the effect of the scattered photon in Compton interaction and only consider the contribution of the recoil electron. This is a reasonable assumption for "thin" detectors where multiple interactions of the scattered photon are unlikely, and is appropriate for the portal imaging system. The other simplifying assumption for "thin" detectors is made in which the multiple scattering of recoil electron is ignored and the path of recoil electron is a straight line along which the secondary ionizations are independently generated. This assumption could be removed
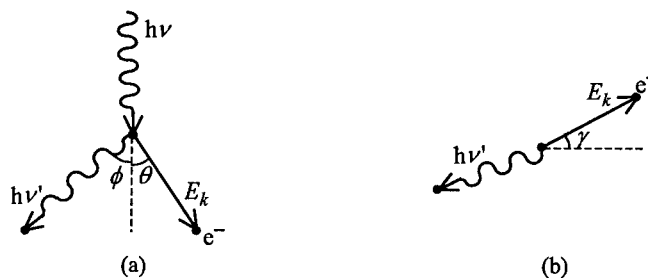
**Figure 1.** Compton interaction of an x-ray photon of energy h$\nu$ with a free electron. The scattered photon has energy h$\nu'$ and angle $\phi$, while the recoil electron departs with kinetic energy $E_k$ at polar angle $\theta$. (a) Cross-sectional view. (b) View from the perspective of the incident photon.

by incorporating a more sophisticated model of electron transport, such as described by Fermi-Eyges small-angle multiple scattering theory.[3,4]

The generation of secondary ionizations in Compton interaction is represented as the combination of a quantum gain process (conversion of x-ray photon to secondary ionizations) and a quantum scatter (random positioning of secondary ionizations along the path of the recoil electron). Since both the conversion mean gain value and scatter point-spread function (PSF) are dependent on the recoil electron path length and direction, and these in turn are functions of the energy of the interacting photon, the cascade used is referred to be "input labeled", shown to be a generalization of earlier work by Van Metter and Rabbani.[5] The result is a description of Compton scatter in the Fourier domain labeled by the scattering angle of recoil electron. We derive the probability density function (PDF) of scattering angle of recoil electron using Klein-Nishina cross section. This leads to averaging the MTF and NPS through Compton process over random angle of recoil electron for each incident photon energy.

The terms "Compton MTF" and "Compton NPS" will be used to represent the MTF and NPS of secondary electrons liberated by the Compton process. The system MTF and NPS may be further degraded by additional processes such as light scatter in the phosphor. While the DQE is generally used to describe overall system performance, we use the term "Compton DQE" to describe the DQE assuming no further degradation subsequent to the Compton scatter. Thus, it represents the best possible DQE that be obtained. The results are applied to the description of a portal imaging system at 6 MV for which non-Compton interactions can be ignored. Analytic expressions for the Compton MTF, NPS and DQE are given as functions of incident x-ray energy. The MTF results are compared with a Monte Carlo calculation.

Throughout the following description, we use a notation where the bold face (eg. **r**) indicates a vector, overhead tilde (eg. $\tilde{\theta}$) indicates a random variable and overline (eg. $\bar{g}$) indicates a mean value.

## 2. THEORY

### 2.1. Compton Scatter

Figure 1 illustrates a Compton interaction in which an x-ray photon of energy h$\nu$ collides with a free electron. The scattered photon has energy h$\nu'$ and angle $\phi$ relative to the incident photon's direction. The recoil electron departs with kinetic energy $E_k$ at polar angle $\theta$. It may be shown from the kinematics of Compton interactions[6] that $E_k$ is related to $\theta$ by

$$E_k = h\nu \cdot \frac{2\alpha \cot^2 \theta}{(1+\alpha)^2 + (1+2\alpha)\cot^2 \theta},\tag{1}$$

where $\alpha = h\nu/m_o c^2$ is the ratio of the incident photon energy to the electron rest energy ($m_o c^2 = 0.511$ MeV). Figure. 1 (b) shows the same interaction from the perspective of the incident photon, where $\gamma$ denotes the azimuthal angle of the recoil electron. The recoil electron and scattered photon travel in opposite directions in this plane due to conservation of energy and momentum.

Compton scatter is represented as a random process, expressed in terms of the three random angles $\tilde{\phi}$, $\tilde{\theta}$ and $\tilde{\gamma}$. For each interaction with a free electron, the PDF of the recoil electron angle $\tilde{\theta}$ is derived in Appendix A using the
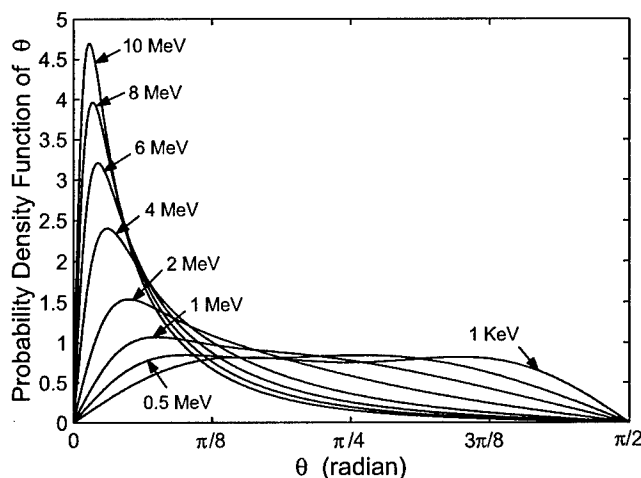
**Figure 2.** The PDF $\mathrm{pr}_{\tilde{\theta}}(\theta)$ of the recoil electron scatter angle for interactions with free electrons over a range of photon energies up to 10 MeV.

Klein-Nishina cross section,[7] giving

$$\mathrm{pr}_{\tilde{\theta}}(\theta) = \frac{8r_0^2\pi}{\sigma}(1+\alpha)^2 \frac{\cot\theta(1+\cot^2\theta)}{(1+\alpha)^2+\cot^2\theta} F(\theta) \tag{2}$$

and

$$F(\theta) = \frac{1}{[(1+\alpha)^2+(1+2\alpha)\cot^2\theta]^2}\left\{\frac{(1+\alpha)^4+\cot^4\theta}{(1+\alpha)^2+\cot^2\theta}+\frac{2\alpha^2\cot^4\theta}{(1+\alpha)^2+(1+2\alpha)\cot^2\theta}\right\}, \tag{3}$$

where $\sigma$ is the Klein-Nishina cross section and $r_0$ denotes the classical electron radius ($2.81794 \times 10^{-13}$ cm).[7] The PDF $\mathrm{pr}_{\tilde{\theta}}(\theta)$ is illustrated in Fig. 2 for photon energies between 1 KeV and 10 KeV. At lower energies, the PDF curve is flatter, which means that the angular distribution tends to be more uniform. With increasing photon energy, the recoil electron tends to be more forward peaked.

In general, the electron scattering cross section is independent of the recoil electron azimuthal angle. The azimuthal angle $\gamma$ is uniformly distributed over all angles from 0 to $2\pi$, and hence the PDF is given by

$$\mathrm{pr}_{\tilde{\gamma}}(\gamma) = \frac{1}{2\pi} \tag{4}$$

independent of energy and other random variables.

## 2.2. Theoretical Representation of Compton Scatter

A cascaded approach[5,8,9] is used to describe Compton scatter so that the results can be incorporated into more complex models of system operation. As illustrated in Fig. 3, the "input" is a spatial distribution of points representing the Compton interaction sites in an image. The output is a spatial distribution of secondary ionizations generated by the recoil electrons. This model describes the conversion from a distribution of Compton events to a distribution of secondary electrons along the paths of recoil electrons.

For the $n$th Compton event, the recoil electron has polar and azimuthal angles given by random variables $\tilde{\theta}_n$ and $\tilde{\gamma}_n$. In travelling through the detector, the recoil electron ionizes along its path until it is stopped or escapes the detector. As a result of electron transport, we use $\bar{g}_n(\theta_n, \gamma_n)$, shortened to $\bar{g}_n$ for simplicity, to denote the total mean number of secondary electrons distributed along the path of the $n$th recoil electron, and the random vector $\tilde{\tau}$ to describe the displacement of each secondary electron with respect to the Compton interaction site. The PDF $\mathrm{pr}_{\tilde{\tau}}(\tau|\theta_n, \gamma_n)$, shortened to $\mathrm{pr}_{\tilde{\tau}}(\tau|n)$, therefore describes the probability per unit area of a secondary being produced at $\tau$ in the image plane. It is equivalent to the normalized PSF for fixed $\theta_n$ and $\gamma_n$. Conversion from the recoil electron to secondaries is thusly represented as a cascade of an amplification and scatter stage. However, these two
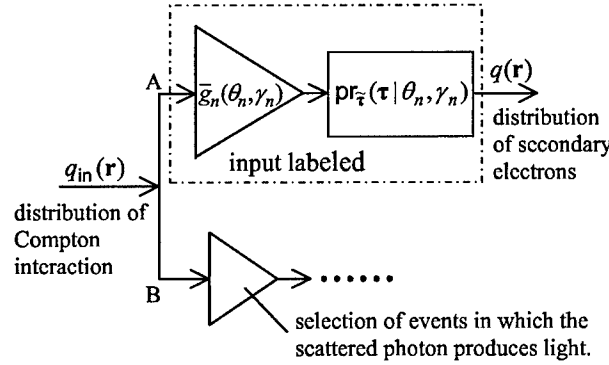
**Figure 3.** Cascade model used to illustrate the production of secondary quanta by the recoil electron for Compton Scatter. The mean gain and scattering PSF are input labeled.

random processes are not independent since both the mean gain and scatter PSF are themselves random, dependent on $\tilde{\theta}_n$ and $\tilde{\gamma}_n$ (and therefore on h$\nu$). Van Metter and Rabbani[5] have shown that dependent processes like these must be described as a pair. The model illustrated in Fig. 3 may be refereed to as "input labeled".

Based on the model shown in Fig. 3, we define a shift-invariant function $p_c(\tau)$ as

$$p_c(\tau) \equiv \langle\langle \bar{g}_n \mathrm{pr}_{\tilde{\tau}}(\tau|n)\rangle\rangle \tag{5}$$

describing the mean number of secondaries per unit area at distance $\tau$ from a Compton event, in which $\langle\langle\ \rangle\rangle$ denotes an average over both $\tilde{\theta}_n$ and $\tilde{\gamma}_n$. The Compton PSF is given by $p_c(\tau)$ normalized to unity, i.e.,

$$\mathrm{psf}_c(\tau) = \frac{\langle\langle \bar{g}_n \mathrm{pr}_{\tilde{\tau}}(\tau|n)\rangle\rangle}{\langle\langle \bar{g}_n\rangle\rangle}. \tag{6}$$

Calculating the Compton PSF for any specified system and geometry therefore requires knowledge of only the two functions $\bar{g}_n$ and $\mathrm{pr}_{\tilde{\tau}}(\tau|n)$ in addition to the PDFs for $\theta$ and $\phi$.

The system characteristic function $S_c(\nu)$, equal to the Fourier transform of $p_c(\tau)$, is given by

$$S_c(\nu) = \mathcal{F}^2\{p_c(\tau)\} = \langle\langle \bar{g}_n T_n(\nu)\rangle\rangle, \tag{7}$$

where $\mathcal{F}^2\{\ \}$ denotes the two-dimensional Fourier transform operator and $T_n(\nu)$ is the Fourier transform of $\mathrm{pr}_{\tilde{\tau}}(\tau|n)$ for fixed $\theta_n$ and $\gamma_n$. The Compton MTF can be expressed as the normalized system characteristic function,

$$\mathrm{MTF}(\nu) = \frac{\langle\langle \bar{g}_n T_n(\nu)\rangle\rangle}{\langle\langle \bar{g}_n\rangle\rangle}. \tag{8}$$

Van Metter and Rabbani[5] considered a dependent pair of gain and scatter processes where the mean gain and PSF are labeled by a single random variable (i.e. random label), and describe transfer of the NPS through this random-labelled model. In Fig. 3, two random variables $\tilde{\theta}_n$ and $\tilde{\gamma}_n$ are applied to label the mean gain and PSF. Since $\tilde{\theta}_n$ is independent of $\tilde{\gamma}_n$, it is straightforward to extend the results in Ref. 5 by changing the average over one label into double, giving the Compton NPS as

$$\mathrm{NPS}(\nu) = [\mathrm{NPS}_{\mathrm{in}}(\nu) - \bar{q}_{\mathrm{in}}]\,|\langle\langle \bar{g}_n T_n(\nu)\rangle\rangle|^2 + \bar{q}_{\mathrm{in}}\langle\langle(\bar{g}_n^2 + \sigma_g^2 - \bar{g}_n)|T_n(\nu)|^2\rangle\rangle + \bar{q}_{\mathrm{in}}\langle\langle \bar{g}_n\rangle\rangle, \tag{9}$$

where $\bar{q}_{\mathrm{in}}$ is the average density of Compton events. Since Compton events are uncorrelated and Poisson distributed, $\mathrm{NPS}_{\mathrm{in}}(\nu) = \bar{q}_{\mathrm{in}}$. In addition, production of secondaries is a random process and the conversion gain $\tilde{g}_n$ almost certainly obeys Poisson distribution so that $\sigma_g^2 \approx \bar{g}_n$. The Compton NPS may be therefore simplified further to

$$\mathrm{NPS}(\nu) = \bar{q}_{\mathrm{in}}\langle\langle \bar{g}_n^2|T_n(\nu)|^2\rangle\rangle + \bar{q}_{\mathrm{in}}\langle\langle \bar{g}_n\rangle\rangle. \tag{10}$$
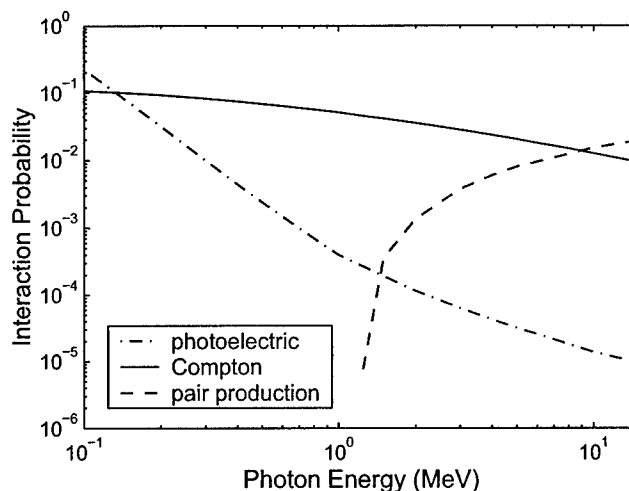
**Figure 4.** Illustration of the quantum efficiency of photoelectric effect, Compton scatter an pair production in 1 mm of Cu. Compton scatter is the dominant interaction between approximately photon energies 0.3 and 4 MeV.

The Compton NPS thus has two significant terms: a correlated noise term proportional to a weighted average of $|T_n(\nu)|^2$ and an uncorrelated noise term independent of frequency.

The Compton DQE can be calculated in terms of the Compton MTF and NPS. By definition,[2] the DQE is expressed as

$$\text{DQE}(\nu) = \frac{\bar{q}_{\text{in}}\left[\langle\langle\bar{g}_n\rangle\rangle\text{MTF}(\nu)\right]^2}{\text{NPS}(\nu)}. \tag{11}$$

Combining Eqs. (8), (10) and (11) gives the Compton DQE as

$$\text{DQE}(\nu) = \frac{\left[\langle\langle\bar{g}_n T_n(\nu)\rangle\rangle\right]^2}{\langle\langle\bar{g}_n^2|T_n(\nu)|^2\rangle\rangle + \langle\langle\bar{g}_n\rangle\rangle}. \tag{12}$$

Equations (8), (10) and (12) describe the "Compton" MTF, NPS and DQE for a combination of random variables required to describe the recoil electron path. They are general results describing how signal and noise are transferred through Compton scatter in a thin detector. In the next section, these results are applied to the description of a portal imaging system in which most interactions are due to Compton scatter.

## 3. APPLICATION TO A FLAT-PANEL PORTAL-IMAGING SYSTEM

Imaging systems designed for use with mega-voltage x rays generally use a metal plate bonded to a scintillating phosphor. Incident x-rays interact primarily in the metal plate. Figure 4 illustrates the probability of a photoelectric interaction, Compton scatter and pair production in a 1-mm copper plate.[7] Compton scatter is the dominant interaction between photon energies of approximately 0.3 and 4 MeV, coinciding with most of the spectrum of a 6-MV therapy beam. In this section, we describe the influence of energy deposited by Compton scatter on the MTF, NPS and DQE for a flat-panel portal-imaging system at 6 MV.

### 3.1. Model description

Recoil electrons generated in the metal plate travel towards a scintillating phosphor as illustrated in Fig. 5. We ignore the effect of variations in interaction depths and assume all interactions occur in the middle of the plate. In Fig. 5, each interacting high-energy x-ray photon ejects one recoil electron from the metal plate. The recoil electron departs from the interaction site at polar angle $\tilde{\theta}_n$ and is assumed to travel along a straight line through the phosphor. Figure 5b illustrates the image-plane view, where line segments represent the projected recoil-electron paths in the phosphor. The $n$th Compton interaction at position $\tilde{\mathbf{R}}_n$ in the image plane results in the non-isotropic distribution of secondaries along the line segment $ab$.
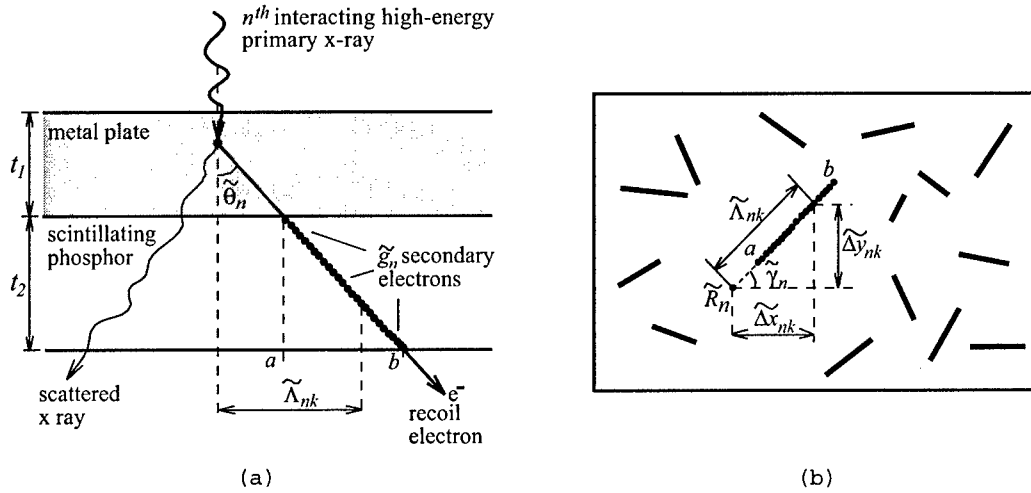
**Figure 5.** Illustration of the generation of secondaries along the path of the Compton recoil electron, assumed to be a straight line. (a) Cross-sectional view; (b) Image-plane view.

For the given incident photon energy h$\nu$ and scattering angle $\theta_n$, the kinetic energy $E_k$ of a recoil electron is determined by Eq. (1). Then from the range of electron with $E_k$ and the passing length $t_1/2 \times \sec\theta_n$, where $t_1/2$ is the half thickness of the metal plate, we may calculate the lost energy of the recoil electron in the metal plate, and give the initial energy $E_a$ of the recoil electron in the phosphor.[7] This calculation can be done, for any fixed kinetic energy, by interpolation of the range data for electron tabulated in Ref. 10. Note that if $E_k$ is very small or $\theta_n$ is large enough, the recoil electron has insufficient energy to exit the metal plate and does not contribute the imaging. The path length of a recoil electron with initial energy $E_a$ in the phosphor, denoted by $l_{ab}$, is expressed as[7]

$$l_{ab} = R\left(\frac{\mathrm{g}}{\mathrm{cm}^2}\right) \times \frac{1}{\rho\,(\mathrm{g/cm}^3)}, \quad \cdot \tag{13}$$

where $R$ is the range for electron with initial energy $E_a$ and $\rho$ is the density of the phosphor. If the recoil electron has sufficient remaining energy to exit the phosphor, then $l_{ab} = t_2 \sec\theta_n$, where $t_2$ is the thickness of the phosphor. Due to geometric consideration, the length of $ab$ is given by $b - a = l_{ab}\sin\theta_n$ and the direction depends on the azimuthal angle $\gamma_n$.

This article describes only the production of secondary ionizations in the phosphor. Conversion by Compton scatter to secondaries in the phosphor is represented by the input-labeled model as shown in Fig. 3. Additional stages are required to describe conversion to light and scatter in the phosphor, but are not considered here.

We use the continuous slowing down approximation of the energy deposition and assume secondaries are generated with uniform probability along the recoil-electron path. Letting $g_0$ be the average number of secondary quanta per unit length, the average number of secondary quanta generated along the path $l_{ab}$ is expressed as

$$\bar{g}_n = g_0 \times l_{ab}. \tag{14}$$

Note that $\bar{g}_n$ only depends on $l_{ab}$ (and therefore on $\theta_n$), and is independent of the angle $\gamma_n$. In Fig. 5, the one-dimensional random variable $\widetilde{\Lambda}_{nk}$ describes the position of the $k$th secondary due to the $n$th Compton event in the image plane, thus the corresponding PDF $\mathrm{pr}_{\widetilde{\Lambda}}(\Lambda|\theta_n)$ extends with a value $1/(b-a)$ between $a$ and $b$ only as illustrated in Fig. 6. In the following discussion, Compton metrics are expressed in terms of $\mathrm{pr}_{\widetilde{\Lambda}}(\Lambda|\theta_n)$.

### 3.2. Compton Metrics

The distribution of secondaries along the straight line between $a$ and $b$ is described by the 1-D PDF, $\mathrm{pr}_{\widetilde{\Lambda}}(\Lambda|\theta_n)$. The 2-D PDF describing the distribution of secondaries in the image can be derived by the transformation of polar variables into Cartesian and using the fundamental transformation theorem[11] of random variables, giving

$$\mathrm{pr}_{\widetilde{T}}(\tau|\theta_n, \gamma_n) = \frac{1}{\Lambda}\mathrm{pr}_{\widetilde{\Lambda}}(\Lambda|\theta_n)\delta(\gamma - \gamma_n) \tag{15}$$
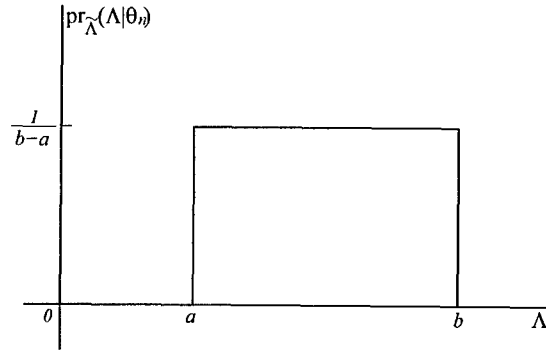
**Figure 6.** Illustration of the 1-D PDF $\text{pr}_{\tilde{\Lambda}}(\Lambda|\theta_n)$, describing the distribution of secondaries along the recoil electron path.

for fixed $\theta_n$ and $\gamma_n$. $\text{pr}_{\tilde{\tau}}(\tau|\theta_n, \gamma_n)$ is not circularly symmetric in the image plane as the secondaries are distributed only along a straight line. Averaging this PDF over $\tilde{\gamma}_n$ results in

$$\langle \text{pr}_{\tilde{\tau}}(\tau|\theta_n, \gamma_n) \rangle_{\tilde{\gamma}_n} = \int_0^{2\pi} \text{pr}_{\tilde{\tau}}(\tau|\theta_n, \gamma_n) \text{pr}_{\tilde{\gamma}}(\gamma_n) \, d\gamma_n$$

$$= \frac{1}{2\pi\Lambda} \int_0^{2\pi} \text{pr}_{\tilde{\Lambda}}(\Lambda|\theta_n) \delta(\gamma - \gamma_n) \, d\gamma_n = \frac{1}{2\pi\Lambda} \text{pr}_{\tilde{\Lambda}}(\Lambda|\theta_n). \tag{16}$$

Since $\Lambda = |\tau|$, we can rewrite Eq. (16) as a circularly symmetric function $p_1(\tau|\theta_n)$, i.e.,

$$p_1(\tau|\theta_n) \equiv \langle \text{pr}_{\tilde{\tau}}(\tau|\theta_n, \gamma_n) \rangle_{\tilde{\gamma}_n} = \frac{1}{2\pi|\tau|} \text{pr}_{\tilde{\Lambda}}(|\tau||\theta_n). \tag{17}$$

The function $p_1(\tau|\theta_n)$ describes the distribution density of secondaries, conditional on having a recoil angle $\theta_n$ in the Compton interaction. Using Eq. (6) and including the quantum efficiency $\eta$ of a Compton interaction, the Compton PSF is therefore given by averaging over $\tilde{\theta}_n$,

$$\text{psf}_c(\tau) = \frac{\langle \eta \, \bar{g}_n \, p_1(\tau|\theta_n) \rangle_{\tilde{\theta}_n}}{\langle \eta \, \bar{g}_n \rangle_{\tilde{\theta}_n}} = \frac{\langle \bar{g}_n p_1(\tau|\theta_n) \rangle_{\tilde{\theta}_n}}{\langle \bar{g}_n \rangle_{\tilde{\theta}_n}}. \tag{18}$$

The Compton MTF is the 2-D Fourier transform of $\text{psf}_c(\tau)$, giving

$$\text{MTF}(\nu) = \frac{\langle \bar{g}_n T_1(\nu|\theta_n) \rangle_{\tilde{\theta}_n}}{\langle \bar{g}_n \rangle_{\tilde{\theta}_n}} \tag{19}$$

where $T_1(\nu|\theta_n)$ is the Fourier transform of $p_1(\tau|\theta_n)$ and is given in Appendix B. Substituting Eq. (14) into Eq. (19) and calculating the average over $\tilde{\theta}_n$, we have the Compton MTF given by

$$\text{MTF}(\nu) = \frac{\int_0^{\frac{\pi}{2}} l_{ab} \, T_1(\nu|\theta_n) \, \text{pr}_{\tilde{\theta}}(\theta_n) \, d\theta_n}{\int_0^{\frac{\pi}{2}} l_{ab} \, \text{pr}_{\tilde{\theta}}(\theta_n) \, d\theta_n}. \tag{20}$$

The Compton NPS in Eq. (10) can be written as

$$\text{NPS}(\nu) = \eta \, \bar{q}_{\text{in}} \langle \bar{g}_n^2 \langle |T_n(\nu)|^2 \rangle_{\tilde{\gamma}_n} \rangle_{\tilde{\theta}_n} + \eta \, \bar{q}_{\text{in}} \langle \bar{g}_n \rangle_{\tilde{\theta}_n}$$

$$= \eta \, \bar{q}_{\text{in}} \langle \bar{g}_n^2 T_2(\nu|\theta_n) \rangle_{\tilde{\theta}_n} + \eta \, \bar{q}_{\text{in}} \langle \bar{g}_n \rangle_{\tilde{\theta}_n}, \tag{21}$$

**Table 1.** Values used to determine the Compton MTF, NPS and DQE of a Lanex Regular detector for portal imaging at 6 MV.

| Variable | Value | Physical Meaning |
|---|---|---|
| $t_1$ | 1 mm | copper plate thickness |
| $t_2$ | 0.192 mm | scintillating phosphor thickness |
| $\rho$ | 3.72 g/cm$^3$ | density of phosphor |
| $g_0$ | $1.244 \times 10^5$ quanta/mm | average number of secondaries per unit length in phosphor |
| $\bar{q}_{in}$ | $3.46 \times 10^6$ quanta/mm$^2$ | average number of incident x-ray |

where the averaging $|T_n(\nu)|^2$ over $\tilde{\gamma}_n$ has been defined by the function $T_2(\nu|\theta_n)$ for brevity. $T_2(\nu|\theta_n)$, derived in Appendix C for the uniform PDF $\mathrm{pr}_{\tilde{\Lambda}}(\Lambda|\theta_n)$, can be expressed as the 2-D Fourier transform of a circularly symmetric function $p_2(\tau|\theta_n)$ defined by

$$p_2(\tau|\theta_n) \equiv \frac{1}{\pi|\tau|} \left[ \mathrm{pr}_{\tilde{\Lambda}}(|\tau||\theta_n) \star \mathrm{pr}_{\tilde{\Lambda}}(|\tau||\theta_n) \right], \tag{22}$$

where $\star$ denotes the spatial correlation-integral operator. The function $p_2(\tau|\theta_n)$ describes the statistical correlation in the distribution of secondaries due to a Compton scatter (described by $\theta_n$). When the spatial distant of two secondaries is approximately equal to the projected range $b - a$ of the recoil electron, the correlation drops to zero. Similar to Eq. (20), the Compton NPS is expressed as

$$\mathrm{NPS}(\nu) = \eta \, \bar{q}_{in} \int_0^{\frac{\pi}{2}} \left[ g_0^2 \, l_{ab}^2 \, T_2(\nu|\theta_n) + g_0 \, l_{ab} \right] \mathrm{pr}_{\tilde{\theta}}(\theta_n) \, \mathrm{d}\theta_n. \tag{23}$$

Finally, the Compton DQE can be expressed as

$$\mathrm{DQE}(\nu) = \frac{\eta \, g_0 \left[ \int_0^{\frac{\pi}{2}} l_{ab} \, T_1(\nu|\theta) \, \mathrm{pr}_{\tilde{\theta}}(\theta) \, \mathrm{d}\theta \right]^2}{\int_0^{\frac{\pi}{2}} \left[ g_0 \, l_{ab}^2 \, T_2(\nu|\theta) + l_{ab} \right] \mathrm{pr}_{\tilde{\theta}}(\theta) \, \mathrm{d}\theta}. \tag{24}$$

Equations (20), (23) and (24) give the Compton MTF, NPS and DQE, in terms of the uniform distribution of secondary quanta along a recoil-electron path for a flat-panel portal-imaging system.

### 3.3. Results

Results are applied to the description of a Lanex Regular detector for portal imaging at 6 MeV. The Compton MTF, NPS and DQE are obtained from numerical evaluations of Eqs. (20), (23) and (24) respectively, and using values listed in Table 1.

Figure 7 shows the results of Compton MTF for photon energies of 1.5, 2, 4, 6 MeV. For comparison, we also show the secondary radiation MTF obtained by a Monte Carlo simulation (El-Mohri *et al.*[12]). There are some difference between our result and Monte Carlo result at low spatial frequency, while our result is in agreement with Monte Carlo study at high spatial frequency. The reason for this difference is thought to be one assumption that the path of the recoil electron is a straight line in the phosphor.

Figure 8 shows the results of Compton NPS. For photon energy of 1.5 MeV, most kinetic energy of recoil electron is absorbed in copper plate and does not contribute the imaging. Corresponding, the NPS is smaller. For photon energy of 2 Mev, the NPS has approximately the maximum value. With an increase in photon energy, the NPS becomes smaller.

Figure 9 shows results for the Compton DQE. At zero spatial frequency, the DQEs have different values for photon energies due to both an energy dependent quantum efficiency and average conversion gain due to energy dependent recoil electron path length in the phosphor. The DQE falls to a small value near 2 cycles/mm for all energies.
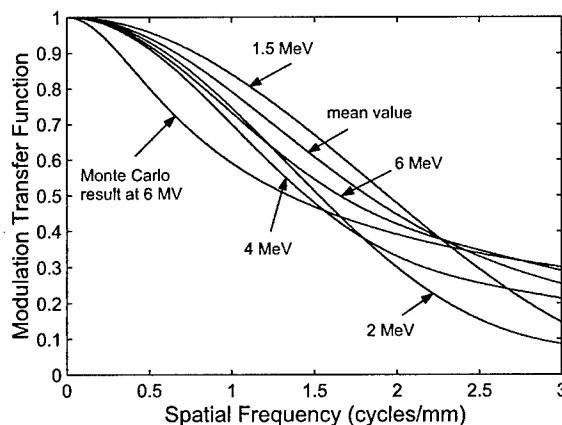
**Figure 7.** The MTF corresponding to Compton scatter for incident photon energies between 1.5 and 6 MeV, and by a Monte Carlo simulation quoted from Ref. 12.
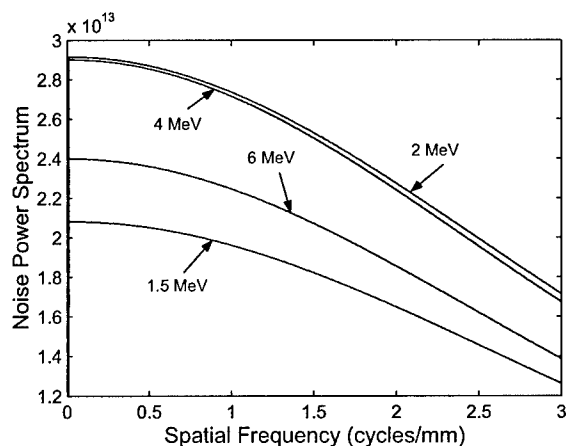


**Figure 8.** The NPS corresponding to Compton scatter for incident photon energies between 1.5 and 6 MeV.
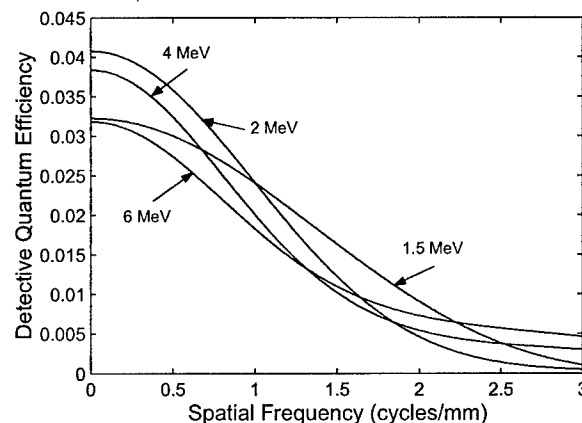
**Figure 9.** The DQE corresponding to Compton scatter for incident photon energies between 1.5 and 6 MeV.

## 4. CONCLUSIONS

In this study it has been shown that conversion of x-ray energy to secondary ionizations due to Compton scatter can be described by an input-labeled cascade of the amplification and scattering processes. Although Monte Carlo techniques have been developed and used for particular system designs where only Compton scatter is significant, this is the first model of how Compton interactions in the metal-plate/phosphor combination degrade image quality in terms of signal and noise. Based on the analysis of Compton scatter and the transfer model developed in this study, the expressions of the Compton MTF, NPS and DQE are derived. It is shown that Compton MTF depends on energy of x-ray photon in a complex way, and Compton scatter imposes a fundamental limitation on both the MTF and DQE of x-ray imaging system, consistent with experimental and Monte Carlo observations. Use of analytic model obtained with the transfer-theory analysis provides additional insight into the physical reasons for these limitations.

## APPENDIX A. PROBABILITY DENSITY FUNCTION OF SCATTERING ANGLE $\theta$

In this appendix, the probability density functions (PDF) of $\tilde{\theta}$ is derived, representing the mean probability per radian of scatter occurring with that angle.

We denote by $\mathcal{A}$ the event of a Compton interaction occurring when a single photon impinges on a layer of medium of thickness $\Delta z$ electrons per square. The probability of event $\mathcal{A}$ may be evaluated using the total Klein-Nishina

cross section $\sigma$,[7] i.e.,

$$P(\mathcal{A}) = \sigma \left(\text{cm}^2/\text{el}\right) \times \Delta z \left(\text{el}/\text{cm}^2\right). \tag{25}$$

Denote by $\mathcal{B}$ the event of a recoil electron scattered into the cone contained between 0 and $\theta$. The probability of $\mathcal{B}$ due to Compton scatter is therefore given by the conditional probability $P(\mathcal{B}|\mathcal{A})$. It is obvious that the PDF $\text{pr}_{\tilde{\theta}}(\theta)$ for the recoil electron is the PDF of the event $\mathcal{B}$ assuming $\mathcal{A}$, given by the derivative of $P(\mathcal{B}|\mathcal{A})$ with respect to $\theta$, i.e., $\text{pr}_{\tilde{\theta}}(\theta) = \text{d}P(\mathcal{B}|\mathcal{A})/\text{d}\theta$. By definition[11]

$$P(\mathcal{B}|\mathcal{A}) = \frac{P(\mathcal{B}\mathcal{A})}{P(\mathcal{A})}. \tag{26}$$

The joint probability $P(\mathcal{B}\mathcal{A})$ can be interpreted as a probability line mass[11] on the event of Compton interaction, giving the probability of a Compton event producing a recoil electron between angles 0 and $\theta$. It can be obtained from the Klein-Nishina equation.[7]

If the scattered photon angle $\phi$ is known for a given Compton interaction, then the recoil electron angle $\theta$ is determined by[6]

$$\cot\theta = (1+\alpha)\tan\left(\frac{\phi}{2}\right). \tag{27}$$

Thus, the corresponding Klein-Nishina equation on the scattering angle $\theta$ of a recoil electron may be expressed as

$$\frac{\text{d}\sigma}{\text{d}\theta} = 8r_0^2\pi(1+\alpha)^2\frac{\cot\theta(1+\cot^2\theta)}{(1+\alpha)^2+\cot^2\theta}F(\theta), \tag{28}$$

and

$$F(\theta) = \frac{1}{[(1+\alpha)^2+(1+2\alpha)\cot^2\theta]^2}\left\{\frac{(1+\alpha)^4+\cot^4\theta}{(1+\alpha)^2+\cot^2\theta} + \frac{2\alpha^2\cot^4\theta}{(1+\alpha)^2+(1+2\alpha)\cot^2\theta}\right\}. \tag{29}$$

where $r_0$ denotes the classical electron radius ($2.81794 \times 10^{-13}$cm). $\text{d}\sigma/\text{d}\theta$ gives the "Compton fraction" of recoil electron that is scattered into the cone contained between $\theta$ and $\theta + \text{d}\theta$. Consequently,

$$P(\mathcal{A}\mathcal{B}) = \Delta z \int_0^\theta \frac{\text{d}\sigma}{\text{d}\theta} \, \text{d}\theta, \tag{30}$$

which results in that

$$P(\mathcal{B}|\mathcal{A}) = \frac{P(\mathcal{A}\mathcal{B})}{P(\mathcal{A})} = \frac{1}{\sigma}\int_0^\theta \frac{\text{d}\sigma}{\text{d}\theta} \, \text{d}\theta. \tag{31}$$

Based on the above results, we obtain

$$\text{pr}_{\tilde{\theta}}(\theta) = \frac{\text{d}\,P(\mathcal{B}|\mathcal{A})}{\text{d}\theta} = \frac{8r_0^2\pi}{\sigma}(1+\alpha)^2\frac{\cot\theta(1+\cot^2\theta)}{(1+\alpha)^2+\cot^2\theta}F(\theta), \tag{32}$$

where $F(\phi)$ is given by Eq. (29).

## APPENDIX B. FUNCTION $T_1(\nu|\theta)$

The function $T_1(\nu|\theta)$ is the 2-D Fourier transform of $p_1(\tau|\theta)$ defined in Eq. (17). For the uniform PDF $\text{pr}_{\tilde{\Lambda}}(\Lambda|\theta_n)$ as shown in Fig. 6, $p_1(\tau|\theta)$ is given by

$$p_1(\tau|\theta_n) = \begin{cases} \dfrac{1}{2\pi|\tau|} \cdot \dfrac{1}{b-a} & a < |\tau| < b \\[2mm] 0 & \text{otherwise} \end{cases}. \tag{33}$$

Since $p_1(\tau|\theta_n)$ is circularly symmetric, $T_1(\nu|\theta_n)$ can be expressed as the Hankel transform of $p_1(\tau|\theta_n)$,[13] giving

$$T_1(\nu|\theta_n) = 2\pi \int_0^\infty p_1(\tau|\theta_n)J_0(2\pi\nu\tau)\tau \, \text{d}\tau, \tag{34}$$

where $\tau = |\tau|$ and $J_0(2\pi\nu\tau)$ is the zero-order Bessel function of the first kind.[14] Substituting Eq. (33) into Eq. (34), we have

$$T_1(\nu|\theta_n) = \frac{1}{b-a}\int_a^b J_0(2\pi\nu\tau) \, \text{d}\tau. \tag{35}$$

## APPENDIX C. FUNCTION $T_2(\nu|\theta)$

In this appendix, the average of $|T_n(\nu)|^2$ over $\tilde{\gamma}_n$, defined as the function $T_2(\nu|\theta_n)$, is determined where $T_n(\nu)$ is the 2-D Fourier transform of $\mathrm{pr}_{\tilde{\tau}}(\tau|n)$ given by Eq. (15). Calculating the 2-D Fourier transform of $\mathrm{pr}_{\tilde{\tau}}(\tau|n)$ in polar coordinates, we obtain

$$T_n(\nu) = \int_0^\infty \mathrm{pr}_{\tilde{\Lambda}}(\tau|\theta_n) \, e^{-j2\pi\nu\tau\cos(\gamma_n-\beta)} \, \mathrm{d}\tau, \tag{36}$$

where $\nu$ and $\beta$ is the magnitude and angular components in the frequency domain, and $\tau = |\tau|$. The modulus of $T_n(\nu)$ may be expressed in terms of the product of its conjugate pairs, giving

$$|T_n(\nu)|^2 = T_n(\nu)T_n^*(\nu) = \int_0^\infty \int_0^\infty \mathrm{pr}_{\tilde{\Lambda}}(\tau|\theta_n) \, \mathrm{pr}_{\tilde{\Lambda}}(\tau'|\theta_n) \, e^{-j2\pi\nu(\tau-\tau')\cos(\gamma_n-\beta)} \, \mathrm{d}\tau \, \mathrm{d}\tau'. \tag{37}$$

Since $\tilde{\gamma}_n$ is a random angle with the uniform PDF $\mathrm{pr}_{\tilde{\gamma}_n}(\gamma_n) = 1/2\pi$, the average of $|T_n(\nu)|^2$ over $\tilde{\gamma}_n$, is

$$\begin{aligned}
T_2(\nu|\theta_n) &\equiv \langle |T_n(\nu)|^2 \rangle_{\tilde{\gamma}_n} = \frac{1}{2\pi} \int_0^{2\pi} |T_n(\nu)|^2 d\gamma_n \\
&= \frac{1}{2\pi} \int_0^\infty \int_0^\infty \mathrm{pr}_{\tilde{\Lambda}}(\tau|\theta_n) \, \mathrm{pr}_{\tilde{\Lambda}}(\tau'|\theta_n) \left[ \int_0^{2\pi} e^{-j2\pi\nu(\tau-\tau')\cos(\gamma_n-\beta)} \, \mathrm{d}\gamma_n \right] \mathrm{d}\tau \, \mathrm{d}\tau' \\
&= \int_0^\infty \int_0^\infty \mathrm{pr}_{\tilde{\Lambda}}(\tau|\theta_n) \, \mathrm{pr}_{\tilde{\Lambda}}(\tau'|\theta_n) J_0[2\pi\nu(\tau-\tau')] \, \mathrm{d}\tau \, \mathrm{d}\tau'
\end{aligned} \tag{38}$$

where $J_0(\ )$ is the zero-order Bessel function of the first kind.[14] Performing the change of variables $\tau'' = \tau' - \tau$ in the $\tau$ integral for Eq. (38) yields

$$T_2(\nu|\theta_n) = 2 \int_0^\infty [\mathrm{pr}_{\tilde{\Lambda}}(\tau''|\theta_n) \star \mathrm{pr}_{\tilde{\Lambda}}(\tau''|\theta_n)] J_0(2\pi\nu\tau'') \, \mathrm{d}\tau'', \tag{39}$$

where $\star$ is the spatial correlation-integral operator. If we define a circularly symmetric function $p_2(\tau|\theta_n)$ such that

$$p_2(\tau|\theta_n) \equiv \frac{1}{\pi|\tau|} [\mathrm{pr}_{\tilde{\Lambda}}(|\tau||\theta_n) \star \mathrm{pr}_{\tilde{\Lambda}}(|\tau||\theta_n)], \tag{40}$$

then Eq. (39) is recognized as the 2-D Fourier transform of $p_2(\tau|\theta_n)$, expressed as the form of the Hankel transform. Therefore, $T_2(\nu|\theta_n)$ and $p_2(\tau|\theta_n)$ are the Fourier transform pair.

For the uniform PDF $\mathrm{pr}_{\tilde{\Lambda}}(\Lambda|\theta_n)$ as shown in Fig. 6, we obtain the expression of $p_2(\tau|\theta_n)$ given by

$$p_2(\tau|\theta_n) = \begin{cases} \dfrac{1}{\pi|\tau|(b-a)^2} (b-a-|\tau|) & 0 \le |\tau| < b-a \\ \\ 0 & \text{otherwise} \end{cases} \tag{41}$$

Similar to the calculation of $T_1(\nu|\theta)$ shown in Appendix B, we can obtain

$$T_2(\tau|\theta_n) = \frac{1}{\pi\tau(b-a)} \left\{ \int_0^{2\pi\tau(b-a)} J_0(\tau) \, \mathrm{d}\tau - J_1 \left[ 2\pi\nu(b-a) \right] \right\}, \tag{42}$$

where the function $J_1(\ )$ is the first-order Bessel function of the first kind.[14]

## REFERENCES

1. K. Rossmann, "Point spread-function, line spread-function, and modulation transfer function," Radiology **93**, 257–272 (1969).
2. J. C. Dainty and R. Shaw, *Image Science* (Academic, New York, 1974).
3. L. Eyges, "Multiple scattering with energy loss," Phys. Rev. **74**, 1534 (1948).

4. D. Jette, "Electron dose calculation using multiple-scattering theory A. Gaussian multiple-scattering theory," Med. Phys. **15**, 123–137 (1988).

5. R. Van Metter and M. Rabbani, "An application of multivariate moment-generating functions to the analysis of signal and noise propagation in radiographic screen-film systems," Med. Phys. **17**, 65–71 (1990).

6. F. H. Attix, *Introduction to Radiological Physics and Radiation Dosimetry* (John Wiley & Sons, New York, 1986).

7. H. E. Johns and J. R. Cunningham, *The Physics of Radiology*, 4th ed. (Thomas, Springfield, IL, 1983).

8. M. Rabbani, R. Shaw, and R. Van Metter, "Detective quantum efficiency of imaging systems with amplifying and scattering mechanisms," J. Opt. Soc. Am. A **4**, 895–901 (1987).

9. I. A. Cunningham, "Applied linear-systems theory," in *Handbook of Medical Imaging*, Physics and Psychophysics Vol. 1, edited by J. Beutel, H. L. Kundel, and R. Van Metter, (SPIE, Bellingham, 2000), pp. 79–160.

10. "Physical reference data—stopping power and range tables for electrons," NIST physics Laboratory, http://physics.nist.gov/PhysRefData/Star/Text/ESTAR.html.

11. A. Papoulis, *Probability, Random Variables, and Stochastic Processes*, 3rd ed. (McGraw Hill, New York, 1991).

12. Y. El-Mohri, K.-W. Jee, L. E. Antonuk, M. Maolinbay, and Q. Zhao, "Determination of the detective quantum efficiency of a prototype, megavoltage indirect detection, active matrix flat-panel imager," Med. Phys. **28**, 2538–2550 (2001).

13. R.N. Bracewell, *The Fourier Transform and Its Applications*, 2nd ed. (McGraw Hill, New York, 1986).

14. N. W. McLachlan, *Bessel Functions for Engineers*, 2nd ed. (Oxford University Press, London, 1955).

# Cascaded Models and the DQE of Flat-Panel Imagers: Noise Aliasing, Secondary Quantum Noise and Reabsorption*

I.A. Cunningham, J. Yao and V. Subotic
Imaging Research Laboratories, The John P. Robarts Research Institute;
Department of Diagnostic Radiology, London Health Sciences Center;
Lawson Health Research Institute; and, The University of Western Ontario,
London, Ontario, Canada

## ABSTRACT

Theoretical models of the detective quantum efficiency (DQE) provide insight into fundamental performance limitations and standards to which particular systems can be compared. Over the past several years, cascaded models have been developed to describe the DQE of several flat panel detectors. This article summarizes the governing principles of cascaded models, and conditions that must be satisfied to prevent misuse. It is shown how to incorporate: a) poly-energetic x rays; b) Swank noise; c) the Lubberts effect; d) reabsorption of K x rays from photo-electric interactions; e) secondary quantum noise; and, f) noise aliasing.

Cascaded models involve cascading theoretical expressions of the noise-power spectrum (NPS) through multiple stages. Most expressions involve two or three terms, requiring the manipulation of algebraic expressions consisting of hundreds of terms. This practical limitation is alleviated using MATLAB's Simulink programming environment and symbolic math manipulations. It is shown that even for an "indirect" detector, noise aliasing reduces the DQE by up to 50% at the cut-off frequency. Secondary quantum noise is generally a small effect, but reabsorption can reduce the DQE by 20-25% over a wide range of spatial frequencies.

Key words: flat panel detectors, cascaded models, noise power spectrum, detective quantum efficiency

## 1. INTRODUCTION

Medical x-ray imaging systems must be designed to ensure that maximum image quality is obtained for a specified radiation dose to the patient, and quality assurance programs are used to ensure these standards are maintained. The view that an imaging system must faithfully *transfer* the input image signal to the output suggests the use of principles used in the study of communications theory, and in particular, the Fourier-transform linear-systems approach.[1] Linear-systems theory was initially applied in the imaging sciences by Rossmann and co-workers,[2,3] including use of the modulation-transfer function (MTF) and related concepts. General works have subsequently been published by Dainty & Shaw,[4] Gaskill,[5] Papoulis,[6] Doi, Rossmann and Haus,[7] Metz and Doi,[8] and many others. Possibly the most extensive use of linear-systems theory in the medical imaging field is by Barrett and Swindell[9] who use this approach to describe fundamental principles and characteristics of many imaging systems in radiography, computed tomography (CT), nuclear medicine, ultrasound and other areas.

Cascaded models describing the transfer of quantum-based images have gained popularity recently and have been used successfully to develop theoretical models of the DQE of various flat-panel detectors. This article summarizes how these models have been used, some caveats, and how they can be used to develop more sophistical models of new detector designs.

## 2. GOVERNING PRINCIPLES OF CASCADED MODELS

Block diagrams are useful as graphical representations of cascaded models. They illustrate the logical sequence of events that connect the input to output as required to represent the physical operation of an imaging system. Each block represents a particular process with known input and output relationships, such as conversion from x rays to light, or the scattering of that light in a screen.

### 2.1. Point Processes

Some elementary processes are summarized below. They consist of two types. Point processes[10] are necessary to describe quantum-based processes. Both the input and output of each point process must necessarily be a spatial distribution (ie. an "image") of points, represented as the random function $\tilde{q}(\mathbf{r})$ here. The overhead tilde is used to indicate a random variable, characterized in terms of a mean distribution $\bar{q}$ and either the autocorrelation function $K(\mathbf{r})$ in the spatial domain, or the Wiener (noise-power) spectrum $NPS(\mathbf{k})$ in the spatial-frequency domain (see assumptions below), describing second-order statistics of this distribution. The mean $\bar{q}$ has dimension $\text{area}^{-1}$, such as the mean number of quanta/mm$^2$ in an image. The NPS of a point distribution has the same units as the distribution, such as mm$^{-2}$.

It is critical that each point distribution be rigourously and unambiguously defined, both in terms of what each point represents, and the mean and NPS. Failure to do so is the primary cause of misuse of the cascaded approach. A point distribution $\tilde{q}(\mathbf{r})$ can always be represented in terms of a spatial distribution of impulse functions, such as the Dirac function $\delta(\mathbf{r})$:

$$\tilde{q}(\mathbf{r}) = \sum_{i=1}^{\tilde{N}} \delta(\mathbf{r} - \tilde{\mathbf{r}}_i) \tag{1}$$

where each $\delta$ function represents one point (one quantum) in the distribution (the image), $\tilde{N}$ is a random variable describing the total number of points and $\tilde{\mathbf{r}}_i$ is a random vector describing the spatial position of the $i$th point. Each $\delta$ function in this example has units mm$^{-2}$. They are generalized functions and distribution theory[11] must be used to describe the distributions.

### 2.2. Non Point Processes

Other processes are non point processes. The input may be a point process or not, but the output is always a regular random function, such as $\tilde{d}(\mathbf{r})$. The output units are specific to the model used. An example of such a process is the integration of quanta in a detector element represented as a convolution integral, where the output $\tilde{d}(\mathbf{r})$ represents the (unitless) presampling detector output (described below).

### 2.3. Assumptions

Several assumptions are implicit in the linear-systems cascaded approach.

1. The first assumption is that the system be linear (or linearizable). This implies that the mean output signal is proportional to the mean input signal. That is, $\bar{q}_{out} \propto \bar{q}_{in}$. If this is true for each process, it is also true for the overall system response.

2. Each process must be shift invariant. In practice, this generally means that cascaded models do not describe edge effects properly. Aliasing in digital systems may result in a non shift-invariant response.

3. While the positions of points in a distribution may be statistically correlated, the interactions of any point must be independent of all other points. Thus, a particular quantum in an image undergoing a particular interaction in a detector has no bearing on what other quanta will do.

4. All noise processes must be wide-sense stationary (WSS) or wide-sense cyclostationary (WSCS). Wide-sense stationarity[11] means the mean and autocovariance are the same in all regions of the image. This is generally violated near image edges, and in addition is only applicable for low-contrast, uniform-exposure conditions. Wide-sense cyclostationarity[11] means the mean and autocovariance are periodic in an image, required for the description of digital imaging systems.

## 3. ELEMENTARY POINT PROCESSES

The most commonly used elementary processes were first described by Rabbani, Shaw and Van Metter.[12] A brief summary is given here for completeness. These are stochastic linear processes, linear in terms of the mean response.

### 3.1. Quantum Gain

Quantum gain corresponds to an increase or decrease in the number of points in the point distribution. Both the input and output are necessarily point processes. Examples include conversion of x-ray quanta to optical quanta in a radiographic screen, where each input quantum is converted to $\tilde{g}$ output quanta and $\tilde{g}$ is a random variable with mean $\bar{g}$ and variance $\sigma_g^2$, but does not include the scattering of light quanta. A point process is called marked if it has overlapping points and orderly if it does not.

It is assumed that each conversion is independent of all others, and only one random variable $\tilde{g}$ is used to describe all conversions. For the radiographic screen, this requires that all incident x ray quanta have the same energy and the system response to each quantum must be the same.

Quantum gain can be expressed as a random process as

$$\tilde{q}_{out}(\mathbf{r}) = \tilde{g}\ \tilde{q}_{in}(\mathbf{r}) \tag{2}$$

where the mean density of points in each distribution are related by

$$\bar{q}_{out} = \bar{g}\ \bar{q}_{in}. \tag{3}$$

Rabbani, Shaw and Van Metter[12] described noise transfer through this gain stage, giving

$$\text{NPS}_{out}(\mathbf{k}) = \bar{g}^2 \text{NPS}_{in}(\mathbf{k}) + \sigma_g^2 \bar{q}_{in} \tag{4}$$

expressed in terms of the two-dimensional spatial-frequency vector $\mathbf{k}$. This result consists of two terms. The second term is always independent of frequency (extending to "infinite" frequency), and represents uncorrelated image noise. Thus, the output of a quantum gain process is never band-limited and always contains an uncorrelated component.

### 3.2. Quantum Selection

Quantum selection is a special case of quantum gain in which $\tilde{g}$ is a Bernoulli random variable[†] that can assume sample values of 0 or 1 only. That is, each quantum in the input is either transferred (probability $\bar{g}$), or not (probability $1 - \bar{g}$), to the output where $0 \le \bar{g} \le 1$. Examples include the quantum efficiency of a radiographic screen, and Fig. (1) illustrates a sparse quantum image $q_{in}(\mathbf{r})$ being passed through a quantum selection process with $\bar{g} = 0.5$.

The variance $\sigma_g^2$ is given by $\sigma_g^2 = \langle |\tilde{g}|^2 \rangle - |\langle \tilde{g} \rangle|^2$, and since $\tilde{g}$ can take values of 0 or 1 only,

$$\sigma_g^2 = \bar{g} - \bar{g}^2 = \bar{g}(1 - \bar{g}). \tag{5}$$

---

[†]A Bernoulli RV can have only two possible values, such as 1 or 0. The toss of a coin can be represented in terms of a Bernoulli RV.
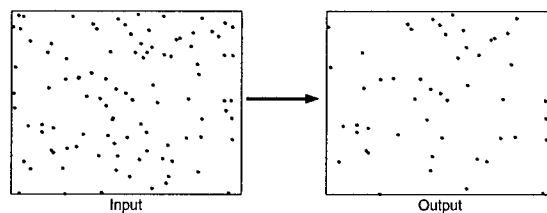
**Figure 1.** Illustration of the quantum selection process. In this example, half of the points in the input image ($q_{in}(\mathbf{r})$, left) are transferred to the output image ($q_{out}(\mathbf{r})$, right).
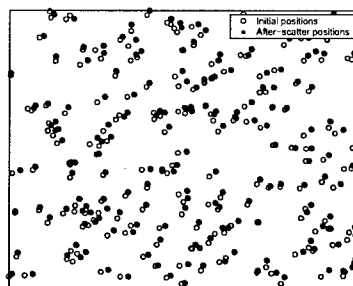


**Figure 2.** In a scatter process, image quanta are relocated by a random displacement with a probability given by the scatter PSF. Open circles represent initial positions, solid circles represent locations after being scattered. Some quanta near the edges have been scattered out of the displayed image area.

The quantum selection process can thus be characterized solely in terms of the probability $\bar{g}$. Noise transfer through the process is given by

$$\text{NPS}_{out}(\mathbf{k}) = \bar{g}^2 \left[\text{NPS}_{in}(\mathbf{k}) - \bar{q}_{in}\right] + \bar{g}\bar{q}_{in}. \tag{6}$$

The component $\text{NPS}_{in}(\mathbf{k}) - \bar{q}_{in}$ is called the *correlated* noise component of the input, and $\bar{q}_{in}$ is called the *uncorrelated* component. It is sometimes said that the correlated component is "passed through" $\bar{g}^2$ in keeping with the idea of a transfer model, while the uncorrelated component is passed though $\bar{g}$. A significant correlated component necessarily exists in the input distribution of quanta when $\text{NPS}_{in}(\mathbf{k}) \gg \bar{q}_{in}$. When the input quanta are uncorrelated, such as with a distribution of incident x rays, then $\text{NPS}_{in}(\mathbf{k}) = \bar{q}_{in}$, corresponding to the smallest value that $\text{NPS}_{in}(\mathbf{k})$ can have, and $\text{NPS}_{out}(\mathbf{k}) = \bar{g}\,\bar{q}_{in}$.

## 3.3. Quantum Scatter

Most image-blurring processes, such as blur caused by the scattering of optical quanta in a radiographic screen, are quantum-scattering processes. That is, each quantum is randomly relocated to a new position with a probability described by the normalized PSF of the blur as illustrated by Fig. 2. This differs from the blur described by a linear filter (described below) which can be viewed as a redistribution of signal by weights as described by the convolution integral, while scatter must be viewed as a redistribution by probabilities. This distinction has been recognized for some time, but noise transfer relationships were first described by Rabbani, Shaw and Van Metter,[12] and more recently using point-process theory by Barrett *et al.*[13]

The output of a scatter stage is always a point process and can be written as

$$\tilde{q}_{out}(\mathbf{r}) = \tilde{q}_{in}(\mathbf{r}) *_s \text{psf}(\mathbf{r}) \tag{7}$$
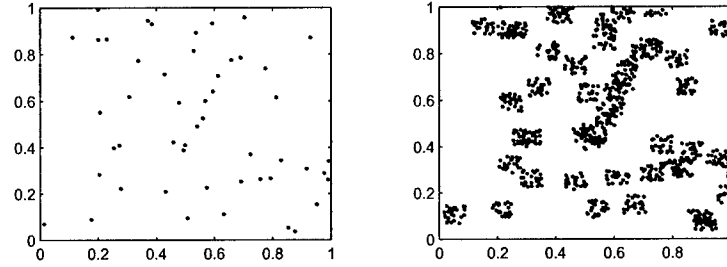
**Figure 3.** Conversion of input quanta into a cluster of secondary quanta can be represented by cascading a gain and scatter stage. Input quanta (left) are uncorrelated in this example, but the resulting output secondary quanta are correlated (right).

where psf($\mathbf{r}$) is the scatter PSF normalized to unity and $*_s$ represents the scatter operator. Rabbani *et al.*[12] showed that $\bar{q}$ and NPS($\mathbf{k}$) are transferred through a scatter process according to

$$\bar{q}_{out} = \bar{q}_{in} \qquad (8)$$

and

$$\text{NPS}_{out}(\mathbf{k}) = [\text{NPS}_{in}(\mathbf{k}) - \bar{q}_{in}]\,|\text{MTF}(\mathbf{k})|^2 + \bar{q}_{in}, \qquad (9)$$

where MTF($\mathbf{k}$) is the modulus of the Fourier transform of the scatter PSF. Unlike the linear filter (Eq. 13), only the correlated noise component is passed through the squared scatter MTF. The frequency-independent uncorrelated component is passed unchanged.

### 3.4. Cascading Point Processes

More complex processes can often be represented as a cascade of these simple processes. For example, a radiographic screen converts each interacting x ray into a large number of optical quanta. The optical quanta are subsequently scattered before they leave the screen. For a thin transparent screen with quantum efficiency $\alpha$ (ignoring Swank noise and the Lubberts effect), the distribution of light leaving the screen is the cascade of a selection, gain and scatter stage, described by

$$\tilde{q}_{out}(\mathbf{r}) = [\tilde{g}\,\tilde{\alpha}\,\tilde{q}_{in}(\mathbf{r})] \ *_s \ \text{psf}(\mathbf{r}). \qquad (10)$$

The mean number of quanta and NPS are obtained by cascading the appropriate transfer expressions. Figure (3) shows sample input and output functions passing through this cascaded process.

## 4. NON POINT PROCESSES

Any process that can be represented in terms of linear operators, such as convolution or multiplication, is a linear process. The following processes are all linear.

### 4.1. Integrating Quanta in a Detector Element: Linear Filter

Another elementary process is a linear filter, describing situations where image blur is accurately expressed as a convolution. The input can be either a point process $q(\mathbf{r})$ or an analog signal, but the output is always an analog signal such as $d(x)$ where

$$\tilde{d}_{out}(\mathbf{r}) = \tilde{q}_{in}(\mathbf{r}) * \text{p}(\mathbf{r}) \qquad (11)$$

where $p(\mathbf{r})$ is the filter kernel. Therefore,

$$\bar{d}_{out} = A\,\bar{q}_{in} \qquad (12)$$

Sampling with Sinc Interpolation
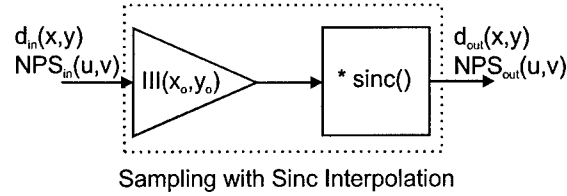
**Figure 4.** Sampling is represented as the combination of multiplication with an array of $\delta$ functions followed by sinc interpolation. The result is a linear operator relating a presampling analog input image to an analog output image.

where $A$ is the integral of the kernel, $A = \int_{-\infty}^{\infty} p(\mathbf{r}) \, d^2\mathbf{r}$, and,

$$\mathrm{NPS}_{out}(\mathbf{k}) = \mathrm{NPS}_{in}(\mathbf{k})|P(\mathbf{k})|^2 = A^2 \mathrm{NPS}_{in}(\mathbf{k})\mathrm{MTF}^2(\mathbf{k}) \tag{13}$$

where $P(\mathbf{k})$ is the Fourier transform of $p(\mathbf{r})$. Thus, the input NPS (both correlated and uncorrelated components) is passed through the MTF. As a result, the output from a linear filter is always band limited and the noise power spectrum does not have an uncorrelated component.

Integration of image quanta in a detector element can be represented as a linear filter. If all input quanta incident on elements $a_x \times a_y$ are detected, and if $m$ is the scaling factor relating the number of interacting quanta to the output signal, the detector presampling signal $\tilde{d}(x, y)$ is given in Cartesian coordinates by

$$\tilde{d}_{out}(x, y) = m \, \tilde{q}_{in}(x, y) * \Pi\left(\frac{x}{a_x}, \frac{y}{a_y}\right) \tag{14}$$

where $*$ represents a two-dimensional convolution integral. The mean detector signal $\bar{d}_{out}$ is given by

$$\bar{d}_{out} = m \, a_x \, a_y \, \bar{q}_{in} \tag{15}$$

which is unitless and the NPS by

$$\mathrm{NPS}_{out}(u, v) = m^2 \, a_x^2 \, a_y^2 \, \mathrm{NPS}_{in}(u, v) \, \mathrm{MTF}^2(u, v) \, \mathrm{sinc}^2(\pi a_x u) \, \mathrm{sinc}^2(\pi a_y v) \tag{16}$$

in units of $\mathrm{mm}^2$. It is at this stage, after integration of quanta in detector elements, that one must start representing the image as an analog image rather than as a quantum image. As a consequence, units of the NPS are $\mathrm{mm}^2$ rather than $\mathrm{mm}^{-2}$.

## 4.2. Sampling with Interpolation

The process of sampling a presampling signal to produce a discrete digital image has been represented as a cascaded process by several authors.[14,15] Our description of the sampling operator consists of multiplication by a two-dimensional array of $\delta$ functions at spacings $x_o$ and $y_o$ followed by a sinc interpolation as illustrated in Fig. 4:

$$\tilde{d}_{out}(x, y) = \left[\tilde{d}_{in}(x, y) \times \sum_{n_x=-\infty}^{\infty} \sum_{n_y=-\infty}^{\infty} \delta(x - n_x x_o, y - n_y y_o)\right] * \mathrm{sinc}(\pi x/x_o) * \mathrm{sinc}(\pi y/y_o). \tag{17}$$

This representation makes sampling a linear operator (two cascaded linear operations) and results in the analog image $d_{out}(x, y)$ one gets from a sinc interpolation of a digital image. It also has two attractive benefits. The first is that it avoids the problem of representing a digital image as an array of scaled $\delta$ functions that one gets after multiplication with the $\delta$ functions, thereby avoiding undefined values and

Labelled Quantum Amplification and Scatter
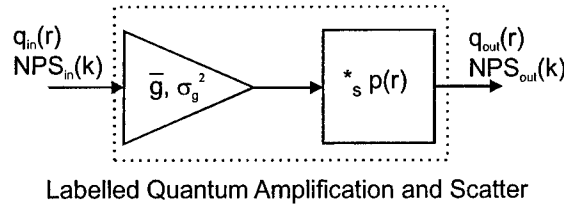
**Figure 5.** A simple model of a radiographic screen consists of the cascade of quantum amplification and scatter processes.

generalized functions. The second is that the resulting analog image is shift invariant as long as the image is not undersampled and there is no aliasing of image signals. In this case, the same output image is obtained regardless of where the sampling grid is located within the image for a noise-free image. This requirement does not apply to image noise, as noise aliasing is not affected by a shift in the sampling positions for stationary noise processes.

The mean digital values can be expressed as

$$\bar{d}_{out} = \bar{d}_{out}(x, y) = \bar{d}_{in}(x, y) \tag{18}$$

and the output NPS as

$$\text{NPS}_{out}(u, v) = \text{NPS}_{in}(u, v) + \sum_{n_x=1}^{\infty} \sum_{n_y=1}^{\infty} \text{NPS}_{in}\left(u \pm \frac{n_x}{x_o}, v \pm \frac{n_y}{y_o}\right) \tag{19}$$

for frequencies below the sampling cut-off frequencies of $u_c = 1/2x_o$ and $v_c = 1/2y_o$. The output NPS has units of mm$^2$.

## 5. COMPLEX PROCESSES

Rabbani and Van Metter[16] described a number of modifications of the elementary point processes in which the parameters of the processes (gain, PSF) are themselves functions of a random variable. This random variable may characterize the input quanta (e.g. x-ray energy) and be independent of position in the image, or it may characterize position in the image and treat all input quanta equivalently. These relationships are summarized in Appendix A.

### 5.1. Lubberts Effect

If both the screen conversion gain and MTF is known as a function of x-ray energy (including a thick non-transparent phosphor), Rabbani and Van Metter[17] showed the NPS is given by an input-labelled gain and scatter process averaged over phosphor depth:

$$\text{NPS}_{out}(\mathbf{k}) = \left[\left\langle (\bar{g}^2 + \sigma_g^2 - \bar{g})|\text{T}(\mathbf{k})|^2\right\rangle + \langle\bar{g}\rangle\right] \bar{q}_{in}. \tag{20}$$

### 5.2. X-Ray Spectral Effects and Swank Noise

For most x-ray detectors, such as a CsI phosphor, the mean conversion gain $\bar{g}$ is a function of x-ray energy. Thus, the input-labelled quantum gain stage can be used to describe NPS transfer. If $\theta$ is a random variable with a probability density function proportional to the energy spectrum of the interacting x rays, the resulting NPS is given by Rabbani and van Metter [16]

$$\text{NPS}_{out}(\mathbf{k}) = \left[\langle\bar{g}\rangle^2 + \left\langle\sigma_g^2\right\rangle + \left\langle|\bar{g} - \langle\bar{g}\rangle|^2\right\rangle\right] \bar{q}_{in} = \langle\bar{g}\rangle^2 \bar{q}_{in} + \left[\left\langle\sigma_g^2\right\rangle + \left\langle|\bar{g} - \langle\bar{g}\rangle|^2\right\rangle\right] \bar{q}_{in} \tag{21}$$
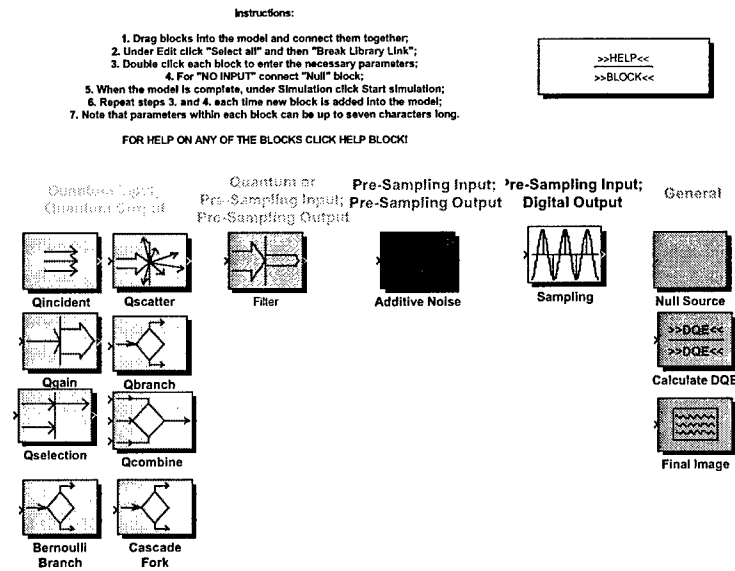
**Figure 6.** Cascaded-systems graphical programming environment with graphical user interface.

where $\langle\rangle$ means an average over the spectrum of interacting x rays. The term with the square brackets in the final form of this expression describes Swank noise for a thin transparent phosphor.[18] Rowlands and Taylor,[19] Hillen *et al.*[20] and others have described the variance of the conversion gain as a function of energy for CsI which can be used in this calculation for a specific spectrum. While this description includes the variable conversion gain, it does not describe the spatial-frequency-dependent aspects of reabsorption.

## 5.3. Reabsorption - Parallel Cascades

One reason for a variable conversion gain is the random production, escape and reabsorption of characteristic x rays from photo-electric interactions. If the K x ray is reabsorbed and the overall conversion gain is not affected by the fluorescence radiation, the spatial dependence of secondary-quanta production is. This affects the spatial-frequency-dependence of the NPS and can be described using parallel cascades of elementary processes requiring the cross-spectral density[21,22] of quantum images (Appendix A).

## 6. CASCADED-SYSTEMS GUI PROGRAMMING ENVIRONMENT

A potential limitation to the use of complex cascaded models is the number of algebraic terms that must be manipulated. For instance, in the model described below, 11 processes are used giving rise to 192 separate terms in the NPS (not including the effect of noise aliasing) that must be simplified and grouped, plus many more terms for the MTF. While many simplifications are possible, this results in tedious calculations requiring verification. To overcome this issue, a GUI programming environment has been developed using the Simulink package of Matlab as illustrated in Fig. 6. A model is generated by selecting blocks representing processes from a "library" of such processes and connecting the appropriate inputs and outputs. Transfer functions for each block are manipulated using the symbolic math package of Matlab resulting in analytic expressions for the overall system MTF, NPS and DQE. In this way, models of arbitrary complexity can be analyzed.

## 7. FLAT PANEL DETECTOR

The model of a "generic" CsI-based flat-panel detector generated with the GUI is illustrated in Fig. 7. This model includes the effect of reabsorption (and thereby Swank noise for thin transparent phosphor),
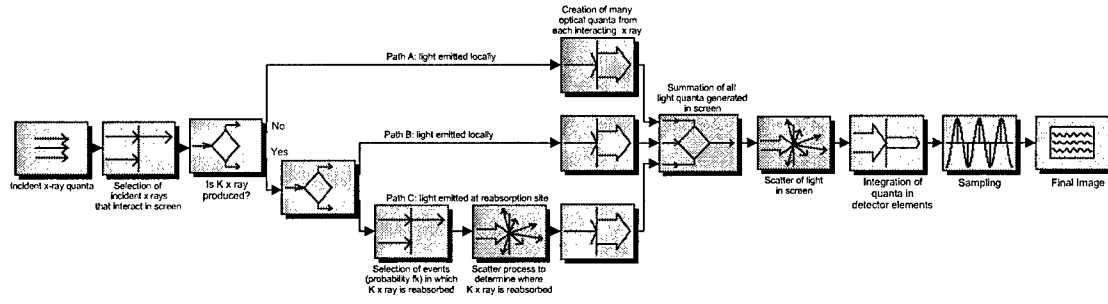
**Figure 7.** Model of a CsI-based flat-panel detector generated with the GUI programming environment.

secondary quantum noise and noise aliasing, but does not include Lubberts effect.

The average large-area gain of this system at energy $E$ calculated with this model is given by

$$\dot{G}(E) = \eta a \bar{m} \qquad (22)$$

where $\eta$ is the quantum efficiency of CsI (0.25 g/cm$^2$) and $\bar{m} = (1 - \omega\xi)\bar{m}_A + \omega\xi\bar{m}_B + \omega\xi f_K\bar{m}_C$ is the average total number of optical quanta emitted from the screen and absorbed in the flat panel detector per interacting x ray. The number of optical quanta detected per keV of an interacting x ray is $\bar{m}_o$. Therefore, $\bar{m}_A = E\bar{m}_o$, $\bar{m}_B = (E - E_K)\bar{m}_o$, $\bar{m}_C = E_K\bar{m}_o$, and hence $\bar{m} = [E - \omega\xi E_K(1 - f_K)]\bar{m}_o$. The physical quantities used are defined in Table 1.

The reabsorption MTF $T_K(u)$ is approximated as the normalized zero-order Hankel transform of an exponential PSF with linear attenuation coefficient $\mu(E_K) = 2.8$ mm$^{-1}$. The optical MTF, $T_o(u)$, is the most difficult parameter to estimate. Illustrated in Fig. 8a, it is chosen to give agreement between the measured MTF and the theoretical MTF given by

$$\text{MTF}(u : E) = \left[\frac{(1 - \omega\xi)\bar{m}_A + \omega\xi\bar{m}_B + \omega\xi f_K\bar{m}_C T_K(u)}{\bar{m}}\right] T_o(u)\text{sinc}(\pi a u). \qquad (23)$$

The presampling NPS is given by

$$\text{NPS}(u : E) = \eta q_o a^2 \left[\left((1 - \omega\xi)\bar{m}_A^2 + \omega\xi\bar{m}_B^2 + \omega\xi f_K\bar{m}_C^2 + 2\omega\xi f_K\bar{m}_B\bar{m}_C T_K(u) - \bar{m}\right) T_o^2(u) + \bar{m}\right]\text{sinc}^2(\pi a u). \qquad (24)$$

The resulting DQE, showing the model results with increasing degrees of sophistication, is shown in Fig. 8b using values in Table 1.

## 8. CONCLUSIONS

This work describes an energy-dependent, cascaded, spatial-frequency-dependent theoretical model of the DQE of a flat-panel detector that includes the effects of secondary quantum noise, noise aliasing and K x ray reabsorption. The factor $\bar{m}_o$ describes the number of optical quanta that are detected by the active matrix per keV of the interacting x ray, and is the least well known aspect of the model. The value $\bar{m}_o = 5.5$ is only an estimate but is typical for CsI[23] and gives reasonable agreement with experiment as shown in Fig. 8b. The theoretical DQE passes directly through the experimental points over all frequencies if this value is reduced to approximately 1.0, increasing the effect of secondary quantum noise.

Secondary quantum noise reduces the DQE by up to 10% close to the sampling cut-off frequency. Also at these high frequencies, noise aliasing degrades the DQE by approximately 50%. Reabsorption causes a 20-25% degradation of the DQE over most non-zero frequencies, consistent with other works (Metz and
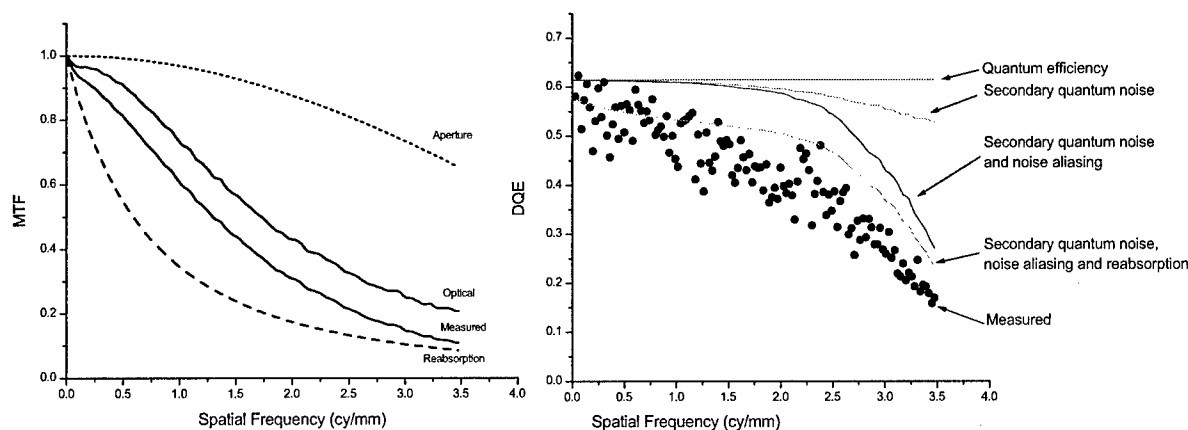
**Figure 8.** Left: comparison of measured MTF, theoretical reabsorption MTF $T_K(\mathbf{k})$, estimated optical MTF $T_o(\mathbf{k})$, and aperture (sinc) MTF. Right: comparison of measured DQE (117 kV, 4 cm Al) with theoretical model.

Vyborny,[24] Hillen *et al.*[20]). The value of $f_K$ was obtained from a numerical estimate based on the CsI thickness and solid-angle considerations; however, the theoretical DQE result is insensitive to variations in $f_K$ between 0.6 and 1.0. It is important to note that a large-area model or measurement of the DQE (zero-frequency value) would miss most of these effects, emphasizing the importance of a proper frequency-based model.

## 9. ACKNOWLEDGEMENTS

| Name | Value | Quantity |
|---|---|---|
| $\bar{q}_o$ | | Average number of incident quanta per mm$^2$ in energy bin E. |
| $E_K$ | 33 keV | K-edge energy of CsI (average of Cs and I). |
| $\omega$ | 0.89 | Fluorescence yield of K-$\alpha$ photoelectric interactions in CsI (average). |
| $\xi$ | 0.85 | Probability that an interacting x ray undergoes K shell interaction. |
| $f_K$ | 0.88 | Probability that characteristic x ray is reabsorbed. DQE is insensitive to changes between 0.6 and 1.0. |
| $\bar{m}_o$ | 5.5 | Number of optical quanta detected per keV of an interacting x-ray quantum. Includes coupling efficiency from CsI to detector, fill factor, etc. |
| $a$ | 0.14 mm | Pixel dimension. |

**Table 1.** Definition of terms used in the model DQE.

# APPENDIX A. SUMMARY OF 1-D NPS TRANSFER RELATIONS

| PROCESS | OUTPUT NPS | REF (Eq) |
|---|---|---|
| **QUANTUM GAIN** | | |
| Uncorrelated (mean gain constant) | $\bar{g}^2 \text{NPS}_{in}(u) + \sigma_g^2 \bar{q}_{in}$ | 12 |
| Input-labelled (eg. mean gain varies with energy) | $\langle \bar{g} \rangle_\theta^2 \, \text{NPS}_{in}(u) + \left[ \langle \sigma_g^2 \rangle_\theta + \text{var}_\theta\{\bar{g}\} \right] \bar{q}_{in}$ | 16 (26) |
| Uncorrelated position-labelled (mean gain random with position) | $\langle \bar{g} \rangle_\theta^2 \, \text{NPS}_{in}(u) + \left[ \langle \sigma_g^2 \rangle_\theta + \text{var}_\theta\{\bar{g}\} \right] \bar{q}_{in}$ | 16 (48) |
| Correlated position-labelled (mean gain spatially correlated) | $\langle \bar{g} \rangle_\theta^2 \, \text{NPS}_{in}(u) + \text{NPS}_{in}(u) * W_g(u) + \left[ W_g(u) + \langle \sigma_g^2 \rangle_\theta \right] \bar{q}_{in}$ | 16 (43) |
| **QUANTUM SCATTER** | | |
| Uncorrelated scatter | $[\text{NPS}_{in}(u) - \bar{q}_{in}] \, \|T(u)\|^2 + \bar{q}_{in}$ | 12 |
| Input-labelled PSF (eg. psf varies with energy) | $[\text{NPS}_{in}(u) - \bar{q}_{in}] \, \| \langle T(u) \rangle_\theta \|^2 + \bar{q}_{in}$ | 16 (63) |
| Uncorrelated position-labelled PSF (psf varies randomly with position) | $[\text{NPS}_{in}(u) - \bar{q}_{in}] \, \| \langle T(u) \rangle_\theta \|^2 + \bar{q}_{in}$ | 16 (81) |
| Correlated position-labelled PSF (psf spatially correlated) | $[\text{NPS}_{in}(u) - \bar{q}_{in}] \, \| \langle T(u) \rangle_\theta \|^2 + S_I(u) + \left[ \bar{q}_{in} S_{II}(u) - \sigma_T^2(u) + 1 \right] \bar{q}_{in}$ | 16 (77) |
| **GAIN AND SCATTER** | | |
| Uncorrelated | $\left[ \bar{g}^2 \text{NPS}_{in}(u) + (\sigma_g^2 - \bar{g}) \bar{q}_{in} \right] \|T(u)\|^2 + \bar{g} \bar{q}_{in}$ | 12 |
| Input-Labelled gain/PSF (eg. both mean gain and psf vary with energy) | $[\text{NPS}_{in}(u) - \bar{q}_{in}] \, \| \langle \bar{g} T(u) \rangle_\theta \|^2 + \bar{q}_{in} \left\langle (\bar{g}^2 + \sigma_g^2 - \bar{g}) \|T(u)\|^2 \right\rangle_\theta + \langle \bar{g} \rangle_\theta \bar{q}_{in}$ | 16 (20) |
| **OTHER** | | |
| Linear filter (eg. integration of quanta in detector elements) | $A^2 \text{NPS}_{in}(u) \text{MTF}^2(u)$ | 25 |
| Sampling and noise aliasing | $\text{NPS}_{in}(u) + \sum_{n=1}^{\infty} \text{NPS}_{in}\left( u \pm \frac{n}{x_o} \right)$ | 15 (2.200) |
| Cross-covariance of two subsets of a quantum image | $\left[ \bar{\xi}\bar{\zeta} \text{NPS}_{in}(u) + K_{\xi\zeta} \bar{q}_{in} \right] \bar{g}^A \bar{g}^B T^A(u) T^{B*}(u)$ | 22 (94) |

$$\text{var}_\theta\{\bar{g}\} = \langle \bar{g}^2 \rangle - \langle \bar{g} \rangle^2$$
$W_g(u) = $ power spectrum of gain function $g(x)$ (FT of cross covariance of g(x))
$$S_I(u) = \int \int T_R(u,\theta) T_R^*(u,\theta') \left[ G(\theta,\theta',u) * \text{NPS}_{in}(u) \right] d\theta d\theta'$$
$$S_{II}(u) = \int \int T_R(u,\theta) T_R^*(u,\theta') G(\theta,\theta',u) d\theta d\theta'$$
$$\sigma_T^2(u) = \left\langle |T(u)|^2 \right\rangle_\theta - |\langle T(u) \rangle_\theta|^2$$

1  I.A.Cunningham and R.Shaw, "Signal-to-noise optimization of medical imaging systems," J Opt Soc Am A 16 621-32 (1999).

2  K.Rossmann, "Measurement of the modulation transfer function of radiographic systems containing fluoroscent screens," Phys Med Biol 9 551-7 (1964).

3  K.Rossmann, "The spatial frequency spectrum: A means for studying the quality of radiographic imaging systems," Radiology 90 1-13 (1968).

4  J.C.Dainty and R.Shaw, Image Science,(Academic Press, New York, 1974).

5  J.D.Gaskill, Linear Systems, Fourier Transforms, and Optics,(John Wiley & Sons, New York, 1978).

6  A.Papoulis, Systems and Transforms with Applications in Optics,(McGraw-Hill, New York, 1968).

7  K.Doi, K.Rossmann, and A.G.Haus, "Image quality and patient exposure in diagnostic radiology," Photographic Science and Engineering 21 269-77 (1977).

8  C.E.Metz and K.Doi, "Transfer function analysis of radiographic imaging systems," Phys Med Biol 24 1079-106 (1979).

9  H.H.Barrett and W.Swindell, Radiological Imaging - The Theory of Image Formation, Detection, and Processing,(Academic Press, New York, 1981).

10  D.L.Snyder and M.I.Miller, Random Point Processes in Time and Space,(Springer Verlag, New York, 1991).

11  A.Papoulis, Probability, random variables, and stochastic processes, 3 ed.(McGraw Hill, New York, 1991).

12  M.Rabbani, R.Shaw, and R.L.Van Metter, "Detective quantum efficiency of imaging systems with amplifying and scattering mechanisms," J Opt Soc Am A 4 895-901 (1987).

13  H.H.Barrett, R.F.Wagner, and K.J.Myers, "Correlated point processes in radiological imaging" Van Metter, R. L. and Beutel, J., Proc SPIE Vol. 3032 (1997).

14  W.Zhao and J.A.Rowlands, "Digital radiology using active matrix readout of amorphous selenium: theoretical analysis of detective quantum efficiency," Med Phys 24 1819-33 (1997).

15  I.A.Cunningham, "Applied linear-systems theory," Ch 2, in Handbook of Medical Imaging: Vol 1, physics and psychophysics J. Beutel, H. L. Kundel, and R. Van Metter (SPIE Press, Bellingham, 2000) pp.79-159.

16  M.Rabbani and R.L.Van Metter, "Analysis of signal and noise propagation for several imaging mechanisms," J Opt Soc Am A 6 1156-64 (1989).

17  R.Van Metter and M.Rabbani, "An application of multivariate moment-generating functions to the analysis of signal and noise propagation in radiographic screen-film systems," Med Phys 17 65-71 (1990).

18  R.K.Swank, "Absorption and noise in x-ray phosphors," J Appl Phys 44 4199-203 (1973).

19  J.A.Rowlands and K.W.Taylor, "Absorption and noise in cesium iodide x-ray image intensifiers," Med Phys 10 786-95 (1983).

20  W.Hillen, W.Eckenbach, P.Quadflieg, and T.Zaengel, "Signal-to-noise performance in cesium iodide x-ray fluorescent screens" in Medical Imaging V: Image Physics, Schneider, R. H., Proc SPIE Vol. 1443 (1991).

21  I.A.Cunningham, "Linear-systems modeling of parallel cascaded stochastic processes: The NPS of radiographic screens with reabsorption of characteristic radiation" in Medical Imaging 1998: Physics of Medical Imaging, Dobbins, J. T. and Boone, J. M., Proc SPIE Vol. 3336 (1998).

22  J.Yao and I.A.Cunningham, "Parallel cascades: new ways to describe noise transfer in medical imaging systems," Med Phys 28 2020-38 (2001).

23  H.Wieczorek, G.Frings, P.Quadflieg, and U.Schiebel, "CsI:Tl for solid state x-ray detectors" Proceedings of the International Conference on Inorganic Scintillators and their Applications, Delft, Netherlands (1995).

24  C.E.Metz and C.J.Vyborny, "Wiener spectral effects of spatial correlation between the sites of characteristic x-ray emission and reabsorption in radiographic screen-film systems," Phys Med Biol 28 547-64 (1983).

25  R.N.Bracewell, The Fourier Transform and its Applications, 2 ed.(McGraw-Hill Book Company, New York, 1978).

# A framework for noise-power spectrum analysis
# of multidimensional images

J. H. Siewerdsen[a]
*Department of Radiation Oncology, William Beaumont Hospital, Royal Oak, Michigan 48073*
*and Ontario Cancer Institute, Princess Margaret Hospital, University Health Network, Toronto,*
*ON M5G 2M9, Canada*

I. A. Cunningham
*Imaging Research Laboratories, Robarts Research Institute, London ON N6A 5K8, Canada*

D. A. Jaffray
*Department of Radiation Oncology, William Beaumont Hospital, Royal Oak, Michigan 48073*
*and Radiation Physics, Princess Margaret Hospital, University Health Network, Toronto,*
*ON M5G 2M9, Canada*

A methodological framework for experimental analysis of the noise-power spectrum (NPS) of multidimensional images is presented that employs well-known properties of the $n$-dimensional ($n$D) Fourier transform. The approach is generalized to $n$ dimensions, reducing to familiar cases for $n=1$ (e.g., time series) and $n=2$ (e.g., projection radiography) and demonstrated experimentally for two cases in which $n=3$ (viz., using an active matrix flat-panel imager for x-ray fluoroscopy and cone-beam CT to form three-dimensional (3D) images in spatiotemporal and volumetric domains, respectively). The relationship between fully $n$D NPS analysis and various techniques for analyzing a "central slice" of the NPS is formulated in a manner that is directly applicable to measured $n$D data, highlights the effects of correlation, and renders issues of NPS normalization transparent. The spatiotemporal NPS of fluoroscopic images is analyzed under varying conditions of temporal correlation (image lag) to investigate the degree to which the NPS is reduced by such correlation. For first-frame image lag of ~5–8 %, the NPS is reduced by ~20% compared to the lag-free case. A simple model is presented that results in an approximate rule of thumb for computing the effect of image lag on NPS under conditions of spatiotemporal separability. The volumetric NPS of cone-beam CT images is analyzed under varying conditions of spatial correlation, controlled by adjustment of the reconstruction filter. The volumetric NPS is found to be highly asymmetric, exhibiting a ramp characteristic in transverse planes (typical of filtered backprojection) and a band-limited characteristic in the longitudinal direction (resulting from low-pass characteristics of the imager). Such asymmetry could have implications regarding the detectability of structures visualized in transverse versus sagittal or coronal planes. In all cases, appreciation of the full dimensionality of the image data is essential to obtaining meaningful NPS results. The framework may be applied to NPS analysis of image data of arbitrary dimensionality provided the system satisfies conditions of NPS existence. © *2002 American Association of Physicists in Medicine.* [DOI: 10.1118/1.1513158]

## I. INTRODUCTION

The detectability of fine and low-contrast structures in medical images can be strongly affected by the magnitude and frequency content of stochastic variations in image signal. Therefore, quantitative measurement of imager noise characteristics is an important aspect of the development and assessment of imaging technologies. The image noise-power spectrum (NPS) quantifies the frequency characteristics of fluctuations in image signal and encapsulates many of the physical factors affecting image quality, such as gain, spatial resolution, additive noise, and aliasing. Furthermore, it is fundamental to analysis of figures of merit for imager per-formance, such as detective quantum efficiency (DQE) and noise-equivalent quanta (NEQ), which in turn are related to object and observer-dependent measures such as detectability index and receiver operating characteristic.[1] Since errors in NPS estimation translate directly to errors in such metrics of performance, the motivation for accurate NPS estimation is clear. The strong interest in establishing standard methods for NPS measurement is evidenced by the AAPM Task Group[2] concerning NPS analysis of two-dimensional (2D) x-ray projection images.

Analysis of image noise is especially important in the development, characterization, and optimization of novel im-

aging technologies.[3] Such is evident in the development of active matrix flat-panel imagers (FPIs) in the last decade[4–7] for 2D projection imaging. Currently, there is strong interest in application of FPIs to three-dimensional (3D) imaging, as in fluoroscopy[8,9] (i.e., acquisition of 2D projection images in temporal succession, constituting 3D data in the spatio-temporal domain) and cone-beam CT[10–12] (i.e., reconstruction of 3D volume images from 2D projection views). Similarly, technologies are being pursued for 4D imaging, as in volume fluoroscopy[13] (i.e., reconstruction of 3D volume images in temporal succession). The development of these technologies will also benefit from a quantitative understanding of imager noise characteristics. However, as the technologies advance and the dimensionality of image data grows, straightforward application of established NPS analysis techniques can be fraught with error, and accurate characterization of the noise properties of multidimensional imaging systems poses a challenge.

This paper presents a formal description of image NPS analysis in $n$ dimensions that uses well-known properties of the $n$D Fourier transform.[14–18] It reduces to familiar cases for $n=1$ (i.e., 1D data) and $n=2$ (i.e., 2D data such as a projection radiograph) and makes explicit the factors affecting the NPS for $n=3$ (i.e., 3D data) and beyond. While the measurements are based on an experimental system for 3D imaging using an FPI, the objective is not to report on the performance of a particular system (e.g., in comparison to image intensifiers or CT scanners), nor to present a theoretical method (e.g., using cascaded systems analysis[19–23]) for prediction of the NPS. Rather, the $n$D approach is intended as a framework for experimental analysis of multidimensional image noise (within the constraints of NPS existence), particularly concerning the effects of $n$D correlations and the requisite normalization factors associated with various NPS analysis techniques.

## II. MATHEMATICAL METHODS

This section outlines the general mathematical framework for analysis of the NPS of multidimensional image data. In Sec. II A, a compact multidimensional notation is introduced along with a generic Fourier description of image NPS in $n$ dimensions. In Sec. II B, the $n$D NPS is derived for the case of a linear, shift-invariant system with a Poisson-distributed input. In Sec. II C, the relationship of the full $n$D NPS to "central slice" analysis techniques is presented in a way that clarifies issues of normalization and quantifies the extent to which such techniques provide an accurate central slice of the $n$D NPS.

### A. Notation and definitions

The notation below follows that of Dainty and Shaw[18] and Cunningham,[24] with forms generalized to $n$ dimensions. (See Table I.) We consider a generalized $n$D image for which the mean and autocorrelation function are constant in all domains; therefore, the process forming the $n$D image is wide-sense[16,17] stationary. The image signal, $d$, is a function

of $n$ dimensions $(x_1, x_2, ..., x_n)$, denoted with the shorthand $d(x_{1:n})$, where the multidimensional domain of a function is written

$$(x_{1:n}) \equiv (x_1, x_2, ..., x_n). \tag{1a}$$

For example, the 3D spatial domain is denoted $(x_{1:3}) = (x_1, x_2, x_3) = (x, y, z)$. Similarly, the domains involving a parameter, e.g., $b_i$, in combination with a dimension, $x_i$, such as $(bx|_{1:n})$ and $(x/b|_{1:n})$ are denoted with the shorthand shown in Table I. A discretized $n$D domain is denoted with square brackets as $[x_{1:n}]$—equivalent to the continuous $(x_{1:n})$ except that locations in each domain are restricted to integer values. Analysis below primarily uses continuous notation, with results given for both the continuous and discrete cases.

The $n$D image has mean signal $\bar{d}$, with fluctuations about the mean denoted $\Delta d(x_{1:n}) \equiv d(x_{1:n}) - \bar{d}$. The image is formed by an $n$D array of rectangular apertures, where the extent in the $i^{th}$ domain is $a_i$, representing extent in spatial, temporal, or other domains and carrying units appropriate to the domain. A shorthand notation like that in Eq. (1a) represents a linear combination

$$a_{1:n} \equiv \prod_{i=1}^{n} a_i. \tag{1b}$$

Parentheses or brackets distinguish a functional domain [Eq. (1a)] from a linear combination [Eq. (1b)]. We write $b_i$ for the pixel size (sampling interval) in the $i^{th}$ domain, $N_i$ for the number of pixels in a realization along the $i^{th}$ domain, and $L_i$ for the extent of a realization in the $i^{th}$ domain. Hence, $L_i = b_i N_i$. Note that the sampling interval, $b_i$ is not necessarily equal to the extent of the integrating aperture, $a_i$, nor to the effective aperture size, $\alpha_i$, discussed below. Integrals are taken to be multiple integrals over the domains associated with the differentials, $df_i$:

$$\int df_{1:n} \equiv \int_{-\infty}^{\infty} df_1 \int_{-\infty}^{\infty} df_2 \cdots \int_{-\infty}^{\infty} df_n. \tag{1c}$$

The image $d(x_{1:n})$ represents the response of a system to a generalized $n$D input distribution, $q(x_{1:n})$, with mean value, $\bar{q}$, and fluctuations about the mean given by $\Delta q(x_{1:n}) \equiv q(x_{1:n}) - \bar{q}$. The input distribution results from a wide-sense stationary random process and can represent a quantum fluence, fluence rate, etc.[25] The mean output signal is related to the mean of the input distribution by a constant, $\gamma$ (referred to loosely as gain), and the $n$D impulse response function, $p(x_{1:n})$, is the output for the case in which the input is an $n$D delta function.

The Fourier conjugate to $(x_{1:n})$ or $[x_{1:n}]$ is the frequency domain $(f_{1:n})$ or $[f_{1:n}]$, respectively. The Fourier transform operator is denoted FT{ }, and the discrete Fourier transform operator is DFT{ }, with the relationship between the two described for digital imaging systems in Ref. 24. The Fourier representations of the zero-mean input and output distributions, respectively, are therefore

TABLE I. Glossary of terms and symbols.

**Generalized $n$D NPS analysis:**

| | |
|---|---|
| $(x_{1:n})$ | Continuous $n$-D domain $(x_1,x_2,...,x_n)$ |
| $[x_{1:n}]$ | Discrete $n$-D domain $[x_1,x_2,...,x_n]$ |
| $(f_{1:n})$ | Continuous $n$-D frequency domain $(f_1,f_2,...,f_n)$ |
| $[f_{1:n}]$ | Discrete $n$-D frequency domain $[f_1,f_2,...,f_n]$ |
| $(ax\|_{1:n})$ | Functional product $(a_1x_1,a_2x_2,...,a_nx_n)$ |
| $(x/a\|_{1:n})$ | Functional quotient $(x_1/a_1,x_2/a_2,...,x_n/a_n)$ |
| $a_i$ | Aperture size in domain $i$ |
| $b_i$ | Pixel size (sampling interval) in domain $i$ |
| $N_i$ | Number of pixels in realization along domain $i$ |
| $L_i$ | Length of realizations in domain $i$ |
| $BWI_i$ | Bandwidth integral over domain $i$ |
| $\alpha_i$ | Effective aperture size in domain $i$ |
| $\Lambda_i$ | Extent of synthesizing aperture in domain $i$ |
| $d(x_{1:n})$ | Image signal |
| $D(f_{1:n})$ | Fourier transform of image signal |
| $q(x_{1:n})$ | Input distribution (generalized function) |
| $Q(f_{1:n})$ | Fourier transform of input distribution (generalized function) |
| $\Pi(x/a\|_{1:n})$ | Rect function: apertures of width $a_i$ |
| $III(x/b\|_{1:n})$ | Comb function: delta functions at intervals of $b_i$ |
| $\gamma$ | Ratio of mean signal output and input (gain) |
| $p(x_{1:n})$ | Impulse response function |
| $T(f_i)$ | Transfer function for domain $i$ |
| $W_{norm}^{cont}$ | NPS normalization for continuous $n$D analysis |
| $W_{norm}^{discrete}$ | NPS normalization for discrete $n$D analysis |
| $W_{norm}^{extract}$ | NPS normalization for analysis by extraction |
| $W_{norm}^{synth}$ | NPS normalization for analysis by synthesis |
| $S(f_{1:n})$ | Noise-power spectrum |
| $\{A\}$ | Units of a quantity "$A$" |

**The spatiotemporal NPS:**

| | |
|---|---|
| $(x,y,t)$ | Spatiotemporal domain |
| $(f_x,f_y,f_t)$ | Spatiotemporal frequency domain |
| $a_x$, $a_y$, $a_t$ | Aperture extent in $x$, $y$, and $t$ domains |
| $Lag\|_k$ | $k^{th}$-frame image lag |
| $IRF(t)$ | Temporal impulse response function |
| $T_{lag}(f_t)$ | Temporal transfer function |
| $\alpha_t$ | Temporal bandwidth integral |

**The volumetric NPS:**

| | |
|---|---|
| $(x,y,z)$ | Volumetric spatial domain |
| $(f_x,f_y,f_z)$ | Volumetric frequency domain |
| $a_x$, $a_y$, $a_z$ | Aperture extent in $(x,y,z)$ domains |
| $H_{win}$ | Apodization window in 3D reconstruction |
| $h_{win}$ | Apodization parameter of reconstruction filter |

$$\Delta Q(f_{1:n}) \equiv FT\{\Delta q(x_{1:n})\}$$

and

$$\Delta D(f_{1:n}) \equiv FT\{\Delta d(x_{1:n})\} \qquad (2a)$$

and for the discrete signal

$$\Delta D[f_{1:n}] \equiv DFT\{\Delta d[x_{1:n}]\}. \qquad (2b)$$

While $Q(f_{1:n})$ tends to infinity for $q(x_{1:n})$ of infinite extent, in practice $q(x_{1:n})$ is bounded and terms involving $Q(f_{1:n})$ are defined such that the result is finite. Similarly, the $n$D transfer function for the system is given by the Fourier transform of the normalized impulse response function: $T(f_{1:n}) = |FT\{p(x_{1:n})\}|$.

We consider the "direct-digital" technique[18] of NPS analysis in which the NPS is determined from the ensemble average of the modulus-squared of the Fourier transform of the zero-mean image signal. A simple block diagram illustrating the technique is shown in Fig. 1. For the $n$D case, the NPS is denoted $S(f_{1:n})$,

$$S(f_{1:n}) \equiv W_{norm}^{cont} \langle |\Delta D(f_{1:n})|^2 \rangle, \qquad (3)$$

where the normalization factor, $W_{norm}^{cont}$, accounts for the finite extent of image realizations forming the ensemble as discussed below. For discrete data, $\Delta d[x_{1:n}]$, with discrete Fourier transform, $\Delta D[f_{1:n}]$, the NPS is

$$S[f_{1:n}] \equiv W_{norm}^{discrete} \langle |\Delta D[f_{1:n}]|^2 \rangle. \qquad (4)$$

The normalization factors associated with the continuous and discrete cases can be simply related by considering the transforms.[24] The NPS for the discrete case [Eq. (4)] is equivalent to that of Eq. (3) evaluated at discrete frequencies, where the frequency interval in the $i^{th}$ domain is $1/L_i$. Denoting the NPS evaluated at discrete frequencies as $S(f_{1:n})|_{eval}$, gives

$$S(f_{1:n})|_{eval} = S[f_{1:n}],$$

$$W_{norm}^{cont} \langle |\Delta D(f_{1:n})|^2 \rangle|_{eval} = W_{norm}^{discrete} \langle |\Delta D[f_{1:n}]|^2 \rangle, \qquad (5a)$$

$$\frac{W_{norm}^{cont}}{W_{norm}^{discrete}} = \frac{\langle |\Delta D[f_{1:n}]|^2 \rangle}{\langle |\Delta D(f_{1:n})|^2 \rangle|_{eval}}.$$

Evaluation at discrete frequencies corresponds to multiplication in the frequency domain with the comb function $L_{1:n}III(Lf|_{1:n}) = b_{1:n}N_{1:n}III(Lf|_{1:n})$. Writing the continuous and discrete Fourier transforms as in Sec. 2.4 of Ref. 24 and employing the sifting property gives

$$\frac{W_{norm}^{cont}}{W_{norm}^{discrete}} = \frac{|\Sigma_{k=1}^N \Delta d[x_{1:n}]e^{-i2\pi k_{1:n}m_{1:n}/N_{1:n}}|^2}{|\int \Delta d(x_{1:n})e^{-i2\pi f_{1:n}x_{1:n}}dx_{1:n}|^2|_{eval}}$$

$$= \frac{|\Sigma_{k=1}^N \Delta d[x_{1:n}]e^{-i2\pi k_{1:n}m_{1:n}/N_{1:n}}|^2}{|\Sigma_{k=1}^N \Delta d[x_{1:n}]e^{-i2\pi k_{1:n}m_{1:n}/N_{1:n}}b_{1:n}|^2}$$

$$= \frac{1}{b_{1:n}^2} = \frac{N_{1:n}^2}{L_{1:n}^2}. \qquad (5b)$$

The normalization factors associated with the discrete and continuous cases are therefore related by

$$W_{norm}^{discrete} = \frac{L_{1:n}^2}{N_{1:n}^2} W_{norm}^{cont}. \qquad (6)$$

Several special cases are considered below where $(x_{1:n})$ represents spatial and/or temporal domains. The case $n=2$ represents the familiar case of 2D imaging (e.g., projection radiography), where the domain is the 2D spatial domain denoted $(x,y)$. For $n=3$, two cases are considered. The first involves the spatiotemporal domain in which $(x_{1:3})$ is denoted $(x,y,t)$ and pertains to the 3D domain of projection data in the image plane acquired as a function of time, as in x-ray fluoroscopy. The second involves the volumetric domain in which $(x_{1:3})$ is denoted $(x,y,z)$ and pertains to the 3D spatial domain in volume reconstructions, as in cone-beam CT.
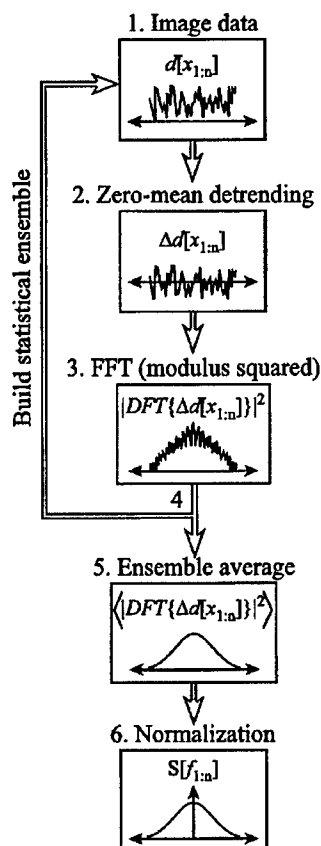
**1. Image data**

$d[x_{1:n}]$

**2. Zero-mean detrending**

$\Delta d[x_{1:n}]$

**3. FFT (modulus squared)**

$|DFT\{\Delta d[x_{1:n}]\}|^2$

4

**5. Ensemble average**

$\langle |DFT\{\Delta d[x_{1:n}]\}|^2 \rangle$

**6. Normalization**

$S[f_{1:n}]$

Build statistical ensemble

FIG. 1. Functional block diagram illustrating the essential steps of NPS analysis. (1) $n$-dimensional image data, $d[x_{1:n}] = d[x_1, x_2, ..., x_n]$ are considered. (2) The data are corrected for low-frequency trends (long-range image nonuniformity), and the mean image value is subtracted to form zero-mean realizations. (3) The modulus of the $n$D FFT is computed, and the result is squared. (4) The process is repeated for each realization in the data ensemble, and (5) the results are averaged. (6) The properly scaled NPS estimate is obtained upon application of a normalization factor that accounts for the finite length of the realizations and, depending on the analysis technique, tapering, extraction, and/or synthesis of the data. (See text for details.)

## B. Derivation of the $n$D NPS

The sections below convey the relationship between an $n$D image and the NPS in a manner that is directly applicable to measured $n$D data, highlights the effects of $n$D correlations, and makes the issues of normalization, units, and convergence among various NPS analysis techniques completely transparent. Derivations are cast in a form that reduces to familiar 1D and 2D cases. For a linear, shift-invariant system with deterministic response (i.e., one in which the processes of image formation introduce correlation, but not noise, to the input distribution[21]) it is straightforward to show[20,26] that the presampling signal is

$$\Delta d(x_{1:n}) = \gamma \Delta q(x_{1:n}) * p(x_{1:n})$$

$$= \gamma \Delta q(x_{1:n}) * \left[ p'(x_{1:n}) * \frac{1}{a_{1:n}} \Pi\left(\frac{x}{a}\right)\Big|_{1:n} \right], \quad (7)$$

where the second line separates components associated with

the integrating apertures ($n$D rect functions) from all other sources of image correlation [denoted $p'(x_{1:n})$]. While a deterministic model rarely gives a precise description of the signal and noise characteristics of real physical systems (due to complicating factors in the process of signal formation[27-29]), such is invoked simply to provide a relationship between the signal, input distribution, integrating apertures, etc. The general framework described below does not rely on the deterministic assumption and is applicable to measured data that satisfy the basic requirements of NPS existence.[18,24,30] The corresponding presampling NPS is simply

$$S(f_{1:n}) = \gamma^2 a_{1:n}^2 \bar{q} T^2(f_{1:n}). \quad (8a)$$

As discussed in detail elsewhere,[4,21,24,31,32] for a discretely sampled digital signal the NPS may be increased due to aliasing, as given by the presampling NPS convolved with the Fourier transform of the sampling function

$$\hat{S}(f_{1:n}) = \gamma^2 a_{1:n}^2 \bar{q} T^2(f_{1:n}) * b_{1:n} \text{III}(bf|_{1:n}), \quad (8b)$$

where $\text{III}(bf|_{1:n})$ represents an $n$D array of delta functions at multiples of the sampling frequency. Note that $\hat{S}(f_{1:n})$ is a measurable quantity evaluated at frequencies below the Nyquist frequency, $f_{i\text{Nyq}} = 1/2a_i$. In the context of projection radiography, the relationship between the presampling signal, the digital image, and the resulting NPS is well known.[21] Extension to $n$D is straightforward though notationally cumbersome, and offers the same essential result: $n$D sampling increases the NPS by $n$D convolution in the frequency domain.

To derive the $n$D NPS, the Fourier transform term in Eq. (3) for the system described above is

$$\langle |\Delta D(f_{1:n})|^2 \rangle = \gamma^2 a_{1:n}^2 \langle |\Delta Q(f_{1:n})|^2 \rangle T^2(f_{1:n}). \quad (9a)$$

The ensemble consists of finite-length realizations (a fact imposed by finite detector size, measurement time, etc.). These are equivalent to realizations of infinite extent truncated by a rect function, $(1/L_{1:n})\Pi(x/L|_{1:n})$. In the conjugate domain, this corresponds to convolution with a sinc function, $L_{1:n} \text{sinc}(Lf|_{1:n})$. Truncation in this manner corresponds to the crudest form of tapering window[14-17]—a boxcar function. Use of special tapering windows simply incurs a normalization factor associated with the window function, which can be computed in the same manner as described here. For finite-length realizations, the NPS becomes

$$S(f_{1:n}) = W_{\text{norm}}^{\text{cont}} \gamma^2 a_{1:n}^2 \langle |\Delta Q(f_{1:n})$$

$$\times T(f_{1:n}) * L_{1:n} \text{sinc}(Lf|_{1:n})|^2 \rangle. \quad (9b)$$

The length of the realizations is assumed much greater than the correlation lengths characteristic of $T(f_{1:n})$, giving

$$S(f_{1:n}) = W_{\text{norm}}^{\text{cont}} \gamma^2 a_{1:n}^2 T^2(f_{1:n})$$

$$\times \langle |\Delta Q(f_{1:n}) * L_{1:n} \operatorname{sinc}(Lf|_{1:n})|^2 \rangle$$

$$= W_{\text{norm}}^{\text{cont}} \gamma^2 a_{1:n}^2 T^2(f_{1:n}) L_{1:n}^2 \overline{\Delta Q^2(f_{1:n})}$$

$$\times \int \operatorname{sinc}^2(Lf|_{1:n}) df_{1:n}$$

$$= W_{\text{norm}}^{\text{cont}} \gamma^2 a_{1:n}^2 L_{1:n}^2 \frac{1}{L_{1:n}} \overline{q} T^2(f_{1:n})$$

$$= W_{\text{norm}}^{\text{cont}} \gamma^2 a_{1:n}^2 L_{1:n} \overline{q} T^2(f_{1:n}), \qquad (9\text{c})$$

where the assumption of a Poisson-distributed input distribution has been invoked (valid, e.g., when the input distribution consists of discrete quanta), and the $L_{1:n}$ results from truncation to finite-length realizations. Comparing to Eq. (8a), the normalization factor for truncation of the realizations is given by the reciprocal

$$W_{\text{norm}}^{\text{cont}} = \frac{1}{L_{1:n}} \qquad (10)$$

which is seen to be a straightforward $n$D extension of the normalization constant shown for 1D and 2D in Dainty and Shaw[18] and other texts. For discrete data, therefore, the normalization factor is

$$W_{\text{norm}}^{\text{discrete}} = \frac{L_{1:n}^2}{N_{1:n}^2} W_{\text{norm}}^{\text{cont}} = \frac{b_{1:n}}{N_{1:n}}. \qquad (11)$$

Therefore, the NPS evaluated by $n$D discrete Fourier transform of finite length realizations, written in a form directly applicable to the zero-mean measurements is

$$S[f_{1:n}] = \frac{b_{1:n}}{N_{1:n}} \langle |\text{DFT}\{\Delta d[x_{1:n}]\}|^2 \rangle. \qquad (12)$$

This straightforward derivation closely follows the familiar "direct-digital" method of NPS analysis[18] and provides a useful perspective on factors affecting measurement of the multidimensional NPS. First, it is generalized to n dimensions. So rather than "building up" inductively from lower dimensions to infer the $n$D NPS (e.g., applying one's knowledge of the 1D and 2D NPS to ascertain the 3D NPS), we have a simple "top-down" approach that describes the NPS for any dimensionality. Second, the form does not restrict the nature of the image domain. Thus the $n$ dimensions may represent any combination of domains of space, time, etc., provided the system satisfies the assumptions for NPS existence. Third, the approach emphasizes the role of correlations on the NPS—e.g., spatial correlation (1D, 2D, or 3D "blur"), temporal correlation ("image lag"), etc.—and provides a starting point from which such correlations can be accommodated in measurements of NPS. As shown below for two cases of 3D imaging, failure to appreciate such correlation can result in significant error. Finally, the approach provides a framework for understanding the relationship and continuity between the full $n$D NPS analyzed by $n$D Fourier transform and the "central slice" NPS analyzed by other

methods (e.g., "extraction" and "synthesis," described below).

A final note regarding the units of the NPS, which can be understood by a simple rule of thumb: for an image signal, $d(x_{1:n})$, with units denoted {signal}, the NPS has units given by the those of the signal squared times the linear combination of units for all domains. That is, the units of the NPS {NPS}, are related to the units of the signal {signal}, and the units of each domain {domain$_i$}, by the rule:

$$\{\text{NPS}\} = \{\text{signal}\}^2 \prod_{i=1}^{n} \{\text{domain}_i\}. \qquad (13)$$

In all cases below, we consider a dimensionless $n$D signal. Therefore: (i) for the 2D projection domain [$n=2$ and $(x_{1:2}) = (x,y)$], the NPS has units mm$^2$; (ii) for the 3D spatiotemporal domain [$n=3$ and $(x_{1:3}) = (x,y,t)$], the NPS has units mm$^2$ s; (iii) for the 3D volumetric domain [$n=3$ and $(x_{1:3}) = (x,y,z)$], the NPS has units mm$^3$; (iv) for the 4D fully spatiotemporal domain, {NPS} = mm$^3$ s. Furthermore, the $n$D integral of the NPS equals the variance in image pixel values.[18]

## C. Central slice NPS analysis: extraction and synthesis

Historically, full $n$D spectral analysis as in Eq. (11) was uncommon for $n>1$ due to practical limitations in computing speed and multidimensional fast Fourier transform (FFT) algorithms. Techniques in which portions of the NPS (e.g., slices along major axes) are analyzed have become common—e.g., by (1) "extracting" realizations from the $n$D image; or (2) "synthesizing" realizations along one or more domains. The former technique is subject to significant error unless attention is paid to correlations orthogonal to the domain of the extracted data. The latter technique requires that the extent over which data are synthesized (i.e., summed or averaged) be sufficient that the resulting NPS converge upon a central slice of the $n$D NPS (e.g., in the "synthesized slit" technique for 2D images). As noted by Dobbins et al.,[33] analysis of the full $n$D NPS can reveal off-axis noise characteristics that would otherwise be missed. Still, there are several reasons that a reduced-dimensionality approach may be desirable or necessary: for a given body of data, such an approach can yield a larger number of realizations and reduced standard error; constraints of display media make representation of the $n$D NPS awkward for $n>2$; computer memory requirements can be strained for large realizations in which $n \geq 3$; finally, the amount of useful data may be limited (e.g., by experimental technique or by wide-sense stationarity) to "extractions" from the full $n$D data—e.g., a single fluoroscopy frame, a single volumetric slice, etc. As shown below, the general framework for $n$D NPS analysis removes the distinction between such techniques and describes a methodology for analysis of the full $n$D NPS or central slices therein.

### 1. Central slice NPS analysis by extraction

Extraction of realizations directly from $n$D data (see Fig. 2) is usually recognized as a problematic starting point for NPS analysis, since it requires account of correlation orthogonal to the direction of extraction. If realizations are extracted unwittingly, the resulting NPS will underestimate the true NPS in a manner related to the ignored correlations. We consider an $n$D image from which realizations of dimensions $(n-m)$ are extracted to analyze the NPS, $S(f_{1:n-m})$. We dignify the process with the term "$m^{th}$-order extraction." The dimensions can be arbitrarily reordered such that the lower domains $1:(n-m)$ are extracted, while the higher domains $(n-m+1):n$ are excluded. Furthermore, data are extracted along the entire extent of the data—i.e., data are not "cropped" from within $d(x_{1:n})$ (which would simply introduce truncation terms) but are extracted in entirety along domains $(x_{1:n-m})$. The extracted data, $d(x_{1:n-m})$, are therefore equal to $d(x_{1:n})$ multiplied by a set of $n$D delta functions in domains $(x_{(n-m+1):n})$. Without loss of generality, the origin is chosen such that data are extracted at $(x_{(n-m+1):n}) = 0$:

$$d(x_{1:n-m}) = d(x_{1:n}) \, \delta(x_{(n-m+1):n} - 0) \qquad (14a)$$

which in the Fourier domain corresponds to convolution with a constant. The term of interest in the NPS is

$$\Delta D(f_{1:n-m}) = \int \Delta D(f_{1:n}) df_{(n-m+1):n}$$

$$= \gamma a_{1:n} \int \Delta Q(f_{1:n}) T(f_{1:n}) df_{(n-m+1):n} \qquad (14b)$$

and the NPS in the reduced $(f_{1:n-m})$ domain is

$$S(f_{1:n-m}) = W_{norm}^{cont} W_{norm}^{extract} \gamma^2 a_{1:n}^2 \left\langle \left| \int \Delta Q(f_{1:n}) \right. \right.$$

$$\left. \left. \times T(f_{1:n}) df_{(n-m+1):n} \right|^2 \right\rangle, \qquad (14c)$$

where $W_{norm}^{cont}$ accounts for truncation to finite length, and $W_{norm}^{extract}$ accounts for extraction. To put the equation in a simple, intuitive form, the system transfer function is assumed to be separable

$$T(f_{1:n}) = \prod_{i=1}^{n} T(f_i). \qquad (15)$$

While this is not a necessary assumption, it renders the effect of extraction on the NPS transparent. The assumption is reasonable to varying degrees among different technologies and image domains. Separability of spatial and temporal components is often valid. For FPIs, the imaging array may have a separable MTF of the form $|\text{sinc}(a_x x)\text{sinc}(a_y y)|$; however, the detector system MTF may involve effects that are radially symmetric, such as $K$-fluorescence and choice of x-ray converter. In volume CT, separability between transverse and axial domains is reasonable to the extent that ramp and

**(a)** $n=2$: (e.g., Projection Radiography):

$m=1$: $1^{st}$-order extraction
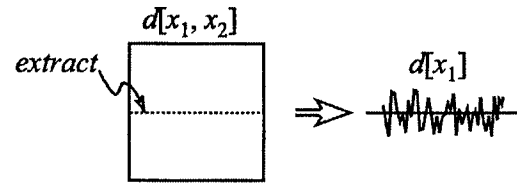


**(b)** $n=3$: (e.g., Fluoro, CT Fluoro, or Volume CT):

$m=1$: $1^{st}$-order extraction
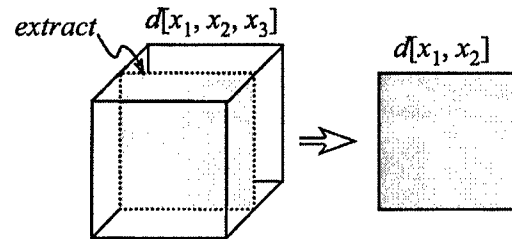


$m=2$: $2^{nd}$-order extraction
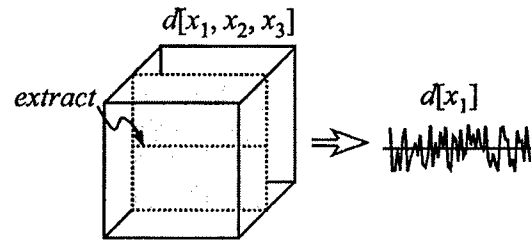


FIG. 2. Extraction of realizations from $n$D data. Extraction is the simpler of the two dimension–reduction techniques discussed in the text for analysis of the central slice NPS. It is also the more prone to error, since it requires full account of correlations orthogonal to the extracted data. (a) Illustration of extraction from 2D data, such as extraction of individual "rows" from a 2D digital radiograph. (b) Illustration of extraction from 3D data, such as extraction of individual "frames" from a fluoroscopic sequence or individual "slices" from a volume CT image. Higher order extraction is also illustrated, such as extraction of individual 1D "rows" from 3D data.

apodization filters are applied only in the transverse direction, but attention must be paid to the degree to which the detector MTF is separable.

Taking the ensemble average of the modulus squared as in Eqs. (9) yields the same $L_{1:n}$ term for the length of the realizations, with the transfer function now distinct between the extracted domains $(f_{1:n-m})$ and orthogonal domains $(f_{(n-m+1):n})$:

$$S(f_{1:n-m}) = W_{norm}^{cont} W_{norm}^{extract} \gamma^2 a_{1:n}^2 L_{1:n-m} \overline{q} T^2(f_{1:n-m})$$

$$\times \int T^2(f_{(n-m+1):n}) df_{(n-m+1):n}. \qquad (16)$$

Therefore, the NPS is reduced by a factor given by the integral over the transfer functions in all domains orthogonal to

the extracted signal. This factor represents a bandwidth integral over the orthogonal domains, similar to that in Wagner et al.,[34] where the bandwidth integral for the domain $f_i$ is

$$BWI_i \equiv \int T^2(f_i) df_i \tag{17a}$$

the reciprocal of which is an effective aperture for the $i^{th}$ domain

$$\alpha_i \equiv \frac{1}{BWI_i} \tag{17b}$$

The effective aperture has units corresponding to that of the domain (e.g., length or time for the spatial or temporal domains). Furthermore, for the special case in which the transfer function in the $i^{th}$ domain is a sinc function for which the first zero exactly equals the sampling frequency (i.e., system response is uniform throughout each sampling interval), the effective aperture equals the aperture: $\alpha_i = a_i$.

The normalization factor such that the resulting NPS analyzed by extraction is a central slice of the full $n$D NPS is therefore the reciprocal of the bandwidth integral

$$W_{norm}^{extract} = \left[ \int T^2(f_{(n-m+1):n}) df_{(n-m+1):n} \right]^{-1}$$

$$= \alpha_{(n-m+1):n} \tag{18}$$

and the NPS evaluated by extraction can be written in a form directly applicable to the extracted data

$$S[f_{1:n-m}] = W_{norm}^{discrete} W_{norm}^{extract} \langle |DFT\{\Delta d[x_{1:n-m}]\}|^2 \rangle$$

$$= \frac{b_{1:n-m}}{N_{1:n-m}} \alpha_{(n-m+1):n} \langle |DFT\{\Delta d[x_{1:n-m}]\}|^2 \rangle, \tag{19}$$

where the $\alpha$ term represents the linear combination of effective apertures for the excluded domains $(n-m+1)$ to $n$.

## 2. Central slice NPS analysis by synthesis

The process of synthesis is illustrated in Fig. 3. We consider $n$D image data from which realizations of dimensions $(n-m)$ are synthesized by integrating the data along domains $(x_{(n-m+1):n})$. We dignify the process with the term "$m^{th}$-order synthesis." The methodology for the case $n=2$ and $m=1$ (i.e., the synthesized slit technique) is described in numerous sources,[3,4,27] with the goal being estimation of the NPS along a subset of the major axes [i.e., a "central slice" of the NPS, where the slice has dimensionality $(n-m)$]. Following Dainty and Shaw,[18] the central slice of the NPS is

$$S(f_{1:n-m}) = S(f_{1:n})|_{f_{(n-m+1):n}=0}$$

$$= \int S(f_{1:n}) T_{synth}^2(f_{1:n}) df_{(n-m+1):n}, \tag{20a}$$

where $T_{synth}(f_{1:n})$ is the transfer function associated with synthesis (i.e., integration over an $n$D synthesizing aperture). As in Eq. (16), therefore

**(a)** $n=2$: (e.g., Projection Radiography):

$m=1$: $1^{st}$-order synthesis
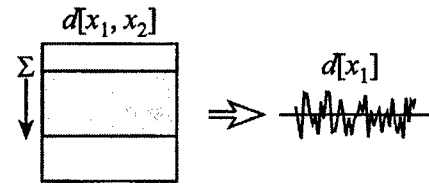


**(b)** $n=3$: (e.g., Fluoro, CT Fluoro, or Volume CT):

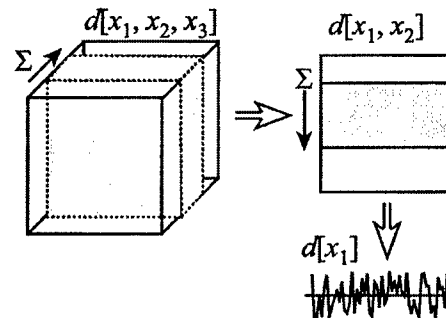$m=1$: $1^{st}$-order synthesis
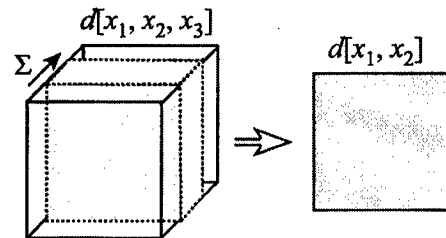


$m=2$: $2^{nd}$-order synthesis



FIG. 3. Synthesis of realizations from $n$D data, in which realizations of reduced dimensionality are obtained by integrating across a synthetic aperture (illustrated by the shaded regions and the summation symbol). (a) Illustration of synthesis from 2D data, equivalent to the well-known synthesized slit technique of NPS analysis of 2D radiographs. (b) Illustration of synthesis from 3D data, such as integration over multiple "frames" of a fluoroscopic sequence or multiple "slices" of a volume CT image. Higher order synthesis is illustrated in which 3D data is integrated along a given domain to yield a 2D "synthesized slice," which in turn is integrated to yield a 1D synthesized realization.

$$S(f_{1:n-m}) = W_{norm}^{cont} W_{norm}^{synth} \gamma^2 a_{1:n}^2 L_{1:n-m} \bar{q} \int T^2(f_{1:n})$$

$$\times T_{synth}^2(f_{1:n}) df_{(n-m+1):n}, \tag{20b}$$

where the normalization factor $W_{norm}^{synth}$ accounts for synthesis. Assuming separability as in Eq. (15) gives

$$S(f_{1:n-m}) = W_{norm}^{cont} W_{norm}^{synth} \gamma^2 a_{1:n}^2 L_{1:n-m} \bar{q} T^2(f_{1:n-m})$$

$$\times T_{synth}^2(f_{1:n-m}) \int T^2(f_{(n-m+1):n})$$

$$\times T_{synth}^2(f_{(n-m+1)}) df_{(n-m+1):n}. \tag{20c}$$

The synthesizing aperture is chosen such that $T_{\text{synth}}(f_{1:n})$ satisfies two assumptions related to "convergence" of the resulting NPS upon a central slice. First, for the domains $(f_{1:n-m})$ correlations associated with $T_{\text{synth}}(f_{1:n-m})$ are negligible compared to those associated with the system transfer function, $T(f_{1:n-m})$. Therefore, the product $T^2(f_{1:n-m})T_{\text{synth}}^2(f_{1:n-m})$ is approximately $T^2(f_{1:n-m})$, and Eq. (20c) becomes

$$S(f_{1:n-m}) = W_{\text{norm}}^{\text{cont}} W_{\text{norm}}^{\text{synth}} \gamma^2 a_{1:n}^2 L_{1:n-m} \overline{q} T^2(f_{1:n-m})$$

$$\times \int T^2(f_{(n-m+1):n})$$

$$\times T_{\text{synth}}^2(f_{(n-m+1):n}) df_{(n-m+1):n} . \tag{20d}$$

Second, for the domains $(f_{(n-m+1):n})$ correlations associated with the synthesizing aperture are much greater than those associated with the system transfer function. Therefore, the product $T^2(f_{(n-m+1):n})T_{\text{synth}}^2(f_{(n-m+1):n})$ is approximately $T_{\text{synth}}^2(f_{(n-m+1):n})$, and Eq. (20d) becomes

$$S(f_{1:n-m}) = W_{\text{norm}}^{\text{cont}} W_{\text{norm}}^{\text{synth}} \gamma^2 a_{1:n}^2 L_{1:n-m} \overline{q} T^2(f_{1:n-m})$$

$$\times \int T_{\text{synth}}^2(f_{(n-m+1):n}) df_{(n-m+1):n} . \tag{21}$$

This is the general form for the "central slice" of the full $n$D NPS evaluated by synthesis. A common case is where the synthesizing aperture is an $n$D rect function, chosen "narrow" in $(x_{1:n-m})$ and "long" in $(x_{(n-m+1):n})$. Then $T_{\text{synth}}(f_{1:n})$ is a sinc determined by sidelengths, $\Lambda_i$, of the synthesizing aperture, and Eq. (21) becomes

$$S(f_{1:n-m}) = W_{\text{norm}}^{\text{cont}} W_{\text{norm}}^{\text{synth}} \gamma^2 a_{1:n}^2 L_{1:n-m} \overline{q} T^2(f_{1:n-m})$$

$$\times \int \left( \prod_{i=n-m+1}^{n} \text{sinc}^2(\Lambda_i f_i) \right) df_{(n-m+1):n}$$

$$= W_{\text{norm}}^{\text{cont}} W_{\text{norm}}^{\text{synth}} \gamma^2 a_{1:n}^2 L_{1:n-m} \overline{q} T^2(f_{1:n-m})$$

$$\times \frac{1}{\Lambda_{(n-m+1):n}} . \tag{22}$$

The normalization factor is therefore the reciprocal of the term associated with synthesis, $\Lambda_{(n-m+1):n}$,

$$W_{\text{norm}}^{\text{synth}} = \left[ \int_{(n-m+1)} \left( \prod_{i=n-m+1}^{n} \text{sinc}^2(\Lambda_i f_i) \right) df_{(n-m+1):n} \right]^{-1}$$

$$= \Lambda_{(n-m+1):n} \tag{23}$$

and the NPS evaluated by synthesis can be written in a form directly applicable to the synthesized data:

$$S[f_{1:n-m}] = W_{\text{norm}}^{\text{discrete}} W_{\text{norm}}^{\text{synth}} \langle |\text{DFT}\{\Delta d[x_{1:n-m}]\}|^2 \rangle$$

$$= \frac{b_{1:n-m}}{N_{1:n-m}} \Lambda_{(n-m+1):n} \langle |\text{DFT}\{\Delta d[x_{1:n-m}]\}|^2 \rangle . \tag{24}$$

A requirement for convergence is that the synthesizing aperture be of much greater extent than the corresponding effective apertures of the system. Choosing a synthesizing

aperture that is too short results in underestimation of the central slice. In practice, progressively "longer" synthesizing apertures may be chosen until the resulting NPS converges upon the central slice. A method for quantifying the degree of NPS convergence is demonstrated below. Note, however, that even when this requirement is not satisfied, the underestimation can be corrected by dividing out the integral of Eq. (21)—similar to the bandwidth integral for the extraction case. In fact, extraction and synthesis are seen to be endpoints on a continuum of techniques. That is, "extraction" can be viewed as a case where the "synthesizing" aperture has extent equal to the apertures. In each case, the bandwidth integral provides appropriate normalization and units for the NPS.

## III. NOISE-POWER SPECTRUM MEASUREMENTS

The NPS was measured for two cases in which $n=3$ using a single experimental platform. In the first case, $(x_{1:3}) = (x,y,t)$, corresponding to acquisition of projection images in temporal succession (as in x-ray fluoroscopy), and the spatiotemporal NPS was analyzed. In the second case, $(x_{1:3}) = (x,y,z)$, corresponding to cone-beam CT, and the volumetric NPS was analyzed. In each case, the NPS was investigated under conditions of varying correlation: for the spatiotemporal case, temporal correlation was examined by varying the image lag; for the volumetric case, correlation in the transverse plane was varied through adjustment of the reconstruction filter.

### A. Experimental platform

The experimental 3D imaging bench has been described in detail elsewhere.[10] The primary components of the bench are an x-ray tube [Dunlee PX1415 tube with Picker MTX 360 generator] and a flat-panel imager, FPI [PerkinElmer RID-1640]. The FPI incorporates a $41 \times 41$ cm$^2$ array of $a$-Si:H photodiodes and TFTs at 400 $\mu$m pixel pitch ($\sim$80% fill factor) in combination with a 250 mg/cm$^2$ CsI:Tl x-ray converter. Pixel values were digitized to 16 bits, and the detector could be read at frame rates up to 3.5 frames per second (fps). The imaging geometry corresponds to a system under development for image-guided radiation therapy,[35] with a source-to-isocenter distance of 100 cm and a source-to-detector distance of 160 cm.

### B. Case $n=3$: The spatiotemporal NPS

For measurement of spatiotemporal noise characteristics, the 3D image domain is $(x,y,t)$, with $x$ and $y$ along detector rows and columns, respectively, and $t$ the temporal domain. The x-ray tube was operated at 120 kVp, with 2.5 mm Al + 0.625 mm Cu of added filtration, and the exposure per frame at the detector was varied from 340 $\mu$R ($\sim$20% of sensor saturation) to 1630 mR ($\sim$100% saturation). The FPI was operated at 1.1 fps, synchronized with the x-ray generator such that x-ray pulses were delivered between frames (i.e., radiation was not incident during detector read). Although the frame rate was significantly less than that common to clinical fluoroscopy, the purpose of this study re-

quired only that projections were acquired in temporal succession [giving 3D image data in $(x,y,t)$] with a given level of spatiotemporal correlation (blur and image lag).

The magnitude of temporal correlation (image lag) was investigated by measurement of the impulse response function (IRF) and temporal transfer function ($T_{lag}$) as described previously[36] at 11 exposure levels ranging from ~20% to ~100% of sensor saturation. The response from an ensemble of 100 pixels distributed across the FPI was measured. For each IRF, 50 frames were read in the dark (giving the average dark pixel values), a single x-ray pulse was delivered prior to the 51st frame, and the signal decay was measured for an additional 50 frames. The procedure was repeated 5 times, giving 500 IRFs for each exposure level. The $k^{th}$-frame lag was analyzed from the relative residual signal in the $k^{th}$ frame following the radiation impulse:

$$\text{Lag}|_k = \frac{\text{Sig}|_k}{\text{Sig}|_{k=0}}, \tag{25a}$$

where $\text{Sig}|_k$ is the dark-subtracted pixel signal in the $k^{th}$ frame following the radiation impulse. $\text{Lag}|_{k=1}$ is the commonly reported first-frame lag. The transfer function associated with temporal correlation was computed from the Fourier transform of the area-normalized IRF:[36]

$$T_{lag}[f_t] = |\text{DFT}\{\text{IRF}[t]\}| \tag{25b}$$

The spatiotemporal NPS was analyzed from three-dimensional image data $d[x,y,t]$ consisting of flood-field projections acquired in temporal succession. Projections were gain-offset corrected using 20 dark fields and 20 flood fields acquired immediately prior. A 512×1024 region of the FPI containing few pixel defects was selected, and the remaining defects (~2000 pixels in total) were masked by 3 ×3 median filter. Pixel values were scaled to units of charge (electrons) according to the manufacturer-specified calibration. The magnitude of temporal correlation was varied by two means: (1) variation of the exposure; and (2) variation of the number of "dark" frames read between each exposure. The second method corresponds to frame "flushing" or "scrubbing" [37,38] as a means of reducing correlation between frames. The number of frames flushed between exposures, $N_{flush}$, varied from $N_{flush}=0$ (projections read in succession, with radiation incident for each frame) to $N_{flush}=30$ (radiation delivered prior to every 30th frame, for which the degree of correlation between projections was negligible).

The NPS was analyzed from the fluoroscopic data via the "extraction" method described above, where 2D projections $d[x,y]$ were extracted from the 3D data set [as in Fig. 2(b)]. This quantifies the effect of temporal correlation on the spatiotemporal NPS and shows the error (underestimation) incurred if such correlation is ignored. The method for NPS analysis was similar to that reported elsewhere,[4,6,33] with realizations of 100×100 pixels taken from each projection, giving an ensemble of 2500 nonoverlapping realizations, zero-mean detrended by subtraction of a planar fit. No tapering window[16] was applied. The NPS, $S[f_x, f_y]$, was computed from the ensemble average of 2D FFTs as described

above. As a check on normalization, the volume under the resulting NPS was compared to the mean pixel variance and in all cases agreed to better than 1%. Central slice "strips" $S[f_x]$ and $S[f_y]$ were taken from the average of the two central rows (columns) from the resulting NPS matrix.[33] The effect of temporal correlation on the NPS was investigated as a function of exposure level and number of frames flushed between projections. The bandwidth integral associated with temporal correlation was computed from the temporal transfer function and compared to the observed differences in $S[f_x, f_y]$ at various levels of image lag.

Finally, an idealized model was constructed to convey a simple rule of thumb regarding the effect of image lag on the NPS. The model considers a discrete time-sampled system for which the detector response follows a simple exponential decay. While such a model describes typical FPI response only in rough approximation, it gives a convenient, transportable result for understanding the effect of temporal correlation on noise.

## C. Case $n=3$: The volumetric NPS

For volume images, the image domain is $(x,y,z)$, with the origin at the center of reconstruction (i.e., at the intersection of the central ray of the beam and the axis of rotation), $x$ along detector rows, $y$ along the direction joining the source and detector, and $z$ along detector columns. An additional 2 mm Cu filter was used, and the exposure per projection at the detector was varied from 100 $\mu$R (~5% saturation) to 860 $\mu$R (~45% saturation). A rotation stage supporting the object was positioned at a source-to-axis distance of 100 cm. As described previously,[10] projection images were acquired at 1.2° angular increments through 360°, and volume images were reconstructed using the FDK algorithm for cone-beam filtered back-projection.[39] Volume images were reconstructed from projections of a 20 cm diameter water cylinder and of air. Spatial correlation was varied through adjustment of the apodization window, $H_{win}(f)$, applied in the transverse direction:

$$H_{win}(f) = [h_{win} + (1 - h_{win})\cos(2\pi f x_{inc})], \tag{26}$$

where $f$ is the frequency domain associated with the $x$-direction in the detector plane (rows), and $x_{inc}$ is the sampling step size of the detector elements. The apodization window was adjusted through variation of $h_{win}$, ranging from 0.5 to 1. Special cases include $h_{win}=0.5$ (Hanning filter), $h_{win}=0.54$ (Hamming filter), and $h_{win}=1$ (Ram-Lak filter). The reconstruction filter, $H_{recon}(f)$, is the apodization window times the ramp function.

The effect of the apodization window on volumetric spatial resolution and noise was examined in volume reconstructions of a wire phantom, a water cylinder, and air. The wire phantom consisted of a 0.127 mm diameter stainless steel wire suspended longitudinally (along $z$) in the water cylinder. Volume images of the wire phantom were reconstructed at various settings of $h_{win}$, and the full-width-at-half-maximum (fwhm) of the wire in transverse slices was computed. Similarly, the image noise (i.e., standard deviation in voxel val-

ues) was measured from volume images of the water cylinder and air as a function of the apodization parameter, $h_{win}$.

Volumetric NPS were first analyzed by the (first order) "synthesis" method illustrated in Fig. 3(b). First, volume images with $600 \times 600 \times 400$ voxels (0.25 mm voxel size) were reconstructed at various apodization, $h_{win}$. Examination of the mean and variance throughout the reconstructions showed that wide-sense stationarity was satisfied to a far greater extent for images of air compared to images of the water cylinder. For the air volumes, the mean voxel value was constant throughout the reconstruction, and the standard deviation in voxel values was constant within 5%. For the water volume, the mean varied radially by up to ~30% (due to x-ray scatter[12]) and the standard deviation varied by ~10% between the center of reconstruction and 10 cm off-axis (due to the lack of a bow-tie filter). Therefore, air volume reconstructions were used in the NPS analysis. Implementation of scatter correction and incorporation of a bow-tie filter should improve stationarity and are subjects of ongoing work.

Second, the extent of the synthesizing aperture (i.e., the length of integration along $x$, $y$, or $z$) required such that the resulting NPS was convergent upon a central slice of the 3D NPS was examined. The volume under the NPS analyzed for various integration lengths was compared to the voxel variance. An asymptotic behavior was observed in which NPS volume increased with integration length, depending on the degree of correlation, and converged upon a value consistent with the voxel variance. An integration length (viz., 10 mm, as shown in Sec. IV C) was selected such that the NPS volume was convergent within 1% of the asymptotic limit for all cases. This technique helps remove the subjectivity noted by Dobbins et al.[33] regarding the synthesis technique and allows one to quantify the degree to which the result is a convergent central slice of the NPS. For transverse realizations of 100 $\times 100$ voxels, this choice of synthesizing aperture gave a total of $6 \times 6 \times 10 = 360$ realizations for each volume reconstruction. As described above, each realization was zero-mean detrended by subtraction of a planar fit. The 2D central slices of the NPS—$S[f_x, f_y]$, $S[f_x, f_z]$, and $S[f_y, f_z]$, referred to as transverse, coronal, and sagittal NPS, respectively—were computed by 2D FFT of realizations synthesized along the $z$, $y$, and $x$ directions, respectively. Transverse, coronal, and sagittal central slice NPS are displayed as grayscale images, and 1D curves at various settings of $h_{win}$ were obtained by averaging the two central rows or columns within a central slice.

Finally, the full 3D volumetric NPS, $S[f_x, f_y, f_z]$, was analyzed by 3D Fourier transform. A total of ($6 \times 6 \times 4$ $= 144$) nonoverlapping 3D realizations of size $100 \times 100$ $\times 100$ voxels were taken from each reconstruction. Each was zero-mean detrended by a 3D polynomial fit, and the 3D FFT was computed (using the fftn function in Matlab, The MathWorks, Natick MA). Central slices of the 3D NPS were compared to the 2D transverse, coronal, and sagittal NPS analyzed by the synthesis method (above) and found to agree within experimental error. The 3D NPS was viewed as a

series of 2D grayscale images and as shaded-surface renderings.

It is worth noting that acquisition and reconstruction of volume images is in fact, a 4D process involving $x$, $y$, $z$, and $t$, since 2D projection views are acquired in temporal succession and then reconstructed in the volume domain; therefore, the process involves the projection space domain $(x,z)$, the temporal domain $(t)$ in which views are acquired at various angles, and the volume domain $(x,y,z)$ of image reconstructions. However, the result (i.e., the volume image) is strictly a 3D (and not a 4D) signal distribution. Volume reconstruction acts upon the projections in $(x,z)$ and exploits the angular (temporal) domain to produce a third spatial domain for images in $(x,y,z)$. Therefore, there is no temporal dimension to the volume reconstruction. However, correlation in the temporal domain during acquisition (e.g., due to image lag) reduces the projection space NPS, and therefore the volumetric NPS as well. Reconstruction artifacts associated with image lag are discussed elsewhere.[38]

## IV. RESULTS

The methodological framework for NPS analysis is illustrated below for a variety of cases. In Sec. IV A, specific cases are examined that make explicit the NPS normalization for 2D and 3D imaging, illustrate the continuum nature of the factors associated with extraction and synthesis, and demonstrate the analogy between multidimensional imaging modalities (e.g., fluoroscopy and volume CT). In Secs. IV B and IV C, the measured NPS is reported for two cases of 3D imaging—fluoroscopy and cone-beam CT—using methods of extraction, synthesis, and full $n$D analysis and examining the effects of correlation on the NPS.

### A. Framework for multidimensional NPS analysis

Table II illustrates the NPS framework for various modalities. For radiography [$(x_{1:2}) = (x,y)$], the input is a fluence (mm$^{-2}$), and the NPS has units mm$^2$. The $(b_x / N_x)$ term accounts for the finite-length realizations, and for analysis by extraction $\alpha_y$ accounts for correlation orthogonal to the extracted data. The term $\alpha_y$ is critical to ensure the result is a meaningful central slice of the NPS. If there is no spatial correlation beyond that of the apertures in $y$, $T(f_y)$ is a sinc function, and $\alpha_y = a_y$. If correlation exists beyond the extent of the apertures, however, the bandwidth integral is the factor by which the result is reduced compared to the full 2D NPS, and failure to account for the orthogonal correlation guarantees an inaccurate NPS estimate. Similarly for analysis by synthesis (viz., the synthesized slit technique), the term $\Lambda_y$ accounts for integration along the synthesizing aperture.

For fluoroscopy, the input distribution is a fluence rate (mm$^{-2}$ s$^{-1}$), and the spatiotemporal[40] NPS has units mm$^2$ s. As shown in Table II, extraction yields the term $\alpha_t$, which accounts for correlation in the time domain as given by the temporal bandwidth integral. If there is no temporal correlation other than the sampling interval, $a_t$, the effective temporal aperture equals the sampling interval. If temporal correlation exceeds the sampling interval (e.g., due to image

TABLE II. Illustration of the framework for multidimensional image NPS analysis for various modalities, including radiography ($n=2$), fluoroscopy ($n=3$), and volume CT ($n=3$). In each case, forms for the NPS analyzed by full $n$D DFT, extraction, and synthesis are shown. The bottom two rows illustrate cases of higher-order extraction and synthesis, respectively, for generalized 3D image data.

| Modality/ dimensionality | Image domain | NPS units | Analysis | Noise-power spectrum |
|---|---|---|---|---|
| Radiography ($n=2$) | $[x,y]$ | $mm^2$ | Full $n$D | $S[f_x,f_y] = \dfrac{b_x b_y}{N_x N_y} \langle |DFT\{\Delta d[x,y]\}|^2 \rangle$ |
| | | | Extraction | $S[f_x] = \dfrac{b_x}{N_x} \alpha_y \langle |DFT\{\Delta d[x,y]\}|^2 \rangle$ |
| | | | Synthesis | $S[f_x] = \dfrac{b_x}{N_x} \Lambda_y \langle |DFT\{\Delta d[x,y]\}|^2 \rangle$ |
| Fluoroscopy ($n=3$) | $[x,y,t]$ | $mm^2 s$ | Full $n$D | $S[f_x,f_y,f_t] = \dfrac{b_x b_y b_t}{N_x N_y N_t} \langle |DFT\{\Delta d[x,y,t]\}|^2 \rangle$ |
| | | | Extraction | $S[f_x,f_y] = \dfrac{b_x b_y}{N_x N_y} \alpha_t \langle |DFT\{\Delta d[x,y,t]\}|^2 \rangle$ |
| | | | Synthesis | $S[f_x,f_y] = \dfrac{b_x b_y}{N_x N_y} \Lambda_t \langle |DFT\{\Delta d[x,y,t]\}|^2 \rangle$ |
| Volume CT ($n=3$) | $[x,y,z]$ | $mm^3$ | Full $n$D | $S[f_x,f_y,f_z] = \dfrac{b_x b_y b_z}{N_x N_y N_z} \langle |DFT\{\Delta d[x,y,z]\}|^2 \rangle$ |
| | | | Extraction | $S[f_x,f_y] = \dfrac{b_x b_y}{N_x N_y} \alpha_z \langle |DFT\{\Delta d[x,y,z]\}|^2 \rangle$ |
| | | | Synthesis | $S[f_x,f_y] = \dfrac{b_x b_y}{N_x N_y} \Lambda_z \langle |DFT\{\Delta d[x,y,z]\}|^2 \rangle$ |
| General ($n=3$) | $[x_1,x_2,x_3]$ | $\{x_1\}\{x_2\}\{x_3\}$ | Second order extraction | $S[f_{x1}] = \dfrac{b_{x1}}{N_{x1}} \alpha_{x2}\alpha_{x3} \langle |DFT\{\Delta d[x_1,x_2,x_3]\}|^2 \rangle$ |
| | | | Second order synthesis | $S[f_{x1}] = \dfrac{b_{x1}}{N_{x1}} \Lambda_{x2}\Lambda_{x3} \langle |DFT\{\Delta d[x_1,x_2,x_3]\}|^2 \rangle$ |

lag), the bandwidth integral reduces the NPS, and $\alpha_t$ is the correction factor such that the result represents a central slice of the spatiotemporal NPS. This case is demonstrated experimentally in Sec. IV B. For synthesis, in which data are integrated in the temporal domain (frame integration), $\Lambda_t$ is the time for which frames are summed, assuming that such is much greater than the length of temporal correlation.

For volume CT, the input distribution is a number density ($mm^{-3}$), and the volumetric NPS has units $mm^3$. As shown in Table II, NPS analysis by extraction of transverse slices requires account of $\alpha_z$, the effective aperture in the $z$ domain. If there is no longitudinal correlation beyond that of slice thickness, $a_z$ (e.g., in sequential, stacked slice CT) the effective longitudinal aperture equals the slice thickness. If correlation exceeds the slice thickness (e.g., due to blur in the 2D detector), the integral reduces the transverse NPS and $\alpha_z$ is the correction applied for the result to represent a central slice of the full 3D NPS. Using Eq. (19), similar expressions can be written for extraction along other dimensions (e.g., coronal or sagittal slices). Similarly, the "synthesized slice" technique is shown in Table II, where 2D realizations are formed by integrating (averaging) along a synthetic aperture in $z$, and $\Lambda_z$ normalizes for the length of the synthesizing aperture, assuming that this length is much greater

than longitudinal correlation in the data. This case is demonstrated experimentally in Sec. IV C.

Finally, Table II illustrates higher order extraction and synthesis. In each case, a linear combination of apertures accounts for extraction or synthesis, respectively, along each domain. Moreover, the framework provides a simple manner of accounting for combined extraction and synthesis among various domains, with the integrals of Eqs. (19) and (24) applied, respectively, in a building-block fashion for proper NPS normalization.

### B. Case $n=3$: The spatiotemporal NPS

#### 1. Measurements of image lag and NPS

Figure 4 summarizes the temporal response characteristics of the system. In Fig. 4(a), IRFs are plotted at three exposure levels out to the 10th frame following the x-ray impulse. First-frame lag is typically 5–8 %, comparable to results reported previously for other FPIs, (see, e.g., Table I in Ref. 36) and Lag$|_k$ increases with exposure. The curves are parametric fits based on Fig. 4(b), where the $k^{th}$-frame lag is plotted versus exposure level. The top-most curve in Fig. 4(b) represents the exposure dependence of the first-frame lag, increasing from ~5% to ~8% across the sensitive range,
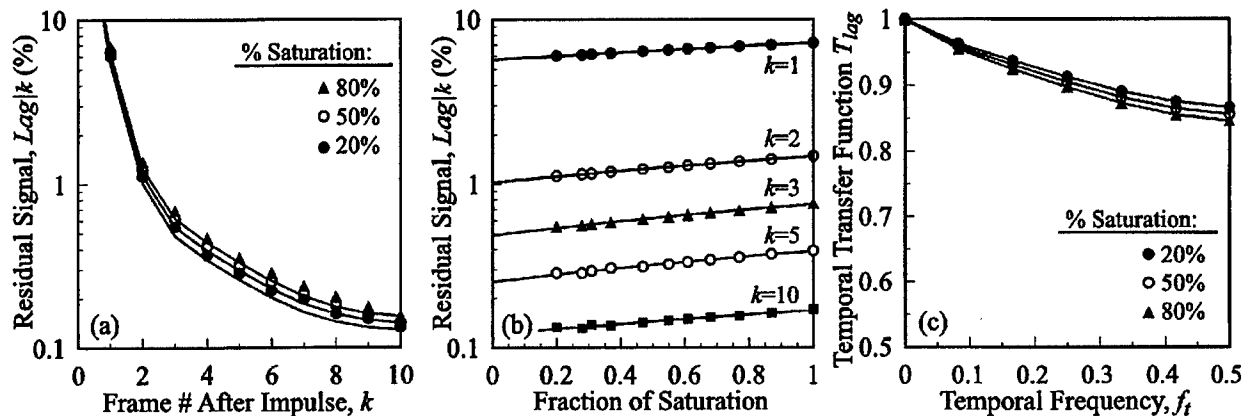
FIG. 4. Temporal response characteristics of the FPI-based imaging system employed in this work. (a) Impulse response functions plotted at three exposure levels corresponding to ~20%, 50%, and 80% of sensor saturation. (b) The $k^{th}$-frame lag, $Lag|_k$, plotted as a function of exposure level for various values of $k$ ($k=1$ corresponds to 1st-frame lag, $k=2$ to 2nd-frame lag, etc.). The curves are linear fits that provide a convenient parameterization of the exposure-dependent temporal response characteristics. (See text for details.) (c) Temporal transfer functions, $T_{lag}(f_t)$, computed for the example IRFs in (a). The abscissa is the temporal frequency relative to the Nyquist frequency such that the temporal bandwidth integral [frame$^{-1}$] and effective temporal aperture [frames] give the correction factor associated with temporal correlation.

and the lower curves show the behavior for higher values of $k$—e.g., the 10th-frame lag nearly constant at ~0.12% across the sensitive range of the detector. The exposure dependence of $Lag|_k$ is well described by linear fits of the form $Lag|_k(X_{sat})=mX_{sat}+b$ as shown by the curves in Fig. 4(b), where $X_{sat}$ is the abscissa (fraction of saturation), providing a convenient parametrization of the exposure-dependent temporal response characteristics. For $k=1$, $Lag|_1$ $=(1.51)X_{sat}+5.70$; for $k=2$, $Lag|_2=(0.46)X_{sat}+1.02$; for $k=3$, $Lag|_3=(0.27)X_{sat}+0.49$; for $k=5$, $Lag|_5$ $=(0.14)X_{sat}+0.25$; and for $k=10$, $Lag|_{10}=(0.05)X_{sat}$ $+0.12$. The $m$-values (slope) quantify the exposure dependence, and the $b$ values the intrinsic offset in $k^{th}$-frame image lag in the limit of low exposure. The temporal transfer functions for the three IRFs in Fig. 4(a) are shown in Fig. 4(c),

where $T_{lag}(f_t)$ is seen to decrease with increasing levels of image lag. The frequency axis shown is dimensionless (i.e., frame$^{-1}$, with $f_{Nyq}=\frac{1}{2}$). Earlier work[36] showed that such temporal correlation is dominated by the charge trapping and release characteristics of the $a$-Si:H detector elements[41] rather than afterglow in the x-ray converter or incomplete charge transfer in the readout electronics.

Figure 5 shows the spatiotemporal NPS measured from fluoroscopic data by extracting projections $d[x,y]$ from the fluoroscopic sequence and correcting by the temporal bandwidth integral as in Eq. (19). A 2D central slice of the NPS, $S[f_x,f_y]$, is shown in Fig. 5(a) for the lag-free case (i.e., $N_{flush}=30$, giving negligible temporal correlation) at an exposure level of $X_{sat}=20\%$. The NPS was found to agree with
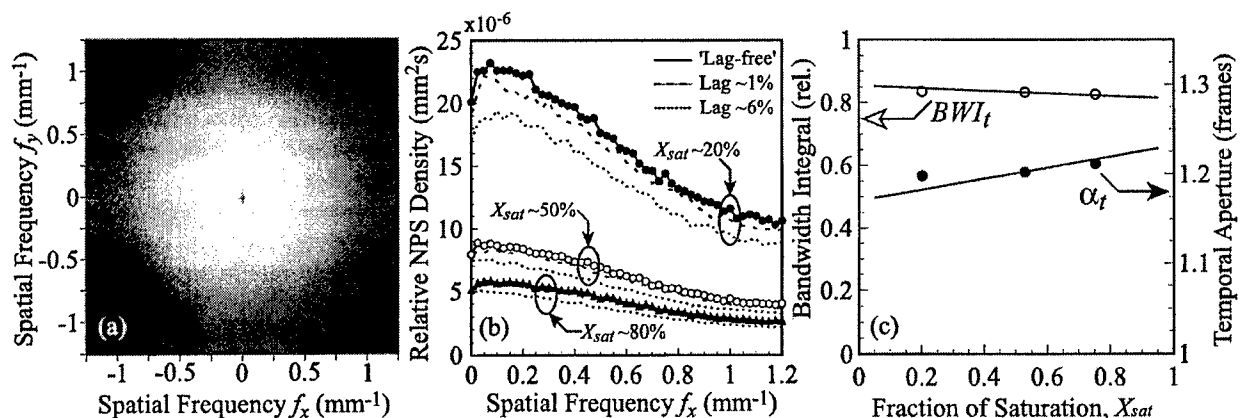


FIG. 5. The spatiotemporal NPS analyzed by extraction. (a) A 2D central slice in the spatial-frequency domain, $S[f_x,f_y]$, exhibits the band-limited NPS characteristic of indirect-detection FPIs. The magnitude of the spectral density implied by the grayscale representation is evident in the top-most curve of (b) (the $X_{sat}\sim20\%$, Lag-free case). (b) Relative NPS measured at three exposure levels (fraction of saturation, $X_{sat}$, ~20%, 50%, and 80%) and three levels of temporal correlation (Lag-free, Lag~1%, and Lag~6%), grouped by the superimposed ellipses. Temporal correlation is seen to reduce the NPS uniformly at all frequencies, in agreement with the discussion of Sec. II C. (c) Temporal bandwidth integral (left axis) and corresponding effective temporal aperture (right axis) plotted as a function of exposure level. The points correspond to ratios of the NPS in (b), and the curves are calculations based on the measurements in Fig. 4. Agreement between the two gives experimental validation of the approach described in Sec. II C.

prediction from a simple linear cascaded systems model,[4] with spatial-frequency-dependence determined by the characteristic MTF of the x-ray converter and the sinc function MTF of the pixel apertures. There is no evidence of correlated noise (streaks in the NPS), and the slight rolloff near zero-frequency is an artifact of zero-mean detrending.

In Fig. 5(b), three groups of NPS measurements are plotted (exposure levels, $X_{sat} \sim 20\%$, 50%, and 80%), where each group contains the NPS measured at three levels of temporal correlation: (1) Lag-free ($N_{flush} = 30$ and temporal correlation is negligible); (2) Lag $\sim 1\%$ ($N_{flush} = 1$ and correlation is $\sim 1$–2%, depending on exposure level); and (3) Lag $\sim 6\%$ ($N_{flush} = 0$, i.e., projections read continuously with x-ray exposure incident on every frame, and correlation is $\sim 6$–8%, depending on exposure level). In each case, the relative NPS is shown—i.e., the NPS divided by the mean signal squared—which decreases with exposure level. As expected for the Lag-free case the absolute NPS increases linearly with exposure level. For each group, the Lag-free case exhibits the highest spectral density, and the Lag $\sim 1\%$ and Lag $\sim 6\%$ cases exhibit progressively lower NPS density due to increased temporal correlation. Note that for the higher-lag cases, the NPS is reduced uniformly at all spatial frequencies relative to the Lag-free case. This agrees with the description of Eqs. (14)–(19) and with intuition, since the temporal domain in which these correlations are introduced is separable from the spatial domain.

Figure 5(c) demonstrates the effect of temporal correlation on the NPS, where the temporal bandwidth integral [$BWI_t$ in Eq. (17a); left axis] and effective temporal aperture [$\alpha_t$ in Eq. (17b); right axis] are plotted as a function of detector signal. The bandwidth integral (units of frame$^{-1}$) corresponds to the integral of the transfer functions in Fig. 4(c). The temporal aperture, therefore, corresponds to $\sim 1.2$ frames. The points plotted represent the ratio of the measured NPS in the high-lag (Lag $\sim 6\%$) case and in the Lag-free case. [See Fig. 5(b) for the three exposure levels ($X_{sat} \sim 20\%$, 50%, and 80%)]. The curves are calculations of the temporal bandwidth integral based on the parametrized IRF and $T_{lag}$ measurements in Fig. 4, showing reasonable agreement with the measured reduction in NPS and providing experimental validation of the approach described in Sec. II C.

## 2. A simple model for image lag and NPS

A simple model for the effect of image lag on the NPS can be constructed that does not rely on the FPI-specific parameterization of image lag measured above, but is idealized to the case of a simple exponential response. For the one-sided, discrete time-sampled, exponential signal,[42] one has $Sig|_k = \lambda^k$, where $\lambda$ is the first-frame lag (i.e., the residual signal in the first frame following exposure), and the residual signal in the second, third, etc., is $\lambda^2$, $\lambda^3$, etc., respectively. The normalized IRF is

$$p[k] = (1 - \lambda)\lambda^k \tag{27a}$$

and the corresponding transfer function is[42]

$$T[f] = \frac{(1 - \lambda)}{1 - \lambda e^{-if}} \tag{27b}$$

$$T^2[f] = \frac{(1 - \lambda)^2}{1 - 2\lambda \cos f + \lambda^2} \tag{27c}$$

The temporal bandwidth integral is obtained by integrating Eq. (27c) over the frequency domain, giving

$$BWI_t = \frac{1 - \lambda}{1 + \lambda} 4 \tan^{-1}\left[\frac{1 - \lambda}{1 + \lambda} \tan\left(\frac{f_{Nyq}}{2}\right)\right]. \tag{27d}$$

Taking the dimensionless frequency domain (frames) as described above such that $f_{Nyq} = \frac{1}{2}$ and using a trigonometric series expansion for tangent, we have to first order

$$BWI_t = \frac{1}{\alpha_t} = \left(\frac{1 - Lag|_1}{1 + Lag|_1}\right)^2. \tag{27e}$$

Equation (27e) is a quick rule of thumb for the NPS correction due to image lag, where the response function is fully characterized by the first-frame lag, $Lag|_1$. For example, for a detector with $Lag|_1 = 1\%$, the correction is $\alpha_t = 1.04$; similarly, for $Lag|_1 = 2\%$, 5%, and 10%, the correction is $\alpha_t = 1.08$, 1.22, and 1.49, respectively. Therefore, even a relatively low degree of image lag (e.g., $\sim 2\%$), results in appreciable reduction of the NPS (e.g., $\sim 8\%$). Furthermore, this factor is the amount by which DQE or NEQ would be overestimated if the effect of temporal correlation is ignored. While the response of FPIs is typically more complicated than a single exponential,[38,43] the model is easily adapted to a multiple exponential model, since a sum of exponentials (e.g., characterized by $Lag|_1$, $Lag|_2$, $Lag|_3$, etc.) corresponds to a sum of temporal transfer functions.

## C. Case n=3: The volumetric NPS

Figure 6 summarizes the variation in spatial correlation in volume reconstructions and the corresponding effect on spatial resolution and NPS. Figure 6(a) plots the apodization window, $H_{win}$, at settings of $h_{win}$ ranging from 0.5 to 1. The reconstruction filters, $H_{recon}$, are plotted as dotted curves. Variation of $h_{win}$ adjusts the degree of spatial correlation in the $(x,y)$ domain and was used to investigate the effect of correlations on the volumetric NPS (analogous to the results of Sec. IV B regarding the effects of temporal correlation on the spatiotemporal NPS). Figure 6(b) shows the effect of the apodization filter on basic measures of spatial resolution and noise. The left axis plots the fwhm in images of a thin wire in the $(x,y)$ domain, showing that spatial resolution in the transverse plane improves from $\sim 0.65$ mm for a Hanning filter to $\sim 0.3$ mm for the Ram-Lak filter. The result asymptotically approaches $\sim 0.25$ mm, which is the detector pixel size at isocenter. Conversely, the right axis shows the increase in noise for sharper apodization windows, increasing by a factor $\sim 2$ between the Hanning and Ram-Lak filters.

In Fig. 6(c), the effect of apodization on NPS convergence is illustrated by plotting the volume of the NPS (normalized by voxel variance) versus the synthesizing aperture, $\Lambda_y$, for various settings of $h_{win}$. The solid curves correspond to the coronal NPS in which synthesis is performed along $y$. The
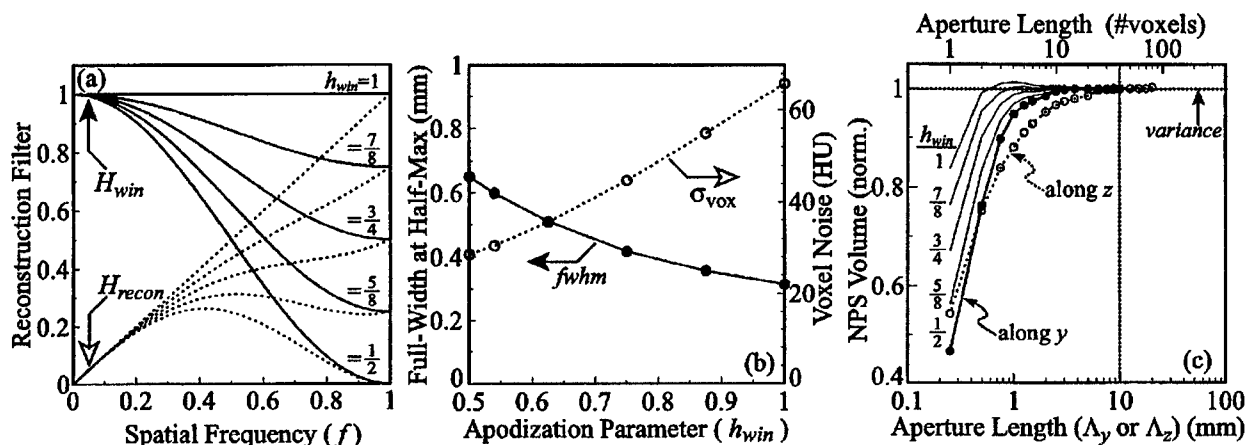
FIG. 6. Transverse spatial correlation in volume CT reconstructions. (a) Apodization windows, $H_{win}$, and reconstruction filters, $H_{recon}$, for various settings of the apodization parameter, $h_{win}$. Spatial correlation in the transverse plane of image reconstructions $(x,y)$ was controlled through variation of apodization from $h_{win} = 0.5$ (Hanning filter) to $h_{win} = 1$ (Ram-Lak filter). (b) Effect of apodization on basic measures of spatial resolution and noise, the former characterized by the full-width at half-maximum of the point-spread function (left axis) and the latter measured in Hounsfield units, HU (right axis). Higher values of $h_{win}$ correspond to reduced spatial correlation (i.e., improved spatial resolution) in the transverse plane at the expense of image noise. (c) Convergence of the central slice NPS analyzed by the synthesis technique. The volume of the computed NPS (normalized by the image variance) is plotted versus the length of the synthesizing aperture for various settings of $h_{win}$. Solid lines demonstrate convergence for cases of synthesis along $y$ (i.e., analysis of the coronal NPS), with the corresponding $h_{win}$ values shown at the left of each curve. The dotted line with open circles is for synthesis along $z$ (i.e., analysis of the transverse NPS), which was independent of $h_{win}$. An aperture length of 10 mm was chosen in order to give convergence in all cases (i.e., computed NPS volume within 1% of the true variance).

solid curve with solid circles is for $h_{win} = 0.5$, showing that for $\Lambda_y < 5$ mm ($<20$ voxels), the result underestimates the NPS. The thin solid curves also correspond to synthesis along $y$, but for volume images reconstructed using various apodization windows, with the values of $h_{win}$ shown at the left. Note that for larger settings of $h_{win}$ [i.e., reduced correlation in $(x,y)$] the NPS converges more quickly. Also shown is the transverse NPS in which synthesis is performed along $z$ (dotted line with open circles), where convergence is independent of $h_{win}$, since the apodization window does not affect correlation in $z$. Convergence of the transverse NPS (i.e., synthesis along $z$) is more gradual than convergence of the coronal NPS, suggestive of asymmetry in the 3D spatial resolution. To ensure convergence in all cases (NPS volume within 1% of the voxel variance), a synthesizing aperture of 10 mm (40 voxels) was chosen.

Figure 7 summarizes the volumetric NPS analyzed by synthesis and full 3D FFT. Figure 7(a) shows central slice cuts of the transverse NPS at varying apodization, and a characteristic "filtered-ramp" spectrum similar to conventional CT,[34,44,45] is observed in which NPS increases at low frequencies (due to the ramp filter) and rolls off at higher frequencies (due to band-limiting processes, such as blur, apodization, and interpolation). The correlation imposed by apodization has a strong effect on the transverse NPS, consistent with the transfer functions in Fig. 6(a), with an increase in high-frequency noise for increasing $h_{win}$. The magnitude and slope of the low-frequency NPS are nearly independent of $h_{win}$, in agreement with Hanson,[44] who showed that the slope of the low-frequency NPS is proportional to NEQ; therefore, the NEQ is unaffected by the apodization to first order.

Figure 7(b) shows the coronal NPS at varying apodiza-

tion, exhibiting a low-pass characteristic resulting from longitudinal correlation (blur and interpolation in the projection data). Such dependence in $f_z$ is reasonable, since ramp and apodization filters are not applied in $z$. Moreover, the result is different from what might be expected, e.g., for a set of stacked slices in conventional CT, in which case the longitudinal component of the NPS is constant (i.e., "white"). Choice of apodization affects the magnitude, but not the shape, of the longitudinal NPS, since the apodization filter operates in a domain orthogonal to $z$ [in a manner analogous to Fig. 5(b), where image lag was found to affect the magnitude, but not the shape, of the $(f_x, f_y)$ components of the spatiotemporal NPS]. Note the difference in scale between Figs. 7(a) and 7(b), with the various central slice representations of the 3D NPS sharing a common scale value at $f_x = f_y = f_z = 0$ mm$^{-1}$. As noted by Kijewski et al.[45] the non-zero scale value is attributed to aliasing—in this case 3D aliasing[46] of the NPS in the 3D Fourier domain of the volumetric sampling matrix. As shown in Fig. 7(c), apodization has a measurable effect on the NPS scale value (i.e., on the amount of aliasing), increasing from $\sim10.1$ mm$^3$ for $h_{win} = 0.5$ (Hanning) to $\sim12.2$ mm$^3$ for $h_{win} = 1$ (Ram-Lak). Also shown are the moderate effect of apodization on mid-frequency noise [i.e., spectral density at $(f_x = 0.5$ mm$^{-1}$; $f_y = f_z = 0$ mm$^{-1})$] and the large effect near the Nyquist frequency [i.e., at $(f_x = 2$ mm$^{-1}$; $f_y = f_z = 0$ mm$^{-1})$].

The transverse and coronal NPS are illustrated in Figs. 7(d) and 7(e) for $h_{win} = 0.5$. Separate grayscales were applied to accentuate contrast in each case. The NPS magnitude implied by the gray values is evident in the plots of Figs. 7(a) and 7(b), respectively. The transverse NPS is radially symmetric and spectrally "green" (i.e., the spectrum is greatest at mid-frequencies), characteristic of reconstruction employ-
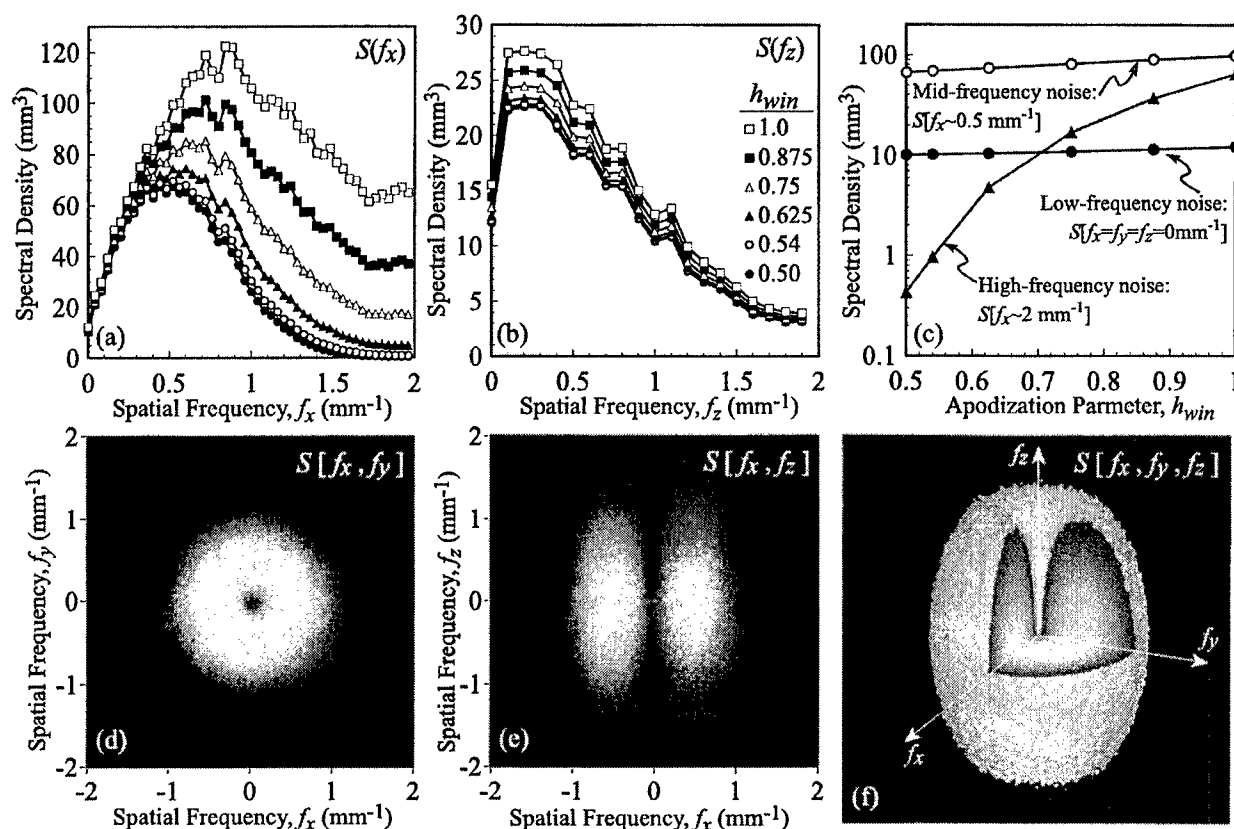
FIG. 7. The volumetric NPS analyzed by synthesis (a)–(e) and full 3D analysis (f). In (a) and (b), central slice cuts of the transverse and coronal NPS—$S[f_x]$ and $S[f_z]$, respectively—are shown at various settings of apodization filter. The apodization parameter, $h_{win}$, corresponding to each curve is shown in the legend of (b). (c) Spectral density at various spatial frequencies in the transverse plane as a function of $h_{win}$. Note in particular the slight increase in the zero-frequency NPS value with increasing $h_{win}$, attributable to increased NPS aliasing for cases of reduced spatial correlation. In (d) and (e), the central slice transverse and coronal NPS are represented as grayscale images for the case $h_{win}=0.5$. [The relationship between spectral density and grayscale is evident in comparing to the respective curves in (a) and (b).] The transverse NPS is radially symmetric and spectrally "green" (i.e., peaking at mid-frequencies), characteristic of images reconstructed using a ramp filter. The coronal NPS is highly asymmetric—"green" in the transverse domain and "red" (i.e., band-limited) in the longitudinal direction—characteristic of images reconstructed by cone-beam filtered back-projection. (f) Shaded surface rendering of the full 3D NPS with cut-planes introduced in the first octant to allow visualization of the spectral density within the shaded surface. Frequency axes are as labeled, and the region displayed (including black areas outside the windowed surface) corresponds to the full 3D Nyquist region.

ing a ramp filter in combination with band-limiting processes such as interpolation. The coronal NPS is highly asymmetric, exhibiting noise characteristics that are "green" in the $f_x$ direction and "red" (i.e., high spectral density at low frequencies) in the $f_z$ direction. This highly asymmetric 3D NPS is characteristic of cone-beam CT images reconstructed using filtered back-projection, where the ramp and apodization affect correlation in the transverse plane, but correlation in the longitudinal direction is governed by (1) the $f_z$-component of the 2D detector MTF; and (2) interpolation of the projection data in $(x,z)$ upon reconstruction. For purposes of visualization, the 3D NPS is shown in Fig. 7(f) as a shaded surface rendering. The 3D domain in the figure corresponds to the full 3D Nyquist zone, with grayscale window similar to that in Fig. 7(d) and cut-planes to allow visualization of the spectral density within the surface. There is no evidence of off-axis noise features beyond that described by the three central slice representations.

## V. DISCUSSION AND CONCLUSIONS

The methods described above provide a general framework for NPS analysis of multidimensional image data. For example: taking $n=2$ for the domain $(x,y)$ describes the familiar case of NPS analysis of 2D projections; taking $n=3$ for the domain $(x,y,t)$ describes the spatiotemporal NPS of fluoroscopic data; similarly, taking $n=3$ for the domain $(x,y,z)$ describes the volumetric NPS of volume image reconstructions. For all cases, the framework illustrates the continuity between analysis of the full $n$D NPS and techniques that analyze a "central slice" of the NPS, highlights the effects of correlations on the NPS, and makes issues of normalization and units transparent.

The methods for full $n$D and central slice NPS analysis are summarized in Table III. In each case, the normalization associated with finite-length realizations is given by $W_{norm}^{discrete}$ as in Eq. (11). For central slice NPS analysis by extraction, the normalization $W_{norm}^{extract}$ incorporates the bandwidth integral

TABLE III. Summary of methodological forms and normalization factors for NPS analysis. For discrete measured data, $W_{\mathrm{norm}}^{\mathrm{discrete}}$ gives normalization for the full $n$D NPS analyzed by $n$D discrete Fourier transform. For the NPS analyzed by extraction and/or synthesis along various domains, the terms $W_{\mathrm{norm}}^{\mathrm{extract}}$ and $W_{\mathrm{norm}}^{\mathrm{synth}}$ are applied as appropriate to the extracted and/or synthesized domains. See Table II for specific cases of 2D and 3D data.

| NPS analysis | Equation | Normalization | Noise-power spectrum |
|---|---|---|---|
| Discrete, finite-length data | (12) | $W_{\mathrm{norm}}^{\mathrm{discrete}} = \dfrac{b_{1:n}}{N_{1:n}}$ | $S[f_{1:n}] = \dfrac{b_{1:n}}{N_{1:n}} \langle |\mathrm{DFT}\{\Delta d[x_{1:n}]\}|^2 \rangle$ |
| Central slice: Extraction | (19) | $W_{\mathrm{norm}}^{\mathrm{extract}} = \alpha_{(n-m+1):n}$ | $S[f_{1:n-m}] = \dfrac{b_{1:n-m}}{N_{1:n-m}} \alpha_{(n-m+1):n} \langle |\mathrm{DFT}\{\Delta d[x_{1:n-m}]\}|^2 \rangle$ |
| Central slice: Synthesis | (24) | $W_{\mathrm{norm}}^{\mathrm{synth}} = \Lambda_{(n-m+1):n}$ | $S[f_{1:n-m}] = \dfrac{b_{1:n-m}}{N_{1:n-m}} \Lambda_{(n-m+1):n} \langle |\mathrm{DFT}\{\Delta d[x_{1:n-m}]\}|^2 \rangle$ |

associated with correlations orthogonal to the extracted data as in Eq. (18). For central slice NPS analysis by synthesis, the normalization $W_{\mathrm{norm}}^{\mathrm{synth}}$ accounts for the extent of the synthesizing aperture as in Eq. (23). The techniques of extraction and synthesis are seen to be limiting cases of the same basic approach—the former fully incurring correlations orthogonal to realizations, and the latter negating such correlations by integrating across orthogonal domains.

The specific cases in Table II are relevant to current investigations in multidimensional imaging—viz., fluoroscopy and cone-beam CT. For fluoroscopy, it is important to note that the image data is three dimensional in $(x,y,t)$, with significant correlation possible in all three domains [e.g., in $(x,y)$ due to image blur and in $t$ due to image lag]. Correspondingly, the NPS is spatiotemporal in nature,[40] and is described by the general framework in the special case $n = 3$ $[(x_{1:3}) = (x,y,t)]$. The measurements presented here demonstrate that analysis of the spatiotemporal NPS requires account of temporal correlation. For the FPI-based system employed, with (first-frame) image lag $\sim5-8\%$ [see Fig. 4], the correction factor is $\sim1.2$ [Fig. 5(c)]. A simple model for a detector with exponential response was shown to provide a convenient rule of thumb [Eq. (27e)] for the degree to which image lag reduces NPS. Failure to account for such correlation guarantees inaccurate NPS results.

For the volumetric case, the 3D NPS of cone-beam CT images was investigated by 3D FFT and by the "synthesized slice" technique, with normalization, units, etc. described by the general framework in the case $n = 3$ $[(x_{1:3}) = (x,y,z)]$. The volumetric NPS was found to be highly asymmetric: transverse planes exhibit a spectrum typical of filtered back-projection,[44,45] with NPS increasing at low-mid frequencies (due to the ramp filter), and decreasing at high frequencies (due to band-limiting processes); sagittal and coronal planes, on the other hand, exhibit a combination of this ramp-like characteristic in the transverse direction and a band-limited characteristic in the longitudinal ($z$) direction. The band-limited nature of the longitudinal NPS is attributed to blur in the 2D detector and 2D interpolation of the projection data upon reconstruction. Moreover, it is different from the NPS of volume data formed by "stacking" 2D slices (e.g., in conventional CT), where the transverse NPS exhibits a similar "filtered-ramp" shape, but lack of correlation in $z$ would result in constant longitudinal NPS. The asymmetry of

the volumetric NPS of cone-beam CT images and its distinction from that of "stacked-slice" CT images could have implications for the detection of structures in volume data, suggesting that detectability[1] may vary, depending on the plane in which a given structure is visualized. Such effects are subjects of ongoing work.

The general framework provides a unified approach to NPS analysis of multidimensional image data, reducing to familiar cases for 2D images (e.g., projection radiography) and allowing direct application to 3D images (e.g., fluoroscopy, CT fluoroscopy, and cone-beam CT) and 4D images (e.g., volume fluoroscopy). It highlights the effect of correlation on the NPS and quantifies how spatial and temporal correlations (e.g., blur and lag) are accommodated in NPS analysis. Furthermore, the approach renders issues of NPS normalization transparent, giving absolute measure of the NPS without recourse to self-normalizing techniques,[47] which in turn is applicable to absolute measures of imager performance, such as NEQ.

## ACKNOWLEDGMENTS

[a] Corresponding author: Ontario Cancer Institute, Princess Margaret Hospital, Toronto, ON M5G 2M9. Phone: 416-946-4501 ext. 5516; Fax: 416-946-6529; Electronic mail: jsiewerd@uhnres.utoronto.ca

[1] International Commission on Radiation Units and Measurements Report No. 54, *Medical Imaging—the Assessment of Image Quality* (ICRU, Bethesda, MD, 1996).
[2] The American Association of Physicists in Medicine (AAPM) Task Group #16 (forthcoming).

[3] M. L. Giger, K. Doi, and C. E. Metz, "Investigation of basic imaging properties in digital radiography. 2. Noise Wiener spectrum," Med. Phys. **11**, 797–805 (1984).

[4] J. H. Siewerdsen, L. E. Antonuk, Y. El-Mohri, J. Yorkston, W. Huang, and I. A. Cunningham, "Signal, noise power spectrum, and detective quantum efficiency of indirect-detection flat-panel imagers for diagnostic radiology," Med. Phys. **25**, 614–628 (1998).

[5] W. Zhao, I. Blevis, S. Germann, J. A. Rowlands, D. Waechter, and Z. Huang, "Digital radiology using active matrix readout of amorphous selenium: construction and evaluation of a prototype real-time detector," Med. Phys. **24**, 1834–1843 (1007).

[6] P. R. Granfors and R. Aufrichtig, "Performance of a 41×41 cm² amorphous silicon flat panel x-ray detector for radiographic imaging applications," Med. Phys. **27**, 1324–1331 (2000).

[7] S. Vedantham et al., "Full breast digital mammography with an amorphous silicon-based flat panel detector: physical characteristics of a clinical prototype," Med. Phys. **27**, 558–567 (2000).

[8] L. E. Antonuk et al., "Strategies to improve the signal and noise performance of active matrix, flat-panel imagers for diagnostic x-ray applications," Med. Phys. **27**, 289–306 (2000).

[9] R. E. Colbeth et al., "Characterization of a third generation, multi-mode sensor panel," Medical Imaging 1999: Physics of Medical Imaging, Proc. SPIE **3659**, 491–500 (1999).

[10] D. A. Jaffray and J. H. Siewerdsen, "Cone-beam computed tomography with a flat-panel imager: initial performance characterization," Med. Phys. **27**, 1311–1323 (2000).

[11] R. Ning, D. Lee, X. Wang, Y. Zhang, D. Conover, D. Zhang, and C. Williams, "Selenium flat panel detector-based volume tomographic angiography imaging: phantom studies," Medical Imaging 1998: Physics of Medical Imaging, Proc. SPIE **3336**, 316–324 (1998).

[12] J. H. Siewerdsen and D. A. Jaffray, "Cone-beam computed tomography with a flat-panel imager: magnitude and effects of x-ray scatter," Med. Phys. **28**, 220–231 (2001).

[13] Y. Saito, H. Aradate, H. Miyazaki, K. Igarahi, and H. Ide, "Large area 2-dimensional detector for real-time 3-dimensional CT (4D-CT)," Medical Imaging 2001: Physics of Medical Imaging, Proc. SPIE **4320**, 775–782 (2001).

[14] R. B. Blackman and J. W. Tukey, The Measurement of Power Spectra (Dover, New York, 1958).

[15] R. N. Bracewell, The Fourier Transform and Its Applications (McGraw-Hill, Boston, 1965).

[16] J. S. Bendat and A. G. Piersol, Random Data: Analysis and Measurement Procedures (Wiley, New York, 1986).

[17] A. Papoulis, Probability, Random Variables, and Stochastic Processes, 3rd ed. (McGraw-Hill, New York, 1991).

[18] J. C. Dainty and R. Shaw, Image Science: Principles, Analysis and Evaluation of Photographic-Type Imaging Processes (Academic, London, 1974).

[19] M. Rabbani, R. Shaw, and R. Van Metter, "Detective quantum efficiency of imaging systems with amplifying and scattering mechanisms," J. Opt. Soc. Am. A **4**, 895–901 (1987).

[20] I. A. Cunningham, M. S. Westmore, and A. Fenster, "A spatial-frequency dependent quantum accounting diagram and detective quantum efficiency model of signal and noise propagation in cascaded imaging systems," Med. Phys. **21**, 417–427 (1994).

[21] I. A. Cunningham, "Analyzing system performance," in The Expanding Role of Medical Physics in Diagnostic Imaging, edited by G. D. Frey and P. Sprawls (AAPM, Madison WI, 1997), pp. 231–263.

[22] J. H. Siewerdsen, L. E. Antonuk, Y. El-Mohri, J. Yorkston, W. Huang, J. M. Boudry, and I. A. Cunningham, "Emprical and theoretical investigation of the noise performance of indirect detection, active matrix flat-panel imagers (AMFPIs) for diagnostic radiology," Med. Phys. **24**, 71–89 (1997).

[23] W. Zhao and J. A. Rowlands, "Digital radiology using active matrix readout of amorphous selenium: theoretical analysis of detective quantum efficiency," Med. Phys. **24**, 1819–1833 (1997).

[24] I. A. Cunningham, "Applied linear systems theory," Chap. 2, in Handbook of Medical Imaging: Volume 1 Physics and Psychophysics, edited by J. Beutel, H. L. Kundel, and R. Van Metter (SPIE, Bellingham, 2000), pp. 79–159.

[25] J. Freim, Jr. and A. Feldman, in Medical Physics Handbook of Units and Measures, edited by S. Shahabi (Medical Physics Publishing, Madison, WI, 1992).

[26] J. H. Siewerdsen, Ph.D. dissertation, Bell and Howell Publishing, Ann Arbor, MI, 1998.

[27] A. D. Maidment and M. J. Yaffe, "Analysis of the spatial-frequency-dependent DQE of optically coupled digital mammography detectors," Med. Phys. **21**, 721–729 (1994).

[28] J. Yao and I. A. Cunningham, "Parallel cascades: new ways to describe noise transfer in medical imaging systems," Med. Phys. **28**, 2020–2038 (2001).

[29] W. Zhao, W. G. Ji, and J. A. Rowlands, "Effects of characteristic x rays on the noise power spectra and detective quantum efficiency of photoconductive x-ray detectors," Med. Phys. **28**, 2039–2049 (2001).

[30] H. H. Barrett and W. Swindell, Radiological Imaging: The Theory of Image Formation, Detection, and Processing, Volume 1 (Academic, New York, 1981).

[31] J. P. Moy, "Image quality of scintillator based x-ray electronic imagers," Medical Imaging 1998: Physics of Medical Imaging, Proc. SPIE **3336**, 187–194 (1998).

[32] W. G. Ji, W. Zhao, and J. A. Rowlands, "Digital x-ray imaging using amorphous selenium: reduction of aliasing," Med. Phys. **25**, 2148–2162 (1998).

[33] J. T. Dobbins III, D. L. Ergun, L. Rutz, D. A. Hinshaw, H. Blume, and D. C. Clarke, "DQE(f) of four generations of computed radiography acquisition devices," Med. Phys. **22**, 1581–1593 (1995).

[34] R. F. Wagner, D. G. Brown, and M. S. Pastel, "Application of information theory to the assessment of computed tomography," Med. Phys. **6**, 83–94 (1979).

[35] J. H. Siewerdsen and D. A. Jaffray, "Optimization of x-ray imaging geometry (with specific application to flat-panel cone-beam computed tomography," Med. Phys. **27**, 1903–1914 (2000).

[36] J. H. Siewerdsen and D. A. Jaffray, "A ghost story: spatiotemporal response characteristics of an indirect-detection flat-panel imager," Med. Phys. **26**, 1624–1641 (1999).

[37] J. M. Boudry, "Operation of amorphous silicon detectors for chest radiography within system latency requirements," Medical Imaging 1999: Physics of Medical Imaging, Proc. SPIE **3659**, 336–344 (1999).

[38] J. H. Siewerdsen and D. A. Jaffray, "Cone-beam computed tomography with a flat-panel imager: effects of image lag," Med. Phys. **26**, 2635–2647 (1999).

[39] L. A. Feldkamp, L. C. Davis, and J. W. Kress, "Practical cone-beam algorithm," J. Opt. Soc. Am. A **1**, 612–619 (1984).

[40] I. A. Cunningham, T. Moschandreou, and V. Subotic, "The detective quantum efficiency of fluoroscopic systems: The case for a spatial-temporal approach," Medical Imaging 2001: Physics of Medical Imaging, Proc. SPIE **4320**, 479–488 (2001).

[41] R. A. Street, Hydrogenated Amorphous Silicon (Cambridge University Press, New York, 1991).

[42] J. G. Proakis and D. G. Manolakis, Digital Signal Processing: Principles, Algorithms, and Applications (Macmillan, New York, 1992).

[43] L. E. Antonuk, J. Yorkston, W. Huang, J. Siewerdsen, and R. A. Street, "Considerations for high frame rate operation of two-dimensional a-Si:H imaging arrays," Mater. Res. Soc. Symp. Proc. **297**, 945–950 (1993).

[44] K. M. Hanson, "Detectability in computed tomographic images," Med. Phys. **6**, 441–451 (1979).

[45] M. F. Kijewski and P. F. Judy, "The noise power spectrum of CT images," Phys. Med. Biol. **32**, 565–575 (1987).

[46] J. H. Siewerdsen and D. A. Jaffray, "Cone-beam CT with a flat-panel imager: noise considerations for fully 3-D imaging," Medical Imaging 2000: Physics of Medical Imaging, Proc. SPIE **3336**, 546–554 (2000).

[47] K. Stierstorfer and M. Spahn, "Self-normalizing method to measure the detective quantum efficiency of a wide range of x-ray detectors," Med. Phys. **26**, 1312–1319 (1999).

# Fundamental limitations imposed by x-ray interactions on the modulation transfer function of existing x-ray detectors

G. Hajdok[1,2,3], J.J. Battista[2,3] and I.A. Cunningham[1,3,4]

[1] Robarts Research Institute, [2] London Regional Cancer Centre, [3] University of Western Ontario, and [4] London Health Sciences Centre, London, Ontario, Canada

## ABSTRACT

The development of new detectors for diagnostic x-ray imaging is a complex and expensive endeavour. An understanding of fundamental performance potential and limitations is therefore critical to the wise allocation of research resources. We present a Monte Carlo study in which the fundamental spatial resolution limitations imposed by x-ray interactions were determined for both direct conversion amorphous selenium (a-Se) and indirect conversion cesium iodide (CsI) detectors. Using a simulated infinitesimal x-ray beam, the absorbed energy point spread function (PSF) in each detector material was scored within rectilinear bin sizes of 5 μm for incident x-ray energies between 10 and 100 keV. The modulation transfer function (MTF) was determined from each simulated PSF and characterized in terms of the 50% MTF frequency, $f_{50}$, and the equivalent passband, $N_e$. Both materials demonstrated: (i) a drop in $f_{50}$ (a-Se: 25%, CsI: 85%) and $N_e$ (a-Se: 45%, CsI: 75%) immediately above the K-edge energy due to re-absorption of characteristic radiation, and (ii) a moderate recovery of $f_{50}$ and $N_e$ levels with further increase in energy. In addition, within the diagnostic energy range and spatial frequency range of 0 – 20 cycles/mm, the values of the fundamental MTF due to x-ray interactions remain above 50%. In general, we conclude that existing amorphous selenium and cesium iodide detectors operate far from fundamental spatial resolution limits in both mammography and radiography applications. Further reduction in detector element size will potentially improve spatial resolution in these detectors.

Keywords: x-ray interactions, amorphous selenium, cesium iodide, Monte Carlo simulation, MTF

## 1. INTRODUCTION

Over the past decade, dramatic improvements have occurred in the performance of digital detector technology for medical imaging[1]. The motivation for advancing towards a digital approach stems from a further need to improve image quality, reduce patient dose, increase patient throughput in the imaging centre, and decrease overall costs. The most promising digital system to date has been the flat-panel (FP) detector[2]. The FP detector is based on a large-area active-matrix readout structure, made from amorphous silicon. Coupling the active-matrix component to a traditional x-ray converter material, such as a photoconductor or phosphor, forms the basis of the detector.

The difference between photoconductors and phosphors is important since the type of x-ray converter material will dictate the overall performance of the digital detector[2]. A photoconductor is generally referred to as a *direct* x-ray conversion material because x rays are directly converted to electrical charge with no intermediate stage. In contrast, a phosphor is designated as an *indirect* x-ray conversion material because x rays are first converted to optical light, then finally to electrical charge. The most popular photoconductor and phosphor materials in practice or in development include amorphous selenium and cesium iodide, respectively.

When designing a new x-ray imaging system, the general requirements of the detector depend on the imaging task. One important requirement is high spatial resolution, which is especially necessary in: (i) mammography[3] to visualize fine-details of micro-calcifications and thin fibres protruding from a tumour mass in the breast, and (ii) micro-computed tomography[4] (CT) to visualize the intricate anatomy of small animals (e.g. mice).

The factors that limit spatial resolution in a digital detector depend upon the technology used. In digital detectors using either a photoconductor or scintillating phosphor, spatial resolution is generally limited by detector element (*del*) size and optical light dispersion, respectively. However, from a fundamental point-of-view, the physical nature of x-ray interactions determines the upper bounds on spatial resolution. Incident x-ray energy is not transferred and absorbed on the spot within a detector material. Rather, x-ray interactions produce secondary radiation that spreads the incident x-ray energy away from the primary interaction site. The spread of energy is attributed to a combination of: (a) re-absorption of fluorescent or scatter x rays, and (b) deposition of energy along charged particle tracks.

Several theoretical studies have been performed on the intrinsic spatial resolution of converter materials used in diagnostic x-ray detectors. Two in particular deserve attention. Que and Rowlands[5,6] have used analytic calculations to isolate the main factors that limit spatial resolution in amorphous selenium, based on estimations of the MTF in the diagnostic energy range. They found that re-absorption of K-fluorescent x rays significantly degraded the MTF. Boone *et al.*[7] used Monte Carlo simulations to study the effects of x ray scattering and x-ray fluorescence in a wide variety of x-ray converter materials (e.g. a-Se, CsI, $Gd_2O_2S$). They determined the radial distribution of re-absorbed x-ray energy, but did not associate the results with the modulation transfer function.

Photoconductors and phosphors have been studied and developed for many years and have reached a high level of optimization. The question at this point is which technology has potential for further improvements? In particular, which approach has the greatest potential for achieving high-resolution images in areas demanding improved performance (e.g. mammography or small-animal imaging). In this article, we use Monte Carlo simulations to examine the fundamental limitations imposed by the various x-ray interaction processes on the modulation transfer function (MTF) for typical direct (amorphous selenium) and indirect (cesium iodide) conversion detector materials used in mammography and radiography. For each type of converter material, the importance of each x-ray interaction process is identified as a function of x-ray energy. In addition, recently published MTF data for each material is compared to simulated MTF data, in order to evaluate whether existing digital detectors based on these conversion materials are close to being "x-ray interaction limited".

## 2. THEORY

In the diagnostic x-ray energy range (10–100 keV), the relevant x-ray interaction processes are photoelectric absorption, Rayleigh scatter and Compton scatter. The relative probability of occurrence for each interaction is presented in Fig. 1 as a function of x-ray energy for both selenium and cesium. As seen from the graph, photoelectric absorption is dominant over the entire diagnostic energy range. At energies below the K-edge of a given material, Rayleigh scatter is significant, while Compton scatter is negligible. Immediately above the K-edge, both Rayleigh and Compton scatter are negligible compared to photoelectric events, but steadily increase with x-ray energy thereafter.

### 2.1 Photoelectric absorption

In the photoelectric effect, an atom fully absorbs an incident x ray, and then ejects an electron from an atomic shell[9,10]. The most probable shell from which the photoelectron is emitted is generally the most tightly bound shell of the atom. Following the emission of the photoelectron, the atom is left in an excited state, and returns to the ground state through a cascade of electron transitions, resulting in the isotropic emission of characteristic (fluorescent) x rays and Auger electrons. Since x-ray detectors are generally made from high atomic number materials, the method of atomic relaxation most likely occurs through fluorescent emissions. A photoelectric interaction involving the K-shell of the atom, given the incident x-ray energy is larger than the binding energy of the K-shell (i.e. K-edge), has the greatest impact in degrading image quality. Filling an electron vacancy in the K-shell leads to the emission of a K-fluorescent x ray, which in turn has significant energy to either interact a large distance away from the initial photoelectric interaction site or escape the detector medium entirely.
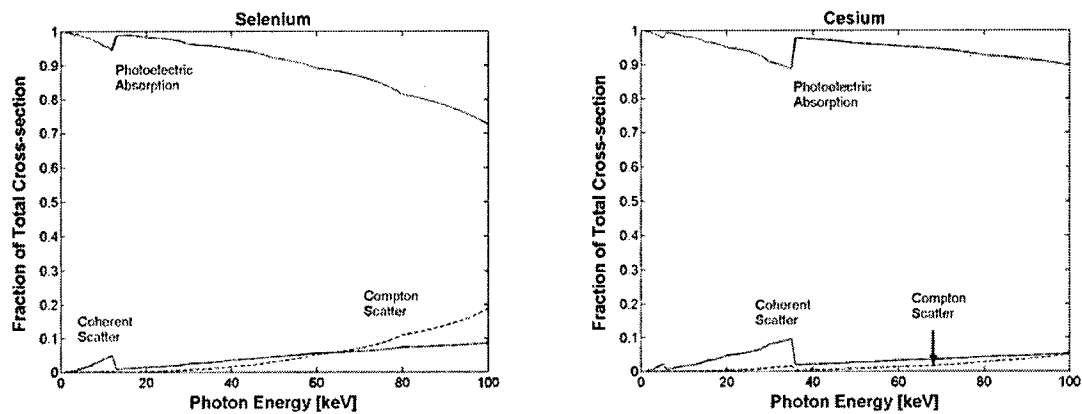
**Figure 1** *Relative probability of each x-ray interaction as a function of diagnostic x-ray energy for selenium and cesium*[8]

| Quantity | Selenium | Iodine | Cesium |
|---|---|---|---|
| K-fluorescent Yield [%] | 60 | 88 | 90 |
| K-edge Energy [keV] | 12.658 | 33.169 | 35.985 |
| Average K-fluorescent Energy [keV] | 11.858 | 30.451 | 32.977 |
| Average K-fluorescent Mean Free Path [μm] | 75.4 | 267.9 | 288.2 |

**Table 1** *Fluorescent relaxation data for selenium, iodine, and cesium*[11]

## 2.2 Rayleigh scatter

Rayleigh scatter involves an interaction of an incident x ray with all the electrons in the atom[9]. The electric field of the incident x ray causes these electrons to vibrate in synchrony, and subsequently, emit radiation that combine to form an x ray that departs the atom at an angle relative to the incident x ray. Large scatter angles occur at low x-ray energy and in high atomic number detector materials. Rayleigh scatter is referred to as an *elastic* (coherent) process because the departing x ray possesses the same energy as the incident x ray. Therefore, since the atom is neither excited nor ionized, no direct absorption of energy will result.

## 2.3 Compton scatter

Compton scatter involves a collision of an incident x ray with a 'loosely' bound electron[9,10]. The incident x ray is scattered, with reduced energy, at an angle with respect to the original direction. Some fraction of the incident x-ray energy is transferred to the electron, which recoils in a direction within the same plane as the scattered x ray. Large scatter angles for the x ray occur at low x-ray energy. In contrast to Rayleigh scatter, Compton scatter is referred to as an *inelastic* (incoherent) process because the scattered x ray does not retain the same energy as the incident x ray.

## 2.4 X-ray interactions and spatial resolution

Depending on the energy of the incident x ray and the physical properties of the detector material, the secondary radiation (i.e. scatter/fluorescence photons and charged particles) from the above interactions can significantly degrade spatial resolution. Loss of spatial resolution is attributed to the 'blurring' or 'spreading' of the incident energy away from the primary interaction site. The degree of spread depends not only on the energy of the secondary radiation, but the direction that the radiation is launched from the primary interaction site. Both of these factors ultimately affect whether the radiation is re-absorbed by the

detector material. The angle from which the radiation departs the primary interaction site is generally a complex function of radiation energy and detector composition (e.g. atomic number). Hence, Monte Carlo methods are required to properly simulate and isolate the effects of the x-ray interaction processes on spatial resolution.

In the diagnostic x-ray energy range, the kinetic energy of electrons produced in photoelectric or Compton interactions is low enough to assume that the deposition of energy essentially occurs at the primary interaction site (the range of electrons in typical detector media is on the order of 1–20 $\mu$m)[12]. Therefore, the main cause of spatial resolution degradation is attributed to the re-absorption of secondary x rays (the mean free path of K-fluorescent x rays is on the order of 100–300 $\mu$m)[13].

# 3. METHODS

## 3.1 Monte Carlo code and detector geometry

The latest version of the Electron Gamma Shower (EGSnrc) Monte Carlo code[14,15] was used to determine the absorbed energy distributions for diagnostic x rays incident on common x-ray converter materials. The user code DOSXYZnrc simulated the coupled photon-electron transport within a rectangular slab geometry and scored the amount of energy deposited within the detector volume for each photon history.

The modeled detector geometry, shown schematically in Fig. 2, consisted of an infinitesimal pencil beam of photons incident perpendicularly on a planar slab of x-ray converter material. Each slab was subdivided into 1025 x 1025 voxels, whereby each voxel had a planar area of 5 x 5 $\mu$m$^2$ (slab area of 0.5125 x 0.5125 cm$^2$). Two types of x-ray converter materials were modeled in our study: (i) amorphous selenium, and (ii) cesium iodide. Two different converter thicknesses for each material were considered that would be commonly found in existing digital x-ray detectors used in mammography and radiography (a-Se: 250 $\mu$m and 500 $\mu$m, CsI: 150 $\mu$m and 500 $\mu$m, respectively). The appropriate density for each converter was chosen to account for the physical nature of each material (a-Se: 4.20 g/cm$^3$, CsI: 4.51 g/cm$^3$).

## 3.2 Scoring the spatial distribution of absorbed energy

Monte Carlo simulations were used to generate dose deposition maps, d(x,y), which represent the two-dimensional spatial distribution of energy absorbed within the detector material. These maps form the basis of the two-dimensional point spread function (PSF), p(x,y), when normalized to unit area (see Eqn. 1).

$$p(x,y) = \frac{d(x,y)}{\iint d(x,y)\,dx\,dy}$$ 

(1)

Dose deposition maps were determined for each x-ray converter material at several monoenergetic x-ray energies, ranging from 5 keV to 100 keV, in approximately 5 keV intervals. These energies adequately represent the different energies encountered in mammography and radiography x-ray spectra. Each Monte Carlo run simulated the transport of ten million x-ray histories, which was sufficient to reduce the statistical uncertainty in the dose deposition maps to less than 1% in voxels with dose values within two orders of magnitude of the maximum value.

## 3.3 Modulation transfer function

The modulation transfer function (MTF) is an important objective measure of the spatial resolution in an imaging system. Due to the inherent azimuthal symmetry in the dose deposition maps, the PSF was transformed into a one-dimensional radial profile, p(r). Therefore, based on p(r), the modulation transfer function, MTF(u), was calculated using the zero-order Hankel transform[16] (see Eqn. 2). As a reminder, the
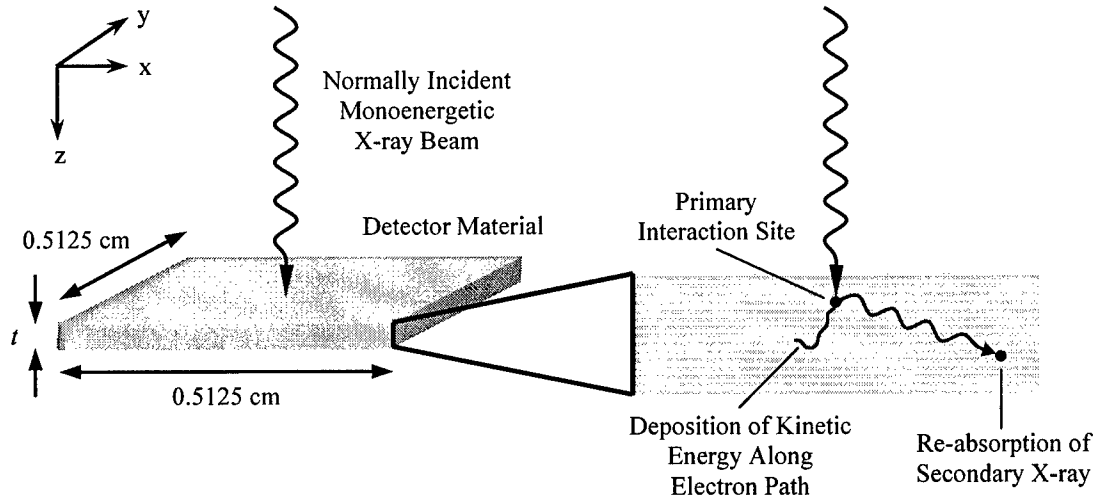
**Figure 2** *Detector geometry modeled in the Monte Carlo simulations. Two different thicknesses, t, for each detector material were used (a-Se: 250 and 500 μm, CsI: 150 and 500 μm).*

MTF calculated from the Monte Carlo simulations only represents contributions from the spread of energy from fundamental x-ray interactions.

$$MTF(u) = 2\pi \int_0^\infty p(r) J_0(2\pi ur) r\, dr \qquad (2)$$

### 3.4 Equivalent passband

Representation of the spatial-frequency-dependence of the MTF and the x-ray energy dependence of the x-ray interaction processes for a given detector material requires an appropriate figure of merit for grading the spatial resolution. We chose to use the 50% MTF frequency, $f_{50}$, and the one-dimensional equivalent passband[17], $N_e$. In our opinion, the equivalent passband is a more robust parameter because it represents the area under the squared MTF over all spatial frequencies (see Eqn. 3). In other words, the shape of the MTF is implicitly incorporated into the equivalent passband figure of merit.

$$N_e = \int_{-\infty}^\infty MTF^2(u)\, du \qquad (3)$$

Since in our case the MTF is an even function, the equivalent passband can be re-written (see Eqn. 4).

$$N_e = 2 \int_0^\infty MTF^2(u)\, du \qquad (4)$$

In practice, the MTF cannot be determined to infinite frequency, so we choose to integrate the squared MTF up to the first zero crossing frequency, $f_1$ (see Eqn. 5). This is a valid assumption because most of the area (over 90%) under the squared MTF occurs within the first lobe.

$$N_e = 2 \int_0^{f_1} MTF^2(u)\, du \qquad (5)$$

### 3.5 Comparison with experimental data

To assess the impact of the fundamental spatial resolution limits on existing amorphous selenium and cesium iodide detectors, a comparison of modulation transfer functions was made between results of Monte Carlo simulations and published experimental measurements. Additional Monte Carlo simulations were needed to match the imaging conditions listed in Table 2. In the simulations, the incident x-ray energy was chosen to be half the maximum x-ray energy in the experimental spectra.

| Imaging Task | Detector Material | X-ray Beam Quality [kVp] | Detector Thickness [µm] | Detector Element Size [µm] | Nyquist Frequency [mm⁻¹] |
|---|---|---|---|---|---|
| Mammography | a-Se [18] | 28 | 200 | 85 | 5.88 |
| | CsI [20,22] | 28 | 146 | 100 | 5.00 |
| Radiography | a-Se [19] | 70 | 300 | 134* | 3.73 |
| | CsI [21,22] | 80 | 350 | 200 | 2.50 |

**Table 2** *Parameter summary of published imaging systems based on amorphous selenium (Rowlands group) and cesium iodide (Granfors group) detectors. The asterisk indicates an approximate size for the asymmetric detector element.*

The experimental MTFs reported in the literature represent pre-sampled values, while the MTFs ($MTF_{int}$) from Monte Carlo simulations represent only the contribution from x-ray interactions. In order to allow for comparison with experimental results, $MTF_{int}$ must be adjusted to account for the digital nature of the existing detectors. The Monte Carlo pre-sampling MTF ($MTF_{pre}$) is obtained including the aperture effect due to the real detector element size ($a_{del}$) (see Eqn. 6).

$$MTF_{pre}(u) = MTF_{int}(u) \times sinc(\pi a_{MC} u) \tag{6}$$

The Monte Carlo pre-sampling MTF does not include the effect of optical light scatter in CsI and other effects that might degrade the MTF further.

## 4. RESULTS AND DISCUSSION

### 4.1 Interaction MTFs for amorphous selenium and cesium iodide

The Monte Carlo "interaction" modulation transfer functions for amorphous selenium and cesium iodide are shown in Figs. 3 and 4 respectively. In each figure, two different x-ray energy ranges and detector thickness are presented characteristic of mammography and radiography. Furthermore, only a select number of MTFs (each based on a single monoenergetic x-ray energy) are plotted to highlight the changing influence of the x-ray interactions at each x-ray energy. Table 3 summarizes the primary cause(s) that limit each MTF in Figs. 3 and 4.

| Detector Material | X-ray Energy [keV] | Main Cause of MTF Degradation |
|---|---|---|
| Amorphous Selenium | 10 | • re-absorption of L-fluorescent and coherent scatter x rays |
| | 13 | • re-absorption of K-fluorescent x rays |
| | 30 | • re-absorption of K-fluorescent x rays |
| | 100 | • re-absorption of Compton scatter x rays and deposition of photoelectron kinetic energy |

| Detector Material | X-ray Energy [keV] | Main Cause of MTF Degradation |
|---|---|---|
| Cesium Iodide | 20 | • re-absorption of L-fluorescent and coherent scatter x rays |
| | 36 | • re-absorption of K-fluorescent x rays |
| | 60 | • re-absorption of K-fluorescent x rays |
| | 100 | • re-absorption of K-fluorescent x rays and deposition of photoelectron kinetic energy |

**Table 3** *Summary of the main physical effects limiting the interaction MTF at selected x-ray energies in amorphous selenium (Fig. 3) and cesium iodide (Fig.4).*

Below the K-edges of a-Se (12.66 keV) and CsI (35.99 keV), the main cause for the drop in the MTF is associated with: (i) the re-absorption of coherent scatter x rays within the spatial frequency range of 0 to 20 cycles/mm, and (ii) the re-absorption of L-fluorescent x rays above 20 cycles/mm. Immediately above the K-edges of a-Se and CsI, the low-frequency (0 – 5 cycles/mm) drop in the MTF is associated with the re-absorption of K-fluorescent x rays. As x-ray energy increases above the K-edge, the magnitude of the low-frequency drop is reduced. The reason for the reduction is attributed to the photoelectron progressively gaining and depositing more energy close to the primary interaction site relative to the amount of energy re-absorbed by characteristic radiation elsewhere. At an x-ray energy of 100 keV, the low-frequency drop in the MTF reaches a minimum, but a dramatic fall-off in the MTF occurs at high spatial frequency (10 to 40 cycles/mm). The latter high-frequency fall-off is attributed to: (i) the re-absorption of Compton scatter x rays (Compton scatter represents 20% of the x-ray interactions at 100 keV) and deposition of photoelectron kinetic energy (~50 μm range for 87 keV electrons) in a-Se, and (ii) the deposition of photoelectron kinetic energy (~35 μm range for 65 keV electrons) in CsI.

In addition, an increase in detector thickness for both detector materials leads to only a modest drop in the MTF at any given x-ray energy due to a higher probability of re-absorbing secondary radiation that has spread from the primary x-ray interaction site.
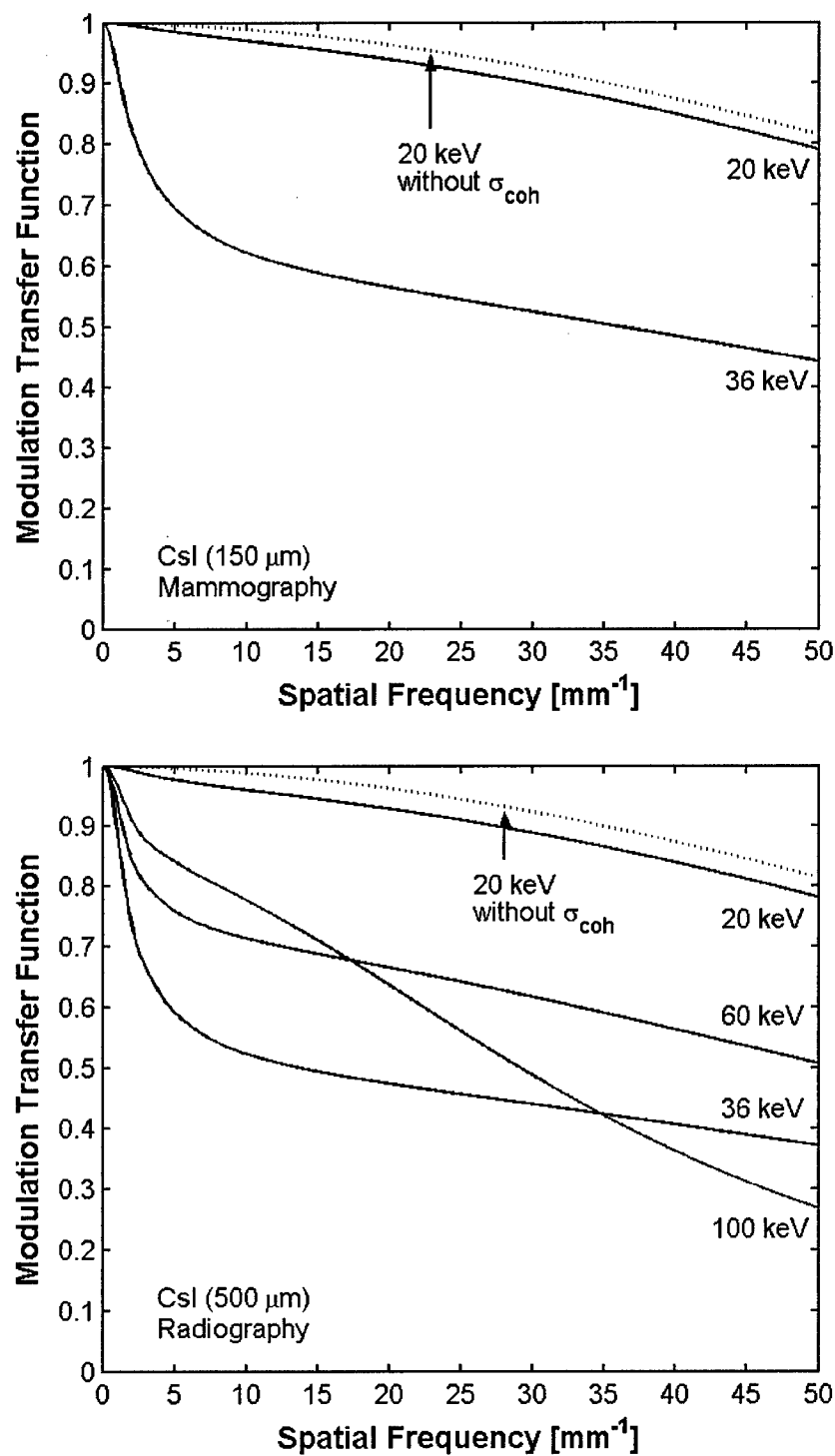
### 4.2 Spatial resolution versus x-ray energy

To clearly quantify the fundamental limitations of the x-ray interactions on spatial resolution, we combine the spatial frequency-dependence of the modulation transfer function with the energy-dependence of the x-ray interactions. As seen in Figs. 5 and 6, fundamental curves based on the 50% MTF frequency, $f_{50}$, and equivalent passband, $N_e$, have been plotted for both amorphous selenium and cesium iodide as a function of incident x-ray energy. Each figure has data for a thickness of x-ray converter material representative of the imaging task (i.e. mammography or radiography).

Each detector material in Figs. 5 and 6 exhibits a unique spatial-frequency *versus* x-ray energy profile. The peaks and valleys in each profile indicate the magnitude of effect that a single or combination of x-ray interactions have on spatial resolution. In these profiles, a low ordinate value reflects a poor spatial resolution, while the opposite is true for a high ordinate value. Since the trend in the mammography profiles (Fig. 5) resemble those in the radiography profiles (Fig. 6), then for brevity, we only discuss the latter over the larger x-ray energy range.

In amorphous selenium, the $f_{50}$ and $N_e$ profiles: (i) drop 25% and 45% respectively at the K-edge, (ii) steadily recover after the K-edge, peaking at an x-ray energy of 35 keV, and (iii) finally drop to 70% and 60% respectively of the post K-edge peak values at 100 keV. While, in cesium iodide, the $f_{50}$ and $N_e$ profiles: (i) drop 85% and 75% respectively at the K-edge, (ii) steadily recover after the K-edge, peaking at an x-ray energy of 60 keV, and (iii) finally drop to 40% and 33% respectively of the post K-edge peak values at 100 keV. The x-ray interactions responsible for the shape of these profiles has already been discussed in the last section (Sec. 4.2).
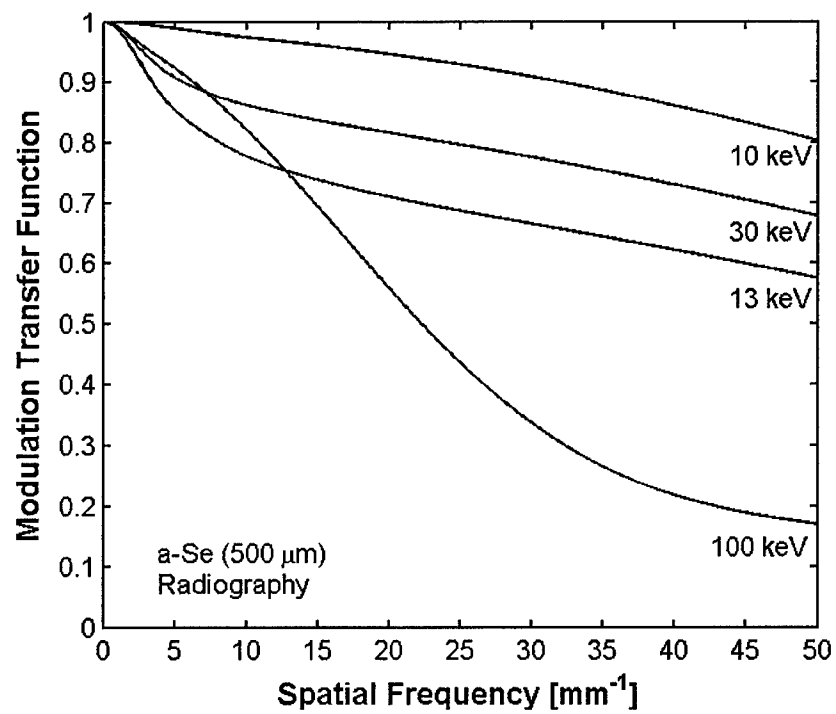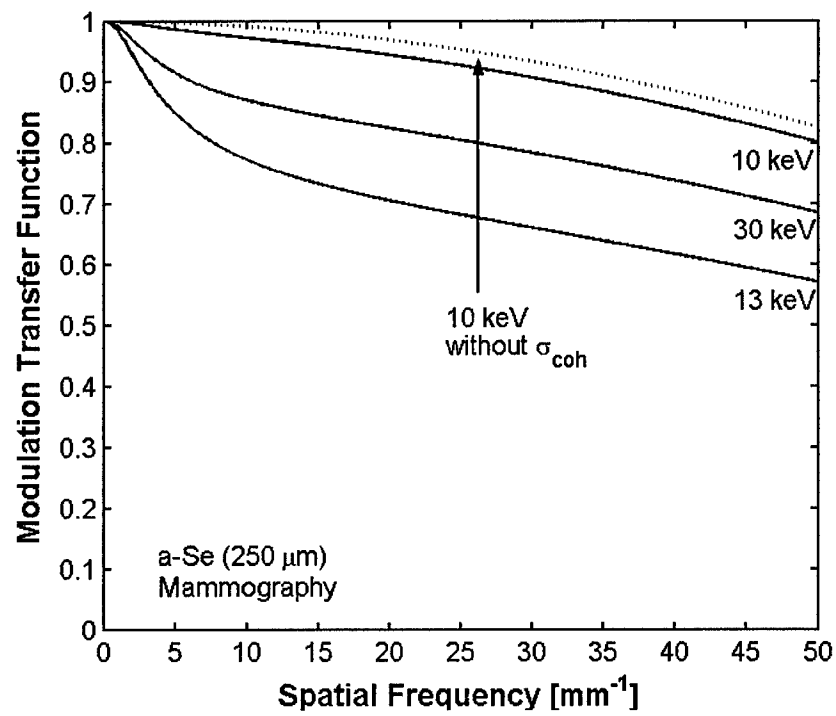
**Figure 3** *Monte Carlo interaction MTFs at selected x-ray energies for two different thicknesses of a-Se*
*($\sigma_{coh}$ ≡ coherent scatter).*

**Figure 4** *Monte Carlo interaction MTFs at selected x-ray energies for two different thicknesses of CsI*
*($\sigma_{coh} \equiv$ coherent scatter).*
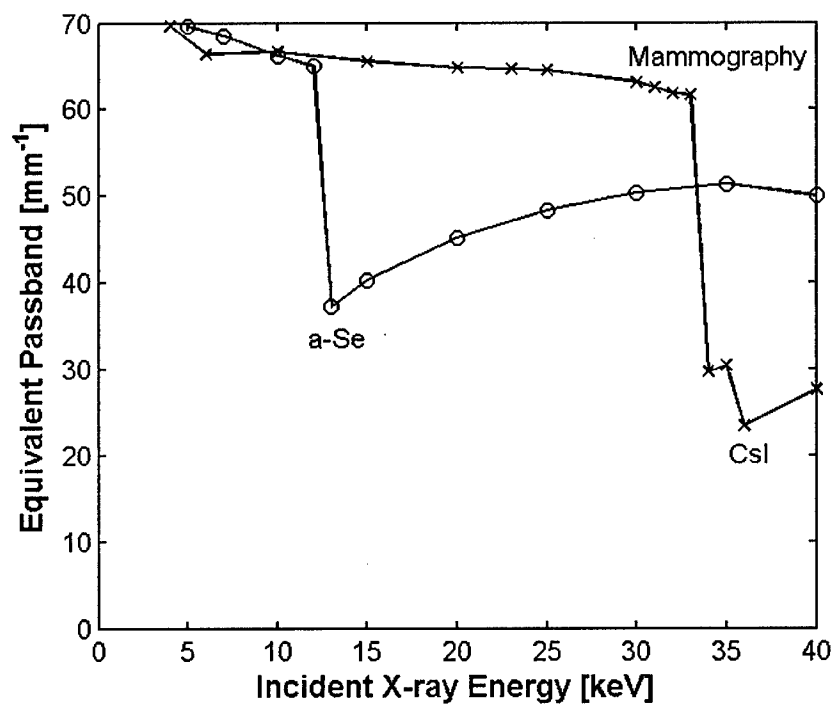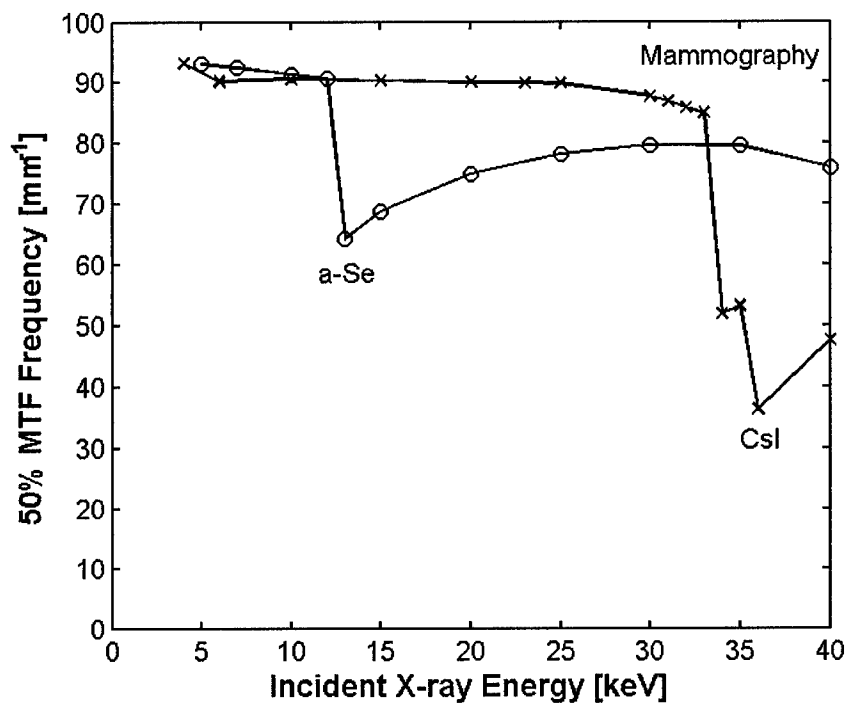
**Figure 5** *Spatial resolution performance, expressed as 50% MTF frequency and equivalent passband, as a function of x-ray energy typical in mammography for both amorphous selenium and cesium iodide detectors. Each point represents a single Monte Carlo simulation.*
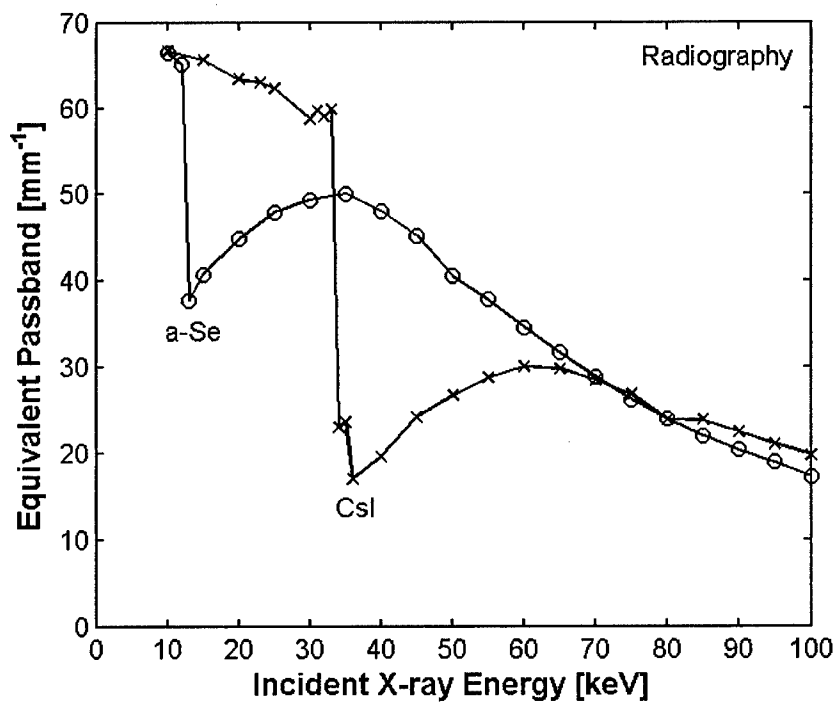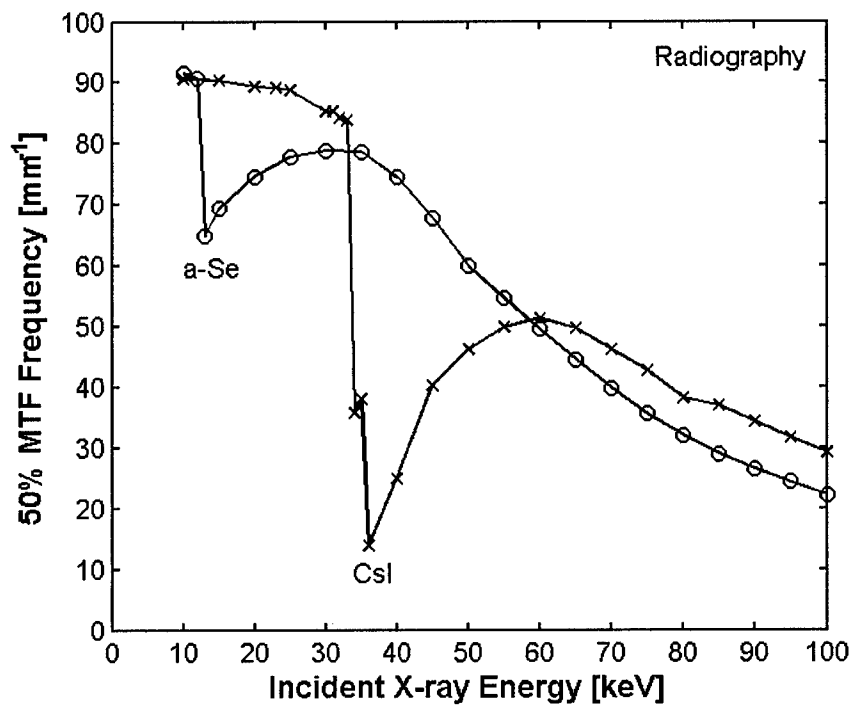
**Figure 6** *Spatial resolution performance, expressed as 50% MTF frequency and equivalent passband, as a function of x-ray energy typical in radiography for both amorphous selenium and cesium iodide detectors. Each point represents a single Monte Carlo simulation.*
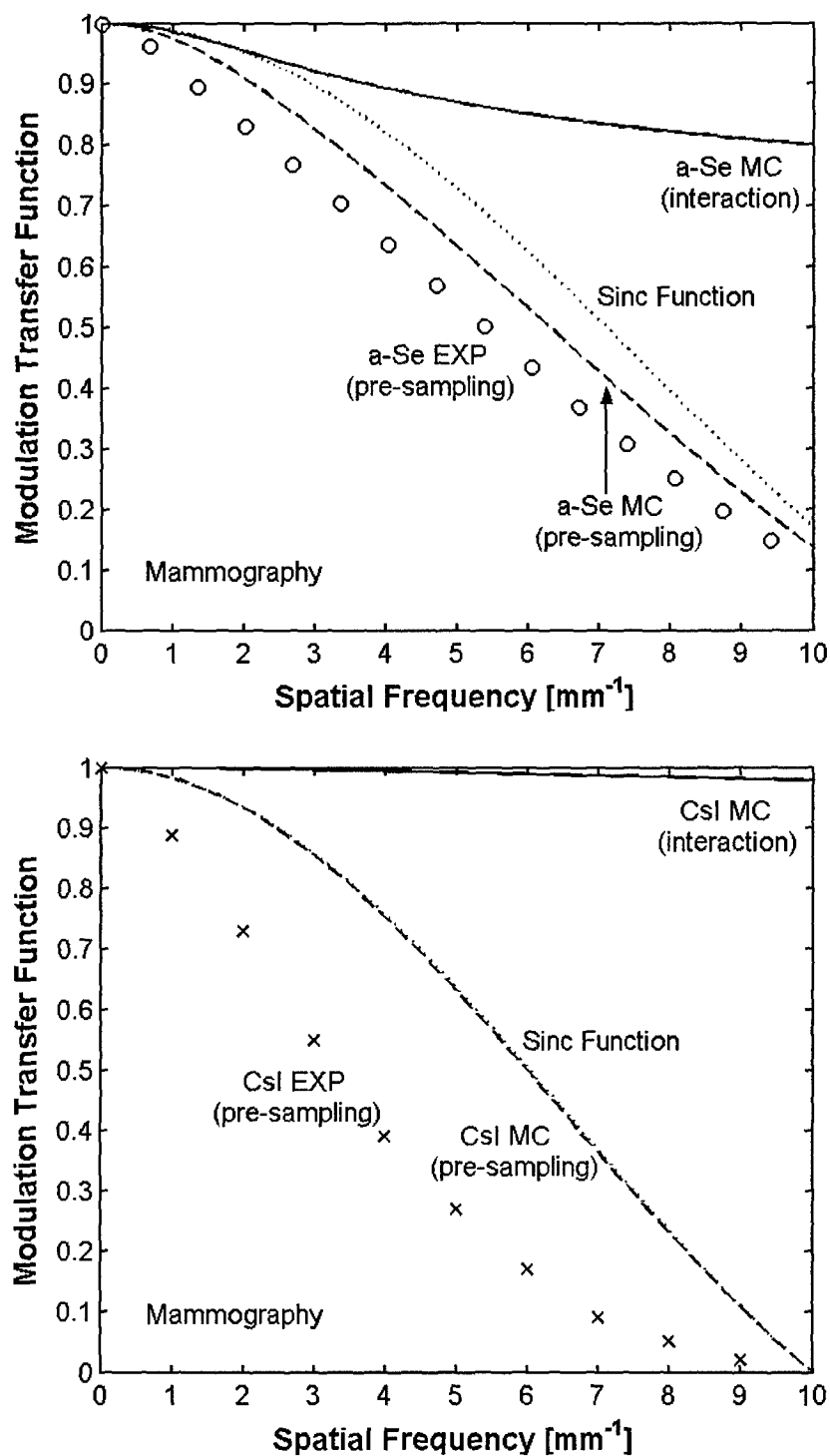
**Figure 7** *Comparison between Monte Carlo (MC) (dashed line) and experimental (EXP) (circles & crosses) pre-sampling MTFs for amorphous selenium (Ref. 18) and cesium iodide (Ref. 20) detectors used in mammography. Also shown are the MC x-ray interaction MTF (solid line) and the sinc aperture function (dotted line). See Table 2 for imaging system parameters.*
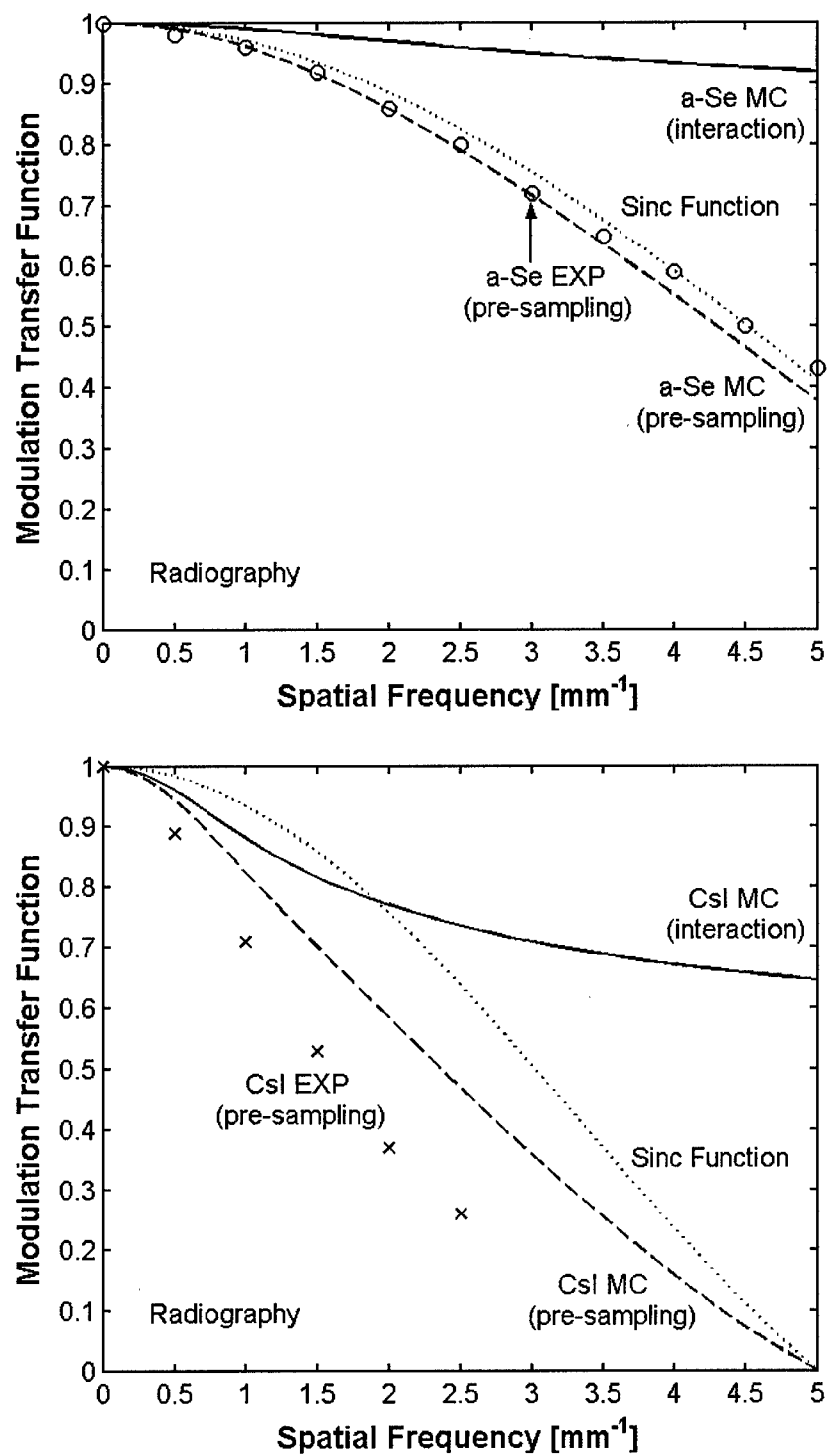
**Figure 8** *Comparison between Monte Carlo (MC) (dashed line) and experimental (EXP) (circles & crosses) pre-sampling MTFs for amorphous selenium (Ref. 19) and cesium iodide (Ref. 20) detectors used in radiography. Also shown are the MC x-ray interaction MTF (solid line) and the sinc aperture function (dotted line). See Table 2 for imaging system parameters.*

## 4.3 Pre-sampling MTFs – comparison with experiment data

Figs. 7 and 8 compare the interaction and pre-sampling MTFs ($MTF_{int}$ and $MTF_{pre}$ respectively) from Monte Carlo (MC) simulations to those ($MTF_{pre}$) from experimental measurements found in the literature, for both amorphous selenium and cesium iodide detectors used in mammography and radiography. Also shown is the sinc aperture function, which accounts for the effect of integrating quanta over a square, finite-size detector element.

In the mammography case (Fig. 7), the MC $MTF_{int}$ for cesium iodide is 18% *higher* than the MC $MTF_{int}$ for amorphous selenium at 10 cycles/mm. The effect of K-fluorescent x ray re-absorption, which is present in a-Se and absent in CsI in the mammography energy range, accounts for the better interaction MTF in CsI. The MC and experimental pre-sampling MTFs for a-Se differ by approximately 5 to 10 percent over the spatial frequency range from 0 to 10 cycles/mm. While for CsI, the experimental $MTF_{pre}$ is 10 to 40 percent lower than the MC $MTF_{pre}$ from 1 to 9 cycles/mm. The disagreement in the experimental pre-sampling MTFs for a-Se and CsI can be generally related to the charge trapping in the blocking layer of the photoconductor, and the optical light scattering within the phosphor respectively.

In the radiography case (Fig. 8), the MC $MTF_{int}$ for cesium iodide is now 25% *lower* than the MC MTF for amorphous selenium at 5 cycles/mm. The better interaction MTF in a-Se is due to the location of K-fluorescent x ray re-absorption being more distant in CsI because of the greater energy of these x rays in CsI than a-Se. The MC $MTF_{pre}$ for a-Se coincides very well with the experimental result (i.e. limited by the detector element size), while for CsI, the experimental $MTF_{pre}$ is 20% lower than the MC $MTF_{pre}$ at 2.5 cycles/mm. Again, the discrepancy between the experimental and MC pre-sampling MTFs for CsI is due to optical light dispersion. More importantly, at low spatial frequency between 0 to 2 cycles/mm, the interaction MTF falls off more rapidly than the sinc function, which suggests that any reduction in detector element size will not affect the contrast transfer of large-scale objects, for CsI detectors operating near the K-edge.

## 5. CONCLUSIONS

We have used Monte Carlo simulations to determine the fundamental spatial distribution of absorbed energy within two common digital detector materials, amorphous selenium and cesium iodide, in order to quantify the fundamental spatial resolution limits in each detector. Each detector material possesses a unique spatial-frequency *versus* x-ray energy profile that provides insight into which x-ray interaction(s) limit spatial resolution within a given x-ray energy range. Within the mammography and radiography energy range, existing amorphous selenium and cesium iodide detectors operate far from fundamental spatial resolution limits. Ignoring charge trapping effects in a-Se and optical light spreading in CsI, any further reduction in detector element size will potentially improve spatial resolution in these x-ray converter materials.

## ACKNOWLEDGEMENTS

## REFERENCES

1.  M.J. Yaffe and J.A. Rowlands, "X-ray detectors for digital radiography", *Phys. Med. Biol.* **42**, 1-39 (1997).

2. J.A. Rowlands and J. Yorkston, "Flat panel detectors for digital radiography", in *Handbook of Medical Imaging Volume 1: Physics and Psychophysics* (ed. J. Beutel, H.L. Kundel, and R.L. van Metter), SPIE Press, Bellingham, WA, 2000.

3. M.J. Yaffe, "Digital Mammography", in *Handbook of Medical Imaging Volume 1: Physics and Psychophysics* (ed. J. Beutel, H.L. Kundel, and R.L. van Metter), SPIE Press, Bellingham, WA, 2000.

4. D.W. Holdsworth and M.M. Thornton, "Micro-CT in small animal and specimen imaging", *Trends in Biotechnology* **20**, S34-S39 (2002).

5. W. Que and J.A. Rowlands, "X-ray imaging using amorphous selenium: Inherent spatial resolution", *Med. Phys.* **22**, 365-374 (1995).

6. W. Zhao, W.G. Ji, and J.A. Rowlands, "Effects of characteristic x-rays on the noise power spectra and detective quantum efficiency of photoconductive x-ray detectors", *Med. Phys.* **28**, 2039-2049 (2001).

7. J.M. Boone, J.A. Seibert, J.M. Sabol, and M. Tecotzky, "A Monte Carlo study of x-ray fluorescence in x-ray detectors", *Med. Phys.* **26**, 905-916 (1999).

8. M.J. Berger, J.H. Hubbell, and S.M. Seltzer, "XCOM: Photon cross sections database", *Report NBSIR* **87-3597**, National Institute of Standards and Technology, 1999.

9. H.E. Johns and J.R. Cunningham, *The Physics of Radiology*, Thomas, Springfield, 1983.

10. F.H. Attix, *Introduction to Radiological Physics and Radiation Dosimetry*, Wiley, New York, 1986.

11. W.H. McMaster, N.K. Del Grande, J.R. Mallett, and J.H. Hubbell, "Compilation of x-ray cross-sections", *Report UCRL*-**50174**, Section 11, Rev. 1, Univ. of California, Livermore, 1969.

12. M.J. Berger, J.S. Coursey, and M.A. Zucker, "ESTAR: Stopping-power and range tables for electrons", *Report NISTIR* **4999**, National Institute of Standards and Technology, 2000.

13. J.H. Hubbell, and S.M. Seltzer, "Tables of x-ray mass attenuation coefficients and mass energy-absorption coefficients", *Report NBSIR* **5632**, National Institute of Standards and Technology, 1999.

14. I. Kawrakow, "Accurate condensed history Monte Carlo simulation of electron transport. I: EGSnrc, the new EGS4 version", *Med. Phys.* **27**, 485-498 (2000).

15. D.W.O. Rogers, B.A. Faddegon, G.X. Ding, C.-M. Ma, J. We, and T.R. Mackie, "BEAM: a Monte Carlo code to simulate radiotherapy treatment units", *Med. Phys.* **22**, 503-524 (1995).

16. H.H. Barrett and W. Swindell, *Radiological Imaging*, Academic, New York, 1981.

17. R.F. Wagner, K.E. Weaver, E.W. Denny, and R.G. Bostrom, "Toward a unified view of radiological imaging systems. Part I: Noiseless images", *Med. Phys.* **1**, 11-24 (1974).

18. W. Zhao, W.G. Ji, J.A. Rowlands, and A. Debrie, "Investigation of imaging performance of amorphous selenium flat-panel detectors for digital mammography", *Proc. SPIE* **4320**, 536-546 (2001).

19. W. Zhao, I. Blevis, S. Germann, J.A. Rowlands, D. Waechter, and Z. Huang, "Digital radiology using active matrix readout of amorphous selenium: Construction and evaluation of a prototype real-time detector", *Med. Phys.* **24**, 1834-1843 (1997).

20. S. Vedantham, A. Karellas, S. Suryanarayanan, D. Albagli, S. Han, J.E. Tkaczyk, C.E. Landberg, P.R. Granfors, I. Levis, C.J. D'Orsay, and R.E. Hendricks, "Full breast digital mammography with an amorphous silicon based flat panel detector: Physical characteristics of a clinical prototype", *Med. Phys.* **27**, 558-567 (2000).

21. P.R. Granfors and R. Aufrichtig, "Performance of a 41 x 41 cm² amorphous silicon flat panel x-ray detector for radiographic imaging applications", *Med. Phys.* **27**, 1324-1331 (2000).

22. J.A. Rowlands and W.G. Ji, "Effect of depth dependent modulation transfer function and K-fluorescence re-absorption on the detective quantum efficiency of indirect conversion flat panel x-ray imaging systems using CsI", *Proc. SPIE* **4320**, 257-267 (2001).

# Can a Fourier-Based Cascaded-Systems Analysis Describe Noise in Complex Shift-Variant Spatially Sampled Detectors?

I.A. Cunningham, M. Sattarivand, G. Hajdok and J. Yao

Imaging Research Laboratories, Robarts Research Institute, and
University of Western Ontario, London, Ontario, Canada

## ABSTRACT

Cascaded-systems analyses have been used successfully by many investigators to describe signal and noise transfer in quantum-based x-ray detectors in medical imaging. However, the Fourier-based linear-systems approach is only valid when assumptions of linearity and shift invariance are satisfied. Digital detectors, in which a bounded image signal is spatially integrated in discrete detector elements, are not shift invariant in their response. In addition, many detectors make use of fiber optics or structured phosphors such as CsI to pass light to a photodetector both of which have a shift-variant response. These issues raise serious concerns regarding the validity of Fourier-based approaches for describing the signal and noise performance of these detectors.

We have used a Monte Carlo approach to compare the image Wiener noise power spectrum (NPS) with that predicted using a Fourier-based approach when these assumptions fail. It is shown that excellent agreement is obtained between Monte Carlo results and those obtained using a Fourier-based wide-sense cyclostationary analysis, including the description of noise aliasing. A simple model of a digital detector coupled to a fiber optic bundle is described using a novel cascaded cyclostationary approach in which image quanta are integrated over fiber elements and then randomly re-distributed at the fiber output. While the image signal sometimes contains significant non-stationary beating artifacts, the Monte Carlo results generally show good agreement with Fourier models of the NPS when noise measurements are made over a sufficiently large region of interest.

Key words: flat panel detectors, cascaded models, noise power spectrum, detective quantum efficiency

## 1. INTRODUCTION

Cascaded models are used widely to describe both signal and noise properties of quantum-based medical imaging systems.[3] These Fourier-based methods[4, 12, 13] can be used to describe noise properties in terms of transfer of the Wiener Noise Power Spectrum (NPS) from input to output, and signal properties in terms of system gain and the modulation transfer function (MTF).[5, 7–10] There are two important assumptions that must be satisfied for any Fourier-based method: the imaging system must have a (i) linear and (ii) shift-invariant response. Linearity is generally not a great problem, as most imaging systems either produce a linear signal (that is the average output digital values scale with the average number of incident x-ray quanta per unit area) over a useful range or the output signal is sufficiently reproducible that it can be linearized. Shift invariance is more of a problem with digital imaging

systems. For example, the size of detector elements (sometimes called "del"s) in a detector array may be sufficiently large to introduce a "pixelated" appearance in the images. In addition, image detectors have finite size and hence all images are spatially bounded, another form of shift variance. In spite of these limitations, Fourier-based methods have enjoyed much success and popularity in describing the performance of many digital imaging systems.

Fourier-based descriptions of image noise also require assumptions of wide-sense stationarity (WSS).[11] This requires that the incident x-ray beam be approximately uniform over the entire image area and is sometimes called the 'low-contrast" assumption. This means that Fourier-based methods only describe image noise in images having only low-contrast structures. While this may appear to be a significant limitation, image noise is generally a limiting factor only for low-contrast detection tasks, and there is an implicit assumption that a description of low-contrast performance is a representative measure of system performance.

Digital detectors act to spatially integrate the image quanta that interact in each detector element, resulting in a spatial "binning" and sampling of image quanta. This has the effect of introducing a "pixelated" appearance to image noise, and as such is no longer WSS. However, binned and sampled WSS noise is wide-sense cyclostationary (WSCS),[11] since the mean and correlation function are invariant to shifts of multiples of the detector-element spacing. Fourier methods can also be applied to WSCS noise processes, giving rise to what is popularly referred to as noise aliasing.

Figure 1 illustrates a hypothetical detector design with an additional wrinkle - a scintillating phosphor coupled to a digital detector array by a fiber-optic bundle. This system consists of two cascaded sampling processes, what we call a "doubly-sampled" design. The first sampling process is a consequence of the fibre-optic bundle while the second is due to the digital detector array. As described in the next section, this results in a cascade of two binning and sampling process.

As a result of binning and sampling by the fiber optic bundle, noise associated with the distribution of light quanta incident on the digital detector array in this system is WSCS rather than WSS. It is therefore expected that the mismatch between size and alignment of the fibers with the detector elements will give rise to interference and beating artifacts. In many cases, the width of optical fibers
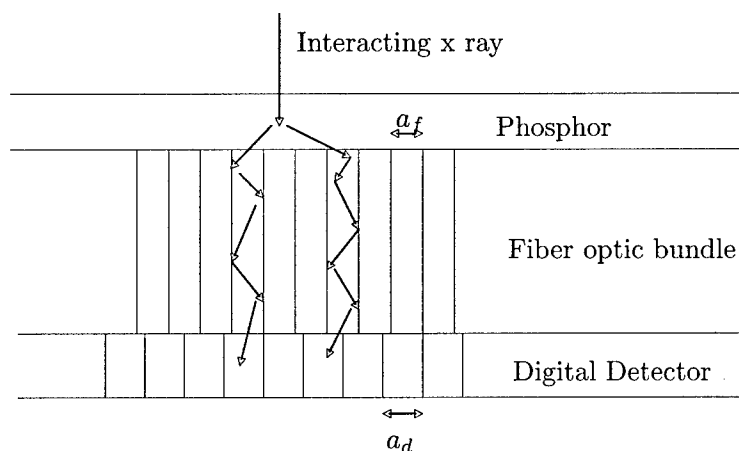
**Figure 1.** Schematic of a simple "double-sampled" digital detector consisting of a phosphor, fiber optic bundle (uniformly spaced fibers having width $a_f$ and pitch $x_f$) and a digital detector array (elements having width $a_d$ and pitch $x_d$). This "doubly sampled" situation occurs as the result of the cascade of these two binning and sampling processes.

is small compared to that of the detector elements and the effect of optical binning in the fibers can be ignored. However, with an ongoing demand for increased spatial resolution detectors (e.g. for mammography and small-animal imaging), we are reaching the point at which the fiber and detector-element sizes may be comparable. In addition, this "doubly sampled" problem exists in many other detector designs such as structured phosphors etc.

There is no reason to believe that Fourier-based theories will be directly applicable to doubly-sampled systems - their images will contain non-stationary noise and noise-related artifacts that may be difficult to predict and quantify. The purpose of this paper is to examine the successes and failings of Fourier-based methods to avoid misplaced confidence and/or naive application of these tools.

## 2. METHODS

The system illustrated in Fig. 1 is a simple doubly-sampled cascaded system and is used for the purposes of assessing the Fourier approach. A cascaded model of signal and noise transfer is developed and used to determine theoretical expressions of the modulation transfer function (MTF), Wiener noise-power spectrum (NPS), noise-equivalent number of quanta (NEQ) and detective quantum efficiency (DQE). In addition, a Monte Carlo model of the same system is developed and used to make numerical estimates of the MTF, NPS, NEQ and DQE. The theoretical and Monte Carlo results are compared and used as the basis of validation of the theoretical results. It is not intended that this model describe any particular imaging system. Rather, it is intended to use this model as a hypothetical doubly-sampled system and to determine how the Fourier-based metrics fail when applied to such a system.

### 2.1. Fourier-Based Cascaded Model

Figures 2 - 4 illustrate the cascade of processes required to represent this simple system. The physical meaning of each process (and associated units) is described in the first column. The second column shows a graphical illustration and mathematical expression of each process. These are generally random processes and the third column gives the associated NPS where applicable. At each step, the overhead tilde ($\sim$) indicates a random variable and the dagger ($\dagger$) superscript indicates a detector digital value represented as a scaled $\delta$ function. One-dimensional geometry is used for simplicity, but the results are directly applicable to the two-dimensional case as well.
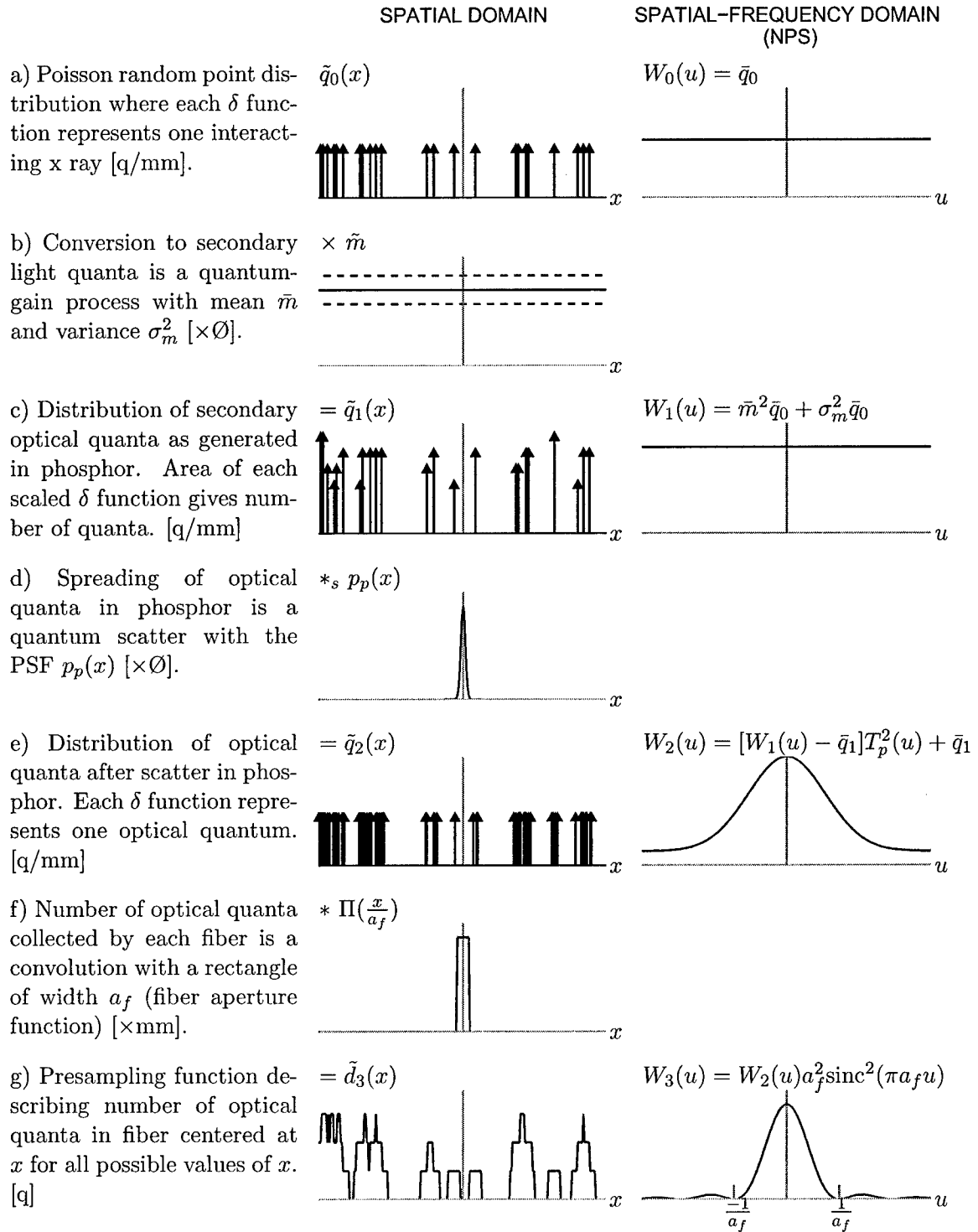
The input to the cascaded model is the random variable $\tilde{q}_0(x)$ (Fig. 2a), a uniform, Poisson-distributed, random point process, with each Dirac $\delta$ function describing the location of an interacting x-ray quantum:

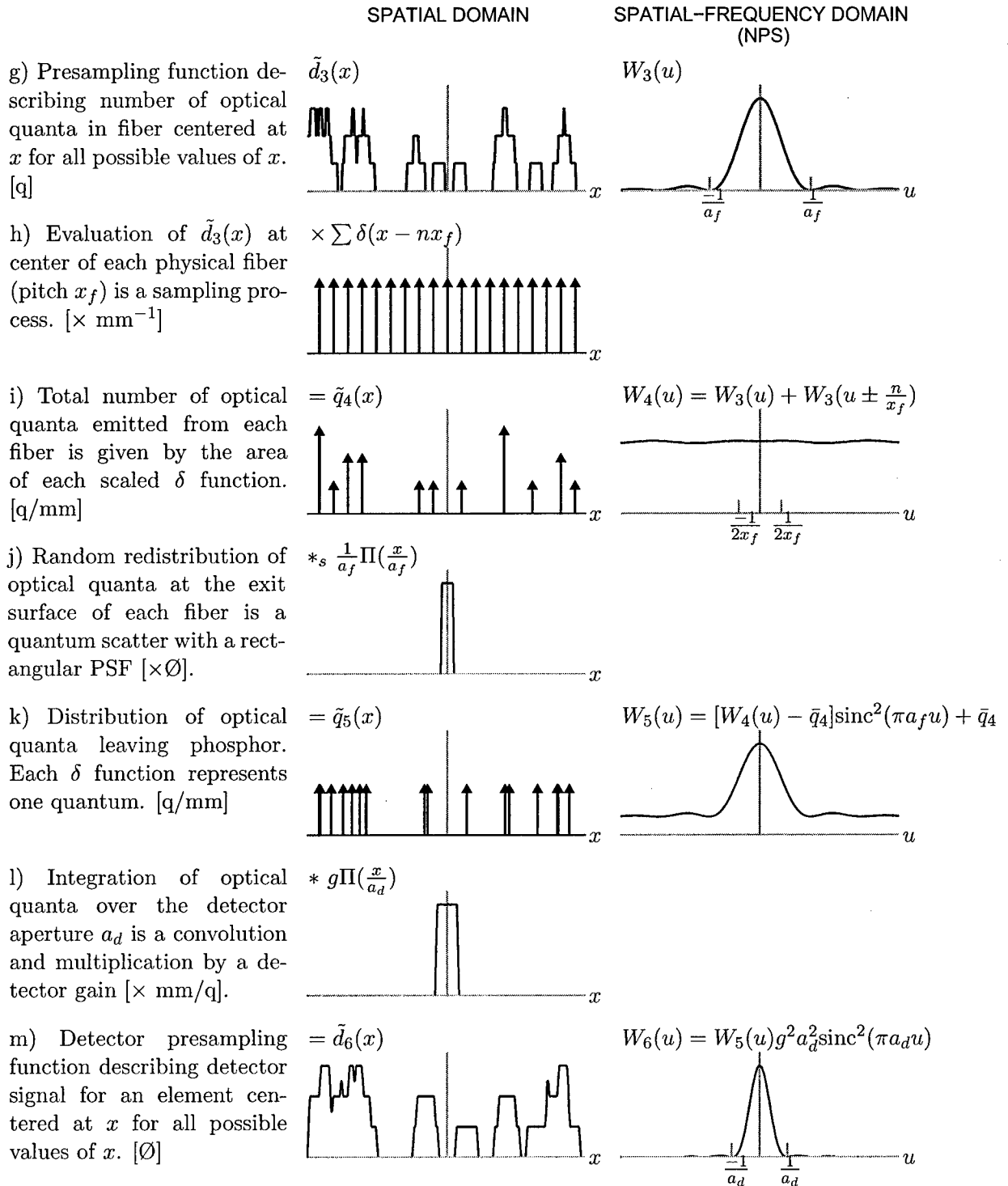$$\tilde{q}_0(x) = \sum_{i=1}^{\tilde{N}} \delta(x - \tilde{x}_i) \tag{1}$$

where $\tilde{N}$ is a random variable describing the total number of quanta and $\tilde{x}_i$ is a random variable describing the spatial position of the $i$th quantum. Each $\delta$ function in this example has units mm$^{-1}$. They are generalized functions and distribution theory[11] must be used to describe these distributions. The Wiener NPS of this distribution is given by $W_0(u) = \bar{q}_0$.[2]

### 2.1.1. Conversion to Light in Phosphor

Each interacting x ray produces $\tilde{m}$ secondary optical quanta in the phosphor, where $\tilde{m}$ is a random variable with mean $\bar{m}$ and variance $\sigma_m^2$. The result is a random distribution of optical quanta $\tilde{q}_1(x)$ as illustrated in Fig. 2c. Note that this distribution is "marked" - that is, the secondary quanta are all

SPATIAL DOMAIN          SPATIAL–FREQUENCY DOMAIN
(NPS)

a) Poisson random point distribution where each $\delta$ function represents one interacting x ray [q/mm].

$\tilde{q}_0(x)$

$W_0(u) = \bar{q}_0$

b) Conversion to secondary light quanta is a quantum-gain process with mean $\bar{m}$ and variance $\sigma_m^2$ [$\times\varnothing$].

$\times\ \tilde{m}$

c) Distribution of secondary optical quanta as generated in phosphor. Area of each scaled $\delta$ function gives number of quanta. [q/mm]

$= \tilde{q}_1(x)$

$W_1(u) = \bar{m}^2\bar{q}_0 + \sigma_m^2\bar{q}_0$

d) Spreading of optical quanta in phosphor is a quantum scatter with the PSF $p_p(x)$ [$\times\varnothing$].

$*_s\ p_p(x)$

e) Distribution of optical quanta after scatter in phosphor. Each $\delta$ function represents one optical quantum. [q/mm]

$= \tilde{q}_2(x)$

$W_2(u) = [W_1(u) - \bar{q}_1]T_p^2(u) + \bar{q}_1$

f) Number of optical quanta collected by each fiber is a convolution with a rectangle of width $a_f$ (fiber aperture function) [$\times$mm].

$*\ \Pi\!\left(\frac{x}{a_f}\right)$

g) Presampling function describing number of optical quanta in fiber centered at $x$ for all possible values of $x$. [q]

$= \tilde{d}_3(x)$

$W_3(u) = W_2(u)a_f^2\mathrm{sinc}^2(\pi a_f u)$
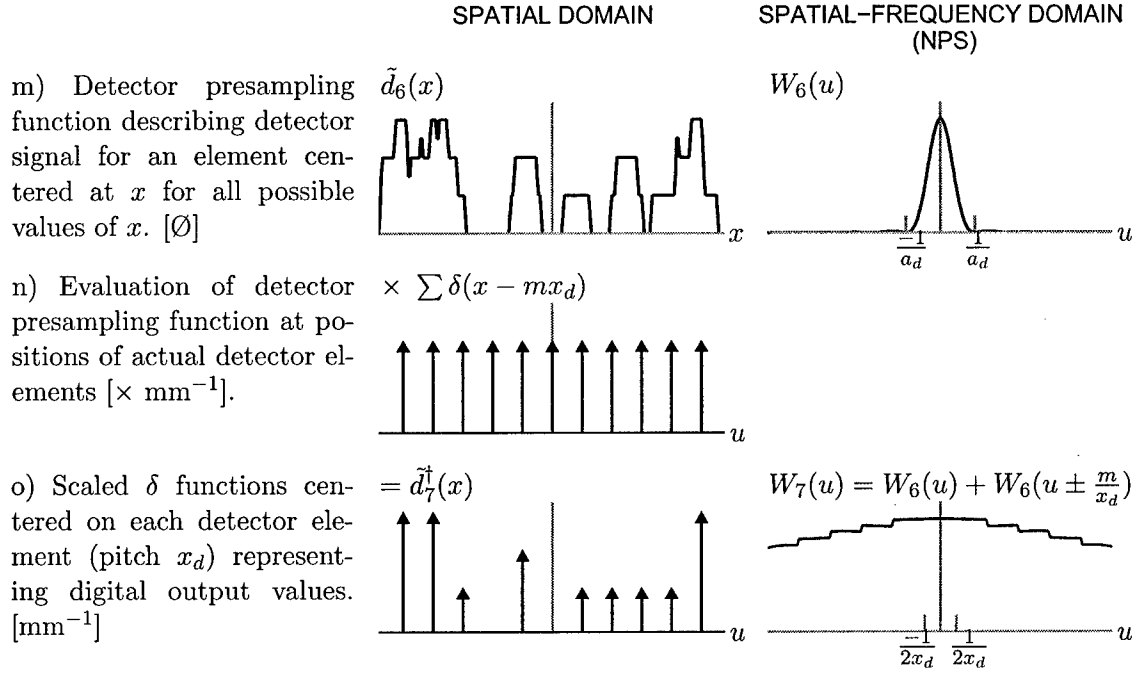
$\dfrac{-1}{a_f}\qquad \dfrac{1}{a_f}$

**Figure 2.** Schematic illustration of the conversion from x rays that interact in a phosphor to the presampling function describing the number of quanta collected by each fiber in a fiber-optic bundle for the system in Fig. 1 (continued in Fig. 3).

SPATIAL DOMAIN          SPATIAL–FREQUENCY DOMAIN
(NPS)

g) Presampling function describing number of optical quanta in fiber centered at $x$ for all possible values of $x$. [q]

$\tilde{d}_3(x)$

$W_3(u)$

$-\frac{1}{a_f}$          $\frac{1}{a_f}$

h) Evaluation of $\tilde{d}_3(x)$ at center of each physical fiber (pitch $x_f$) is a sampling process. [$\times$ mm$^{-1}$]

$\times \sum \delta(x - nx_f)$

i) Total number of optical quanta emitted from each fiber is given by the area of each scaled $\delta$ function. [q/mm]

$= \tilde{q}_4(x)$

$W_4(u) = W_3(u) + W_3(u \pm \frac{n}{x_f})$

$-\frac{1}{2x_f}$   $\frac{1}{2x_f}$

j) Random redistribution of optical quanta at the exit surface of each fiber is a quantum scatter with a rectangular PSF [$\times\emptyset$].

$*_s \frac{1}{a_f}\Pi(\frac{x}{a_f})$

k) Distribution of optical quanta leaving phosphor. Each $\delta$ function represents one quantum. [q/mm]

$= \tilde{q}_5(x)$

$W_5(u) = [W_4(u) - \bar{q}_4]\mathrm{sinc}^2(\pi a_f u) + \bar{q}_4$

l) Integration of optical quanta over the detector aperture $a_d$ is a convolution and multiplication by a detector gain [$\times$ mm/q].

$* g\Pi(\frac{x}{a_d})$

m) Detector presampling function describing detector signal for an element centered at $x$ for all possible values of $x$. [$\emptyset$]

$= \tilde{d}_6(x)$

$W_6(u) = W_5(u)g^2 a_d^2 \mathrm{sinc}^2(\pi a_d u)$

$-\frac{1}{a_d}$   $\frac{1}{a_d}$

**Figure 3.** Schematic illustration of converting the number of optical quanta in each fiber to the presampling function describing detector-element output values (continued in Fig. 4).

m) Detector presampling function describing detector signal for an element centered at $x$ for all possible values of $x$. [Ø]

$\tilde{d}_6(x)$          $W_6(u)$

n) Evaluation of detector presampling function at positions of actual detector elements [× mm$^{-1}$].

$\times \sum \delta(x - mx_d)$

o) Scaled $\delta$ functions centered on each detector element (pitch $x_d$) representing digital output values. [mm$^{-1}$]

$= \tilde{d}_7^\dagger(x)$          $W_7(u) = W_6(u) + W_6(u \pm \frac{m}{x_d})$

**Figure 4.** Schematic illustration of the conversion from the presampling detector function to aliased digital values.

at the exact location of the interacting x ray and therefore overlap. This is why the impulse functions have variable height.

Each optical quantum is relocated to a new location according to the probability density function (PDF) $p_p(x)$ before leaving the phosphor ($\tilde{q}_2(x)$ in Fig. 2e). This is represented as a scatter operation.

### 2.1.2. Optical Fiber Coupling

The fiber optic bundle passes light from the phosphor to the detector. It is assumed all fibers have the same width $a_f$ and uniform spacing $x_f$. In this model, all light quanta incident on the end of each fiber are accepted and passed through the fiber to the exit surface. Due to multiple scatters and reflections within the fiber, each quantum exits from the end of the fiber at a random location that does not correlate with the entrance location. Thus, we represent the fiber optic as a two-step process: i) integration of the number of quanta entering each fiber as a convolution with the rectangle $\Pi(x/a_f)$ to determine the total number of quanta in each fiber (binning and sampling, Figs. 2f and 3h); and ii) scatter with the same rectangular PDF to randomly relocate each optical quantum over the exit surface (Fig. 3j). The result is an "ordered" (non-overlapping) distribution of optical quanta leaving the fiber optic bundle $\tilde{q}_5(x)$ (Fig. 3k).

### 2.1.3. Detection of Light Quanta in Detector

Detection of light in the digital detector is a binning and sampling process, represented as a convolution with $g\Pi(\frac{x}{a_d})$ (Fig. 3l) followed by multiplication by $\sum \delta(x - mx_d)$ (Fig. 4n) where $g$ is a scaling factor relating the number of detected light quanta (per element) to the digital ADC value. The detector output is given by $d_7^\dagger(x) = \sum_m d_m \delta(x - mx_d)$ for $0 \leq m < N$ where $N$ is the number of detector elements.

## 2.2. Theoretical MTF, NPS, NEQ and DQE

A theoretical expression for the "presampling" MTF of this doubly-sampled system is obtained by cascading the frequency-dependent terms from Figs. 2 to 4, resulting in

$$\text{MTF}(u) = T_p(u)\text{sinc}^2(\pi a_f u)\text{sinc}(\pi a_d u) \tag{2}$$

where $T_p(u)$ is the magnitude of the Fourier transform of $p_p(x)$. However, there are serious problems with this model as will be shown in the results section.

A similar approach is used to describe noise in the detector output. The presampling noise at stage 3 is

$$W_3(u) = \bar{q}_0 a_f^2(\bar{m}^2 - 1 + \sigma_m^2)\text{sinc}^2(\pi a_f u) + \bar{q}_0 a_f^2 \bar{m}\text{sinc}^2(\pi a_f u) \tag{3}$$

and the aliased NPS at stage 4 is

$$W_4(u) = W_3(u) + W_3(u \pm \frac{n}{x_f}). \tag{4}$$

Cascading this result to the detector output gives the presampling NPS as

$$W_6(u) = [W_4(u) - \bar{q}_0 a_f^2 \bar{m}]g^2 a_d^2 \text{sinc}^2(\pi a_d u) + \bar{q}_0 g^2 a_f^2 a_d^2 \bar{m}\text{sinc}^2(\pi a_d u) \tag{5}$$

and the aliased NPS as

$$W_7(u) = W_6(u) + W_6(u \pm \frac{m}{x_d}). \tag{6}$$

The "theoretical" DQE is given by

$$\text{DQE}(u) \equiv \frac{\bar{q}_0 g^2 a_f^2 a_d^2 \bar{m}^2 \text{MTF}_7^*(u)}{W_7(u)} \tag{7}$$

where this representation includes MTF aliasing which is not generally accepted practice. The NEQ is given by $\text{NEQ}(u) = \text{DQE}(u)/\bar{q}_0$.

## 2.3. Monte Carlo Calclulation

The MTF of this system was calculated using Monte Carlo data by generating an impulse beam of x rays incident on the system. A one-dimensional geometry was used so that the resulting image profile gives the line-spread function (LSF) directly and the MTF is given as the magnitude of the Fourier transform of the LSF. The Monte Carlo calculation used a matrix of small elements of width $a$ such that the fibers had a width $a_f = 11a$ and the detector elements had a width $a_d = 15a$ in the results presented here.

It should be noted that aliasing in the Monte Carlo MTF is unavoidable in this calculation. Thus, artifacts from both the fiber and detector sampling stages are expected in the calculated MTF. The calculated MTF also depends strongly on the relative alignment of the impulse x-ray beam with respect to the two sampling grids.[6] These artifacts could be avoided, and the true presampling MTF calculated, if the Monte Carlo calculation were modified to implement a "slanted-edge" method.[14]

The NPS was calculated from a line profile corresponding to a uniform distribution of uncorrelated incident x rays.
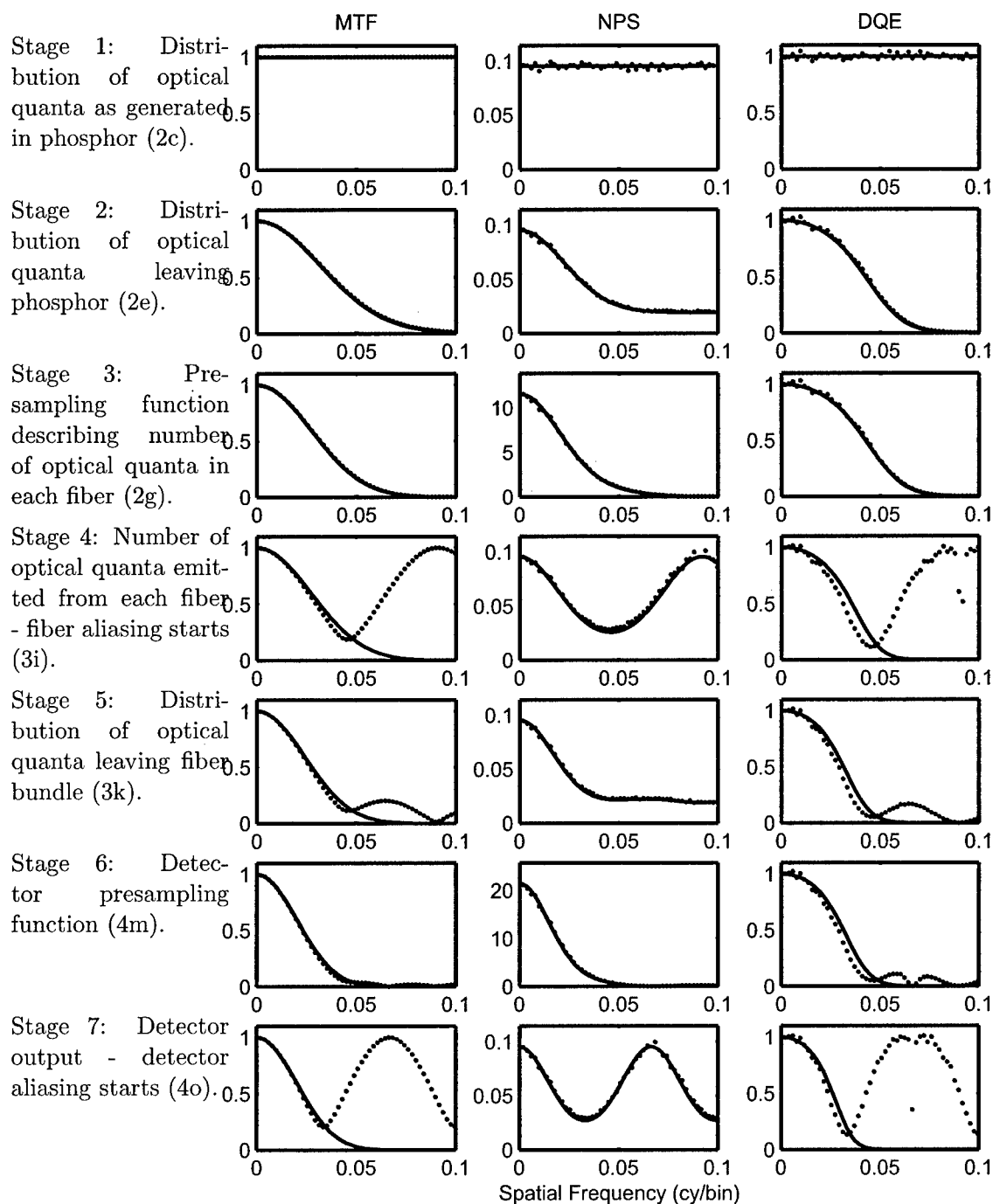
**Figure 5.** Comparison of the MTF, NPS and DQE from the theoretical (solid lines) and Monte Carlo (dotted lines) for each stage in this doubly-cascaded system. The Monte Carlo MTF (and DQE) agree with the theoretical results up to stage 3, but aliasing causes a divergence between these results. The NPS shows excellent agreement for all stages. The DQE shows agreement similar to that of the MTF results.

# 3. RESULTS

Both the theoretical (solid lines) and Monte Carlo (dotted lines) results are shown in Fig. 5 for all seven stages. There is excellent agreement for the MTF, NPS and DQE up to and including stage 3, corresponding to the presampling function describing the number of optical quanta in each fiber (Fig. 2g). While excellent agreement is expected, this result is both comforting and provides validation of both the Monte Carlo and theoretical results.

As a result of aliasing in stage 4, however, the MTF measured from Monte Carlo data does not agree with the theoretical MTF. There are several reasons for this. For example, the theoretical calculation gives the presampling MTF while the MTF measured from the Monte Carlo data includes aliasing, and so agreement is not expected. In addition, the Monte Carlo results depend on the relative alignment of the impulse beam with the (fiber) sampling grid.[6] Depending on this alignment, the Monte Carlo MTF can vary dramatically.

While MTF agreement is qualified, there is excellent agreement in the theoretical and Monte Carlo NPS. This is because noise in stage 4 is WSCS and hence satisfies requirements for use of Fourier-based methods. The NPS result is always aliased and questions regarding the use of a presampling NPS are not raised. In addition, there is no preferred alignment of the input signal. Image quanta are distributed over the entire input area, and hence measured noise is an average over all possible relative alignments with respect to the sampling grid. This result gives direct validation that noise aliasing correctly describes the appearance of noise in digital images.

In the remaining stages 5 to 7, there remains limited agreement between the theoretical and Monte Carlo MTF and DQE. However, there is excellent agreement for the NPS at each stage. This result is somewhat surprising, as there is no good reason to expect that these Fourier-based methods should apply at all after the two sampling processes. However, this good NPS agreement must be qualified with some serious caveats. For example, the Monte Carlo NPS is the average spectral density over the entire image, and may not accurately describe local image noise. This will often be a problem, as relative alignment of the two sampling grids will give rise to complex interference and beating artifacts in the images. These effects may have a significant impact on the appearance of image noise, making it non-WSS and non-WSCS.

# 4. CONCLUSIONS

The conclusions from this study are summarized as follows:

1. The NPS measured from a Monte Carlo simulation of doubly-sampled imaging processes shows excellent agreement with the NPS calculated with a Fourier-based cascaded-systems approach. This is a very surprising result as image noise in these systems is in general neither WSS nor WSCS. However, it must be remembered that the NPS is the power spectrum averaged over the entire image, and as such does not reflect local interference and beating artifacts that are likely present as a consequence of the double-sampling processes.

2. The MTF calculated from Monte Carlo data shows the expected aliasing artifacts. They could be avoided, and the presampling MTF calculated, by implementing a slanted-edge calculation in the Monte Carlo results.

3. Doubly-sampled systems can be well approximated as (more conventional) singly-sampled systems if one of the binning apertures is much smaller than the other. In this case, only the larger aperture needs to be considered when developing a theoretical model of the NPS.

4. While the Fourier-based theoretical model appears to describe global noise correctly, failure to describe local noise due to interference and beating artifacts means that the calculated DQE cannot be used as an indicator of the ideal observer for quantum-noise limited detection tasks - the primary purpose of the DQE.[1]

## 5. ACKNOWLEDGEMENTS

## REFERENCES

1. Medical imaging - the assessment of image quality. *International Commission of Radiation Units and Measurements*, 54, 1995.
2. H. H. Barrett and K. Meyers. *Image Science: Mathematical and Statistical Foundations.* Wiley, 2003.
3. H. H. Barrett and W. Swindell. *Radiological Imaging - The Theory of Image Formation, Detection, and Processing.* Academic Press, 1981.
4. I. A. Cunningham and R. Shaw. Signal-to-noise optimization of medical imaging systems. *J Opt Soc Am A*, 16(3), 1999.
5. J. C. Dainty and R. Shaw. *Image Science.* Academic Press, 1974.
6. J. T. Dobbins. Effects of undersampling on the proper interpretation of modulation transfer function, noise power spectra, and noise equivalent quanta of digital imaging systems. *Med Phys*, 22, 1995.
7. K. Doi, K. Rossmann, and A. G. Haus. Image quality and patient exposure in diagnostic radiology. *Photographic Science and Engineering*, 21, 1977.
8. J. D. Gaskill. *Linear Systems, Fourier Transforms, and Optics.* John Wiley and Sons, 1978.
9. C. E. Metz and K. Doi. Transfer function analysis of radiographic imaging systems. *Phys Med Biol*, 24, 1979.
10. A. Papoulis. *Systems and Transforms with Applications in Optics.* McGraw-Hill, 1968.
11. A. Papoulis. *Probability, random variables, and stochastic processes*, volume 3. McGraw Hill, 1991.
12. K. Rossmann. Measurement of the modulation transfer function of radiographic systems containing fluoroscent screens. *Phys Med Biol*, 9, 1964.
13. K. Rossmann. The spatial frequency spectrum: A means for studying the quality of radiographic imaging systems. *Radiology*, 90, 1968.
14. Samei.E, M. Flynn, and D. A. Reimann. A method for measuring the presampled mtf of digital radiographic systems using an edge test device. *Med Phys*, 25(1), 1998.

# Validation of Complex Cascaded Models of Medical Imaging Systems by Monte Carlo

Mike Sattarivand and Ian A. Cunningham

Biomedical Engineering Graduate Program, University of Western Ontario, and
Imaging Research Laboratories, Robarts Research Institute

## ABSTRACT

Cascaded models have been used by a number of investigators to derive analytic expressions for the Wiener noise power spectrum (NPS) and detective quantum efficiency (DQE) based on design parameters to evaluate the performance of medical x-ray imaging systems. These analytic models are required to establish operating benchmarks and compare the performance of real detectors. Although application of the cascaded approach has had several successes, its contribution is often limited when applied to complex models. This is due to the fact that while final algebraic expressions can be relatively simple, the cascaded approach involves the manipulation of many hundreds of terms. To overcome this limitation a computational engine has been developed using Matlab's Simulink and symbolic math capabilities. Based on a recursive programming approach, this engine generates analytic expressions of NPS and DQE for cascaded models of arbitrary complexity.

In order to validate the resulting expressions, a Monte Carlo (MC) simulation program has been developed that performs an analysis based on C-code generated by the computational engine for each model. The Monte Carlo code generates an incident quantum image as a Poisson distribution of quanta. This distribution is passed through appropriate serial and parallel cascades of modules representing elementary processes and is used to calculate the NPS for comparison with the analytic NPS. Results show excellent agreement between Monte Carlo and theoretical expressions. We are at the stage where complex cascaded modelling is becoming practical tool in the design of new detector systems.

**Keywords:** linear-systems theory, cascaded models, modulation transfer function, noise power spectrum, detective quantum efficiency, Monte Carlo analysis

## 1. INTRODUCTION

Medical x-ray imaging systems must be designed to ensure that maximum image quality is obtained with minimum radiation dose to the patient. The view that an imaging system must be designed such that it faithfully transfers input the image signal to the output image viewed by a physician suggests the use of communication system theory, and in particular Fourier-based linear systems approach.[1] Linear system theory was initially applied in imaging science by Rossmann and co-workers.[2,3] General works have subsequently been published by Dainty and Shaw,[4] Gaskill,[5] Papoulis,[6] Doi, Rossmann, and Haus,[7] Metz and Doi,[8] and many others. Possibly the most extensive use of linear-system theory in medical imaging field is by Barrett and Swindell[9] who used this approach to describe fundamental principles and characteristics of many imaging systems in radiography, computed tomography (CT), nuclear medicine, ultrasound and other areas.

One way to apply linear system theory to evaluate performance of x-ray imaging system is the approach in which a system is modelled as serial or parallel cascades of elementary processes. Transfer of signal and noise throughout the system is predicted from an understanding of transfer properties of each elementary process. Cascaded modelling provides analytic expressions of image quality and system performance metrics. These metrics include: (1) modulation transfer function (MTF), describing spatial resolution; (2) noise power spectrum
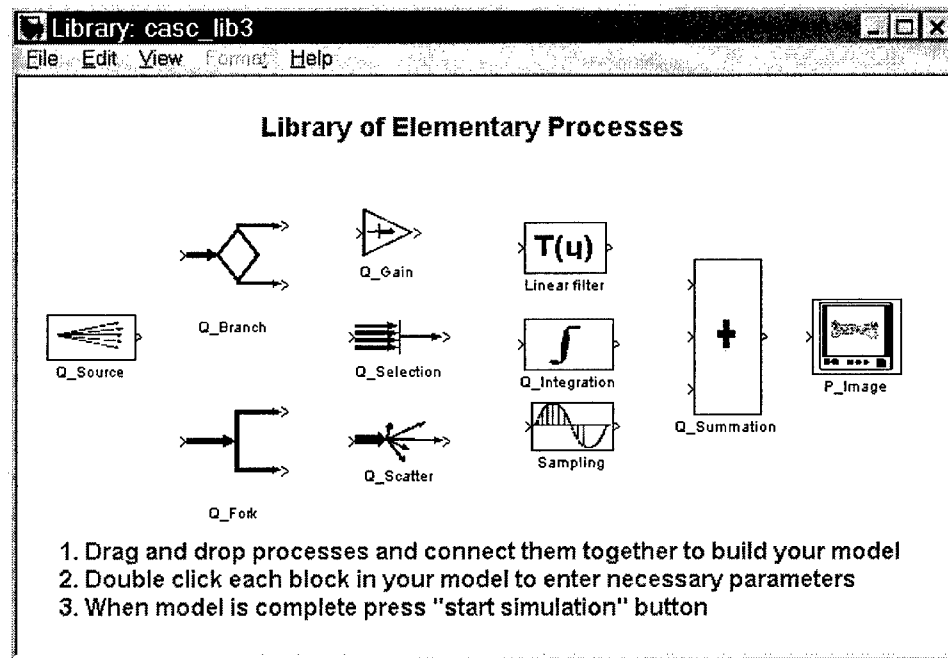
**Figure 1.** Elementary processes built as a library in Simulink package of Matlab

(NPS), describing image noise; and (3) detective quantum efficiency (DQE), describing the ability of the imaging system to make efficient use of incident quanta.

When cascading signal and noise expressions from one elementary process to another, the number of terms grows exponentially. In particular, cascaded models with parallel branches require cross term NPS that contribute to the the final NPS expression. For a relatively simple realistic model an NPS of several hundred terms is not unexpected. This creates a serious limitation to the practical use of complex cascaded models. On the other hand, analytic expressions for most realistic models can be highly simplified. In order to overcome this limitation, we have developed a computational engine that analytically calculates and simplifies MTF, NPS, and DQE using a graphical user interface. Recursive programming is applied in the algorithm to accommodate arbitrarily complex models. In order to verify the generated expressions, we need a mechanism to validate the algorithm. Simple models can be validated directly with manual calculations. However this can be impractical for complex models. We used Monte Carlo (MC) analysis and compared the results with the model's analytic results. The MC analysis is also used in three test models to: (1) validate analytic cross term NPS in order to confirm earlier works,[11] (2) show that cascaded modelling is valid for non-Poisson branch, and therefore for series of parallel cascades, and (3) show it is also valid for nested parallel models. These results extend the application of cascaded models for any arbitrary model with serial or parallel combinations.

## 2. METHODS

### 2.1. COMPUTATIONAL ENGINE FOR CASCADED MODELLING

As illustrated in Fig. 1, a library of elementary processes are defined in the Simulink package of Matlab that can be connected in serial and parallel cascades to create complex detector models in a graphical user interface environment. These processes include generation of incident quantum distribution, quantum gain, quantum scatter, quantum selection, charge integration, linear filter, and sampling to model serial cascades. Parallel cascades are created using what we call quantum branch, Bernoulli branch, cascade fork, and quantum summation processes. Recursive programming is used to calculate signal and noise transfer through models of arbitrary complexity. Based on the model topology and the parameters of the elementary processes, the engine generates
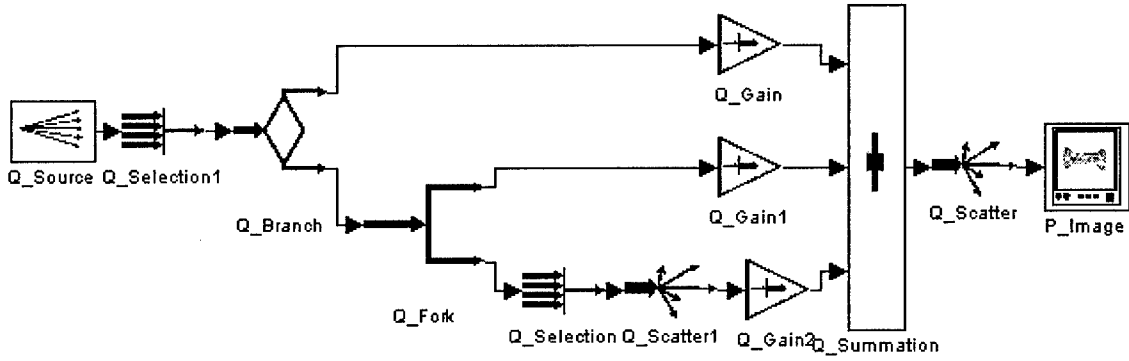
**Figure 2.** A photoelectric interaction model built with computational engine

and simplifies analytic expressions of MTF, NPS, and DQE for the entire system as well as intermediate steps. At each step, symbolic mathematics is used to simplify the analytic expressions. In this method, models of arbitrary complexity can be analyzed. Fig. 2 shows a simple photoelectric model that was built using the computational engine. This is the parallel model used in earlier study[12] to describe reabsorption of characteristic x-rays in a flat-panel detector.

## 2.2. Monte Carlo validation of complex cascaded models

While the computational engine calculates analytic expressions of an arbitrary model, it also generates a C-code source file for the specific topology and parameter values of the cascaded model. When this C-code is compiled with a library of MC routines implementing each of the elementary processes, data-sets of sample functions are generated and passed throughout the model. Instead of 2-D, MC routines generate only 1-D data-sets which is enough for validation purpose.

When the sample function starts off at source with a uniform random distribution of a specified number of incident quanta, the NPS of a sample function at any stage can be found by dividing and binning the sample function into many sub-images and using the equation:[13]

$$NPS(u) = \frac{x_0}{N_x} E\{|DFT\{\Delta d_x\}|^2\}$$

(1)

where $x_0$ is the bin spacing, $N_x$ is the number of bins for each sub-image, and $E\{|DFT\{\Delta d_x\}|^2\}$ calculates an ensemble average of square of the discrete Fourier transform of the zero-mean data set.

For the MC calculation of MTF, sample function starts off at source with a number of incident quanta all at the center of binned image. By passing this image throughout the cascaded model, impulse response functions after any elementary process are found. The MTF is the Fourier transform of the impulse response function. Once the NPS and MTF for the cascaded model are calculated, the DQE is determined. In this paper we only show the results of NPS validations of cascaded models.

We used ran0 routine in Ref. 10 to generate random numbers. The authors claim that the number of random numbers that can be generated without repetition is given by the variable RAND_MAX. For our compiler this number is 2,147,483,647, much greater than the number used in this work.

## 2.3. Validation of our Monte Carlo code

Figure 3 shows a simple model consisting of an input Poisson distribution of quanta, quantum gain, and quantum scatter. This model represents the conversion of input quanta to clusters of secondary quanta. Each point in the input and output images represents one quantum. The image on the left is a sample function of the input that describes a sparse distribution of x-ray quanta. The image on the right is a sample function of the output that describes the distribution of light quanta generated by the x-rays after passing through cascaded gain and
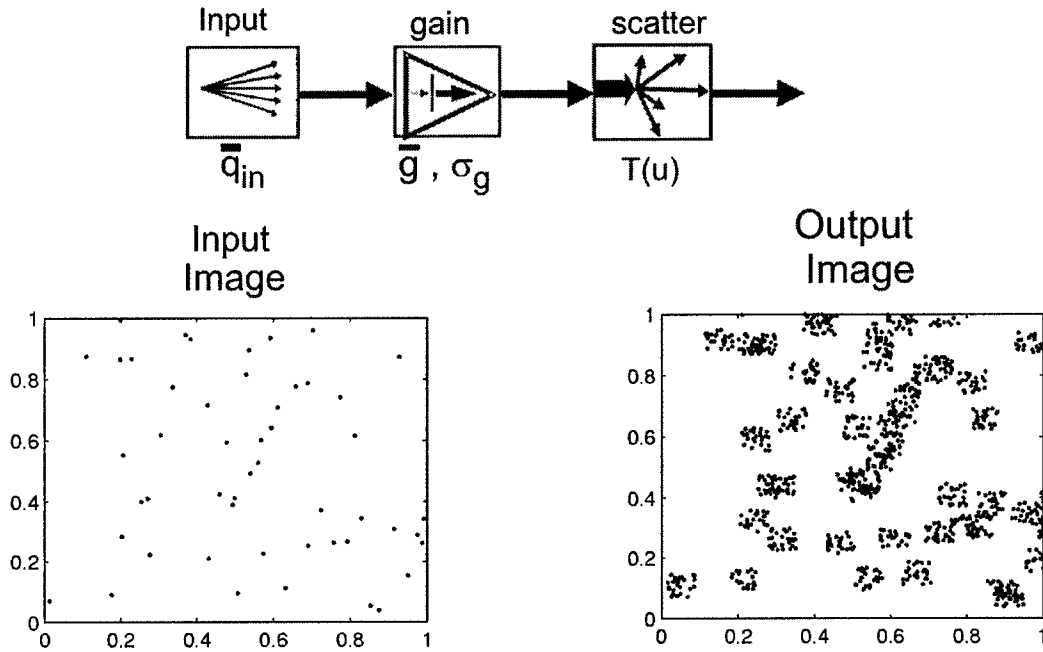
**Figure 3.** A simple cascaded model consists of Poisson source, gain, and scatter processes

scatter processes. As mentioned before, unlike 2-D sample functions shown in Fig. 3, we will only generate 1-D sample functions in our MC routines.

For this model, since analytic expressions of signal and noise are known and can be readily derived manually, there is no need to validate them by MC analysis. However, we will use the analytic NPS for this model to validate our MC approach. The analytic NPS for this model is found to be[13]:

$$NPS(u) = \bar{q}_{in}(\bar{g}^2 + \sigma_g^2 - \bar{g})|T(u)|^2 + \bar{g}\bar{q}_{in} \tag{2}$$

where $\bar{q}_{in}$ is the mean number of input quanta per unit area at the source, each input quanta is converted to $\tilde{g}$ quanta by the gain process and $\tilde{g}$ is a random variable characterized by mean gain $\bar{g}$ and corresponding variance $\sigma_g^2$. After the gain process, each quantum is randomly relocated to a new position by the scatter process with a probability described by the transfer function $T(u)$.

By applying the MC method described above, the NPS of the model is calculated and shown in Fig. 4 for 1,500,000 histories. The results show excellent agreement between MC and analytic NPS of Eq. (2). This indicates that we can get the same analytic results using MC simulation. Figure 4 also shows how MC NPS is increased and still kept the agreement with analytic when mean gain value $\bar{g}$ is increased from 10 to 12. Also note that MC result is always slightly below analytic NPS. This small discrepancy could result from detrending artifact and we will ignore it in this paper and expect to get the same artifact in all our MC results.

## 3. RESULTS

### 3.1. Test1: Validation of analytic cross-term NPS

When two image forming processes contribute to the output signal, the final image is the sum of each. However, the output NPS is not simply the sum of each NPS and a cross-term NPS must be considered due to statistical correlation between two image forming processes.[11] Fig. 5 shows an example of a parallel cascaded model. The
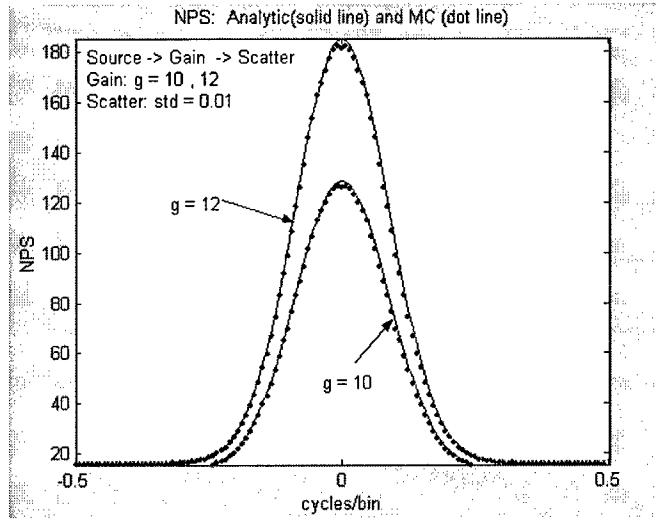
**Figure 4.** Validation of our MC approach
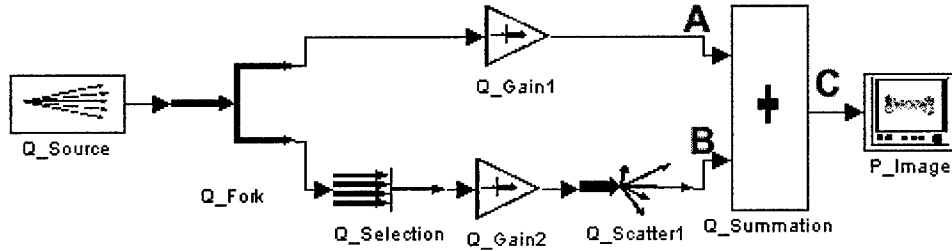


**Figure 5.** Test1: Parallel-cascades model with uncorrelated input quanta to branch.

upper arm has only one gain process whereas the lower arm consists of a selection, a gain and a scatter process. The output NPS at point C is:

$$NPS_C(u) = NPS_A(u) + NPS_B(u) + 2NPS_{AB}(u) \tag{3}$$

where $NPS_{AB}(u)$ is the cross-spectral density between points A and B. This cross term was derived by Yao and Cunningham.[11] For the type of branch points used in this article, the cross term is given by

$$NPS_{AB}(u) = NPS_{in}(u)P_A(u)P_B(u) \tag{4}$$

where $NPS_{in}(u)$ is the NPS at the branch input, and $P_A(u)$ and $P_B(u)$ are the product of the characteristic transfer functions for all process along the arms A and B separated by the branch.

Application of Eq. 4 gives the cross term for this particular model as:

$$NPS_{AB}(u) = \bar{q}_{in}\bar{g}\bar{g}_a\bar{g}_bT(u) \tag{5}$$

where $\bar{q}_{in}$ is the mean number of input quanta per unit area at the source, $\bar{g}$ is the mean selection gain, $T(u)$ is the transfer function of scatter process, and $\bar{g}_a$ and $\bar{g}_b$ are mean gain values of gain processes in upper and lower arms respectively. Results of MC and analytic NPS at points A, B, C as well as cross term NPS are shown in 6. Note that a flat NPS at point A is a result of no correlation in the sample image at this point. These results
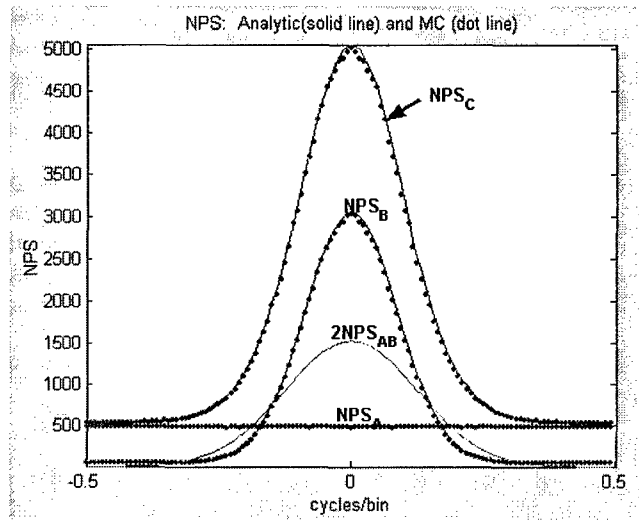
**Figure 6.** Output NPS at point C in parallel model requires cross term $NPS_{AB}$
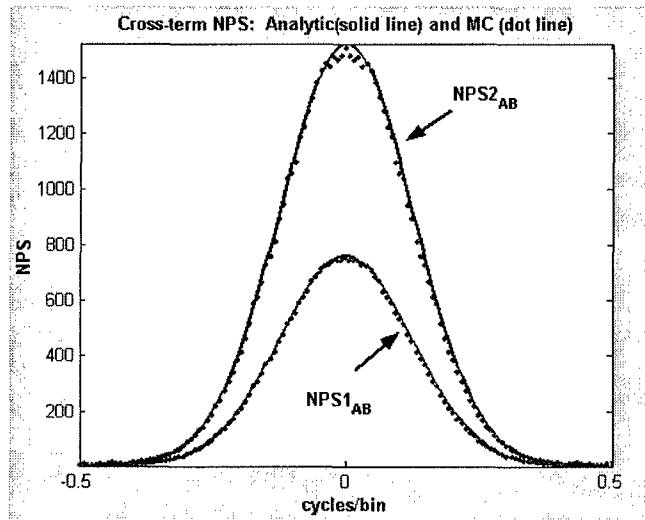


**Figure 7.** Analytic and MC cross-term NPS double when the product of mean gains is doubled, consistent with theory

validate the analytic cross term NPS described in Ref. 11 by MC simulation. Cross term NPS readily can be extended to multiple parallel where there are more than two image forming process arms. In this case cross-term NPS between any possible two arms should be considered. Equation (94) of Ref. 11 also indicates that the cross term NPS depends on pruduct of mean gains along the path of each arm. For example, if we have gain and selection, two very different statistical processes, only product of mean gains along the arms is important in cross term NPS as indicated by $\bar{g}\bar{g}_a\bar{g}_b$ term in equation (5). We confirm this issue by doubling mean gains of both gain processes in upper and lower arm and halving mean gain of selection process in lower arm. Fig. 7 shows MC and analytic cross term NPS before $(NPS1_{AB})$ and after $(NPS2_{AB})$ doubling the product of gains. This result is the first direct validation of the cross-correlation term.
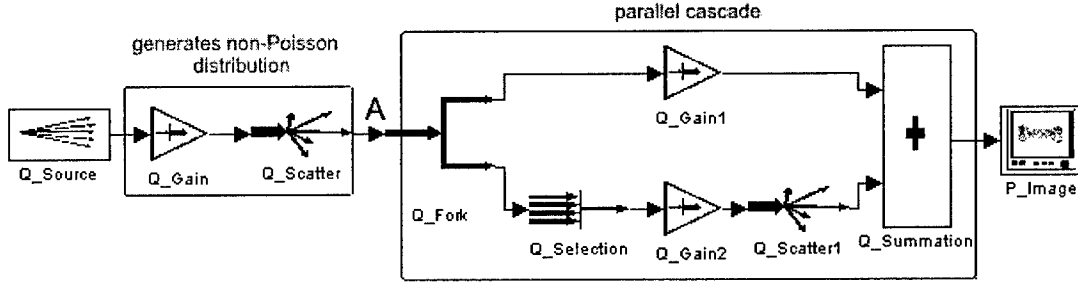
**Figure 8.** Test2: Parallel-cascades model with correlated quanta input to the branch point
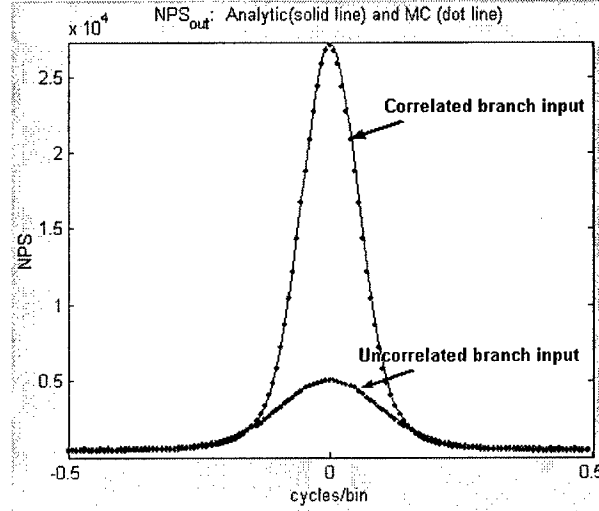


**Figure 9.** NPS of parallel cascaded model with and without correlated quanta input to the branch point

## 3.2. Test2: Validation of non-Poisson branch in parallel cascading

Branches in parallel modelling are introduced[11] for Poisson input branch signal. We will show that the same signal and noise transfer propagations can be applied to non-Poisson input signal and validate this argument with MC analysis. Figure 8 shows an example of non-Poisson input branch. This is the same previous parallel cascade model with added gain and scatter processes to make the input branch signal non-Poisson. The distribution of quanta at point A can be characterized by an MTF equal to normalized transfer function of the first scatter process and an NPS given by Eq. (2). In order to evaluate the output signal, the analytic approach is to pass these MTF and NPS to the parallel cascade part the same way as we would do for Poisson branch input. The final analytic NPS is calculated and compared to the MC NPS in Fig. 9. The close agreement between analytic and MC calculations confirms that signal and noise propagation is valid for non-Poisson case. Figure 9 also shows the NPS of parallel cascades with Poisson input branch which is the same as $NPS_C$ shown in Fig. 6. As expected, output noise is much higher in the Poisson branch input.

## 3.3. Test3: Nested parallels

The NPS cross term in Eq. (4) depends on the NPS at the branch input as well as the product of all transfer functions (including gains) along two branch arms. When cascading arbitrarily complex models, nested parallel cases may happen. Figure 10(a) shows an example of this nested parallel configuration where the resulting NPS is given by

$$NPS_{out}(u) = NPS_C(u) + NPS_D(u) + 2NPS_{CD}(u). \tag{6}$$
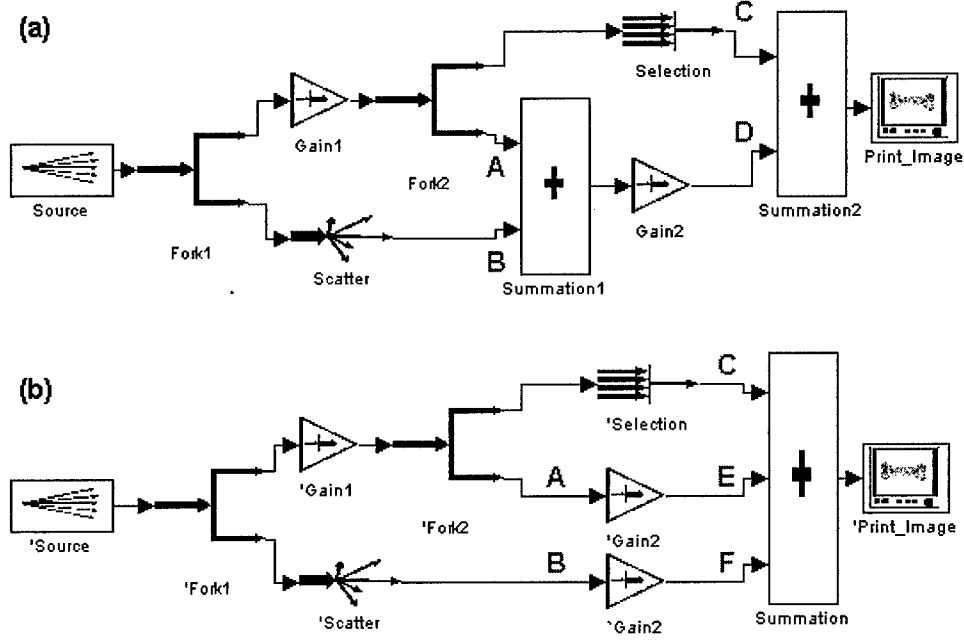
**Figure 10.** Test3: Nested parallel models in two equivalent forms

The cross term $NPS_{CD}(u)$ is not immediately obvious due to the complicated set of statistical correlations between points C and D.

The solution is obtained by noting that while Eq. (4) describes correlations between any two points, correlations between C and D are the result of several connections. Equation (4) must be applied to each possible connection and summed to give the overall cross term.

In Fig. 10(a) there are two such connections, stemming from the two branch points Fork1 and Fork2. From Fork2, the two branch arms are simply connected giving the cross term $NPS_i(u)$ where

$$NPS_i(u) = NPS_A(u)\bar{g}\,\bar{g}_b \tag{7}$$

where $\bar{g}$ and $\bar{g}_b$ are the mean gains of the selection and Gain2 processes respectively and we have used the fact the the input NPS at Fork2 is equal to $NPS_A(u)$, the NPS at point A. From Fork1, the two branch arms give rise to the cross term $NPS_{ii}(u)$ where

$$NPS_{ii}(u) = \bar{q}_{in}\,\bar{g}\,\bar{g}_a\,\bar{g}_b\,T(u) \tag{8}$$

where $\bar{q}_{in}$ is the NPS associated with the input distribution, $\bar{g}_a$ is the mean gain of the process Gain1 and $T(u)$ is the transfer function of the scatter process. The cross term $NPS_{CD}(u)$ is given by

$$NPS_{CD}(u) = NPS_i(u) + NPS_{ii}(u). \tag{9}$$

It is useful to note that the model in Fig. 10(a) is equivalent to that in 10(b). This observation is useful as it provides an alternative (simpler) form for this model. By comparing the final NPS of the two models it can be shown that

$$NPS_{CD}(u) = NPS_{CE}(u) + NPS_{CF}(u). \tag{10}$$

Using this technique we calculated analytic NPS of the nested model in Fig. 10(a) and compared it to the MC NPS performed on the same model. The result is shown in Fig. 11. Despite slightly more fluctuations in MC NPS compared to other MC results due to fewer number of histories, it validates our analytic approach to calculate cross term NPS for nested parallel models.
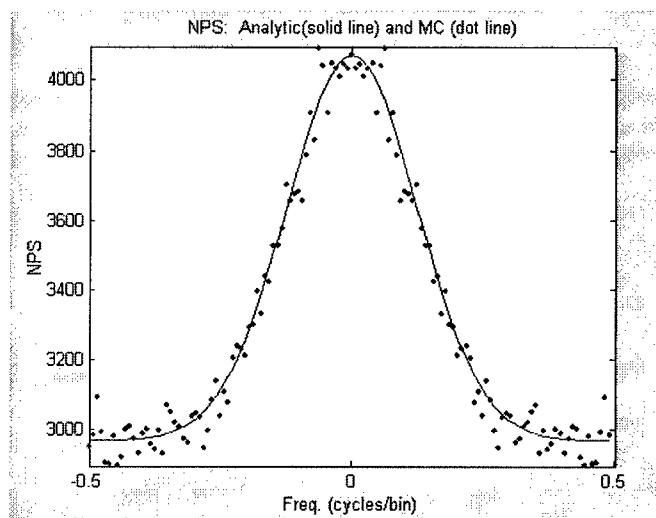
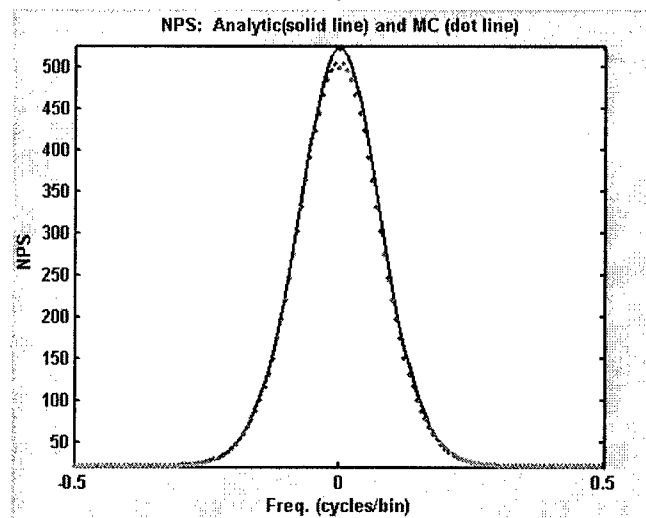**Figure 11.** MC and analytic NPS of nested model



**Figure 12.** MC and analytic NPS of simplified photoelectric model

## 3.4. Simplified photoelectric model

The simplified Photoelectric model shown in Fig 2 is analyzed with our MC method to validate analytic MTF, NPS, and DQE calculated by the computational engine. For the NPS, MC analysis started with 2.7 million x-ray photon histories at the source. Comparison between MC and analytic NPS shown in Fig. 12 demonstrates excellent agreement. The NPS of this model contains cross terms in the NPS because of statistical correlations between the two parallel arms of the model. The agreement between MC and analytic also validates cross term NPS which was addressed directly in section 3.1. Results of MTF and DQE for this model show similar agreement and are not shown here.

# 4. CONCLUSIONS

The MTF, NPS, and DQE are important indicators of image quality and performance of medical imaging systems. Recent developments in understanding noise transfer has resulted in application of generalized transfer-theory approach that can be used to evaluate MTF, NPS, and DQE of the medical imaging systems.

To remove the serious problem of manipulating long analytic expressions, a validated computational engine has been developed to describe signal and noise performance of complex detector designs. Analytic expressions of MTF, NPS, and DQE are generated, making the cascaded method powerful and practical approach. Recursive algorithm implemented in the computational engine accommodates arbitrary complexity.

Analytic results have been validated by Monte Carlo. This is the first such validation of cross terms and is performed for three test models: (1) parallel cascade model with uncorrelated input quanta to the branch point, (2) parallel cascades model with correlated input quanta to the branch point, and (3) nested parallel models. We showed that analytic approach to apply signal and noise transfer theory in these models is valid. The results extend the the application of cascaded modelling to any arbitrary model with serial or parallel combination. Making sure that arbitrarily complex cascaded models are valid may help scientists and engineers to apply transfer-theory in designing new imaging systems with better image quality.

# 5. ACKNOWLEDGMENTS

# REFERENCES

1. I.A.Cunningham and R.Shaw, *Signal-to-noise optimazation of medical imaging systems*, J Opt Soc Am A 16 621-32, 1999.
2. K.Rossmann, *Measurment of the modulation transfer function of radiographic systems containing fluoroscent screens*, Phys Med Biol 9 551-7, 1964
3. K.Rossmann, *The spatial frequency spectrum: A means for studying the quality of radiographic imaging systems*, Radiology 90 1-13, 1968
4. J.C.Dainty and R.Shaw, *Image Science*, (Academic Press, New York, 1974).
5. J.D.Gaskill, *Linear systems, Fourier Transforms, and Optics*, (John Wiley and Sons, New York, 1978)
6. A.Papoulis, *Systems and Transforms with Applications in Optics*, (McGraw-Hill, New York, 1968).
7. K.Doi, K.Rossmann, and A.G.Haus, *Image quality and patient exposure in diagnostic radiology*, Photographic Science and Engineering 21 269-77, 1977
8. C.E.Metz and K.Doi, *Transfer function analysis of radiographic imaging systems*, Phys Med Biol 24 1079-106, 1979
9. H.H.Barrett and W.Swindell, *Radiological Imaging- The Theory of Image Formation, Detection, and Processing*, (Academic Press, New York, 1981)
10. W.H.Press,, B.P.Flannery, S.A.Teukolsky, and W.T.Vetterling, *Numerical Recipes in C*, (Cambridge University Press, New York, 1988)
11. J. Yao and I.A.Cunningham, *Parallel cascades: New ways to describe noise transfer in medical imaging systems*, Med. Phys. 28, pp. 2020-2038, 2001.
12. I.A.Cunningham, J.Yao, and V. Subotic *Cascaded Models and the DQE of Flat-Panel Imagers: Noise Aliasing, Secondary Quantum Noise and Reabsorption*, Medical Imaging 2002: Physics of Medical Imaging, L.E.Antonuk and M.J.Yaffe Eds., Proc SPIE 4682: 61-72, 2002.
13. I.A.Cunningham, "Applied linear-system theory", Ch2, in Handbook of Medical Imaging: Vol 1, physics and psychophysics J.Beutel, H.L.kundel, and R.Van Metter (SPIE Press, Bellingham, 2000) pp. 79-159

# Penalty on the detective quantum efficiency from off-axis incident x rays

George Hajdok and Ian A. Cunningham

Department of Medical Biophysics, University of Western Ontario;
Imaging Research Labs, Robarts Research Institute;
Department of Medical Physics, London Regional Cancer Centre;
London, Ontario, Canada

## ABSTRACT

An often neglected assumption related to detector performance metrics such as the modulation transfer function (MTF), noise power spectrum (NPS), and detective quantum efficiency (DQE) is that they only apply to a small region around the centre of an x-ray image. In the periphery of an image, image formation is from obliquely incident x rays. These off-axis x rays will introduce an additional degrading effect on the above detector performance metrics. In our study, we use Monte Carlo simulations to quantify the effects of off-axis radiation on the MTF, NPS, and DQE on common diagnostic x-ray detectors. In our simulations, we vary the incident angle of x rays between 0° and 12°, which is a typical range of divergence in diagnostic x-ray imaging. In the case of amorphous selenium, our results show that off-axis incident x rays degrade the MTF above 5 cycles/mm with increasing severity at higher incident angles and x-ray energy, and more importantly has very little effect on the NPS. Hence, the impact is more severe on the DQE due to the MTF squared dependency. For an incident x-ray angle of 12° (~13 cm from central axis or chest wall in mammography), the DQE falls to 50% of its initial value at 10 and 7 cycles/mm for x-ray energies of 20 and 40 keV, respectively. This loss of signal-to-noise ratio may be most significant near the skin line in mammography studies.

**Keywords:** detective quantum efficiency, oblique incident x rays

## 1. INTRODUCTION

One important aspect in the assessment and development of x-ray imaging systems is to quantify the performance characteristics of the x-ray detector. A wide variety of metrics can be used to gauge performance, but the customary way to describe the system response of a detector is in the Fourier domain because of the convenience of quantifying spatial correlations in signal and noise. The main metrics of system response include the modulation transfer function (MTF), noise power spectrum (NPS), and detective quantum efficiency (DQE). These metrics are useful descriptors of spatial resolution, noise, and signal-to-noise ratio, respectively, and have been well described in the literature.[1,2] A number of assumptions often need to be made to permit the quantification of the aforementioned metrics, especially in the case of experimental measurement. For example, one assumption usually made pertains to the normal incidence of all x rays on the detector. In reality, x rays will diverge from the focal spot and impinge on the detector over a range of angles. These off-axis or obliquely incident x rays will change the manner in which the incident x-ray energy is distributed within the x-ray converter material. Therefore, a change in energy deposition will introduce a blur that will further degrade spatial resolution, and possibly noise, especially in the periphery of an x-ray image.

The impact of off-axis x rays on image quality will depend on the imaging geometry and the existence of relevant anatomy in the periphery of the image. One imaging application where the effects of off-axis x rays may be of concern is mammography. Mammography is one of the most technically demanding imaging techniques because of the need to perceive the fine-details of micro-calcifications and thin fibres protruding from a tumor mass in the breast. The nominal imaging geometry[3] for mammography consists of a 60 cm source-to-detector

Further author information: (Send correspondence to G.H. or I.A.C.)
G.H.: E-mail: ghajdok@imaging.robarts.ca, Telephone: 1 519 685 8500 xx34030
I.A.C.: E-mail: icunning@imaging.robarts.ca, Telephone: 1 519 685 8500 xx34130

distance with a detector field-of-view of approximately 18 cm × 24 cm. Based on these values, the x-ray angle of incidence can vary by as much as 17° in the anterior/posterior direction of the breast. Unlike other x-ray imaging techniques, mammography requires both high-contrast and high-spatial resolution capability, which can only be achieved using low x-ray energies. A consequence of using low energy x rays is that the intensity or penetrating power of the beam is significantly reduced. The latter statement explains the short source-to-detector distances used in mammography. However, the trade-off of using a short detector distance is an increase in incident x-ray angle for the off-axis portions of the beam. Therefore, the ability to detect fine and low-contrast structures near the skin line of the breast will be compromised because of the effect from off-axis x rays.

Que and Rowlands[5] have derived, from first principles, an analytic expression of the point spread function and MTF that describes the effect of obliquely incident x rays, which they term the *geometric effect*, on spatial resolution. These expressions have not been validated mainly due to the difficulty, or even impossibility, of performing a valid experiment. More importantly, no one to date has described the impact of the geometric effect on the NPS and DQE. An alternate method to study the geometric effect is through Monte Carlo simulation, which is a powerful tool to solve problems that may be too difficult analytically or even experimentally. The objectives our paper are: (i) to quantify the geometric effect in terms of the MTF, NPS, and DQE using Monte Carlo simulations of photon and electron transport in a common x-ray converter material, (ii) to describe the penalty on the DQE from off-axis x rays, and (iii) to report on the implications of the geometric effect in mammography.

## 2. THEORY

As mentioned earlier, the geometric effect has been described analytically with respect to spatial resolution.[5] We briefly summarize the results below. To supplement the equations, a simple schematic diagram of the geometry is provided in Fig. 1.

For an obliquely incident x ray in the x-z plane, the point spread function ($PSF_g$) for the geometric effect has the form[5]

$$PSF_{g,\theta}(x,y) = \delta(y)\, H(L\tan\theta - x)\, H(x)\, \frac{\mu}{2\sin\theta}\, \exp\left(-\frac{\mu x}{\sin\theta}\right) \tag{1}$$

where $H(...)$ is the step function (i.e. equals 1 if the argument is positive, and 0 otherwise), $\mu$ is the linear attenuation coefficient, $\theta$ is the angle of incidence of the x ray, L is the thickness of the x-ray converter, and $\delta(...)$ is the Dirac delta function.

As seen in Fig. 1b, an obliquely incident x-ray can be attenuated anywhere along points A and B. For an infinitely thick x-ray converter material, the mean lateral displacement of the interaction point for an obliquely incident x-ray is equal to $x' = 1/\mu \times \sin\theta$, where $1/\mu$ is the mean free path of the x-ray. For a material with a bounded thickness, $L$, the maximum lateral displacement of the interaction point is equal to $x_{max} = L\tan\theta$. If $x' > x_{max}$, then the x-ray attenuation does not have much effect on the size of the blur, and the geometric effect is determined by the thickness of the x-ray converter layer. If $x_{max} > x'$, then the mean free path of the x-ray is smaller than the pathlength, $AB = L/\cos\theta$, and the geometric effect is limited by the x-ray attenuation.

The corresponding MTF for the PSF in Eqn. 1 is given by[5]

$$MTF_{g,\theta}(u) = \frac{\{[1 - \exp(-\mu L/\cos\theta)]^2 + 4\exp(-\mu L/\cos\theta)\sin^2(\pi u L \tan\theta)\}^{1/2}}{[1 - \exp(-\mu L/\cos\theta)]\,[1 + (2\pi u \sin\theta/\mu)^2]^{1/2}} \tag{2}$$

The functional form of the geometric MTF can be clearly seen in the limit of $\mu \to 0$,

$$MTF_{g,\theta}(u) = \frac{|\sin(\pi u L \tan\theta)|}{\pi u L \tan\theta} \tag{3}$$
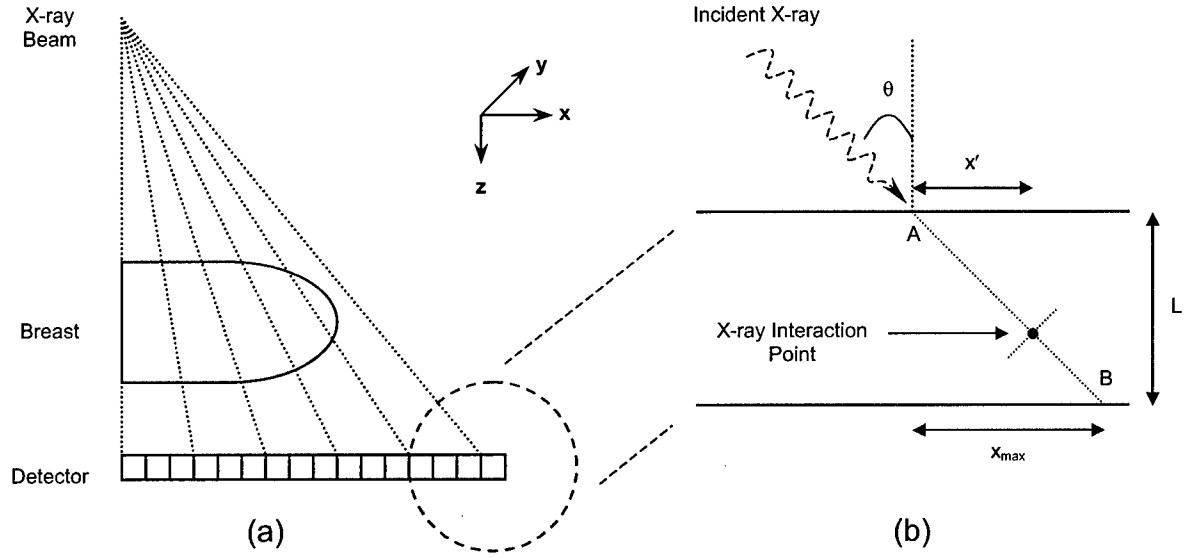
**Figure 1.** Schematic diagram illustrating (a) the mammography imaging geometry and (b) close-up view of the geometric effect for obliquely incident x rays.

## 3. METHODS

### 3.1. Monte Carlo Code and Detector Geometry

The latest version of the Electron Gamma Shower (EGSnrc) Monte Carlo code[6,7] was used to determine the spatial distribution of absorbed energy for x rays incident on a common x-ray converter material. The user code DOSXYZnrc[8,9] was used to simulate the coupled photon-electron transport within a rectangular slab geometry, and to score the amount of energy deposited within the detector volume for each photon history.

The x-ray converter material chosen for our study was direct conversion amorphous selenium (a-Se). A converter density of 4.20 g/cm$^3$ and thickness of 300 $\mu$m were used, which are typical in existing digital x-ray detectors used in mammography.[10–13]

Dose deposition maps, $d_\theta(x, y)$, were determined at various angles of x-ray incidence, $\theta$, and at two monoenergetic x-ray energies of 20 and 40 keV. These energies approximately represent the mean and maximum energies encountered in mammography x-ray spectra. As shown schematically in Fig. 2, two different beam geometries were used in the simulations: an infinitesimal pencil-beam of x rays for the MTF simulations, and a broad (i.e. encompass entire detector area) parallel beam of x rays for the NPS simulations.

Table I summarizes the Monte Carlo parameters related to the x-ray beam and x-ray converter.

### 3.2. MTF Simulations

In order to determine the MTF, Monte Carlo simulations were performed with an infinitesimal pencil-beam of x rays incident on the a-Se slab. In each simulation, $10^7$ incident x-ray histories and a pixel size of 1 $\mu m$ were used. A dose deposition map, $d_\theta(x, y)$, was scored for each x-ray angle of incidence, and represents the two-dimensional point spread function (PSF), $psf_\theta(x, y)$, when normalized to unit area,

$$\mathrm{psf}_\theta(x, y) = \frac{d_\theta(x, y)}{\int \int d_\theta(x, y) \, \mathrm{d}x \, \mathrm{d}y} \tag{4}$$

Based on $psf_\theta(x, y)$, the modulation transfer function, $\mathrm{MTF}_\theta(u, v)$, was calculated using the 2-dimensional Fourier transform via
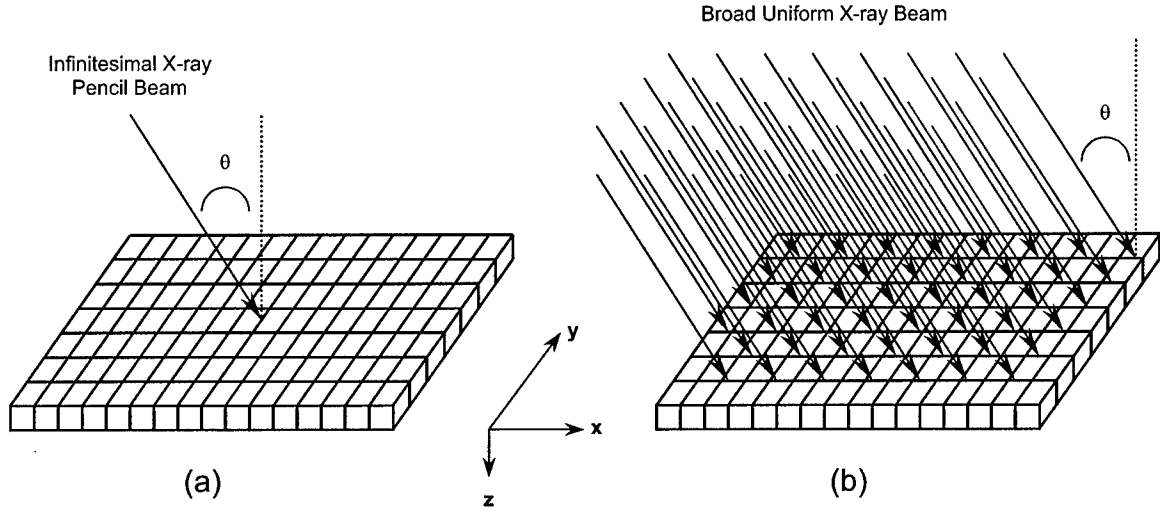
**Figure 2.** Monte Carlo Simulation geometry for (a) modulation transfer function and (b) noise power spectrum.

$$\text{MTF}_\theta(u,v) = \mathcal{F}_2\{\text{psf}_\theta(x,y)\} = \int_{-\infty}^{\infty} \int_{-\infty}^{\infty} \text{psf}_\theta(x,y) \, e^{-i2\pi(ux+vy)} \, dx \, dy \tag{5}$$

which represents the spatial resolution due to the spread of absorbed energy from x-ray and electron interactions within the converter material for a given incident x-ray angle. From Eq. 5, we extracted the 1D MTF along $u$, i.e. the corresponding spatial-frequency direction in which the incident x-ray angle is varied.

### 3.3. NPS Simulations

In order to determine the NPS, a series of ten flat-field noise images were simulated with a uniform, parallel x-ray beam of $8 \times 10^7$ incident x-ray histories per image over an area of $2 \times 2$ cm$^2$ (1 $\mu m$ pixel size). Boundary effects from the Monte Carlo simulation were accounted for by removing 200 pixels at each edge of the image. Each of the final noise images had 1800 × 1800 data points, which was subdivided into 81 images, each with 200 × 200 data points. Therefore, a total of 810 sub-images were generated. The results from the 810 sub-images were averaged to obtain the final NPS curve.

In our study, we considered the "direct-digital" technique of NPS analysis,[14] in which the NPS is determined from the ensemble average of the modulus-squared of the discrete Fourier transform (DFT) of the zero-mean image signal, as given by,

$$\text{NPS}_\theta(u,v) = \frac{x_0 y_0}{N_x N_y} E\left\{\left|DFT^{2D}\{\Delta d_\theta(n_x, n_y)\}\right|^2\right\} \tag{6}$$

where $x_0, y_0$ represent the pixel centre-to-centre spacing in the $x$ and $y$ directions, $N_x, N_y$ are the number of pixels in the $x$ and $y$ directions, $n_x, n_y$ index each pixel location, $E\{...\}$ is the expectation operator, and $\Delta d_\theta(x,y)$ is the zero-mean realization of the 2D dose deposition. With the same reasoning as the MTF case, we only consider the 1D NPS of the 2D noise process in Eq. 6.

### 3.4. Detective Quantum Efficiency

Once the MTF and NPS were determined from the Monte Carlo simulations, they were used to calculate the DQE via[15]

**Table 1.** Summary of x-ray beam and detector parameters for Monte Carlo simulations of MTF and NPS.

| Parameter | Symbol | Value |
|---|---|---|
| X-ray energy | $h\nu$ | $\{20, 40\}$ keV |
| X-ray incident angle | $\theta$ | $\{0, 3, 6, 9, 12\}°$ |
| Converter material | a-Se | amorphous selenium |
| Converter density | $\rho$ | 4.20 g/cm$^3$ |
| Converter thickness | $t$ | 300 $\mu$m |
| **MTF Simulations** | | |
| Number of x-ray histories | $N_{Hist}$ | $10^7$ |
| Number of x, y voxels | $N_x, N_y$ | 512, 512 |
| Size of x, y voxels | $\Delta x, \Delta y$ | 1 $\mu$m, 1 $\mu$m |
| Total area of converter | $A$ | $0.512 \times 0.512$ cm$^2$ |
| **NPS Simulations** | | |
| Number of x-ray histories | $N_{Hist}$ | $8 \times 10^7$ |
| Number of images | $N_{Image}$ | 10 |
| Number of x, y voxels | $N_x, N_y$ | 2000, 2000 |
| Size of x, y voxels | $\Delta x, \Delta y$ | 10 $\mu$m, 10 $\mu$m |
| Total area of converter | $A$ | $2.000 \times 2.000$ cm$^2$ |

$$\text{DQE}_\theta(u) = \frac{\text{MTF}_\theta^2(u)}{\bar{q}\,\text{NPS}_\theta(u)/\bar{d}^2} \tag{7}$$

where $\bar{q}$ is the average number of quanta (i.e. histories) used in the NPS simulations and $\bar{d}$ is the average signal value of a noise image.

## 3.5. Detector Performance Oblique Degradation Ratio (ODR)

For x-ray imaging systems where the angle of incidence of the x ray may be important, we introduce the concept of the detector performance oblique degradation ratio, $\text{ODR}_\theta(u)$. At a selected spatial-frequency, $u$, the $\text{ODR}_\theta(u)$ represents the ratio of the DQE at an oblique incident x-ray angle to the DQE at normal incidence via

$$\text{ODR}_\theta(u) = \frac{\text{DQE}_\theta(u)}{\text{DQE}_{0°}(u)} \tag{8}$$

In simpler terms, for a given angle of incidence, Eqn. 8 quantifies the reduction of the signal-to-noise ratio relative to the assumption of normally incident x-rays.

## 4. RESULTS

The spatial distribution of absorbed energy from a Monte Carlo simulation can be used to obtain the "interaction" modulation transfer function, for the case of an infinitesimal x-ray beam, and the noise power spectrum, for the case of a broad, parallel x-ray beam. From this interaction MTF and NPS, quantities such as the DQE can be calculated. These quantities are summarized in the following sections.

## 4.1. Modulation Transfer Function

The interaction modulation transfer functions for amorphous selenium are shown in Figs. 3(a),(b) for x-ray energies of 20 and 40 keV. In each figure, a select number of MTFs based on a range of incident x-ray angles from 0°–12° are plotted to highlight the variations in spatial resolution due solely to the geometric effect. Above 5 cycles/mm, each MTF curve begins to disperse from one another, indicating a loss of spatial resolution with
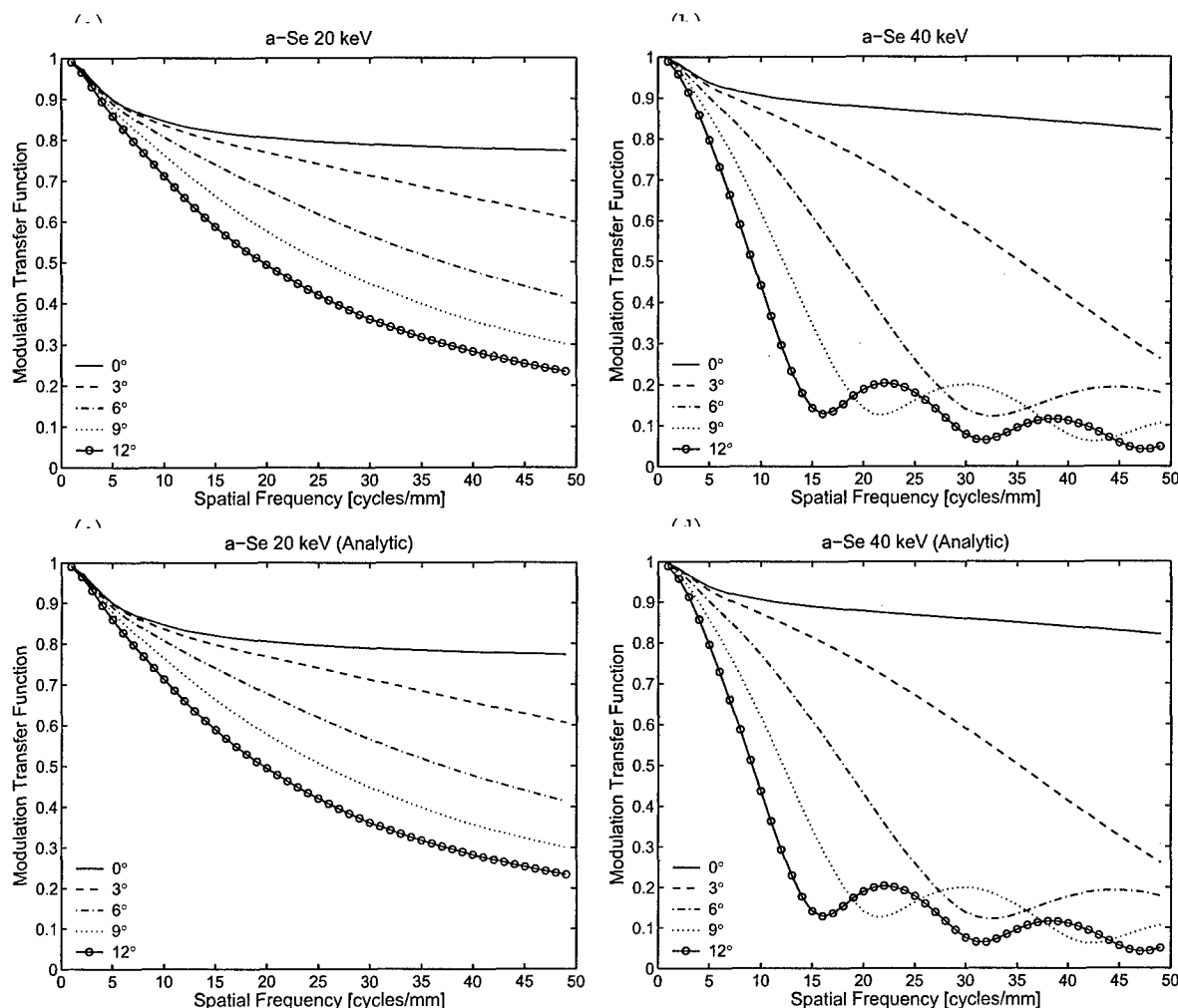
**Figure 3.** Modulation Transfer Function due to obliquely incident x rays. All the curves from (a) and (b) were generated from Monte Carlo simulations, while those in (c) and (d) were calculated by multiplying the 0° result from (a) and (b), respectively, by Eqn. 2 for the appropriate oblique angles. The analytic results agree very well with Monte Carlo simulation.

increasing incident x-ray angle. The fluctuations in a few of the MTF curves in Fig. 3b demonstrate the sinc behaviour of the geometric effect (see Eqns. 2 and 3).

The purpose of Figs. 3(c),(d) is to determine if the behaviour of the geometric effect can be described analytically. In other words, does Eqn. 2 accurately describe the geometric effect? In these plots, the MTF curve from the Monte Carlo simulations at normal x-ray incidence was multiplied by the expression in Eqn. 2 for each oblique angle. As can be seen, there is remarkable agreement. Although, caution must be exercised for this observation because we have only investigated low x-ray energies and small incident x-ray angles. At higher energies and oblique angles, the spatial distribution of absorbed energy from the incident x-ray dramatically spreads out, which in turn complicates the energy deposition within the converter material. These extreme cases are part of an ongoing investigation.
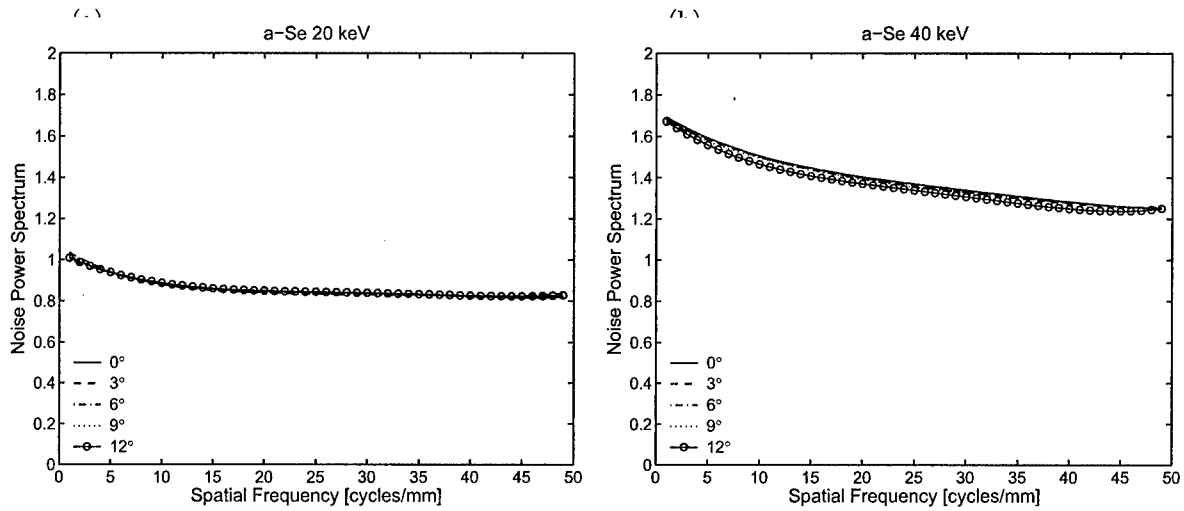
**Figure 4.** Noise Power Spectrum due to obliquely incident x rays. Plotted is the normalized unitless NPS (i.e. denominator of Eqn. 7). For purposes of clarity, each curve is a fourth-order fit to the actual NPS data. Note that obliquely incident x rays have a negligible effect on the noise.

## 4.2. Noise Power Spectrum

The interaction noise power spectra for amorphous selenium are shown in Fig. 4 for x-ray energies of 20 and 40 keV. In these plots, the y-axis values represent the NPS multiplied by the average incident x-ray fluence divided by the square of the average signal in the noise images (i.e. $\bar{q}\,\mathrm{NPS}_\theta(u)/\bar{d}^2$). For the purpose of comparison, the NPS curves at each angle were fitted to a fourth-order polynomial. For the incident x-ray energies and angles presented in our study, the plots demonstrate the fact that the geometric effect does not affect noise. The reason behind that assertion has to do with photoelectric interactions, which is the dominant x-ray interaction process in amorphous selenium at the two energies. The geometric effect does not affect spatial correlations caused by the re-absorption of K-fluorescent x rays because of the isotropic emission of these secondary x rays from the atom. Once again, extrapolation to higher x-ray energies may not yield the same observation, since Compton scatter interactions become dominant. Since Compton scatter x rays are not emitted isotropically, then spatial correlations may possibly be introduced.
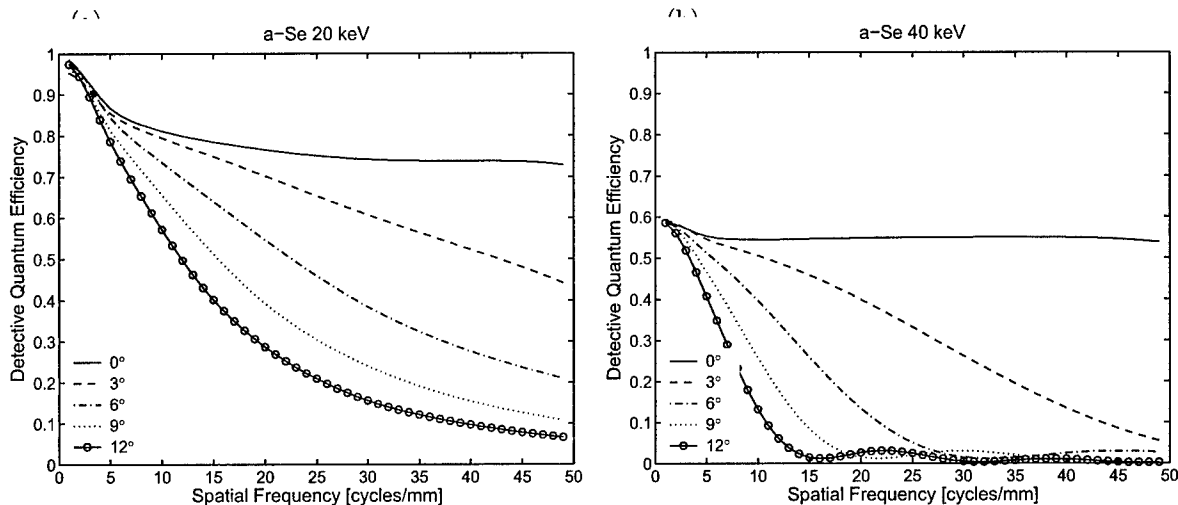
## 4.3. Detective Quantum Efficiency

Based on the Monte Carlo simulations for the modulation transfer function and noise power spectrum, the detective quantum efficiency was calculated for each incident x-ray angle using Eqn. 7. Plots of the DQE for each monoenergetic x-ray energy is shown in Fig. 5. Since the geometric effect does not alter the correlated or uncorrelated noise components of the noise power spectrum, the behaviour of the DQE will solely be dictated by the square of the MTF. Therefore, the DQE for a given incident x-ray angle can be approximated using the DQE at normal x-ray incidence and the MTF due to the geometric effect (Eqn. 2) via

$$\mathrm{DQE}_\theta(u) \approx \mathrm{DQE}_{0^\circ}(u) \times \mathrm{MTF}^2_{g,\theta}(u) \tag{9}$$

Similarly, Eqn. 9 can be inserted into Eqn. 8 to yield a new expression for the detector performance oblique degradation ratio, given by

$$\mathrm{ODR}_\theta(u) \approx \mathrm{MTF}^2_{g,\theta}(u) \tag{10}$$

**Figure 5.** Detective Quantum Efficiency due to obliquely incident x rays. Since the NPS is not affected by the incident x-ray angle, then the DQE is solely determined by the square of the MTF.

## 5. DISCUSSION

To put the results from the DQE into context, we introduced a metric called the detector performance oblique degradation ratio that describes the reduction in DQE caused by the geometric effect. The ODR is shown in Fig. 6 for a spatial-frequency of 10 cycles/mm, which approximately reflects the resolution required to see micro-calcifications in the breast. As expected, the DQE fall-off is more dramatic for: (i) higher incident x-ray angles, and (ii) higher energy x-ray beams, due to the greater penetration of the x-rays. These results suggest that in the periphery of a mammogram (i.e. approximately 13 cm from the central axis to the chest wall in any direction), the DQE falls to approximately 30% of the central DQE value. The implication for a radiologist might be the diagnosis of a false positive or false negative in the front of the breast. Therefore, in the design and development of x-ray detectors for mammography, manufacturers face an interesting compromise in terms of maximizing image quality, due to the simultaneous need of maximizing x-ray intensity and minimizing incident x-ray angle on the detector. As an example, for a chest wall to nipple distance of 13 cm and a source-to-detector distance of 60 cm, the maximum incident x-ray angle that fully subtends the breast would be 12°. From Fig. 6, the corresponding drop in DQE at 10 cycles would be approximately 30%. If the source-to-detector distance is increased to 100 cm, the maximum incident x-ray angle is reduced to 7°, which would lead to only a 15% drop in DQE. However, the x-ray intensity will also fall by 36% due to the inverse square fall-off effect, thus requiring a 36% increase in exposure time and tube heat load.

## 6. CONCLUSIONS

Oblique x rays reduce the MTF and DQE of x-ray detectors. At low spatial-frequencies (below 5 cycles/mm), the geometric effect has a negligible effect on the spatial resolution. Above 5 cycles/mm, the loss of spatial resolution is more pronounced and decreases with higher spatial-frequencies. In addition, the effect of obliquely incident x rays on the modulation transfer function can be described analytically for the x-ray energies used in our study. The noise power spectrum is unaffected by the geometric effect, and we show that the detective quantum efficiency is reduced by a factor called the "oblique degradation ratio" given by $ODR_\theta(u) \propto MTF^2_{g,\theta}(u)$. For the case of mammography, our results suggest that there is a large miss-match in detector performance between the periphery of an image to the central region of the same image. The implication may impair the diagnosis of breast cancer near the front of the skin line. Therefore, detector manufacturers face a practical compromise between maximizing the x-ray intensity incident and minimizing the incident x-ray angle on the detector.
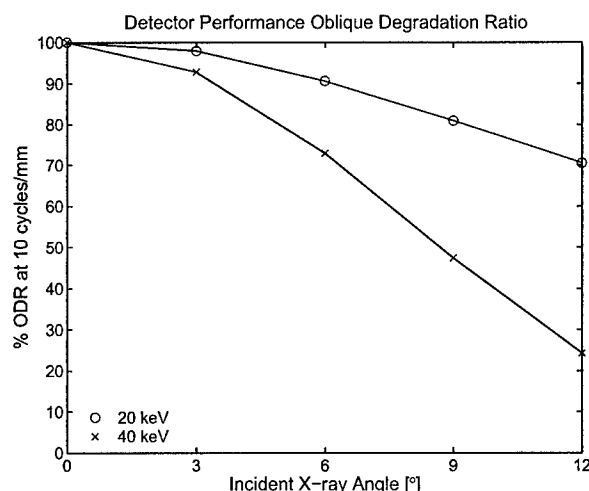
**Figure 6.** Detector performance oblique degradation ratio (ODR) as a function of incident x-ray angle for a spatial-frequency of 10 cycles/mm. The ODR is accurately described by Eqn. 10. The performance at high incident angles drops significantly as the incident x-ray energy increases.

## ACKNOWLEDGMENTS

## REFERENCES

1. J.C. Dainty and R. Shaw, *Image Science*, Academic Press, London, 1974.
2. H.H. Barrett and W. Swindell, *Radiological Imaging*, Academic, New York, 1981.
3. M.J. Yaffe, "Digital Mammography," in *Handbook of Medical Imaging Volume 1: Physics and Psychophysics*, ed. J. Beutel, H.L. Kundel, and R.L. van Metter (SPIE Press, Bellingham, WA, 2000).
4. M.J. Yaffe et al., "Equipment requirements and quality control for mammography," AAPM Report No. 29, 1990.
5. W. Que and J.A. Rowlands, "X-ray imaging using amorphous selenium: Inherent spatial resolution," Med. Phys. **22**, 365–374 (1995).
6. I. Kawrakow and D.W.O. Rogers, "The EGSnrc code system: Monte Carlo simulation of electron and photon transport," Technical Report PIRS-701, National Research Council of Canada, Ottawa, ON, 2000.
7. I. Kawrakow, "Accurate condensed history Monte Carlo simulation of electron transport. I: EGSnrc, the new EGS4 version," Med. Phys. **27**, 485–498 (2000).
8. B.R.B. Walters and D.W.O. Rogers, "DOSXYZnrc Users Manual," Technical Report PIRS-794, National Research Council of Canada, Ottawa, ON, 2002.
9. D.W.O. Rogers, B.A. Faddegon, G.X. Ding, C.-M. Ma, J. We, and T.R. Mackie, "BEAM: a Monte Carlo code to simulate radiotherapy treatment units," Med. Phys. **22**, 503–524 (1995).
10. J.G. Mainprize, N.L. Ford, S. Yin, T. Tumer, and M.J. Yaffe, "Image quality of a prototype direct conversion detector for digital mammography," Proc. SPIE **3659**, 398–406 (1999).
11. J.G. Mainprize, N.L. Ford, S. Yin, T. Tumer, and M.J. Yaffe, "A slot-scanned photodiode-array/CCD hybrid detector for digital mammography," Med. Phys. **29**, 214–225 (2002).
12. W. Zhao, W.G. Ji, J.A. Rowlands, and A. Debrie, "Investigation of imaging performance of amorphous selenium flat-panel detectors for digital mammography," Proc. SPIE **4320**, 536–546 (2001).

13. W. Zhao, W.G. Ji, A. Debrie, and J.A. Rowlands, "Imaging performance of amorphous selenium based flat-panel detectors for digital mammography: Characterization of a small area prototype detector," Med. Phys. **30**, 254–263 (2003).

14. J.H. Siewerdsen, I.A. Cunningham, and D.A. Jaffray, "A framework for noise-power spectrum analysis of multidimensional images," Med. Phys. **29**, 2655–2671 (2002).

15. I.A. Cunningham, "Applied Linear-Systems Theory," in *Handbook of Medical Imaging Volume 1: Physics and Psychophysics*, ed. J. Beutel, H.L. Kundel, and R.L. van Metter (SPIE Press, Bellingham, WA, 2000).

# Computational Engine for Development of Complex Cascaded Models of Signal and Noise in X-Ray Imaging Systems

Mike Sattarivand* and I. A. Cunningham

*Abstract*—The detective quantum efficiency (DQE) is generally accepted as the primary metric of signal-to-noise performance in medical X-ray imaging systems. Simple theoretical models of the Wiener noise power spectrum (NPS) and DQE can be developed using a cascaded-systems approach to assess particular system designs and establish operational benchmarks. However, the cascaded approach is often impractical for the development of comprehensive models due to the complexity and extremely large number of algebraic terms that must be manipulated to describe signal and noise transfer.

We have developed a computational engine that overcomes this limitation. Using a predefined library of elementary physical processes, complex models are assembled and input-output relationships established using a graphical interface. A novel recursive algorithm is described that allows the signal and noise analyses of models with arbitrary complexity including the use of multiple parallel cascades. Symbolic mathematics is used to develop analytic expressions for the NPS and DQE. The algorithm is validated by manual calculation for simple models and by Monte Carlo calculation for complex models. We believe our approach enables the use of complex cascaded models to design better detectors with improved image quality.

*Index Terms*—Cascaded models, detective quantum efficiency (DQE), modulation transfer function (MTF), Monte Carlo, noise power spectrum (NPS).

## I. INTRODUCTION

**M**EDICAL X-ray imaging systems must be designed to achieve maximum image quality for specified radiation dose to the patient. In the scientific and engineering community, image quality and system performance is quantified in the Fourier-based spatial-frequency domain using the modulation transfer function (MTF) [1], [2] to describe spatial resolution and the Wiener noise power spectrum (NPS) to describe image noise. Image signal-to-noise ratio (SNR) is quantified in terms of the noise-equivalent quanta (NEQ) [3]–[6], a fundamental

measure of information content in an X-ray image that can describe the performance of human observers for particular detection tasks under certain idealized conditions [5], [7]. The detective quantum efficiency (DQE) describes the ability of an imaging system to make efficient use of incident quanta in terms of information content. It can be expressed as a function of one-dimensional (1-D) spatial frequency $u$ as [3], [8]

$$\mathrm{DQE}(u) = \frac{\mathrm{NEQ}(u)}{\bar{q}_0} = \frac{\bar{q}_0 G^2 \mathrm{MTF}^2(u)}{\mathrm{NPS}(u)} \qquad (1)$$

where $\bar{q}_0$ is the mean number of X-ray quanta incident per unit area on the detector, $G = \bar{d}/\bar{q}_0$ is the system large-area gain factor and $\bar{d}$ is the corresponding average detector output signal [9]. The DQE has gained great practical merit as a measure of system performance, and describes squared signal-to-noise ratio (SNR) transfer through the imaging system, $\mathrm{DQE}(u) = \mathrm{SNR}_{\mathrm{out}}^2(u)/\mathrm{SNR}_{\mathrm{in}}^2(u)$, for X-ray imaging where the incident quanta are Poisson distributed and, therefore, $\mathrm{SNR}_{\mathrm{in}}^2(u) = \bar{q}_0$ [6], [10].

All Fourier-based methods, including the present work, assume linear and shift-invariant (LSI) imaging systems and wide-sense stationary (WSS) or wide-sense cyclostationary (WSCS) [9] random noise processes [11]. This limits these analyses to noise in images with low contrast structures that are located in regions distant from edge boundaries, generally in the center of the image. Other limitations of Fourier methods have been discussed by Barrett *et al.* [10].

Early application of linear-systems theory, including the use of MTF and related concepts in imaging science, was described by Rossmann and co-workers [1], [2]. General works have subsequently been published by Dainty and Shaw [8], Gaskill [12], Papoulis [13], Doi, Rossmann, and Haus [14], Metz and Doi [15], and many others. Possibly the most extensive use of linear-systems theory in the medical imaging field is the text by Barrett and Swindell [16], who used this approach to describe fundamental principles and characteristics of many imaging systems in radiography, computed tomography (CT), nuclear medicine, ultrasound and other areas. In general however, these early works described signal transfer with simplistic ideas of noise transfer.

Noise propagation is critically important in the design of X-ray imaging systems, which must, therefore, be viewed as stochastic systems. Shockley and Pierce [17], Mandel [18], and Zweig [19] described noise-variance transfer through cascaded quantum gain processes. A more comprehensive Fourier-based description of noise transfer through quantum
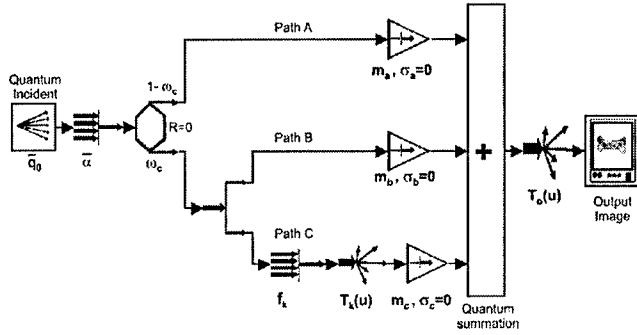
Fig. 1. Cascaded model of a CsI scintillator including reabsorption of $K_\alpha$ characteristic radiation.

gain and scattering processes is given by Rabbani et al. [20], [21], and Barret et al. [10], [22]. These "elementary" processes have well-defined signal and noise-transfer properties [6], [9], [20], [21], [23]–[25]. While a derivation of these transfer expressions is not given here, Table I in Appendix I summarizes the important expressions for reference. Multiple processes can be cascaded to describe transfer of signal and noise in simple models of system performance. The use of parallel cascades to describe noise transfer in quantum-based imaging systems was introduced by Yao and Cunningham [26] and is required when two or more image-forming processes contribute to image formation [27]. Collectively, these works have resulted in a general description of image noise and a comprehensive framework to develop models of imaging-system performance. They are applicable for the description of any quantum-based linear imaging system, including X-ray and optical systems. Use of the DQE and (1) is valid only when the incident distribution of input quanta are Poisson distributed which is always true for X-ray imaging.[8], [10].

Fig. 1 illustrates one such model with three parallel cascades identified as paths A, B, and C. The model describes absorption of X-rays and production of light in a phosphor including the effect of reabsorption of $K_\alpha$ characteristic radiation produced by photoelectric interactions [26]. Path A describes light production at the interaction location when no characteristic X-ray is produced. When a characteristic X-ray is produced, path B describes light production at the interaction location and path C describes light production at the reabsorption location when reabsorption occurs. The role and functionality of each symbol in the model are described in Section II.

When cascading signal and noise expressions from one elementary process to another, the number of terms grows quickly. The model in Fig. 1 involves the manipulation of 38 terms for the NPS while more comprehensive models may require the manipulation of many hundreds of terms [28]. Even though much simplification is generally possible, manipulating the large number of terms is tedious and prone to error, creating a serious limitation to the practical use of complex cascaded models for the optimal design of new X-ray detectors. In this article we describe a computational engine to remove this practical limitation using an automated algorithm that works with parallel-cascade models of arbitrary complexity.

## II. BACKGROUND: ELEMENTARY PROCESSES AND CASCADED MODELS

Cascaded models of X-ray imaging systems describe how quantum-based images are propagated through a system by cascading simple "elementary" processes. A brief summary of these processes is required here to describe how they are used in the present work.

### A. Point Processes

A quantum image is a spatial distribution of quanta, generally in two dimensions. Quanta have negligible size in this context and are represented as point objects. A quantum image is, therefore, represented as the random point process $\tilde{q}(\mathbf{r})$ consisting of a spatial distribution of Dirac impulse functions [6], [9], [10], [29]

$$\tilde{q}(\mathbf{r}) = \sum_{i=1}^{\tilde{N}} \delta(\mathbf{r} - \tilde{\mathbf{r}}_i) \tag{2}$$

where $\tilde{N}$ is a random variable describing the total number of quanta in the image, $\tilde{\mathbf{r}}_i$ is a random vector describing the spatial position of the $i$th quantum and we use the overhead tilde (˜) to indicate a random variable. The image $\tilde{q}(\mathbf{r})$ can be characterized in terms of the mean number of quanta per unit area $\bar{q}$ and by second order statistics including the autocovariance function $K(\mathbf{r})$ in the spatial domain or Wiener noise spectrum $\mathrm{NPS}(u)$ in the spatial-frequency domain. In this work we represent all spatial-frequency quantities in terms of the 1-D frequency $u$ for simplicity, although our results are easily extendible to two dimensions.

An imaging system is, thus, the random process connecting an input X-ray image $\tilde{q}_0(\mathbf{r})$ to an output image $\tilde{d}(\mathbf{r})$, made up of a cascade of a number of elementary processes including those described here.

1) Quantum Gain: Quantum gain [10], [20]–[22] is a random point process in which each input quantum is replaced by $\tilde{g}$ overlapping output quanta

$$\tilde{q}_{\mathrm{out}}(\mathbf{r}) = \tilde{g} \quad \tilde{q}_{\mathrm{in}}(\mathbf{r}) = \sum_{i=1}^{\tilde{N}} \tilde{g}_i \delta(\mathbf{r} - \tilde{\mathbf{r}}_i) \tag{3}$$

where $\tilde{g}$ is an integer random variable with a mean value $\bar{g}$ and standard deviation $\sigma_g$. A graphical representation of this gain process for a sparse 1-D quantum image is shown in Fig. 2. An example of quantum gain is the conversion of X-ray quanta to optical quanta in a scintillator.

The values of $\bar{q}$, NPS and MTF are transferred according to

$$\bar{q}_{\mathrm{out}} = \bar{g}\bar{q}_{\mathrm{in}} \tag{4}$$

$$\mathrm{MTF}_{\mathrm{out}}(u) = \mathrm{MTF}_{\mathrm{in}}(u) \tag{5}$$

$$\mathrm{NPS}_{\mathrm{out}}(u) = \bar{g}^2 \mathrm{NPS}_{\mathrm{in}}(u) + \sigma_g^2 \bar{q}_{\mathrm{in}}. \tag{6}$$

The NPS in (6) consists of two terms. The first, $\bar{g}^2 \mathrm{NPS}_{\mathrm{in}}(u)$, describes transfer of noise by the mean gain $\bar{g}^2$. The second describes additional uncorrelated noise (independent of frequency) resulting from random variations in $\tilde{g}$.
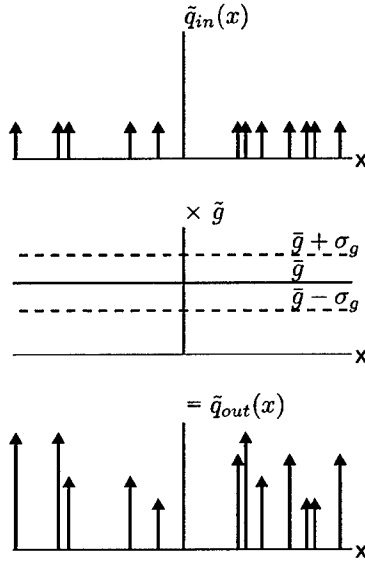
Fig. 2. Each input quantum is replaced by $\tilde{g}$ overlapping output quanta in a quantum gain process where $\tilde{g}$ is an integer random variable with mean $\bar{g}$ and standard deviation $\sigma_g$.



Fig. 3. In a selection process, each input point may appear in the output with a specified probability.

Note that the input to this process need not be a quantum image—it can be a distribution of any type of point events.

*2) Quantum Selection:* Quantum selection is a special case of quantum gain where the gain $\tilde{\alpha}$ is a Bernoulli random variable [11] that can assume values of 0 or 1 only. Hence, $0 \leq \bar{\alpha} \leq 1$ and $\sigma_\alpha^2 = \bar{\alpha}(1-\bar{\alpha})$. This process acts as a binary selection where each input quantum is either passed to the output (probability $\bar{\alpha}$) or not (probability $1 - \bar{\alpha}$)

$$\tilde{q}_{\text{out}}(\mathbf{r}) = \tilde{\alpha} \quad \tilde{q}_{\text{in}}(\mathbf{r}) = \sum_{i=1}^{\tilde{N}} \tilde{\alpha}_i \delta(\mathbf{r} - \tilde{\mathbf{r}}_i). \qquad (7)$$

Signal and noise transfer through a quantum selection process can, thus, be characterized solely in terms of $\bar{\alpha}$ as summarized in Table I of the Appendix. Correlated noise, $\text{NPS}_{\text{in}}(u) - \bar{q}_{\text{in}}$, is passed with a gain of $\bar{\alpha}^2$ while uncorrelated noise, $\bar{q}_{\text{in}}$, is passed with a gain of $\bar{\alpha}$.

Fig. 3 shows the selection process for a sparse 1-D input quantum image. An example of the selection point process is the quantum efficiency of a radiographic screen.

*3) Quantum Scatter:* Quantum scatter is a point process by which each input point is randomly relocated to a new position. Thus, for an input quantum image $\tilde{q}_{\text{in}}(\mathbf{r})$ from (2), we get an output quantum image

$$\tilde{q}_{\text{out}}(\mathbf{r}) = \sum_{i=1}^{\tilde{N}} \delta(\mathbf{r} - \tilde{\mathbf{r}}_i - \tilde{\Delta}_i) \qquad (8)$$

where $\tilde{\Delta}_i$ is a random vector with a probability distribution function (PDF) given by the normalized point spread function $\text{psf}(\mathbf{r})$ that describes the misplacement of the $i$th quantum. The output is expressed in short-hand notation as

$$\tilde{q}_{\text{out}}(\mathbf{r}) = \tilde{q}_{\text{in}}(\mathbf{r}) *_s \text{psf}(\mathbf{r}) \qquad (9)$$

where $*_s$ represents the scatter operation [30]. While this scatter will normally cause blurring of the transferred image by $T(u)$, the Fourier transform of the PSF, scatter differs from convolution used to describe the blurring of a linear filter (described
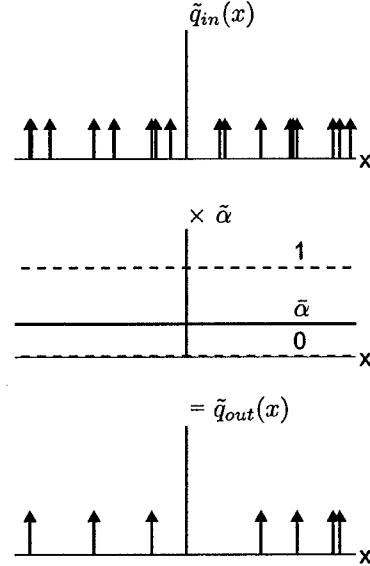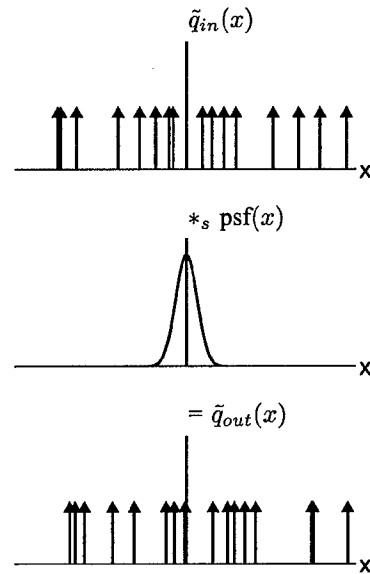


Fig. 4. Each input point is randomly relocated to a new position in the output by the scatter process. The relocation PDF is given by $\text{psf}(x)$.

later) in its noise-transfer properties. The scatter process is illustrated in Fig. 4 for a 1-D quantum image.

Transfer relationships are summarized in Table I. Note that since the scatter operator neither loses nor creates quanta, $\bar{q}_{\text{out}} = \bar{q}_{\text{in}}$. In addition, correlated noise is passed through $|T(u)|^2$ while uncorrelated noise is not. Examples include the scattering of optical quanta in a radiographic screen.

*B. Nonpoint Processes*

*1) Linear Filter:* Linear filters, described in most textbooks on Fourier theory, are used as elementary processes in which blurring at the output image is expressed by a convolution integral

$$\tilde{d}_{\text{out}}(\mathbf{r}) = \tilde{q}_{\text{in}}(\mathbf{r}) * p(\mathbf{r}) \qquad (10)$$

where $p(\mathbf{r})$ is the filter kernel. The mean output signal can be expressed as

$$\bar{d}_{\text{out}} = T(0)\,\bar{q}_{\text{in}}(\mathbf{r}) \tag{11}$$

where $T(u)$ is the filter characteristic function given by the Fourier transform of the kernel and has a zero-frequency value

$$T(0) = \int\limits_{-\infty}^{\infty} p(\mathbf{r})d^2\mathbf{r}. \tag{12}$$

Transfer relationships are given in Table I. Note that unlike quantum scatter, both correlated and uncorrelated noise components are passed through $|T(u)|^2$. The output NPS of a linear filter is, therefore, always band limited and does not have an uncorrelated component.

*2) Quantum Integration:* Many imaging detectors operate by producing an electrical signal proportional to the number of accumulated image quanta (such as electronic charge) in individual detector elements. This "binning" process is a spatial integration of points that represent interacting quanta. If all quanta incident on an element of width $a_x$ are detected the number of quanta interacting in the $n$th element of a detector array at $x = nx_0$ can be written as

$$\tilde{d}_{\text{out}}(x) = \int\limits_{x-\frac{a_x}{2}}^{x+\frac{a_x}{2}} \tilde{q}_{\text{in}}(x')dx'$$

$$= \int\limits_{-\infty}^{\infty} \tilde{q}_{\text{in}}(x')\Pi\left(\frac{x-x'}{a_x}\right)dx' \tag{13}$$

where $\Pi(x/a_x)$ is a rectangular function having the value 1 for $-(a_x/2) < x < (a_x/2)$ and 0 elsewhere. We can, therefore, express integration as a convolution

$$\tilde{d}_{\text{out}}(x) = \tilde{q}_{\text{in}}(x) * \Pi\left(\frac{x}{a_x}\right) \tag{14}$$

giving the value for an element centered at $x$ for all $x$ (physical or not). Thus, quantum integration is a special case of a linear filter

$$T(u) = a_x\text{sinc}(\pi a_x u) = \frac{\sin(\pi a_x u)}{\pi u} \tag{15}$$

where sinc function is defined as $\text{sinc}(X) = \sin(X)/X$. Quantum integration, therefore, changes an input quantum image to an output presampling (analog) image. Signal and noise relationships are provided in Table I.

*3) Sampling:* Sampling of an analog image to produce a discrete digital image has been presented as an elementary process in cascaded systems by a number of authors [9], [31]. We represent sampling as multiplication by an infinite train of uniformly-spaced $\delta$ functions at intervals of $x_o$. Thus, for a 1-D image, the output is

$$\tilde{d}^{\dagger}_{\text{out}}(x) = \tilde{d}_{\text{in}}(x) \times \sum_{n_x=-\infty}^{\infty} \delta(x - n_x x_o)$$

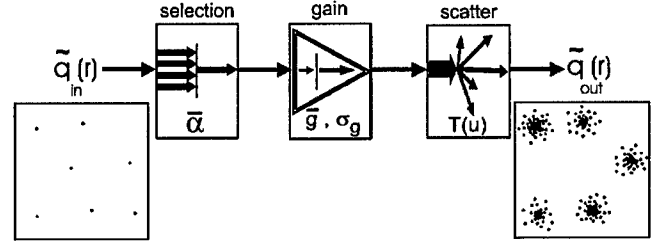$$= \sum_{n_x=-\infty}^{\infty} \tilde{d}_n \delta(x - n_x x_o) \tag{16}$$



Fig. 5. A simple cascaded model of a radiographic screen consists of quantum selection, gain and scatter processes.

where the $\dagger$ superscript is used to indicate a discretely sampled function represented as an infinite train of scaled and uniformly-spaced $\delta$ functions. When $\tilde{d}_{\text{in}}(x)$ is a detector presampling signal, the digital image consists of a set of the random values $\tilde{d}_n$.

This sampling process is a linear operation although it results in a shift-variant output. Fourier-based metrics are still applicable since the output noise, even in the presence of noise aliasing, is a WSCS random process. The shift variance can be removed by sinc-interpolation, regardless of the relative position of the sampling grid, only when there is no aliasing. The signal and noise transfer functions are summarized in Table I for the case of no signal aliasing (the "presampling" signal).

### C. Cascading Elementary Processes

Some X-ray imaging systems can be modeled by cascading elementary processes where the output of one process becomes a virtual input to the next. For example, in a transparent radiographic screen with a quantum efficiency $\eta$, some incident X-ray quanta are absorbed while others escape. This can be modeled as a random selection process with a mean probability $\bar{\alpha} = \eta$. Each interacting quantum is converted into a large number of optical quanta, represented as a quantum-gain process. Subsequently, light quanta are relocated randomly before they leave the screen, a process which can be modeled as a quantum scattering process. Fig. 5 shows a cascaded model representing these three stages. A two-dimensional (2-D) graphical representation of sample input $\tilde{q}_{\text{in}}(\mathbf{r})$ and output $\tilde{q}_{\text{out}}(\mathbf{r})$ are illustrated where each point represents a quantum. Combining (3), (7), and (9), the output quantum image can be expressed as

$$\tilde{q}_{\text{out}}(\mathbf{r}) = [\tilde{\alpha}\,\tilde{g}\,\tilde{q}_{\text{in}}(\mathbf{r})] *_s \text{psf}(\mathbf{r}) \tag{17}$$

where $\tilde{\alpha}$, $\tilde{g}$, and $\text{psf}(\mathbf{r})$ represent the selection probability, gain factor and light scattering distribution respectively. Since the input quantum image is Poisson distributed, $\text{NPS}_{\text{in}}(u) = \bar{q}_{\text{in}}$ [10] and by applying signal and noise transfer for all processes from Table I, the output quantum image can be characterized as

$$\bar{q}_{\text{out}} = \bar{\alpha}\bar{g}\bar{q}_{\text{in}} \tag{18}$$

$$\text{MTF}_{\text{out}}(u) = T(u) \tag{19}$$

$$\text{NPS}_{\text{out}}(u) = \bar{\alpha}\bar{q}_{\text{in}}\left[\bar{g}^2 + \sigma_g^2 - \bar{g}\right]|T(u)|^2 + \bar{\alpha}\bar{g}\bar{q}_{\text{in}}. \tag{20}$$

### D. Parallel Cascades of Elementary Processes

In complex models where the imaging system cannot be represented as a single cascade of elementary processes, it is sometimes necessary to use a number of parallel cascade paths to represent multiple image-forming processes that are summed to
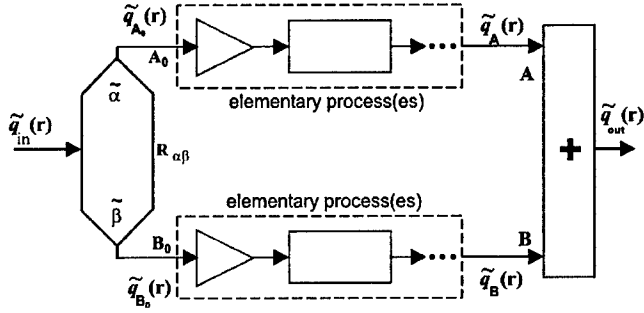
Fig. 6. Schematic illustration of a quantum branch process creating two parallel cascade paths that are summed to produce a single output image.



Fig. 7. A summation process with $N_a$ input cascade paths.

produce the output signal as illustrated in Fig. 6. Each path consists of arbitrary cascades of elementary point processes acting on images $\tilde{q}_{A_0}(\mathbf{r})$ and $\tilde{q}_{B_0}(\mathbf{r})$ respectively, each of which consists of randomly selected points from $\tilde{q}_{in}(\mathbf{r})$. The random variables $\tilde{\alpha}$ and $\tilde{\beta}$ describe the selection of points for each path

$$\begin{cases} \tilde{q}_{A_0}(\mathbf{r}) = \tilde{\alpha} \ \tilde{q}_{in}(\mathbf{r}) = \sum_{i=1}^{\tilde{N}} \ \tilde{\alpha}_i \delta(\mathbf{r} - \tilde{\mathbf{r}}_i) \\ \tilde{q}_{B_0}(\mathbf{r}) = \tilde{\beta} \ \tilde{q}_{in}(\mathbf{r}) = \sum_{j=1}^{\tilde{N}} \ \tilde{\beta}_j \delta(\mathbf{r} - \tilde{\mathbf{r}}_j) \end{cases} \quad (21)$$

where $\tilde{\alpha}_i$ and $\tilde{\beta}_j$ can have values of 0 or 1 only. Therefore, the "quantum branch" process in Fig. 6 acts as a two-way selection process so that at positions $A_0$ and $B_0$

$$\begin{cases} \bar{q}_{A_0} = \bar{\alpha}\bar{q}_{in} \\ \bar{q}_{B_0} = \bar{\beta}\bar{q}_{in} \end{cases} \quad (22)$$

$$\begin{cases} \mathrm{MTF}_{A_0}(u) = \mathrm{MTF}_{in}(u) \\ \mathrm{MTF}_{B_0}(u) = \mathrm{MTF}_{in}(u) \end{cases} \quad (23)$$

$$\begin{cases} \mathrm{NPS}_{A_0}(u) = \bar{\alpha}^2 \left[\mathrm{NPS}_{in}(u) - \bar{q}_{in}\right] + \bar{\alpha}\bar{q}_{in} \\ \mathrm{NPS}_{B_0}(u) = \bar{\beta}^2 \left[\mathrm{NPS}_{in}(u) - \bar{q}_{in}\right] + \bar{\beta}\bar{q}_{in}. \end{cases} \quad (24)$$

For different input points in $\tilde{q}_{in}(\mathbf{r})$ (that is $i \neq j$), the random variables $\tilde{\alpha}_i$ and $\tilde{\beta}_j$ are always independent. That is, selection of any one point for path A or B has no influence on the selection of any other point. However, for any specified input point in $\tilde{q}_{in}(\mathbf{r})$ ($i = j$), $\tilde{\alpha}_i$ and $\tilde{\beta}_j$ may simultaneously be zero (representing a lost quantum, not entering either path) or unity (the input quantum to the branch causes subsequent events in both paths). In general, $\tilde{\alpha}_i$ and $\tilde{\beta}_j$ are correlated random variables with the cross correlation $R_{\alpha\beta}$

$$R_{\alpha\beta} = E\{\tilde{\alpha}_i \tilde{\beta}_j\}\Big|_{i=j}. \quad (25)$$

A properly designed model must necessarily satisfy any applicable laws of conservation. For example, if one quantum enters both paths in Fig. 6, the corresponding conversion gains in each path must collectively satisfy energy conservation laws.

Signal-transfer expressions for the "summation" process in Fig. 6 can be expressed as

$$\bar{q}_{out} = \bar{q}_A + \bar{q}_B \quad (26)$$

$$\mathrm{MTF}_{out}(u) = \frac{\bar{q}_A}{\bar{q}_A + \bar{q}_B}\mathrm{MTF}_A(u) + \frac{\bar{q}_B}{\bar{q}_A + \bar{q}_B}\mathrm{MTF}_B(u). \quad (27)$$

If $\tilde{q}_A(\mathbf{r})$ and $\tilde{q}_B(\mathbf{r})$ are statistically correlated, the cross spectral density of these random processes must be considered, giving

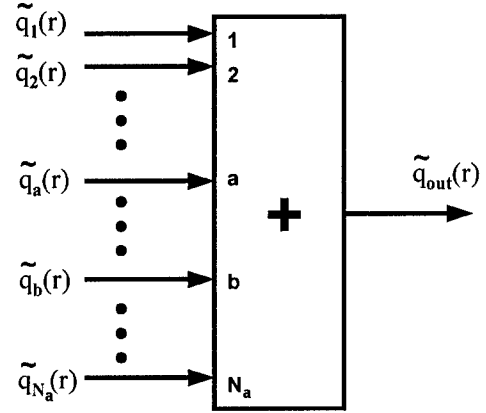$$\mathrm{NPS}_{out}(u) = \mathrm{NPS}_A(u) + \mathrm{NPS}_B(u) + 2\mathrm{NPS}_{AB}(u) \quad (28)$$

where $\mathrm{NPS}_A(u)$ and $\mathrm{NPS}_B(u)$ are the NPS of images $\tilde{q}_A(\mathbf{r})$ and $\tilde{q}_B(\mathbf{r})$ respectively and $\mathrm{NPS}_{AB}(u)$ is the cross spectral density equal to the Fourier transform of the cross covariance of $\tilde{q}_A(\mathbf{r})$ and $\tilde{q}_B(\mathbf{r})$. This term will be nonzero if $\tilde{\alpha}$ and $\tilde{\beta}$ are correlated, i.e. if the cross correlation $R_{\alpha\beta}$ is nonzero.

A general form of the cross spectral density $\mathrm{NPS}_{AB}(u)$ for two point processes $\tilde{q}_A(\mathbf{r})$ and $\tilde{q}_B(\mathbf{r})$ has been described recently for this type of application [26]. We write it here in a form that differs slightly from the original as

$$\mathrm{NPS}_{AB}(u) = P_A(u)P_B^*(u) \left[\mathrm{NPS}_{in}(u) + \frac{\bar{q}_{in}K_{\alpha\beta}}{(\bar{\alpha}\bar{\beta})}\right] \quad (29)$$

where $\mathrm{NPS}_{in}(u)$ and $\bar{q}_{in}$ correspond to the NPS and mean density at the input to the branch point, $P_A(u)$ and $P_B(u)$ are products of all mean gains and scatter characteristic functions in paths A and B respectively (including the branch selection probabilities $\tilde{\alpha}$ and $\tilde{\beta}$), and $K_{\alpha\beta} = R_{\alpha\beta} - \bar{\alpha}\bar{\beta}$ is the cross covariance [11] of $\tilde{\alpha}$ and $\tilde{\beta}$. The asterisk in $P_B^*(u)$ indicates the complex conjugate. Note that this form differs slightly from the original [26] so that factors $P_A(u)$ and $P_B(u)$ are the characteristic functions of paths $A$ and $B$ starting from the connecting branch point, respectively.

This result is generalized for the summation of $N_a$ cascade paths as illustrated in Fig. 7, giving

$$\bar{q}_{out} = \sum_{a=1}^{N_a} \bar{q}_a \quad (30)$$

$$\mathrm{MTF}_{out}(u) = \sum_{a=1}^{N_a} \frac{\bar{q}_a}{\bar{q}_{out}}\mathrm{MTF}_a(u) \quad (31)$$

$$\mathrm{NPS}_{out}(u) = \sum_{a=1}^{N_a} \mathrm{NPS}_a(u) + \sum_{a=1}^{N_a} \sum_{\substack{b=1, \\ b \neq a}}^{N_a} \mathrm{NPS}_{ab}(u) \quad (32)$$

where $a$ and $b$ are indexes representing the cascade paths. The second term in (32) indicates that cross terms between all possible pairs of paths must be considered using (29).

### III. THEORY

Our algorithm to calculate the signal and noise properties of complex cascaded models consists of three steps: 1) determine transfer expressions for the mean signal, MTF and NPS for each
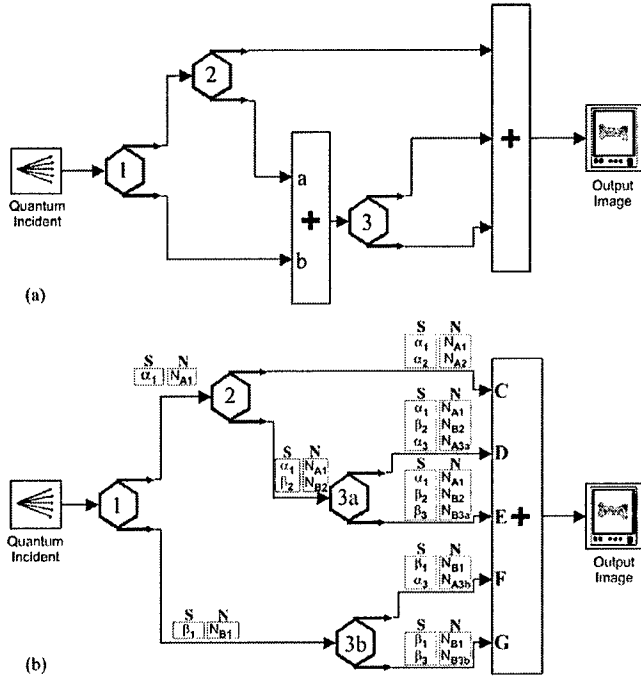
Fig. 8. The distributive-over-addition property of elementary processes are used to convert the model in (a) to the equivalent model in (b). This change avoids nested loops and results in a single summation point close to the model output. Vectors $S$ and $N$ are used to track information required for the cross spectral density calculation.
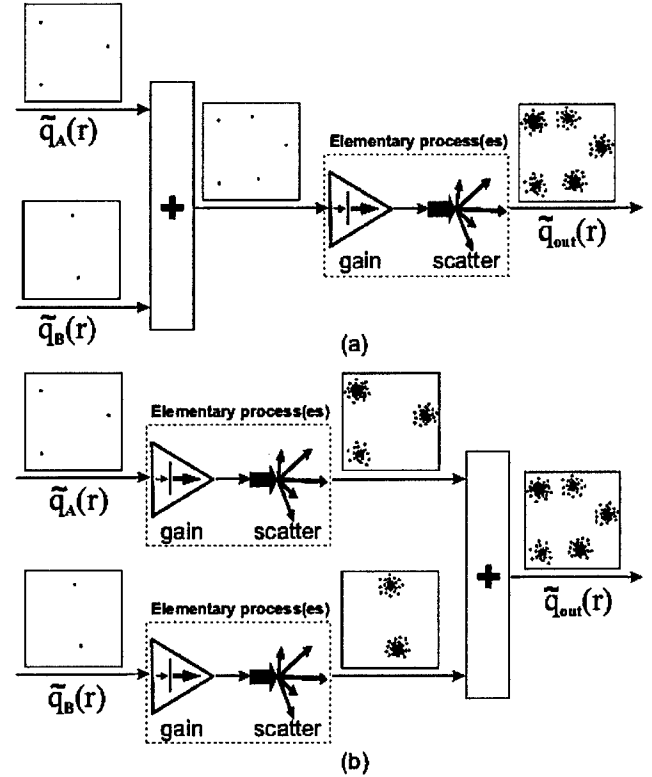


Fig. 9. The distributive-over-addition property of elementary processes means that the output from cascaded models (a) and (b) are equivalent for the same inputs $\tilde{q}_A(\mathbf{r})$ and $\tilde{q}_B(\mathbf{r})$.

process; 2) convert the model into an equivalent model consisting of only one summation process; and 3) cascade transfer expressions for each process including cross spectral density terms. The DQE is then determined using (1).

### A. Step 1: General Form of an Elementary Process

Transfer relationships for the elementary (point and nonpoint) processes described above can be written in the general form of

$$
\begin{cases}
\bar{s}_{\text{out}} = f_1(\bar{s}_{\text{in}}, p_1, p_2, \ldots) \\
\text{MTF}_{\text{out}}(u) = f_2(\text{MTF}_{\text{in}}(u), \bar{s}_{\text{in}}, p_1, p_2, \ldots) \\
\text{NPS}_{\text{out}}(u) = f_3(\text{NPS}_{\text{in}}(u), \bar{s}_{\text{in}}, p_1, p_2, \ldots)
\end{cases}
\tag{33}
$$

where $\bar{s}$ represents a generalized image signal ($\bar{s} = \bar{q}$ for quantum images and $\bar{s} = \bar{d}$ for nonquantum images), $f_1$, $f_2$, and $f_3$ are analytic functionals and $p_1$, $p_2$, etc., are parameters specific to each elementary process. A list of elementary processes and their transfer relationships is given in Table I.

### B. Step 2: Equivalent Model

Cascaded models of real imaging systems can be very complex and contain multiple parallel cascades. While Fig. 1 illustrates a relatively simple model of a scintillator that describes reabsorption of $K_\alpha$ characteristic X-rays, more comprehensive models currently under development [28] accommodate multiple characteristic radiations and scattering mechanisms and require multiple nested parallel cascades. Fig. 8(a) illustrates a (hypothetical) example of nested cascades. The problem is that we do not know how to interpret (29) for these complex models.

We overcome this problem by converting each complex model with nested parallel cascades into an equivalent model

having no nested cascades. This is made possible by noting that each of the point processes described above have signal and noise transfer characteristics that are distributive over addition, as described in Appendix II. This property allows us to move these processes across a summation point as illustrated in Fig. 9. That is, the output image $\tilde{q}_{\text{out}}(\mathbf{r})$ has the same signal and noise independent of whether the process acts on the output of the summation 9(a) or on each of the inputs 9(b) prior to summation. This principle is critical for enabling a generalized algorithm to accommodate complex models. With appropriate application, each cascade path can be extended to a later position in the model. We choose to extend all paths to a single multi-input summation point as illustrated in Fig. 8. This prevents nested loops and allows for simple application of (28). The only requirement for use of these equivalent models is that all elementary processes act independently on each point in the images—a requirement already used in the development of their transfer expressions. Note however that this argument only applies to moving processes across summation points and that the relative positions of elementary processes cannot generally be changed. For example, a scatter followed by a gain is not equivalent to gain followed by scatter.

### C. Step 3: Cascading Signal and Noise in Equivalent Models

Cascading signal and noise involves applying (30)–(32) at the summation point in the equivalent model and then cascading signal and noise to the output. The $\text{NPS}_a(u)$ terms at the summation are obtained by applying the transfer functions from

Table I as required for each process where selection of sub images in branch points is a quantum selection process with probability $\bar{\alpha}$ or $\bar{\beta}$.

Calculation of the cross terms is slightly more complicated. We let $m$ be a "process index" that labels processes along each possible cascade path connecting the source ($m = 0$) to the final summation process ($m = N_m|_a$ where $N_m|_a$ is the number of processes along path "$a$"). We also let $T_m(u)$ be the generalized characteristic function for the $m$th process which may be a mean gain or a scatter transfer function. If we let $m = \kappa$ denote the process index identifying the branch point linking process paths $a$ and $b$, the function $P_a(u)$ can be written as

$$P_a(u) = \left. \prod_{m=\kappa}^{N_m} T_m(u) \right|_a \qquad (34)$$

where $N_m$ is the number of processes along the cascade path including the linking branch. Similar expressions can be written for other paths. In addition, we make the further substitution

$$\begin{cases} N_a(u) \equiv \left[ \text{NPS}_{\kappa-1}(u) + \frac{\bar{q}_{\kappa-1}K_{\alpha_\kappa\beta_\kappa}}{(\bar{\alpha}_\kappa\bar{\beta}_\kappa)} \right]_a \\ N_b(u) \equiv 1 \end{cases} \qquad (35)$$

where $\text{NPS}_{\kappa-1}(u)$ and $\bar{q}_{\kappa-1}$ are the NPS and mean density at the input to the joining branch. Equation (29), therefore, becomes

$$\text{NPS}_{ab}(u) = P_a(u)P_b(u)N_a(u)N_b(u). \qquad (36)$$

For example, the cross term between cascade paths $C$ and $G$ linked through branch point #1 in Fig. 8(b) is

$$\text{NPS}_{CG}(u) = \bar{\alpha}_1\bar{\alpha}_2 \times \bar{\beta}_1\bar{\beta}_3 \times \bar{q}_0 \left[ 1 + \frac{K_{\alpha_1\beta_1}}{(\alpha_1\beta_1)} \right] \times 1. \qquad (37)$$

Similarly for paths $C$ and $D$ connected through branch point #2

$$\text{NPS}_{CD}(u) = \bar{\alpha}_2 \times \bar{\beta}_2\bar{\alpha}_3 \times \bar{q}_0\alpha_1 \left[ 1 + \frac{K_{\alpha_2\beta_2}}{(\alpha_2\beta_2)} \right] \times 1. \qquad (38)$$

The choice of which path is identified as the "$a$" path is arbitrary.

## IV. IMPLEMENTATION

Implementation of the algorithm to calculate signal and noise transfer through the cascaded model is divided into two components: A) a graphical environment for building the model; and B) a computational component to calculate the transfer of $\bar{s}$, MTF, NPS, and DQE of the model system.

### A. GUI Environment for Building Models

The graphical user interface (GUI) was developed to facilitate the design of complex models using the software package Simulink in Matlab [32]. Each physical process is implemented as an "S-Function" block and stored in a library of all processes. Signal and noise transfer properties are implemented using precompiled "mex" files. The user performs a drag-and-drop operation to select appropriate processes from the library, labels the required parameters for each process as desired, and connects inputs and outputs together to build a model with the desired connection topology.

Signal and noise at the input and output of each process is described using a data structure consisting of: 1) a label indicating the image type, i.e., quantum or analog image; 2) ASCII strings for the symbolic math representation of $\bar{s}$, MTF($u$), and

NPS($u$); and, 3) ASCII-string representations of vectors $S$ and $N$ required for the calculation of $P(u)$ and $N(u)$ for each cascade path as described later. Starting with the first process (normally a "source" process that describes the Poisson distribution of X-ray quanta incident on the imaging system), the Simulink package passes the data structure from the output of the one process to the input of the next. In this way, the data structure is passed throughout the model according to the connections between processes appropriate for the model. Feedback loops are not allowed for these models.

### B. Calculation of Signal and Noise Transfer

Each process implements signal and noise transfer using the symbolic math package in Matlab [33] to operate on the input data structure according to specific rules summarized in Table I and illustrated in Figs. 10 and 11. The algorithm follows the inter-process connections in the original model but implements signal and noise transfer as it would be passed through the equivalent model. This is achieved by providing for the passing of a compact data structure that can describe more than one image. For example, the summation "$a + b$" in Fig. 8(a) results in a two-image data structure being passed to branch point #3 in Fig. 8(a). By defining all summation points (except the final one) to simply pass all input structures unchanged, and by allowing for the processing of multiple data structures by each process, signal and noise are effectively passed through the equivalent model without additional coding.

Each process must also maintain the $S$ and $N$ vectors in the data structure required to calculate the NPS cross terms in the summation process according to (34)–(36). The vector $S$ is a linear array of symbolic mathematics expressions for any specified cascade path. The number of elements in $S$ increases with each branch and the $\lambda$th element is the product of all process characteristic functions starting from branch $\lambda$ to the process before branch $\lambda + 1$

$$S_\lambda = \prod_{m=b_\lambda}^{b_{\lambda+1}-1} T_m(u) \qquad (39)$$

where the value of $b_{\lambda+1} - 1$ cannot exceed the process index of the final summation. The $P(u)$ values for any two paths are, therefore, given by

$$P_a(u) = \left. \prod_{\lambda=b_c}^{N_\lambda} S_\lambda \right|_a \qquad (40)$$

where $\lambda = b_c$ is the branch number linking the two paths and $N_\lambda$ is the number of branch processes along the path. The $S$ vector has $N_\lambda$ elements. The algorithm determines the value of $\lambda = b_c$ by comparing entries in $S$ for each cascade path. Starting with $\lambda = 1$, the first entry that differs corresponds to the branch process $\lambda = b_c$. For example, after branch point #1, $S_1$ consists of the variables $\bar{\alpha}_1$ and $\bar{\beta}_1$ in the upper and lower paths respectively, as illustrated in Fig. 8(b). This identifies $\lambda = 1$ as the linking branch between paths $C$, $D$ or $E$ with $F$ or $G$. The algorithm then uses (40) to calculate the $P(u)$ value for each cascade path.

The $N$ vectors contain the $N(u)$ terms for each branch point but are too long to include in Fig. 8(b) and, thus, are represented
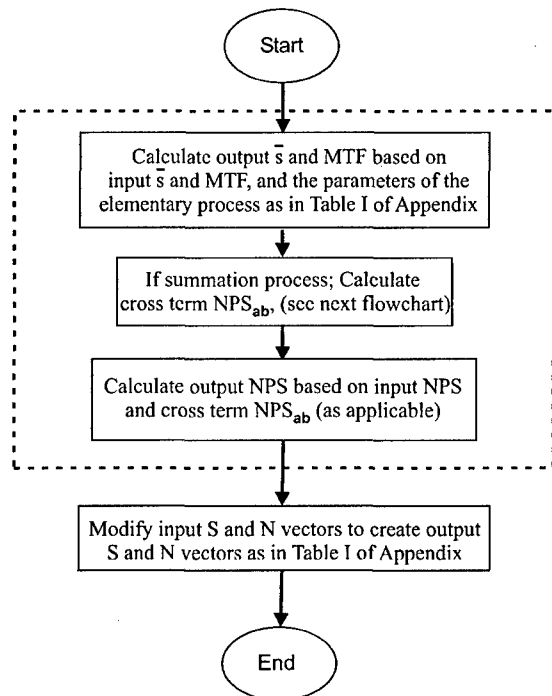
Fig. 10.   A general flowchart of an elementary process to calculate $\bar{s}$, MTF, and NPS.
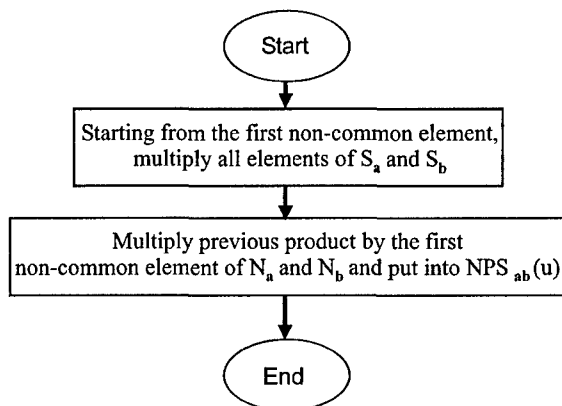


Fig. 11.   Flowchart to calculate NPS cross term between input paths $a$ and $b$ in summation process.

by labels such as $N_{A1}$ representing $N_A(u)$ from (35) evaluated at the input of branch point #1.

Figs. 10 and 11 illustrate a flowchart for the algorithm. After initialization, $\bar{s}_{\text{out}}$ and $\text{MTF}_{\text{out}}(u)$ are calculated using appropriate equations from Table I. If the process is a summation, the NPS cross term is required as indicated by (32) and described later. Otherwise, $\text{NPS}_{\text{out}}(u)$ is only a function of $\text{NPS}_{\text{in}}(u)$ and the parameters of the process. The dotted-line box of the flowchart shows calculations required for $\bar{s}_{\text{out}}$, $\text{MTF}_{\text{out}}(u)$, and $\text{NPS}_{\text{out}}(u)$ expressions. The last step of the flowchart builds up the vectors $S$ and $N$. For each process, $S$ and $N$ are modified, based on (39) and (35), and passed to the output. Table I shows these modifications for each process. For gain, selection, scatter, charge integration, linear filter, and sampling processes, $N$ is

transferred unchanged and the last row of the $S$ vector is multiplied by the characteristic functions of these processes as (39) requires. As mentioned earlier, a branch process adds a new row to $S$ and $N$. The summation process will not change $S$ and $N$ vectors since the equivalent cascaded model has only one summation process where all NPS cross terms are calculated.

Simplification routines are called from within the mex files of each elementary process after the algorithm calculates analytic expressions. This makes sure that the signal and noise expressions are minimally simplified before being cascaded to the next stage. Our reason for simplifying expressions as they are cascaded is to reduce the length of character strings used to represent the expressions. Matlab has a 128-kbyte size limitation on these strings. While this corresponds to an equation that would fill several pages of text, and this limitation has never been reached in practice, it is prudent to simplify expressions whenever possible.

Information on the code used in this research can be obtained at www.imaging.robarts.ca/~icunning/snrtk.

## V. VALIDATION

The algorithm has been validated with manual calculations for simple models. However, this is impractical for complex models and hence a special-purpose Monte Carlo (MC) code described later was developed to generate MTF and NPS results that are compared with analytic results. "Validation" here does not mean underlying models are physically valid—it means only that the models are evaluated correctly by the computational engine.

### A. Monte Carlo Validation

In addition to propagating analytic expressions of signal and noise, the mex files generate the necessary C source code to perform a MC simulation of each physical process they represent. Thus, while the computational engine calculates signal and noise expressions for an arbitrary model, it also generates a numerical simulation of the same system. This guarantees consistency between the analytic and MC calculations. Appropriate choice of model design and parameter values enables validation of any complex model. The number of histories required in MC simulations depends on the complexity of the model and is chosen by trial and error.

Fig. 12 illustrates a MC simulation for a simple model consisting of a single gain and scatter. Although the illustration shows 2-D sample images, all MC calculations are performed using 1-D geometry to simplify the analysis and minimize the number of MC histories required. Two sample images are generated in the simulation. The first describes the system response to a "point" source of incident X-rays at the center of the image. This image is transferred by MC routines for each process to produce the output image that is the impulse response function (IRF) of the model. The MTF is the absolute value of the Fourier transform of the IRF, normalized to unity at $u = 0$.

The second sample image describes the model response to a uniform Poisson distribution of incident X-rays. This image is separated into a large number of sub images and the sample
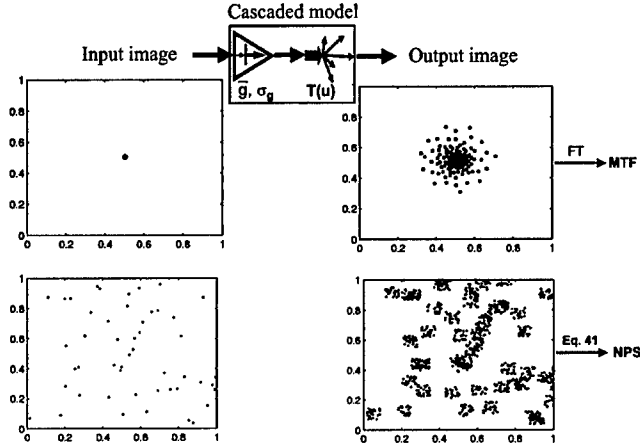
Fig. 12.   Illustration of the MC calculation to determine output MTF and NPS. The MTF is determined from a MC simulation of the point-spread function and the NPS is determined from a simulation of the output image corresponding to a uniform Poisson distribution of input quanta.

power spectrum after subtraction of the mean value is determined for each. The ensemble sample average is the image NPS: [9]

$$\text{NPS}(u) = \frac{x_0}{N_x} E\left\{|DFT\{\Delta d_x\}|^2\right\} \qquad (41)$$

where $x_0$ is the sample spacing, $N_x$ is the number of samples for each sub-image and $E\{\ \}$ represents the expectation value. Once the NPS and MTF for the cascaded model are calculated, the DQE is determined. We show results for NPS calculations, however similar agreement between MC and theoretical results were obtained for the MTF and DQE.

The *ran0* routine in [34] was used to generate uniformly distributed random numbers on a linux-based platform. The authors claim that the number of random numbers that can be generated without repetition is given by variable RAND_MAX. For our compiler this number is 2 147 483 647, much greater than the number used in this work.

### B. Validation of Simple Cascade

The simple cascaded model shown in Fig. 12 represents the conversion of input quanta to clusters of secondary quanta. Using signal and noise transfer relationships listed in Table I, the analytic NPS for this model, validated by manual calculation, is given by

$$\text{NPS}(u) = \bar{q}_{\text{in}}\left(\bar{g}^2 + \sigma_g^2 - \bar{g}\right)|\text{T}(u)|^2 + \bar{g}\bar{q}_{\text{in}}. \qquad (42)$$

By applying the MC method described above, the NPS of the model is shown in Fig. 13 for $1.5 \times 10^6$ histories. The results show excellent agreement between MC and analytic NPS of (42), although the MC results are slightly below theory at spatial frequencies close to zero. This small discrepancy is believed to be a detrending artifact. This artifact is due to truncation of sample images to a noninfinite extent. This affects zero frequency regions in spatial-frequency domain that correspond to image data located at infinitely hight spatial values in spatial domain. We ignore this effect and expect to see it in all our MC results. Excellent agreement is maintained as the mean gain factor is increased from 10 to 12.
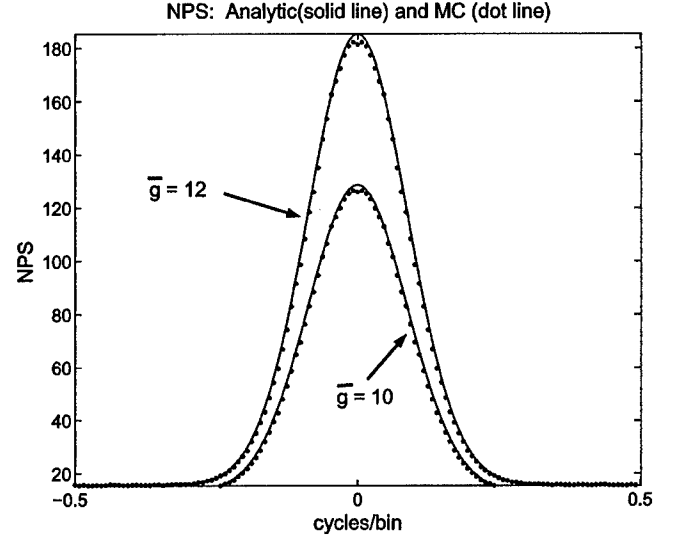


Fig. 13.   Validation of simple cascade with changes in mean gain value.
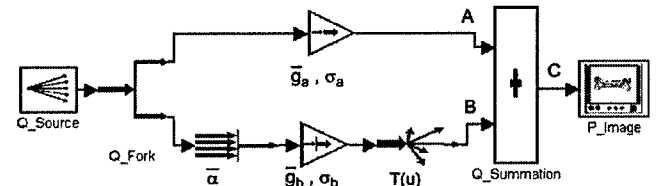


Fig. 14.   A simple parallel-cascades model.

### C. Validation of Cross Spectral Density Term

Fig. 14 shows an example of a simple parallel-cascades model. The upper path has only one gain process whereas the lower path consists of selection, gain and scatter processes. The output NPS at point C can be expressed in the form of (28), where $\text{NPS}_{AB}(u)$ is the cross spectral density between paths A and B at the summation point. This cross term is given by (29), which for this model evaluates to

$$\text{NPS}_{AB}(u) = \bar{q}_{\text{in}}\bar{\alpha}\bar{g}_a\bar{g}_b\text{T}(u). \qquad (43)$$

MC and analytic results at points A, B, and C, as well as the NPS cross term, are compared in Fig. 15. Note that a flat NPS at point A is the result of no autocorrelation in the sample image at this point. Equation (29) also indicates that the cross term depends on the product of mean transfer functions along each path. Thus, the form of the cross term is strongly model dependent.

### D. Validation of Simplified Photoelectric Model

Fig. 1 shows a simple model of photoelectric interactions in a detector and represents the first published use of parallel cascades [26], [27]. The analytic signal and noise expressions obtained using the computational engine are

$$\bar{q}_{\text{out}} = \bar{q}_0\bar{\alpha}\omega_c f_k m_c + \bar{q}_0\bar{\alpha}\omega_c m_b$$
$$+ \bar{q}_0\bar{\alpha}m_a - \bar{q}_0\bar{\alpha}\omega_c m_a \qquad (44)$$

$$\text{MTF}_{\text{out}}(u) = \frac{\omega_c f_k m_c \text{T}_k(u) + \omega_c m_b + m_a - m_a\omega_c}{\omega_c f_k m_c + \omega_c m_b + m_a - m_a\omega_c}$$
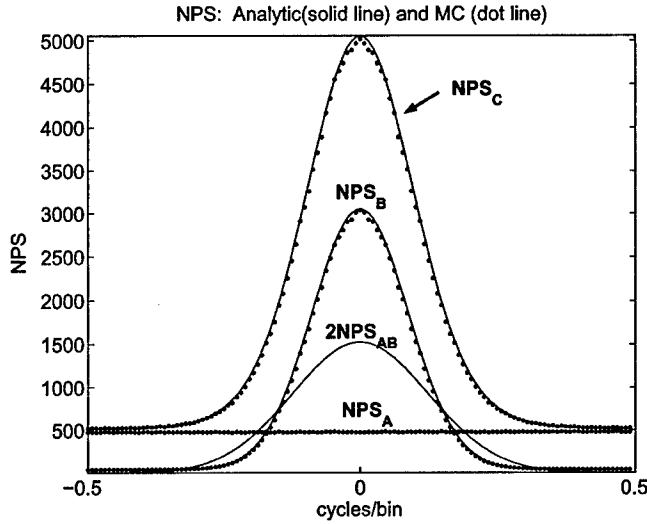$$\times \text{T}_o(u) \qquad (45)$$

Fig. 15.   Output NPS of image C contains a cross term $\text{NPS}_{AB}(u)$.
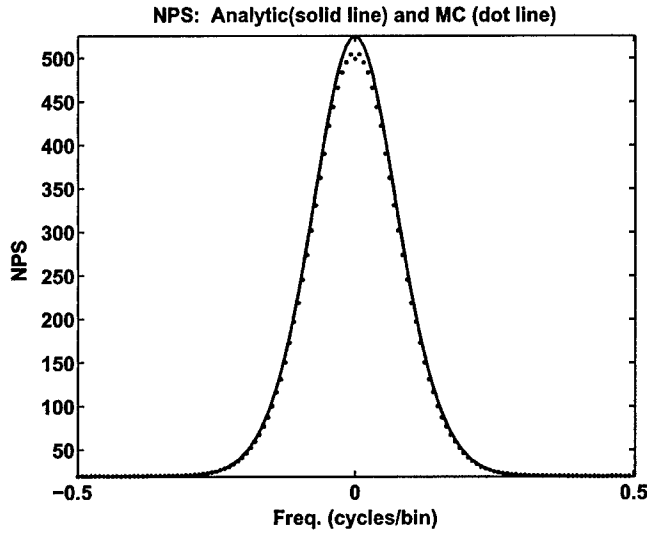


Fig. 16.   MC and analytic NPS of the simplified photoelectric model.

$$\text{NPS}_{\text{out}}(u) = \left[ m_c^2 \bar{q}_0 \bar{\alpha} \omega_c f_k + 2 m_b f_k m_c \bar{q}_0 \bar{\alpha} \omega_c T_k(u) \right.$$
$$\left. + m_b^2 \bar{q}_0 \bar{\alpha} \omega_c + (1 - \omega_c) m_a^2 \bar{q}_0 \bar{\alpha} - \bar{q}_{\text{out}} \right]$$
$$\times \, T_o^2(u) + \bar{q}_{\text{out}} \tag{46}$$

where the parameters are identified in Fig. 1.

The MC and analytic results are compared in Fig. 16 for $2.7 \times 10^6$ X-ray photon histories. Excellent agreement was obtained in all cases.

## VI.  CONCLUSION

The development of better X-ray detectors for improved disease detection or reduced patient dose requires a comprehensive understanding of the relationship between the physics of image-forming processes and quantitative measures of detector performance. Recent works have resulted in the development of comprehensive transfer-theory approaches in cascaded models. However, the need to manipulate large numbers of algebraic terms in the cascaded approach has limited its practical usefulness for complex realistic models.
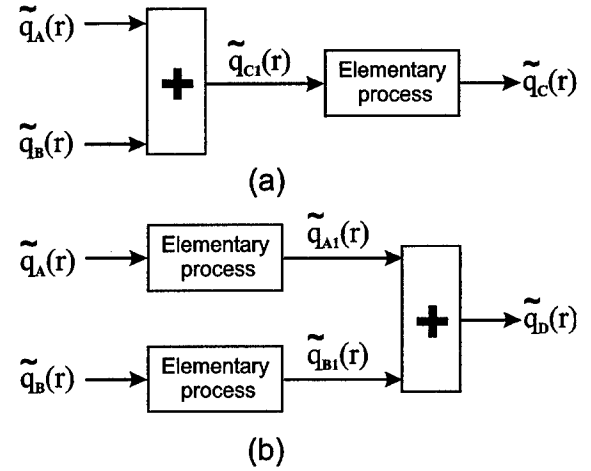


Fig. 17.   The elementary process in model (a) is distributed over the summation to create model (b). The signal and noise expressions for image signal $\tilde{q}_C(\mathbf{r})$ are the same as those of $\tilde{q}_D(\mathbf{r})$.

We developed a novel generalized automated algorithm to perform analytic calculations of signal and noise propagation through X-ray imaging systems. Fourier-based analyses are performed to calculate metrics of image quality and system performance in terms of MTF, NPS, and DQE. The implemented recursive algorithm accommodates parallel cascaded models of arbitrary complexity. This task is achieved by modifying complex models to an "equivalent model" based on the distributive-over-addition property of the elementary processes. A graphical interface is used to build cascaded models in which complex physical processes are represented as cascades of elementary processes selected from a predefined library. Symbolic mathematics is used to generate and simplify analytic expressions at each stage of the calculations.

Analytic results generated by the algorithm have been validated by manual calculations for simple models and special purpose MC calculations for complex models. The MC validation results includes the first validation of the use of parallel cascades in linear-systems transfer theory.

Analytic descriptions of detector performance are particularly important for gaining insight into the physical causes of performance limitation. The algorithm described here is the first general solution of signal and noise transfer in complex systems. Cascaded models are now becoming a practical tool for the optimal design of new imaging systems.

## APPENDIX I
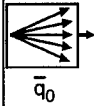### SUMMARY OF SIGNAL AND NOISE-TRANSFER FUNCTIONS
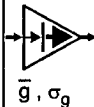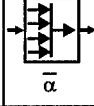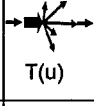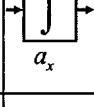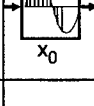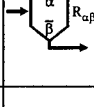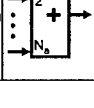
A summary of signal and noise-transfer functions for the physical processes used in this article are summarized in Table I. The "source" process describes a uniform Poisson distribution of X-ray quanta incident on the detector.

## APPENDIX II
### DISTRIBUTIVE-OVER-ADDITION PROPERTY OF ELEMENTARY POINT PROCESSES

The algorithm described in this article to calculate signal and noise transfer in complex cascaded models requires that each

TABLE I
SUMMARY OF SIGNAL AND NOISE-TRANSFER FUNCTIONS FOR THE PROCESSES USED IN THIS STUDY

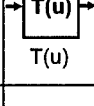| Elementary process (icon-parameters) | mean gain | MTF | $NPS_{out}(u)$ | Output S-vector | Output N-vector |
|---|---|---|---|---|---|
| **Source** | — | 1 | $\bar{q}_0$ | set NULL at source. | set NULL at source. |
| **Quantum gain** $\bar{g}, \sigma_g$ | $\bar{g}$ | 1 | $\bar{g}^2 NPS_{in}(u) + \sigma_g^2 \bar{q}_{in}$ | multiply last row of input S-vector by $\bar{g}$. | is the same as input N-vector. |
| **Quantum selection** $\bar{\alpha}$ | $\bar{\alpha}$ | 1 | $\bar{\alpha}^2 [NPS_{in}(u) - \bar{q}_{in}] + \bar{\alpha}\bar{q}_{in}$ | multiply last row of input S-vector by $\bar{\alpha}$. | is the same as input N-vector. |
| **Quantum scatter** $T(u)$ | 1 | $T(u)$ | $[NPS_{in}(u) - \bar{q}_{in}]|T(u)|^2 + \bar{q}_{in}$ | multiply last row of input S-vector by $T(u)$. | is the same as input N-vector. |
| **Quantum integration** $a_x$ | $a_x$ | $\dfrac{\sin(\pi a_x u)}{\pi a_x u}$ | $NPS_{in}(u)\dfrac{\sin^2(\pi a_x u)}{(\pi u)^2}$ | multiply last row of input S-vector by $a_x \dfrac{\sin(\pi a_x u)}{\pi a_x u}$. | is the same as input N-vector. |
| **Linear filtering** $T(u)$ | $T(0)$ | $\dfrac{T(u)}{T(0)}$ | $NPS_{in}(u)|T(u)|^2$ | multiply last row of input S-vector by $T(u)$. | is the same as input N-vector. |
| **Sampling** $x_0$ | 1 | 1 | $NPS_{in}(u) + \sum\limits_{n=1}^{\pm\infty} NPS_{in}(u \pm \dfrac{n}{x_0})$ | is the same as input S-vector. | is the same as input N-vector. |
| **Quantum branch** $R_{\alpha\beta}$ | $\bar{\alpha}$ | 1 | $\bar{\alpha}^2 [NPS_{in}(u) - \bar{q}_{in}] + \bar{\alpha}\bar{q}_{in}$ | add $\bar{\alpha}$ as a new row to the input S-vector. | add $NPS_{in}(u) + (\dfrac{R}{\bar{\alpha}} - 1)q_{in}$ as a new row $\alpha\beta$ to the input N-vector. |
| | $\bar{\beta}$ | 1 | $\bar{\beta}^2 [NPS_{in}(u) - \bar{q}_{in}] + \bar{\beta}\bar{q}_{in}$ | add $\bar{\beta}$ as a new row to the input S-vector. | add unity as a new row to the input N-vector. |
| **Summation** | $\bar{q}_{out} = \sum\limits_{a=1}^{N_a} \bar{q}_a$ | $MTF_{out}(u) = \sum\limits_{a=1}^{N_a} \dfrac{\bar{q}_a}{\bar{q}_{out}} MTF_a(u)$ | $\sum\limits_{a=1}^{N_a} NPS_a(u) + \sum\limits_{\substack{a=1 \\ a \neq b}}^{N_a}\sum\limits_{b=1}^{N_a} NPS_{ab}(u)$ | is the same as input S-vector. | is the same as input N-vector. |

elementary point process (see Section II) be "distributive over addition." This property means that the position of these processes in a cascaded model can be moved relative to a "summation" process without affecting signal or noise transfer properties of the model. A simple example of this property is illustrated in Fig. 17 where an "elementary process" is moved from the output of a summation process to precede the two inputs. In this appendix, we show that the transfer characteristics of the models in Fig. 17(a) and (b) are the same.

We start by considering only a quantum gain process with gain mean $\bar{g}$ and variance $\sigma_g^2$. Under WSS conditions (mean and autocorrelation of input quanta are uniform throughout image), the mean output signals $\bar{q}_C$ and $\bar{q}_D$ are given by $\bar{q}_C = \bar{g}(\bar{q}_A +$

$\bar{q}_B)$ and $\bar{q}_D = \bar{g}\bar{q}_A + \bar{g}\bar{q}_B$ respectively. Since the gain process defined in Section II is linear, $\bar{q}_C = \bar{q}_D$. A similar approach using (27) can be used to show that the MTF at points C and D are equivalent.

Using the gain noise-transfer expression in Table I, noise at point C in Fig. 17(a) is given by

$$NPS_C(u) = \bar{g}^2 NPS_{C1}(u) + \sigma_g^2 \bar{q}_{C1}. \qquad (47)$$

By noting that $\tilde{q}_{C1} = \tilde{q}_A + \tilde{q}_B$ and using (26) and (28), (47) can be expressed as

$$NPS_C(u) = \bar{g}^2 [NPS_A(u) + NPS_B(u)$$
$$+ 2NPS_{AB}(u)] + \sigma_g^2 [\bar{q}_A + \bar{q}_B]. \qquad (48)$$

For the model in Fig. 17(b), the output NPS can be expressed as

$$\text{NPS}_D(u) = \left[\bar{g}^2 \text{NPS}_A(u) + \sigma_g^2 \bar{q}_A\right]$$
$$+ \left[\bar{g}^2 \text{NPS}_B(u) + \sigma_g^2 \bar{q}_B\right] + 2\text{NPS}_{A1B1}(u). \quad (49)$$

Using (29) for the cross term in Fig. 17(b), $\text{NPS}_{A1B1}(u) = \bar{g}\bar{g}\text{NPS}_{AB}(u) = \bar{g}^2\text{NPS}_{AB}(u)$ and, therefore, $\text{NPS}_C(u) = \text{NPS}_D(u)$, which means that noise transfer in the two models in Fig. 17 are equivalent.

Using a similar approach, it can be shown that the distributive-over-addition property is valid for the other elementary point processes plus the quantum branch process.

### ACKNOWLEDGMENT

### REFERENCES

[1] K. Rossmann, "Measurement of the modulation transfer function of radiographic systems containing fluoroscent screens," *Phys. Med. Biol.*, vol. 9, pp. 551–557, 1964.

[2] ——, "Point spread-function, line spread function, and modulation transfer function," *Radiology*, vol. 93, pp. 257–272, 1969.

[3] R. Shaw, "The equivalent quantum efficiency of the photographic process," *J. Photograph. Sci.*, vol. 11, pp. 199–204, 1963.

[4] R. F. Wagner, "Unified SNR analysis of medical imaging systems," *Phys. Med. Biol.*, vol. 30, pp. 489–518, 1985.

[5] Medical imaging—the assessment of image quality, in ICRU Rep. no. 54 (Int. Comm. Radiation Units and Measurements), Bethesda, MD, 1995.

[6] R. M. Gagne, J. S. Boswell, and K. J. Myers, "Signal detectability in digital radiography: spatial domain figures of merit," *Med. Phys.*, vol. 30, no. 8, pp. 2180–2193, 2003.

[7] K. J. Myers, "Ideal observer models of visual signal detection," in *Handbook of Medical Imaging*, J. Beutel, H. L. Kundel, and R. Van Metter, Eds. Bellingham, WA: SPIE, 2000, vol. 1, Physics and Psychophysics, ch. 9, pp. 559–592.

[8] J. C. Dainty and R. Shaw, *Image Science*. New York: Academic, 1974.

[9] I. A. Cunningham, "Applied linear-systems theory," in *Handbook of Medical Imaging*, J. Beutel, H. L. Kundel, and R. Van Metter, Eds. Bellingham, WA: SPIE, 2000, vol. 1, Physics and Psychophysics, ch. 2, pp. 79–159.

[10] H. H. Barrett and K. J. Myers, *Foundations of Image Science*. New York: Wiley, 2004.

[11] A. Papoulis, *Probability, Random Variables, and Stochastic Processes*, 3rd ed. New York: McGraw-Hill, 1991.

[12] J. D. Gaskill, *Linear Systems, Fourier Transforms, and Optics*. New York: Wiley, 1978.

[13] A. Papoulis, *Systems and Transforms With Applications in Optics*. New York: McGraw-Hill, 1968.

[14] K. Doi, K. Rossmann, and A. G. Haus, "Image quality and patient exposure in diagnostic radiology," *Photograph. Sci. Eng.*, vol. 21, pp. 269–277, 1977.

[15] C. E. Metz and K. Doi, "Transfer function analysis of radiographic imaging systems," *Phys. Med. Biol.*, vol. 24, pp. 1079–1106, 1979.

[16] H. H. Barrett and W. Swindell, *Radiological Imaging—The Theory of Image Formation, Detection, and Processing*. New York: Academic, 1981.

[17] W. Shockley and J. R. Pierce, "A theory of noise for electron multipliers," in *Proc. Inst. Radio. Eng.*, 1938.

[18] L. Mandel, "Image fluctuations in cascade intensifiers," *Br. J. Appl. Phys.*, vol. 10, pp. 233–234, 1959.

[19] H. L. Zweig, "Detective quantum efficiency of photodetectors with some amplifying mechanism," *J. Opt. Soc. Am.*, vol. 55, pp. 525–528, 1965.

[20] P. L. Dillon, J. F. Hamilton, R. Shaw, and R. Van Metter, "Principles governing the transfer of signal modulation and photon noise by amplifying and scattering mechanisms," *Proc. SPIE*, vol. 535, pp. 130–139, 1985.

[21] M. Rabbani, R. Shaw, and R. Van Metter, "Detective quantum efficiency of imaging sytems with amplifying and scattering mechanisms," *J. Opt. Soc. Am. A*, vol. 4, pp. 895–901, 1987.

[22] H. H. Barrett, R. F. Wagner, and K. J. Myers, "Correlated point processes in radiological imaging," *Proc. SPIE*, vol. 3032, pp. 110–125, 1997.

[23] M. Rabbani and R. Van Metter, "Analysis of signal and noise propagation for several imaging mechanism," *J. Opt. Soc. Am. A*, vol. 7, pp. 1156–1164, 1989.

[24] I. A. Cunningham, "Linear-systems modeling of parallel cascaded stochastic: the NPS of radiographic screens with reabsorption of characteristic X radiation," *Proc. SPIE*, vol. 3336, pp. 220–230, 1998.

[25] I. A. Cunningham and R. Shaw, "Signal-to-noise optimazation of medical imaging systems," *J. Opt. Soc. Am. A*, vol. 16, pp. 621–632, 1999.

[26] J. Yao and I. A. Cunningham, "Parallel cascades: new ways to describe noise transfer in medical imaging systems," *Med. Phys.*, vol. 28, pp. 2020–2038, 2001.

[27] I. A. Cunningham, J. Yao, and V. Subotic, "Cascaded models and the DQE of flat-panel imagers: noise aliasing, secondary quantum noise and reabsorption," *Proc SPIE (Medical Imaging 2002: Physics of Medical Imaging)*, vol. 4682, pp. 61–72, 2002.

[28] J. Yao and I. A. Cunningham, "Signal and noise transfer properties of photoelectric interactions," , 2004, submitted for publication.

[29] D. L. Snyder and M. I. Miller, *Random Point Processes in Time and Space*. New York: Springer Verlag, 1991.

[30] I. A. Cunningham and M. S. Westmore, "A quantum scatter in cascaded imaging systems," , 2004, submitted for publication.

[31] W. Zhao and J. A. Rowlands, "Digital radiology using active matrix readout of amorphous selenium: theoretical analysis of detective quantum efficiency," *Med. Phys.*, vol. 24, pp. 1819–1833, 1997.

[32] *Using Matlab*. Natick, MA: The MathWorks Inc., 2000.

[33] *Symbolic Math Toolbox User's Guide*, The MathWorks Inc., Natick, MA, 2000.

[34] W. H. Press, B. P. Flannery, S. A. Teukolsky, and W. T. Vetterling, *Numerical Recipes in C*. New York: Cambridge Univ. Press, 1988.

Corresponding author:
Jingwu Yao, Ph.D.
Imaging Research Laboratories
Robarts Research Institute
P.O. Box 5015, 100 Perth Drive

London, ON, N6A 5K8, Canada
Tel: (519)685-8500 ext. 34035; Fax: (519)663-3900
E-mail: jyao@imaging.robarts.ca

# Signal and noise-transfer properties of photoelectric interactions in diagnostic-imaging detectors

J. Yao[a],* G. Hajdok[abc], J.J. Battista[bc], and I.A. Cunningham[abc]

[a]Robarts Research Institute, P.O. Box 5015,
London, Ontario N6A 5K8, Canada
[b]Department of Medical Biophysics,
The University of Western Ontario
[c]London Health Sciences Centre
(Dated: March 14, 2005)

Image quality in diagnostic radiology is ultimately limited by statistical processes governing how, and where, radiation energy is deposited in a detector. These properties in turn depend on the physics of x-ray interactions. In the mammographic and radiographic x-ray energy range of 10–100 keV, most of the energy deposited in a detector is through photoelectric interactions resulting in local energy absorption plus the potential emission of a cascade of characteristic x rays and Auger electrons. Reabsorption of characteristic x rays causes spatial correlations in the distribution of absorbed energy. We describe a theoretical model of the photoelectric process that specifically addresses the statistical nature of energy absorption through photoelectrons, multiple characteristic x rays, and Auger electrons. A cascaded-systems approach is used that employs a complex structure of parallel cascades. Analytic expressions are obtained for signal and noise propagation through photoelectric interactions in detectors of a single atomic number in terms of the modulation transfer function and Wiener noise power spectrum in the spatial-frequency domain. These results are combined to describe the "photoelectric detective quantum efficiency" in terms of detector thickness, mass density, atomic number and incident photon energy. Excellent agreement is obtained with a Monte Carlo study for an amorphous selenium detector up to a spatial frequency of approximately 30 cy/mm at 60 keV and 13 cy/mm at 80 keV, limited only by electron transport physics for photoelectrons and Auger electrons which are neglected in this model. This work provides a practical tool for the evaluation of signal and noise transfer due to photoelectric interactions as part of an evaluation of new or existing detector designs. Use of the cascaded approach makes it possible to incorporate these results into more comprehensive models of specific detector designs, critical for the development and evaluation of new high-performance detectors.

Keywords: x-ray physics, x-ray detectors, photoelectric interaction, characteristic x rays, Auger electrons, cascaded models, modulation transfer function, noise power spectrum, detective quantum efficiency

## I. INTRODUCTION

Radiographic image quality is in part a balance between system performance and radiation risk to the patient, and it is critical that the best possible image quality be obtained for a specified patient dose. This balance is particularly important for screening programs such as mammography where large numbers of patients are exposed to radiation and high-quality images are essential for the difficult diagnostic tasks of early detection when disease is still *in situ* or minimally invasive.[1-6] While film-screen mammography has been the most reliable method available for the detection of breast cancer in screening programs in the past,[7,8] it is hoped that their limitations in sensitivity and specificity[9-11] will be overcome with new digital systems. This is particularly important for examinations of the radiographically-dense breast,[1,2,12] found more often in younger populations where the benefits of screening mammography remain controversial.[12-14] Studies have shown that past improvements to mammography detectors and instrumentation have resulted in earlier detection[15] and it is generally believed that if we are to continue to achieve earlier detection rates and lower radiation exposures, we must persevere to develop systems capable of even greater image quality.

Fourier-based metrics such as the modulation transfer function (MTF),[16-19] Wiener noise power spectrum (NPS), noise-equivalent number of quanta (NEQ) and detective quantum efficiency (DQE)[20] are generally accepted as primary measures of image quality and detector performance.[21] Fourier methods are normally applicable to linear (or at least linearizable) and shift-invariant (LSI) systems where image noise is due to wide-sense stationary (WSS)[22] or wide-sense cyclostationary (WSCS) random processes.[23] This may sometimes limit Fourier methods to an analysis of central regions of images with low-contrast structures.[24,25] However, this is not necessarily restrictive as there is the implicit assumption that

any imaging system optimized for these conditions will be close to optimal for other conditions. While care must be taken to minimize additional artifacts due to use of the discrete Fourier transform,[22] Fourier-based methods represent a practical balance between computational sophistication and general accessibility.

Image noise in quantum-noise-limited x-ray imaging systems results from the statistical nature of quantum interactions and spatial correlations associated with energy reabsorption in the detector. Photoelectric interactions are the primary mechanism by which x-ray energy is deposited in a detector in the diagnostic energy range, and due to the complex set of atomic electron transitions and the potential production and reabsorption of multiple characteristic (fluorescent) x rays, many complex spatial correlations are introduced into the image signal. The effect of reabsorption has been studied by a number of authors, including Chan, Doi, Boone, Zhao and coworkers[26-31] and others. Using Monte Carlo methods, it has been shown that a significant fraction of total energy absorption in the diagnostic energy range can be due to reabsorption.

While these studies highlighted the relative importance of reabsorption, the first statistical analysis was performed by Metz and Vyborny.[32] They developed a theoretical model of K x-ray reabsorption in a calcium tungstate screen (Dupont Par speed) and described the resulting spatial correlations in terms of the statistical covariance. They also described the first Fourier-based result and showed that reabsorption caused a frequency-dependent increase in image noise by up to 25%. Reabsorption in digital detectors using scintillating phosphors may be even more important as the optical sensors are necessarily on the beam-exit side of the phosphor, unlike film-based systems in which film can be placed on the beam-entrance side where most of the light is generated.[30]

Designing new detector systems optimized to produce the best possible MTF and DQE requires a comprehensive understanding of how the physics of x-ray interactions and energy absorption impacts on image quality in terms of these metrics. Monte Carlo (MC) methods such as EGSnrc[33-35] can be used to simulate x-ray interactions and produce accurate models of particular detectors.[28,30,36,37] However, our own experience shows that calculating the history of a single interacting x-ray photon requires approximately 1 ms on a fast PC (2.4-GHz dual-CPU xeon processor running Linux) depending on the photon energy, and the calculation of a single DQE curve may require $10^8$ histories requiring approximately 10 days of CPU time. Many such calculations are required to optimize a detector design and hence these long calculation times can be prohibitive.

Analytic models based on cascaded-systems theory[21] have been used in the past to develop relatively simple models of detector DQE.[31,38,39] However, these models were generally too simplistic to have great practical value and therefore received limited enthusiasm. In this arti-
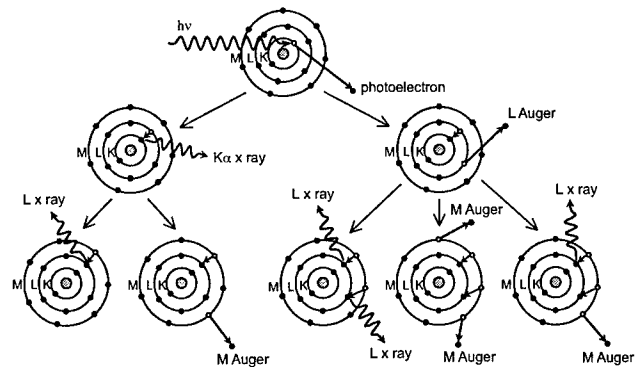


FIG. 1: Partial illustration of the possible transitions following a photoelectric interaction that involve K, L and M shells. The result is a complex series of emitted photoelectrons, characteristic x-ray photons and Auger electrons that introduces spatial correlations in the distribution of absorbed energy.

cle, we develop a comprehensive description of detector performance by extending the use of cascaded-systems theory to include complex parallel cascades.[40] In particular, we develop a description of photoelectric interactions using this approach resulting in a Fourier-based analytic description of signal and noise transfer associated with photoelectric interactions in x-ray detectors. This description specifically addresses noise correlations that result from the emission of characteristic radiation and the resulting impact on image quality in terms of the MTF, NPS, and DQE. Results can be computed with negligible computational effort and are validated by Monte Carlo calculations for an amorphous selenium flat-panel detector.

## II.  THEORY

### A.  Review of the photoelectric effect

The interaction of an x-ray photon with an atom by the photoelectric effect leaves the atom in an excited state with ejection of a bound electron as a photoelectron. The excited atom then emits a complex cascade of characteristic x rays and Auger electrons. While this process is described in many physics texts,[41,42] a very brief summary is required here to define terms as they are used in this work.

The photoelectric interaction is most likely to occur with an inner shell, but may occur with any shell when the x-ray photon energy $h\nu$ is greater than or equal to the binding energy for that shell. For example, a K-shell interaction is possible when $h\nu \geq E_K$ and the photoelectron will have kinetic energy of $h\nu - E_K$. The probability of interaction with the K-shell is called the K participation fraction, $P_K$.[41]

Figure 1 illustrates a series of energy transitions that may occur after an x-ray interacts with a K-shell electron.

Three atomic shells (K, L and M) are shown although the actual number depends on the atomic number of the atom. Ejection of the photoelectron creates a vacancy that will be filled by an atomic electron from a higher shell. If the resulting vacancy is filled by an L-shell electron as shown in Fig. 1, the corresponding K-L transition will be accompanied by one of two possible events. In the first case, as shown in the left of Fig. 1, a $K_\alpha$ characteristic photon is emitted with energy equal to the difference between the binding energy of the shells, $E_K - E_L$. The probability of this $K_\alpha$ emission subsequent to the K-L transition is called the fluorescence yield, $\omega_{KL}$. Emission of the $K_\alpha$ photon creates an L-shell vacancy that will be filled by an electron from the M (or higher) shell, resulting in the emission of either an L characteristic photon or an M-shell Auger electron.

Alternatively, as shown in the right of Fig. 1, an L-shell Auger electron may remove energy equal to $E_K - 2E_L$ (if $(E_K - E_L) \geq E_L$) leaving two electron vacancies in the L shell. This results in one of three possible events as shown in the lower right of Fig. 1.

These internal transitions are repeated for the allowed transitions until the inner-shell vacancy has been transferred to outer-shell vacancies that are filled by conduction band electrons. While only the K-L transition is illustrated in Fig. 1, others are possible.

## B.  Cascaded model of the photoelectric effect

The complex cascade of events following the photoelectric interaction creates many complex statistical spatial correlations in where, and how, energy is transferred to the detector material with the subsequent liberation of what we will call "image-forming" quanta. These quanta will be of different types, such as light photons in a phosphor or charge carriers in a photoconductor, depending on the detector being described. While a statistical analysis of the resulting image correlations is complex, much of that complexity is concealed here using a modular approach to build the model by cascading simple processes having well defined input-output relationships that describe the first and second moment statistics required to determine the DQE. The only limitation to this approach as used here is to ensure that WSS conditions are satisfied and each process in the model operates independently of all others. These are not significant limitations but are discussed below.

Quantum-based imaging systems are well described in terms of random point processes as introduced to the medical imaging community by Barrett, Wagner and Myers.[22,43] A point process is a process for which all inputs and outputs consist of a distribution of points that represent point objects or events. The input to our model is $\tilde{q}_o(\mathbf{r})$, a spatial distribution of randomly located Dirac $\delta$ functions representing the locations of photoelec-
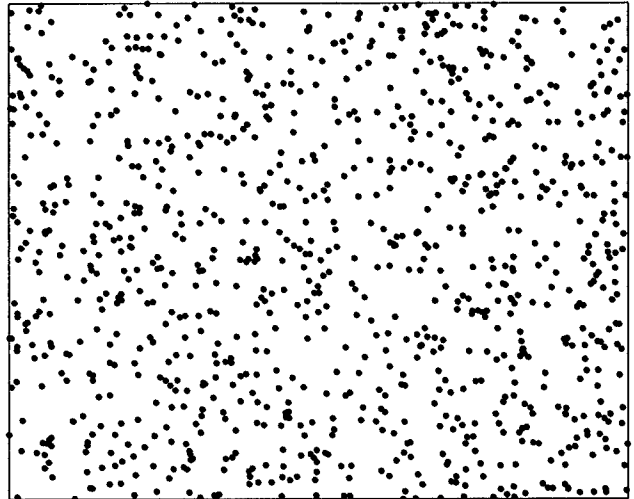


FIG. 2: Sample illustration of $\tilde{q}_o(\mathbf{r})$ given by Eq. (1), a spatial distribution of randomly located points where each point represents the location of a photoelectric event.

tric events in a detector (Fig. 2):

$$\tilde{q}_o(\mathbf{r}) = \sum_{i=1}^{\tilde{N}_{pc}} \delta(\mathbf{r} - \tilde{\mathbf{r}}_i), \qquad (1)$$

where $\tilde{\mathbf{r}}_i$ is a random vector describing the location in the image of the $i$th of $\tilde{N}_{pc}$ photoelectric interactions. We use the overhead tilde ($\tilde{\ }$) to indicate a random variable. The output is a random point process describing the spatial distribution of image-forming quanta liberated by energy absorption in the detector.

An important assumption is made to simplify the analysis. We assume all energy transferred to electrons is absorbed locally. Thus, it is not necessary to describe the random path of electrons and delta rays as they loose energy to the surrounding medium. This is valid only when $R \ll 1/\nu_{max}$ where $R$ is the electron range in the detector material and $\nu_{max}$ is the highest spatial frequency of interest in the image. This is the primary limitation to the results presented here and imposes a limiting condition on the maximum x-ray energy and spatial resolution for which the model is applicable as discussed below.

It is also assumed that incident x rays are monoenergetic although the results are easily generalized to polyenergetic beams with appropriate spectral averaging. In addition, it is assumed that the detector material consists of a single atomic number. This is reasonable for detectors like selenium, but application to some multi-Z detectors may require additional thought due to more complicated characteristic photon emission-absorption relationships that is beyond the scope of this article. Finally, we describe the release of image-forming quanta in the detector as the final end-point in our model and assume that the mean number released is proportional to the absorbed energy, $E_{abs}$, corresponding to a conversion gain

of $\bar{k} = E_{\text{abs}}/W$ where $W$ is the work energy required on average to liberate each image quantum. This ignores statistical variations in $k$ and is reasonable when $\bar{k} \gg 1$ which is always true in this study. We also ignore the practicality of how these quanta (such as light in a phosphor) might be collected by the detector, and scatter or absorption of these quanta. Detector electronic noise and other engineering considerations that might prevent achieving the results described here are also neglected. Thus, our results are truly a description of fundamental signal and noise propagation through the photoelectric interaction itself. They are presented in terms of a cascaded model that could become one component of a more comprehensive model for a specific detector that incorporates some of the other issues identified here.

The final form of the photoelectric interaction model consists of a long algebraic equation. While the terms in the result are relatively simple, it is informative to first describe a simplified model (model "A") that considers only the emission of characteristic K photon fluorescent radiation and then generalize it into a more comprehensive result. The simpler model is easier to describe, and in fact may be entirely adequate for practical use when the distance travelled by low-energy L fluorescent radiation can be neglected. The more comprehensive model (model "B") is valid for a wider range of energies by specifically addressing $K_\alpha$, $K_\beta$ and L characteristic photons, and will be necessary for high atom-number detectors or detectors designed for mammography or small-animal imaging (involving lower energies and higher spatial resolution). In general, the cascaded approach can be tailored to develop models of any required complexity within the constraints of the above assumptions.

*1. Model A*

Our model of K emission is shown in Fig. 3 consisting of four parallel cascades of point processes. Each box represents a particular (random) point process and each connecting line represents a spatial distribution of points connecting the output of one process to the input of the next. The input $\tilde{q}_0(\mathbf{r})$ is a Poisson distribution of photoelectric interaction locations.

The first process encountered is a random process separating $\tilde{q}_0(\mathbf{r})$ into two distributions corresponding to two different scenarios: i) those photoelectric interactions that involve the K shell, with probability $P_K$; and ii) those that involve an L or higher (indicated as $L^+$) shell, with probability $(1 - P_K)$. We have called this process a "Bernoulli branch"[40] in which each input point is randomly assigned to one and only one of the two output distributions.

For each K-shell interaction, a K photoelectron is ejected with energy $h\nu - E_K$ that will result in $\bar{g}_K = (h\nu - E_K)/W$ liberated image quanta (labelled $\tilde{q}_1(\mathbf{r})$ in Fig. 3) where $W$ is the average work energy required to liberate one image-forming quantum. Since we are ne-

glecting the range of the electrons, liberation of image quanta is represented simply as a "quantum gain"[40] process, where electron energy is converted into many image quanta. Thus, $\tilde{q}_1(\mathbf{r})$ is a spatial distribution of points identifying image-forming quanta liberated by K photoelectrons. In this model, some points in $\tilde{q}_1(\mathbf{r})$ may overlap due to the liberation of multiple image quanta at each photoelectric interaction.

In addition to the photoelectron, a fluorescent K photon may be emitted with probability $\omega_K$ (K fluorescence yield). For each K photon emitted, the second path describes liberation of image quanta due to its reabsorption, characterized by $f_K$, the probability of reabsorption, and $\text{CSF}_K(\mathbf{r})$, the probability density function (PDF) describing where the reabsorption may take place in the image with respect to the emission location. In Fig. 3, random selection of K photons that are reabsorbed is a "quantum selection" process.[40] The process of randomly locating where these photons are reabsorbed is represented as a "quantum scatter" process,[40] randomly relocating points according to $\text{CSF}_K(\mathbf{r})$. Thus, output from the process labelled $\text{CSF}_K(\mathbf{r})$ is a spatial distribution of points identifying reabsorption sites. At each such site, the K photon liberates $\bar{g}_{K1} = \overline{h\nu_K}/W$ image quanta, giving $\tilde{q}_2(\mathbf{r})$.

If a K photon is not emitted, energy is absorbed locally through the ejection of an L-Auger electron and outer-shell transitions resulting in the liberation of $\bar{g}_{K2} = E_K/W$ image quanta, giving $\tilde{q}_3(\mathbf{r})$.

If the photoelectric interaction does not involve the K shell, it involves an outer shell (L or higher) and it is assumed all energy is absorbed locally resulting in the liberation of $\bar{g}_L = h\nu/W$ image quanta giving $\tilde{q}_4(\mathbf{r})$.

Our simplified model of the photoelectric interaction illustrated in Fig. 3 therefore consists of four different ran-

TABLE I: Physical constants for $a$-Se used in this study. Selenium data was obtained from Rowlands and Yorkston[44] and atomic data was obtained from Perkins *et al.*[45]

| | |
|---|---|
| Mass density ($\rho$: g/cm$^3$) | 4.20 |
| Average work energy to liberate one image-forming quantum ($W$: keV) | 0.05 |
| K-edge binding energy ($E_K$: keV) | 12.66 |
| L-edge binding energy ($E_L$: keV) | 1.48 |
| $K_\alpha$-fluorescent energy ($h\nu_{K\alpha}$: keV) | 11.21 |
| $K_\beta$-fluorescent energy ($h\nu_{K\beta}$: keV) | 12.50 |
| L-fluorescent energy ($h\nu_L$: keV) | 1.416 |
| K-shell participation fraction ($P_K$) | 0.864 |
| L-shell participation fraction except K-shell ($P_L'$) | 0.859 |
| Probability of KL transition ($\xi_{KL}$) | 0.924 |
| K-fluorescence yield in KL transition ($\omega_{KL}$) | 0.555 |
| K-fluorescence yield in KM transition ($\omega_{KM}$) | 0.965 |
| L-fluorescence yield in LM transition ($\omega_{LM}$) | 0.0176 |
| Probability of L-Auger electron production ($a_L$) | 0.764 |
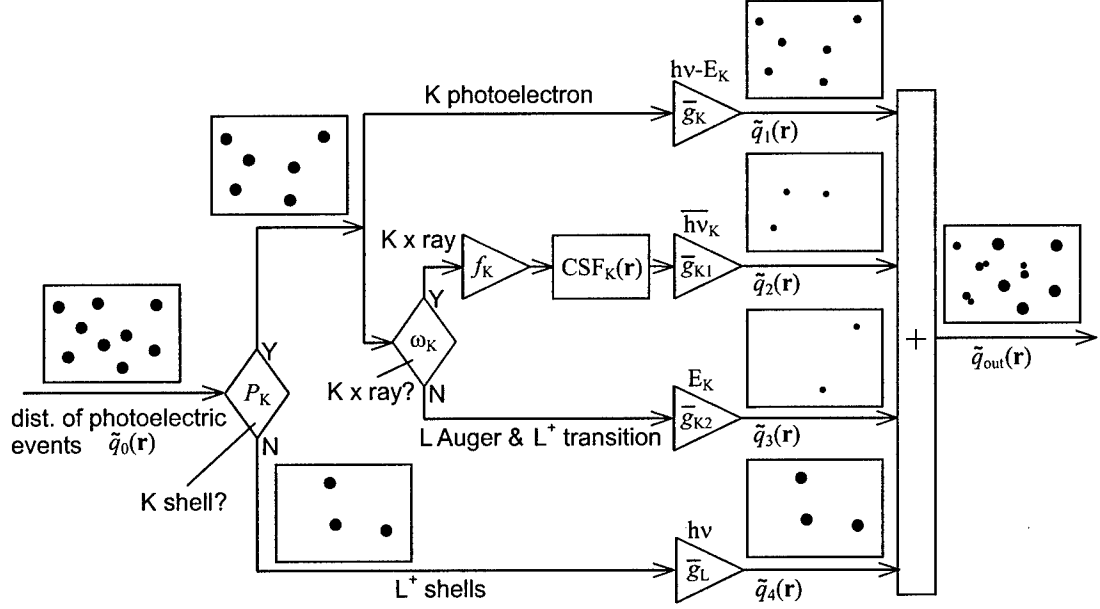
FIG. 3: Parallel-cascades model used to describe signal and noise transfer through photoelectric interactions in Model A. Each object in the flow diagram represents a random point process operating on an input point distribution to produce an output point distribution. The output from one process forms a virtual input to another as indicated by connecting arrows. Input to the model is a distribution of photoelectric events $\tilde{q}_0(\mathbf{r})$ and the output is a spatial distribution of liberated image-forming quanta $\tilde{q}_{out}(\mathbf{r})$. The energy associated with this conversion is indicated by dot sizes and is stated for each path.

dom point distributions identifying the locations of liberated image-forming quanta. Collectively, they describe the total distribution of image quanta resulting from photoelectric interactions in terms of a number of random variables. Distributions associated with the same parent distribution may be correlated which is why this theoretical model is required.

Signal and noise transfer through the photoelectric interaction is characterized in terms of the MTF, NPS and DQE associated with these random distributions, calculated by appropriate cascades of the signal and noise transfer characteristics of each process as summarized in Sec. II C. Values of physical constants used are listed in Table I and expressions for the product of all gain factors along each path are summarized in Table II.

While not necessarily obvious, model A is equivalent to the model described in a previous publication.[40]

TABLE II: Mean gain and MTF for each path in Model A.

| Path | Mean Gain (image quanta per PE event) | MTF |
|------|----------------------------------------|-----|
| 1 | $P_K\,(h\nu - E_K)/W$ | 1 |
| 2 | $P_K\,\omega_K\,f_K\,\overline{h\nu}_K/W$ | $RTF_K(\nu)$ |
| 3 | $P_K\,(1 - \omega_K)\,E_K/W$ | 1 |
| 4 | $(1 - P_K)\,h\nu/W$ | 1 |

### 2. Model B

A more comprehensive model that specifically describes image correlations resulting from both K and L-shell interactions is illustrated in Fig. 4. While the greater variety of shells in this model gives rise to more parallel pathways, model B is a natural extension of model A and the 18 paths collectively describe the resulting distribution of image-forming quanta liberated in the detector. It is evident that photoelectric events occurring in the greater variety of atomic shells leads to greater opportunity for parallel events and image correlations. Expressions for the various gain factors are summarized in Table III.

### 3. Fluorescence Reabsorption

In this section, details of reabsorption probabilities and PDF functions are described. Reabsorption of fluorescent photons is characterized in the above description by two terms: $f_i$, the probability of reabsorption (anywhere) for a characteristic photon identified by transition $i$; and $CSF_i(\mathbf{r})$, the PDF (or characteristic spread function) describing the absorption probability density at location $\mathbf{r}$ in the image with respect to the photoelectric interaction. Both are functions of photon energy and the detector material and geometry.

We describe an analytic derivation of these two parameters similar to that of Metz and Vyborny,[32] Que and
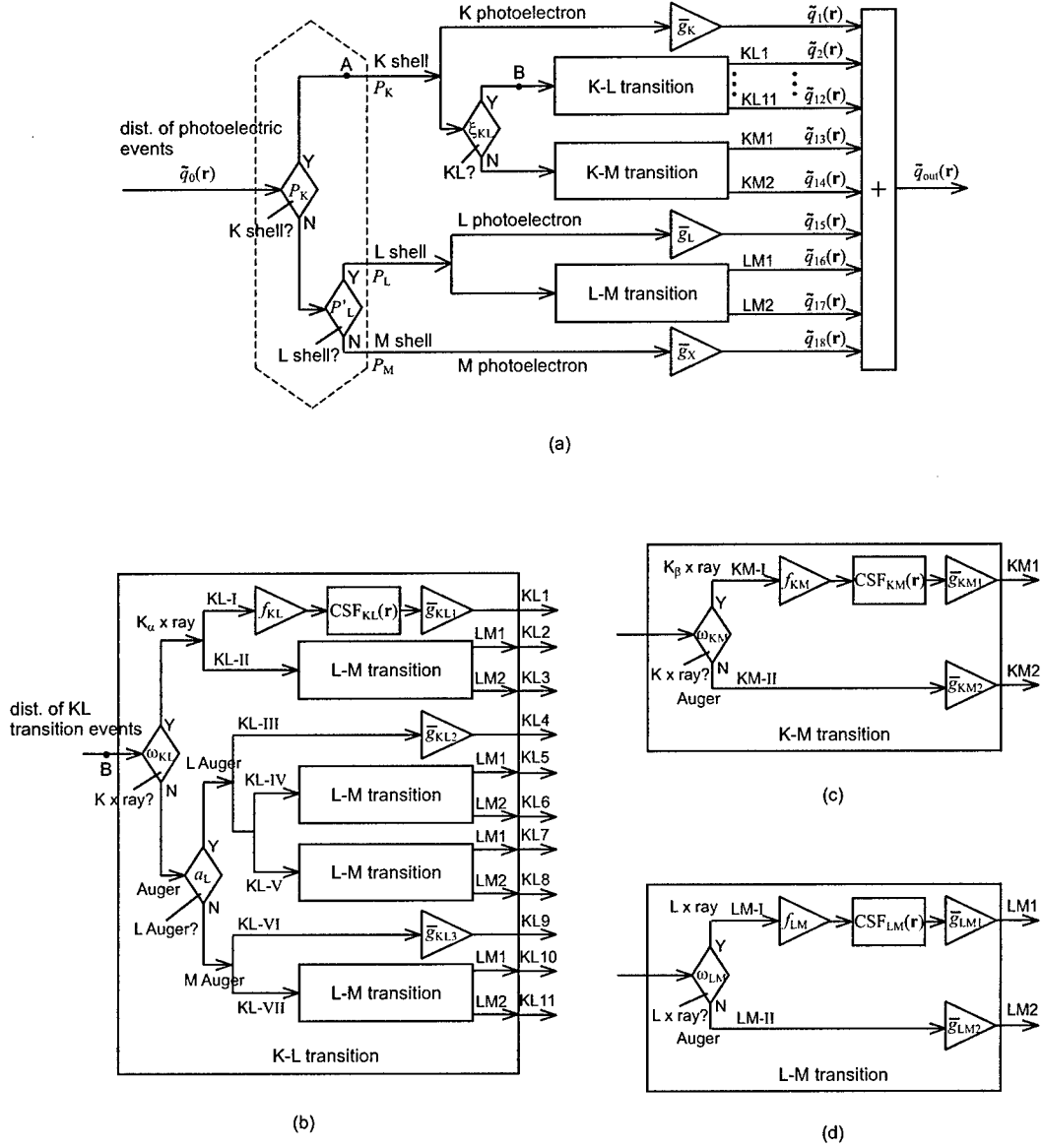
FIG. 4: Model B describes transitions between K, L and M shells.

Rowlands[46] and others, although using a more formal theory of random processes.[47] The calculation is illustrated in Fig. 5 for fluorescence reabsorption in an infinite homogeneous detector of thickness $L$. A normally incident x ray interacts at depth $z$ from the top surface emitting a fluorescent photon at polar angle $\theta$ and azimuthal angle $\phi$. It is reabsorbed after travelling a distance $l$. These are all independent random processes, so we determine the CSF in terms of these variables, $\text{CSF}(\mathbf{r}|\phi, l, \theta, z)$, and then average over each as random variables:

$$\text{CSF}(\mathbf{r}) = \langle\langle\langle\langle\text{CSF}(\mathbf{r}|\phi, l, \theta, z)\rangle_{\tilde{\phi}}\rangle_{\tilde{l}}\rangle_{\tilde{\theta}}\rangle_{\tilde{z}}, \quad (2)$$

where the notion $\langle\ \rangle_{\tilde{\phi}}$ represents an average over the ran-

dom variable $\tilde{\phi}$, and similarly for the other random variables. This CSF is normalized such that the total probability of reabsorption $f$ is equal to the two dimensional integral of the corresponding CSF:

$$f = \int_{-\infty}^{\infty} \text{CSF}(\mathbf{r})\mathrm{d}\mathbf{r}. \quad (3)$$

The CSF has a corresponding characteristic transfer function (CTF) in the Fourier domain:

$$\text{CTF}(\nu) = \mathcal{F}\{\text{CSF}(\mathbf{r})\}, \quad (4)$$

and using the central ordinate theorem of the Fourier transform[48] gives
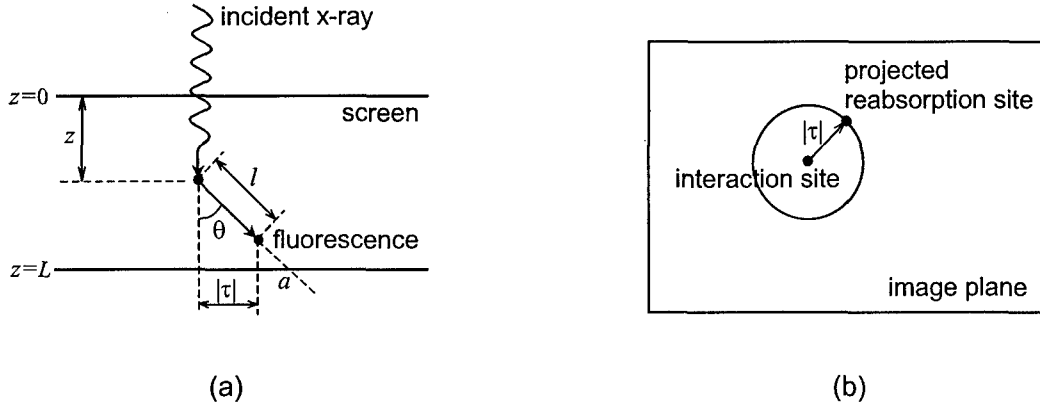
$$f = \text{CTF}(\nu)|_{\nu=0}. \quad (5)$$

FIG. 5: Schematic illustration of fluorescence reabsorption in a screen. A normally incident x ray interacts at depth $z$. A fluorescent photon is emitted at angle $\theta$ and is reabsorbed at a distance $l$. The projected reabsorption site into the image plane may be at any point on a circle of radius $r$ centered at the primary interaction site. (a) Cross-section view; (b) Image-plane view.

In addition, it is convenient to define the normalized "reabsorption transfer function" (RTF) as

$$\mathrm{RTF}(\nu) \equiv \frac{\mathrm{CTF}(\nu)}{\mathrm{CTF}(\nu)|_{\nu=0}}. \tag{6}$$

For specified values of $\phi, l, \theta$ and $z$, the CSF is simply a two-dimensional Dirac $\delta$ function:

$$\mathrm{CSF}(\mathbf{r}|\phi, l, \theta, z) = \delta(r_x - l\sin\theta\cos\phi)\delta(r_y - l\sin\theta\sin\phi), \tag{7}$$

where $r_x$ and $r_y$ are the cartesian coordinates of $\mathbf{r}$. Av-

TABLE III: Mean gain and MTF for each path in Model B.

| Path | Mean Gain (image quanta per PE event) | MTF |
|---|---|---|
| 1 | $P_K(h\nu - E_K)/W$ | 1 |
| 2 | $P_K \xi_{KL} \omega_{KL} f_{KL}(E_K - E_L)/W$ | $\mathrm{RTF}_{KL}(\nu)$ |
| 3 | $P_K \xi_{KL} \omega_{KL}\omega_{LM} f_{LM}(E_L - E_M)/W$ | $\mathrm{RTF}_{LM}(\nu)$ |
| 4 | $P_K \xi_{KL} \omega_{KL}(1 - \omega_{LM})E_L/W$ | 1 |
| 5 | $P_K \xi_{KL}(1 - \omega_{KL})a_L(E_K - 2E_L)/W$ | 1 |
| 6 | $P_K \xi_{KL}(1 - \omega_{KL})a_L \omega_{LM} f_{LM}(E_L - E_M)/W$ | $\mathrm{RTF}_{LM}(\nu)$ |
| 7 | $P_K \xi_{KL}(1 - \omega_{KL})a_L(1 - \omega_{LM})E_L/W$ | 1 |
| 8 | $P_K \xi_{KL}(1 - \omega_{KL})a_L \omega_{LM} f_{LM}(E_L - E_M)/W$ | $\mathrm{RTF}_{LM}(\nu)$ |
| 9 | $P_K \xi_{KL}(1 - \omega_{KL})a_L(1 - \omega_{LM})E_L/W$ | 1 |
| 10 | $P_K \xi_{KL}(1 - \omega_{KL})(1 - a_L)(E_K - E_L)/W$ | 1 |
| 11 | $P_K \xi_{KL}(1 - \omega_{KL})(1 - a_L)\omega_{LM} f_{LM}(E_L - E_M)/W$ | $\mathrm{RTF}_{LM}(\nu)$ |
| 12 | $P_K \xi_{KL}(1 - \omega_{KL})(1 - a_L)(1 - \omega_{LM})E_L/W$ | 1 |
| 13 | $P_K(1 - \xi_{KL})\omega_{KM} f_{KM}(E_K - E_M)/W$ | $\mathrm{RTF}_{KM}(\nu)$ |
| 14 | $P_K(1 - \xi_{KL})(1 - \omega_{KM})E_K/W$ | 1 |
| 15 | $(1 - P_K)P'_L(h\nu - E_L)/W$ | 1 |
| 16 | $(1 - P_K)P'_L \omega_{LM} f_{LM}(E_L - E_M)/W$ | $\mathrm{RTF}_{LM}(\nu)$ |
| 17 | $(1 - P_K)P'_L(1 - \omega_{LM})E_L/W$ | 1 |
| 18 | $(1 - P_K)(1 - P'_L) h\nu/W$ | 1 |

eraging over $\phi$ gives a two-dimensional ring $\delta$ function:[49]

$$\mathrm{CSF}(\mathbf{r}|l, \theta, z)$$
$$= \int_0^{2\pi} \delta(r_x - l\sin\theta\cos\phi)\delta(r_y - l\sin\theta\sin\phi)\mathrm{pr}_{\tilde\phi}(\phi)\mathrm{d}\phi$$
$$= \frac{1}{\pi|\mathbf{r}|}\delta(|\mathbf{r}| - l\sin\theta) \tag{8}$$

where $\mathrm{pr}_{\tilde\phi}(\phi) = 1/(2\pi)$ is the PDF of $\tilde\phi$. At this point it is more convenient to average over the remaining random variables in the Fourier domain. The Fourier transform of a ring $\delta$ function is the zero-order Bessel function.[48] Therefore,

$$\mathrm{CTF}(\nu|l, \theta, z) = \mathcal{F}\{\mathrm{CSF}(r|l, \theta, z)\} = \mathrm{J}_0(2\pi\nu l\sin\theta). \tag{9}$$

Averaging over $l$ must be considered for the two cases of the characteristic photon travelling in forward or backward directions:

$$\mathrm{CTF}(\nu|\theta, z)$$
$$\begin{cases} \mathrm{CTF}_f(\nu|\theta, z) = \displaystyle\int_0^{(L-z)\sec\theta} \mathrm{J}_0(2\pi\nu l\sin\theta)\mathrm{pr}_{\tilde l}(l)\mathrm{d}l \\ \qquad\qquad \text{for } 0 \le \theta \le \pi/2 \\ \mathrm{CTF}_b(\nu|\theta, z) = \displaystyle\int_0^{-z\sec\theta} \mathrm{J}_0(2\pi\nu l\sin\theta)\mathrm{pr}_{\tilde l}(l)\mathrm{d}l \\ \qquad\qquad \text{for } \pi/2 < \theta \le \pi, \end{cases} \tag{10}$$

where $\mathrm{pr}_{\tilde l}(l) = \mu(E)\exp[-\mu(E)l]$ is the absorption PDF along the x-ray path and $\mu(E)$ is the linear attenuation coefficient for the detector material at the energy $E$ of the characteristic photon. These integrals do not have simple solutions. Averaging over $\theta$ gives

$$\mathrm{CTF}(\nu|z) = \int_0^{\pi/2} \mathrm{CTF}_f(\nu|\theta, z)\mathrm{pr}_{\tilde\theta}(\theta)\mathrm{d}\theta$$
$$+ \int_{\pi/2}^{\pi} \mathrm{CTF}_b(\nu|\theta, z)\mathrm{pr}_{\tilde\theta}(\theta)\mathrm{d}\theta \tag{11}$$

where $\mathrm{pr}_{\tilde{\theta}}(\theta) = \sin\theta/2$ is the PDF for $\tilde{\theta}$ after projection into the two-dimensional image plane.[47] For computational convenience, we make the substitution $s = \cos\theta$ so that Eq. (11) is reduced to

$$\mathrm{CTF}(\nu|z) = \frac{1}{2}\int_0^1 [\mathrm{CTF}_f(\nu|s,z) + \mathrm{CTF}_b(\nu|-s,z)]\,ds \tag{12}$$

where $\mathrm{CTF}_f(\nu|s,z)$ and $\mathrm{CTF}_b(\nu|-s,z)$ come from Eq. (10), giving

$$\mathrm{CTF}_f(\nu|s,z)$$
$$= \mu(E)\int_0^{(L-z)/s} \mathrm{J}_0\left[2\pi\nu l\sqrt{1-s^2}\right]\exp\left[-\mu(E)l\right]dl \tag{13}$$

and

$$\mathrm{CTF}_b(\nu|-s,z)$$
$$= \mu(E)\int_0^{z/s} \mathrm{J}_0\left[2\pi\nu l\sqrt{1-s^2}\right]\exp\left[-\mu(E)l\right]dl \tag{14}$$

The PDF $\mathrm{pr}_{\tilde{z}}(z)$ describing the distribution of interaction depths is given by

$$\mathrm{pr}_{\tilde{z}}(z) = \frac{\mu_{pc}(\mathrm{h}\nu)\exp\left[-\mu(\mathrm{h}\nu)z\right]}{1 - \exp\left[-\mu(\mathrm{h}\nu)L\right]} \tag{15}$$

where $\mu_{pc}(E)$ is the linear photoelectric interaction coefficient and $\mathrm{h}\nu$ is the incident x-ray energy. Finally, the CTF is obtained by averaging $\mathrm{CTF}(\nu|z)$ over $\tilde{z}$:

$$\mathrm{CTF}(\nu) = \int_0^L \mathrm{CTF}(\nu|z)\,\mathrm{pr}_{\tilde{z}}(z)dz \tag{16}$$

which can only be solved by numerical integration. The CTF is circularly symmetric, and hence is expressed in terms of the scalar frequency $\nu$.

The parameters $f$ and $\mathrm{RTF}(\nu)$ required for each transition in the photoelectric model are then obtained using Eqs. (5) and (6).

## C. Signal and Noise Transfer

Signal and noise transfer through the photoelectric interaction is described here in terms of several parameters: mean gain $\bar{G}_{pc}$; modulation transfer function $\mathrm{MTF}_{pc}(\nu)$ and noise power spectrum $\mathrm{NPS}_{pc}(\nu)$. Transfer of these quantities is known for each process and are cascaded to determine overall signal and noise transfer for the entire model.

### 1. Mean Gain, $\bar{G}$

The mean gain $\bar{G}_{pc}$ of the photoelectric process is the average number of tertiaries produced per photoelectric event, given by the sum of contributions from each path:

$$\bar{G}_{pc} = \frac{\bar{q}_s}{\bar{q}_o} = \frac{1}{\bar{q}_o}\sum_{i=1}^N \bar{q}_i, \tag{17}$$

where $\bar{q}_i$ is the mean number of image-forming quanta per unit area liberated from the $i$th path, $N$ is the number of paths in the model and $\bar{q}_s$ is the average number of liberated image quanta per unit area in the detector. The mean gain is a measure of overall signal transfer, sometimes called the "large-area" gain.

The gain can also be written as

$$\bar{G}_{pc} = \sum_{i=1}^N \bar{g}_i, \tag{18}$$

where $\bar{g}_i$ is the product of all mean gain values along path $i$ (connecting the output $\bar{q}_i$ with the input $\bar{q}_o$). Expressions for $\bar{g}_i$ for each path are summarized in Table III.

### 2. Modulation Transfer Function, MTF

The MTF associated with photoelectric interactions is equal to the weighted sum of the MTF of each path:

$$\mathrm{MTF}_{pc}(\nu) = \frac{1}{\bar{G}_{pc}}\sum_{i=1}^N \bar{g}_i\,\mathrm{MTF}_i(\nu). \tag{19}$$

Table III shows the MTF for each path of model C, obtained by cascading appropriate combinations of the elementary stages in each path.

### 3. Noise Power Spectrum, NPS

The distribution of incident x rays is assumed uncorrelated and Poisson distributed with a mean $\bar{q}_o$ quanta/mm$^2$ and therefore the input NPS is given by $\mathrm{NPS}_o(\nu) = \bar{q}_o$.[22] The NPS associated with the distribution of image quanta liberated by photoelectric events is obtained by cascading NPS transfer expressions along each path, summing the results, and adding the necessary NPS cross terms between paths:

$$\mathrm{NPS}_{pc}(\nu) = \sum_{i=1}^N \mathrm{NPS}_i(\nu) + \sum_{i=1}^N \sum_{\substack{j=1\\j\neq i}}^N \mathrm{NPS}_{ij}(\nu). \tag{20}$$

The cross term has been described previously[40,50] and is non-zero when correlations exist between the point distributions in different paths.

It is convenient for later use to define a normalized NPS as

$$\mathrm{NNPS}_{pc}(\nu) = \frac{\mathrm{NPS}_{pc}(\nu)}{\bar{q}_o\,\bar{G}_{pc}^2} = \frac{\bar{q}_o\mathrm{NPS}_{pc}(\nu)}{\bar{q}_s^2} \tag{21}$$

which is the ratio of $\mathrm{NPS}_{pc}(\nu)$ to $\bar{q}_o\,\bar{G}_{pc}^2$, the NPS that would be obtained with a noise-free conversion of x-ray energy to image quanta with a gain of $\bar{G}_{pc}$ and no scatter or reabsorption.

### 4. Detective Quantum Efficiency, DQE

The DQE describes the performance of an "ideal observer" for the detection of low-contrast lesions under specific conditions including wide-sense-stationary noise processes,[51] and can be defined as[52]

$$\mathrm{DQE}(\nu) = \frac{\bar{q}_o \bar{G}^2 \, \mathrm{MTF}^2(\nu)}{\mathrm{NPS}(\nu)}. \qquad (22)$$

It has also gained popular use as a general parameter describing transfer of the squared signal-to-noise ratio (SNR) from input to output of an imaging system. We use the term "photoelectric DQE," $\mathrm{DQE}_{\mathrm{pc}}(\nu)$, in the latter sense to describe transfer of the squared SNR through the photoelectric process:

$$\mathrm{DQE}_{\mathrm{pc}}(\nu) = \frac{\mathrm{MTF}_{\mathrm{pc}}^2(\nu)}{\mathrm{NNPS}_{\mathrm{pc}}(\nu)}. \qquad (23)$$

This would be the DQE of an imaging system in which incident x rays undergo photoelectric interactions only and all liberated image-forming quanta contribute to the output signal with no other sources of signal degradation. It therefore represents the greatest DQE that any x-ray imaging system can have in which x rays interact by the photoelectric process, and is interpreted as a fundamental measure of information transfer through the photoelectric effect.

### D. Signal and Noise Transfer Calculation

Analytic expressions for the MTF, NPS and DQE of each model can be calculated by a somewhat tedious process of appropriately cascading expressions of signal and noise transfer. For model A, the photoelectric MTF, NPS and DQE are given by

$$\mathrm{MTF}_{\mathrm{pc}}(\nu) = \frac{\mathrm{h}\nu - P_K \omega_K \overline{\mathrm{h}\nu}_K \left(1 - f_K \mathrm{RTF}_K(\nu)\right)}{\mathrm{h}\nu - P_K \omega_K \overline{\mathrm{h}\nu}_K \left[1 - f_K\right]}, \qquad (24)$$

$$\begin{aligned}
\mathrm{NNPS}_{\mathrm{pc}}(\nu) = \frac{1}{\bar{G}_{\mathrm{pc}}^2} & \Big\{ \left[ (\mathrm{h}\nu - \overline{\mathrm{h}\nu}_K)^2/W^2 + (\mathrm{h}\nu - \overline{\mathrm{h}\nu}_K)/W \right] \\
& + (\overline{\mathrm{h}\nu}_K^2/W^2 + \overline{\mathrm{h}\nu}_K/W) f_K P_K \, \omega_K \\
& + (\mathrm{h}\nu^2/W^2 + \mathrm{h}\nu/W)(1 - P_K \omega_K) \\
& + 2(\mathrm{h}\nu - \overline{\mathrm{h}\nu}_K)/W \overline{\mathrm{h}\nu}_K/W f_K P_K \, \omega_K \, \mathrm{RTF}(\nu) \Big\} (25)
\end{aligned}$$

where $\bar{G}_{\mathrm{pc}} = [\mathrm{h}\nu - P_K \omega_K \overline{\mathrm{h}\nu}_K(1 - f_K)]/W$, $W$ is the work energy and $\mathrm{DQE}_{\mathrm{pc}}$ is given by Eq. (23).

For the more complex models B and C, this calculation was automated using a recently published algorithm.[50] The algorithm uses the Simulink graphical user interface capability of Matlab[53] to design the cascaded model and symbolic mathematics to calculate analytic expressions of signal and noise transfer. Expressions for the MTF and NPS involve many terms and are listed in Appendix A.

### III. MODEL VALIDATION — MONTE CARLO SIMULATIONS

Our theoretical description of $\mathrm{MTF}_{\mathrm{pc}}(\nu)$, $\mathrm{NPS}_{\mathrm{pc}}(\nu)$ and $\mathrm{DQE}_{\mathrm{pc}}(\nu)$ was validated by Monte Carlo calculations for an amorphous selenium ($a$-Se) detector using the latest version of the Electron Gamma Shower (EGSnrc) Monte Carlo code.[33,34] Only photoelectric interactions were simulated. The user code DOSXYZnrc[35] was used to simulate the coupled photon-electron transport within a rectangular slab geometry. Two-dimensional maps of absorbed energy in the detector were calculated from the three-dimensional "dose-deposition maps" produced by the Monte Carlo calculations by summing in the $z$ direction. Two-dimensional "images" describing the number of liberated image quanta in each pixel were generated by dividing the absorbed energy by the work energy $W$ of the detector. This ignores the random nature of generating tertiaries from absorbed energy, but is a reasonable approximation as the electron energies are much greater than $W$ and a large number are generated with each interaction.

The photoelectric MTF was generated by simulating an infinitesimal pencil-beam of x rays incident on a 512-$\mu$m $\times$ 512-$\mu$m slab (1-$\mu$m square pixels) using $10^7$ photon histories. The resulting dose-deposition map gives the total absorbed energy in each pixel. The distribution of liberated image quanta, once projected on to the image plane and normalized to unity volume, represents the two-dimensional point spread function. The one-dimensional MTF was calculated from the two-dimensional Fourier transform of the PSF.

The photoelectric NPS was generated by simulating a series of ten flat-field noise images with a parallel x-ray beam of $8 \times 10^7$ incident photon histories per image over an area of $2 \times 2$ cm$^2$ (1-$\mu$m pixel size). This calculation took approximately 20–40 minutes per image (depending on incident photon energy) for the case without electron transport and 5–21 hours per image with electron transport, using a 2.4 GHz dual-Xeon processor running Linux. Boundary effects from the Monte Carlo simulation were avoided by ignoring 200 pixels (representing 0.2 mm) from each edge of the image. Each of the final noise images had 1800 $\times$ 1800 data points that were subdivided into 81 sub-images, each with 200 $\times$ 200 data points, resulting in a total of 810 sub-images. The one-dimensional power spectrum in the $x$ direction was calculated for each of the 810 sub images and averaged to give the NPS:[23]

$$\mathrm{NPS}(\nu) = \frac{x_0 y_0}{N_x N_y} \, \mathrm{E} \left\{ \left| \mathrm{DFT} \left\{ \sum_{n_y=0}^{N_y-1} \Delta d_{n_x, n_y} \right\} \right|^2 \right\}, \qquad (26)$$

where $x_0$ and $y_0$ are the pixel center-to-center spacings in the $x$ and $y$ directions, $N_x$ and $N_y$ are the sub-image dimensions, E{ } and DFT{ } represent the expectation and discrete Fourier transform (DFT) operators, and

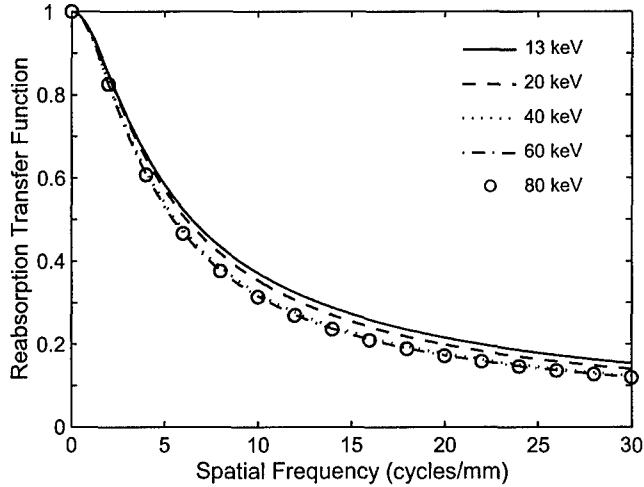FIG. 6: The reabsorption transfer function (RTF) for $K_\alpha$ reabsorption in semi-infinite $a$-Se.
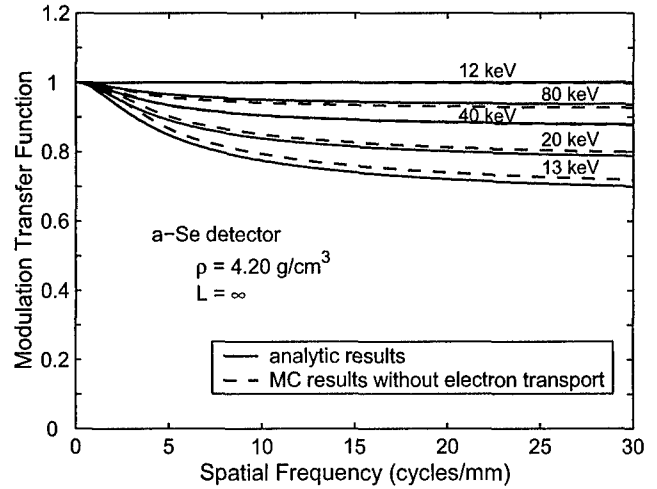


FIG. 7: Excellent agreement is achieved between the MTF obtained with the analytic Model B and the Monte Carlo simulations when the effect of electron transport is ignored.

$\Delta d_{n_x,n_y}$ is the zero-mean realization of the dose deposition at the location of pixel $(n_x, n_y)$. Selection of the $x$ direction is arbitrary as the NPS is equivalent in the $x$ and $y$ directions. Equation (26) is equivalent to the "synthesis" method used for multi-dimensional NPS calculations[54] in which pixel values are summed in the $y$ direction before taking the 1-D Fourier transform. Once $MTF_{pc}(\nu)$ and $NPS_{pc}(\nu)$ were determined from the Monte Carlo simulations, $DQE_{pc}(\nu)$ was calculated using Eq. (23).

A semi-infinite detector thickness was assumed for all calculations. This removes the detector thickness $L$ from the calculation and means that our results represent a pessimistic estimate of $MTF_{pc}$. However, our experience with the Monte Carlo calculations also showed that the MTF and NPS have very little dependence on $L$ if the thickness is great enough to achieve a quantum efficiency of 0.25. It is therefore reasonable to conclude that the MC results obtained with the semi-infinite detector are representative of $a$-Se detectors currently in use.

## IV. RESULTS

The reabsorption transfer function $RTF_{KL}(\nu)$ is shown in Fig. 6 for incident photon energies of 13, 20, 40, 60 and 80 keV. While there is some reduction in the RTF with increasing incident energy due to increases in the average interaction depth, this dependence is surprisingly minor.

Figure 7 shows a comparison of $MTF_{pc}(\nu)$ obtained using model B with Monte Carlo results for $a$-Se for a range of incident x-ray energies with the assumption that all energy transferred to electrons is absorbed locally. This was achieved with the Monte Carlo code by specifying an electron transport cut-off energy greater than that of the incident x ray. In all cases, excellent agreement (within 2%) is obtained between the analytic and MC results up to 30 cycles/mm between energies of 12 and 80 keV. At
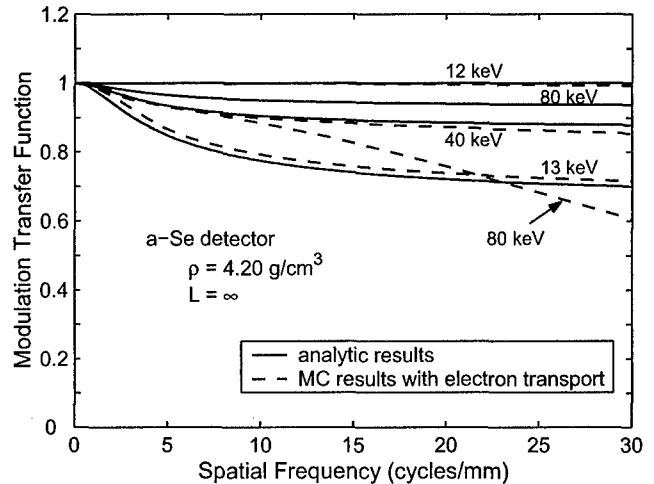


FIG. 8: Comparison of MTF from Model B with Monte Carlo simulations including electron transport. At 80 keV, electrons have an average CSDA range of $R_{CSDA} = 0.039$ mm in Se, resulting in significant degradation of the MTF at frequencies above approximately 13 cycles/mm ($\approx 1/(2R_{CSDA})$).

12 keV (below the K edge), the MTF is close to unity for all frequencies. At 13 keV, the MTF is degraded by over 25% at frequencies greater than approximately 8 cycles/mm due to reabsorption of characteristic radiation. The effect of reabsorption decreases with increasing energy.

Electron transport causes an additional spread in where energy is deposited in the detector by a distance of approximately $R_{CSDA}$ (continuous slowing down approximation range) in either direction, resulting in a further degradation of the MTF. This effect is shown in Fig. 8 where MC results with electron transport enabled (using an electron cut-off energy of 10 keV) are compared to

results obtained with electron transport disabled. Electron transport degrades the MTF by more than approximately 10% only at frequencies greater than approximately $1/(2R_{CSDA}) = 12.7$ cy/mm as summarized in Table IV for $a$-Se. This effect imposes a tradeoff between photon energy and spatial resolution for a specified detector material and determines the limiting range of applicability of the models presented here.

The photoelectric NPS, $NPS_{pc}(\nu)$, is compared with MC calculations without electron transport in Fig. 9, showing excellent agreement at incident photon energies between 12 and 80 keV. When electron transport is included in the MC calculation, shown in Fig. 10, the NPS falls below that of the analytic model at frequencies above approximately $1/(2R_{CSDA})$, similar to the MTF results.

Figure 11 shows excellent agreement between the analytic $DQE_{pc}(\nu)$ and MC simulations without electron transport for $a$-Se at incident energies of 13 to 80 keV. A comparison of the DQE at 12 and 13 keV shows that just above the K edge, reabsorption degrades the zero-frequency value by approximately 15% and at frequencies above 13 cycles/mm by 50%. The effect of reabsorption decreases with increasing energy.

When electron transport is included in the MC calculations (Fig. 12), agreement is excellent between 12 and 40 keV and again degraded at 80 keV by approximately 10% at frequency $1/2R_{CSDA}$ due to degradations in both the MTF and NPS curves.

All results presented here for the Se detector were obtained using model B and are almost equivalent to results obtained using model A. Thus, model A is sufficiently accurate to describe the Se detector over the energy and spatial frequency ranges described. However, model B would be required for detector materials having greater atomic number where the range of $K_\beta$ or L radiations cannot be neglected.

## V. CONCLUSIONS

A Fourier-based description of photoelectric interactions in diagnostic-imaging detectors has been developed to describe signal and noise transfer in terms of the photoelectric MTF, NPS and DQE using a linear cascaded-

TABLE IV: Electron CSDA range in $a$-Se ($\rho = 4.2$ g/cm$^3$). Electron transport only degrades the MTF significantly at spatial frequencies above approximately $1/(2R_{CSDA})$.

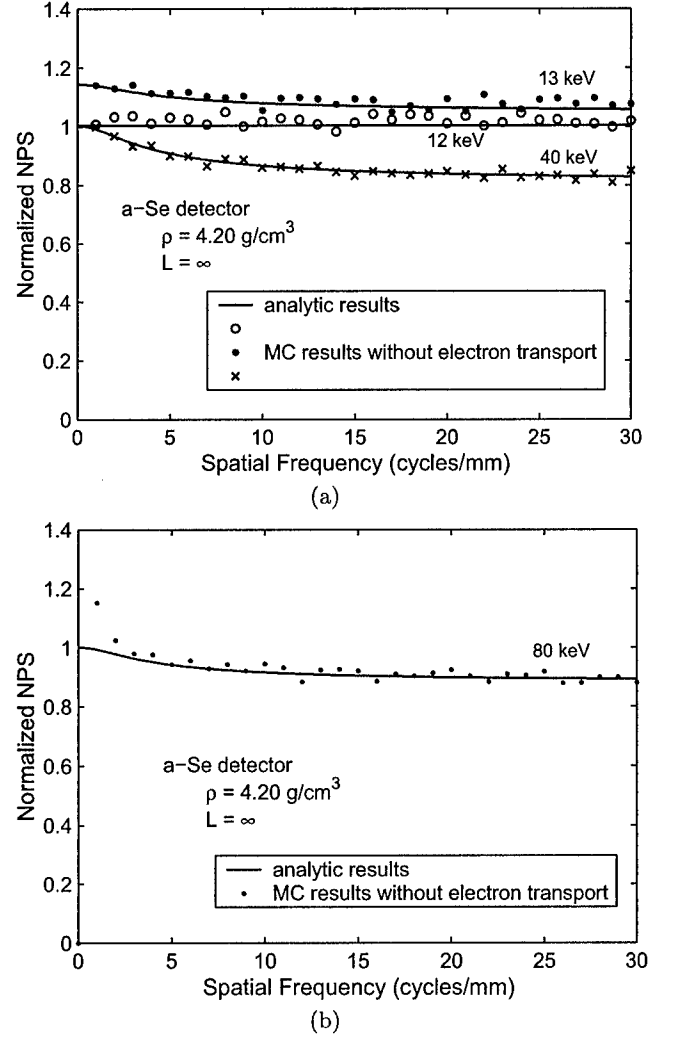| Electron Energy (keV) (keV) | $R_{CSDA}$ (g/cm$^2$) | $R_{CSDA}$ (mm) | $1/(2R_{CSDA})$ (mm$^{-1}$) |
|---|---|---|---|
| 20 | $1.587 \times 10^{-3}$ | $3.78 \times 10^{-3}$ | 132 |
| 40 | $5.129 \times 10^{-3}$ | $1.22 \times 10^{-2}$ | 41 |
| 60 | $1.019 \times 10^{-2}$ | $2.43 \times 10^{-2}$ | 21 |
| 80 | $1.651 \times 10^{-2}$ | $3.93 \times 10^{-2}$ | 13 |
| 100 | $2.391 \times 10^{-2}$ | $5.69 \times 10^{-2}$ | 8.8 |



(a)



(b)

FIG. 9: Excellent agreement is obtained between the NPS from Model B and the Monte Carlo simulations ignoring electron transport in $a$-Se.

systems approach. Two models are described with increasing levels of sophistication. The first includes the potential reabsorption of K characteristic x rays only. The second makes a distinction between $K_\alpha$, $K_\beta$ and L characteristic x rays. Both make use of parallel cascades of random noise processes to describe the resulting statistical correlations in image noise. The first is relatively simple and the analysis can be performed using a relatively simple manual calculation of signal and noise transfer. The second requires extensive use of parallel cascades and represents the first published models using such a complex parallel-cascades analysis. Signal and noise transfer through it is more complex requiring the tedious manipulation of many (30 - 50) algebraic terms even with simplifications. For this model, signal and noise transfer was calculated using an automated software algorithm developed in our laboratory using a
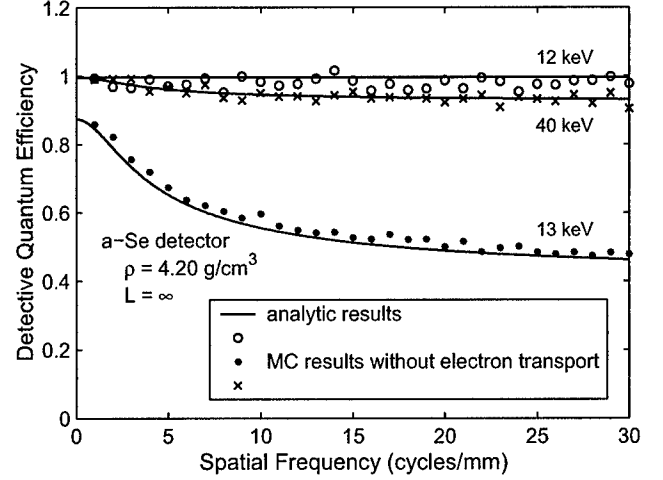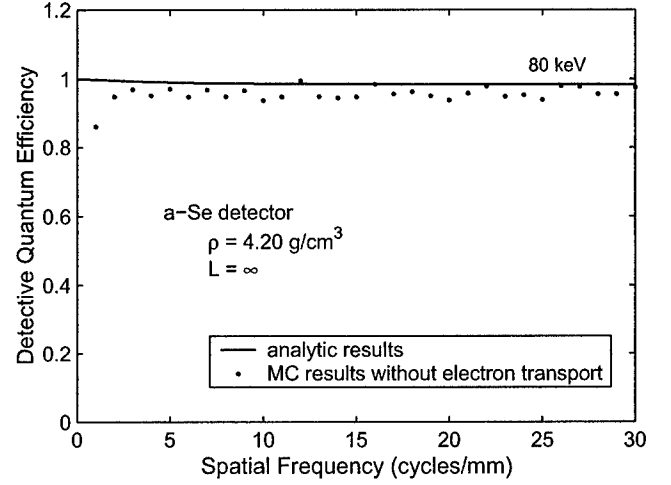
(a)



(a)



(b)
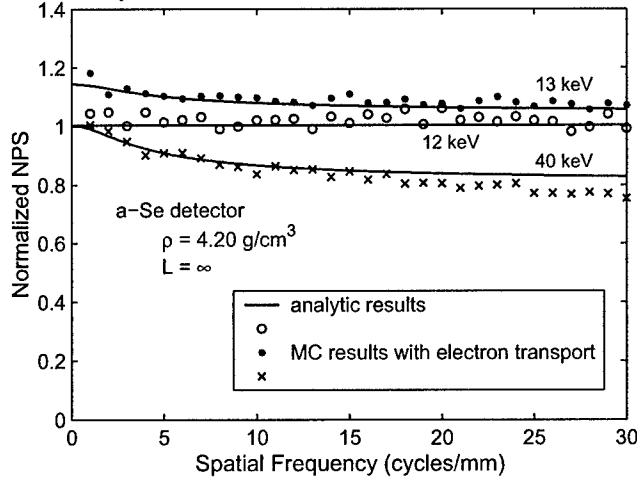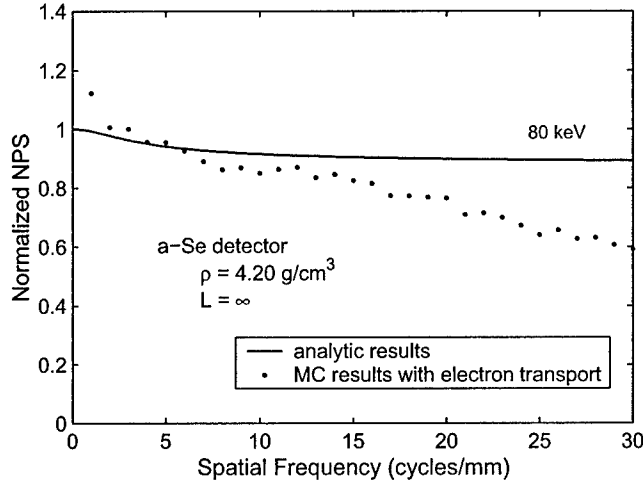


(b)

FIG. 10: The NPS obtained with Monte Carlo calculations for 80 keV deviate from the analytic model at approximately 17 cycles/mm $(1/2R_{\text{CSDA}})$ due to electron transport in $a$-Se.

FIG. 11: Excellent agreement is obtained between analytic DQE and MC DQE when electron transport is neglected.

graphical user interface to design the model and symbolic mathematics to evaluate signal and noise propagation.[50]

Blurring due to electron transport is not included in these models. The photoelectric MTF, NPS and DQE results were validated using a Monte Carlo calculation with electron transport calculations disabled showing agreement with the model within approximately 2% up to 30 cycles/mm for an amorphous selenium detector. This verifies that the analytic model is extremely accurate for the calculation of all photon-based physical processes in the photoelectric interaction. The MC calculation was repeated with electron transport calculation enabled to identify the range over which the model can be expected to be accurate. It was found that the model is accurate within 10% for spatial frequencies up to a maximum spatial frequency $\nu_{max} \approx 1/(2R_{\text{CSDA}})$ where $R_{\text{CSDA}}$ is the CSDA range of electrons at the energy of the incident

x ray. This limiting frequency decreases with increasing x-ray energy. In the Se detector, $\nu_{max} \approx 21$ cy/mm at 60 keV and 13 cy/mm at 80 keV. The relationship $\nu_{max} \approx 1/(2R_{\text{CSDA}})$ was only verified for the Se detector, but it is reasonable to expect it will be valid for other detector materials.

While the expressions for MTF, NPS and DQE obtained with these models may involve many algebraic terms, they are easy to evaluate. Thus, it is practical to evaluate these metrics for a wide range of detector configurations with negligible computational requirements. In addition to reducing the need for extensive Monte Carlo calculations, the analytic models provide more insight into the physical causes limiting detector performance. Use of the cascaded-systems approach makes it easy to incorporate these results as the first stage of more comprehensive models of specific detector designs for the development and evaluation of new detector systems with
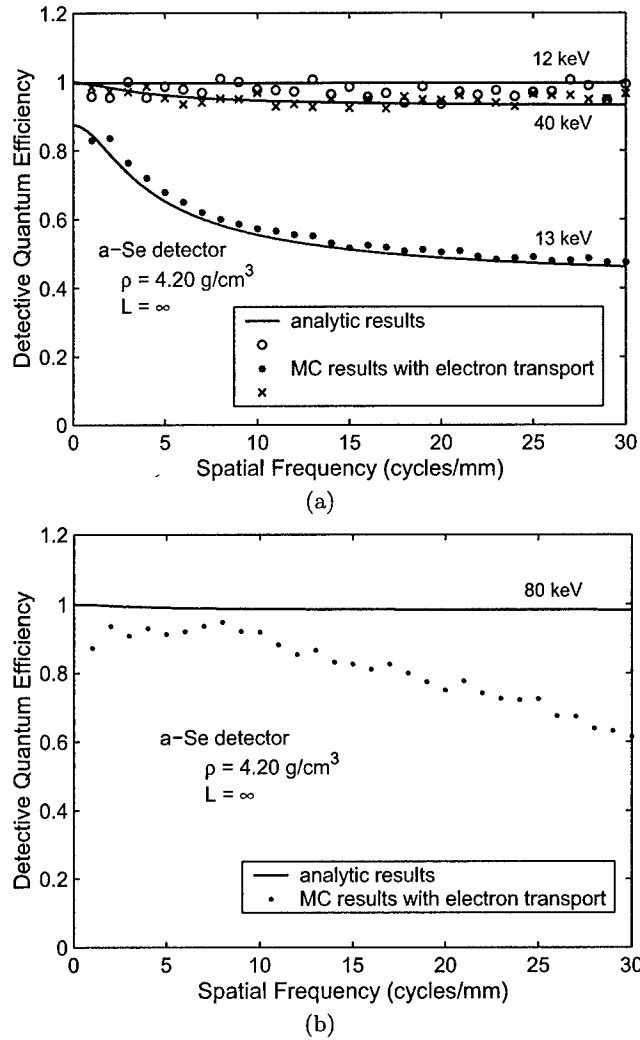
FIG. 12: Comparison of DQE from model B with Monte Carlo simulations including electron transport for $a$-Se.

greater performance specifications.

## Acknowledgments

## APPENDIX A: PHOTOELECTRIC MTF AND NNPS OF MODEL B

Expressions for the photoelectric MTF and NNPS obtained with model B were calculated using an automated algorithm employing symbolic mathematics developed in our laboratory[50] and are listed here for reference.

$$
\begin{aligned}
\mathrm{NNPS}_{\mathrm{pc}}(\nu) = \frac{1}{\bar{G}_{\mathrm{pc}}} \Big\{ & \left[ (\mathrm{h}\nu - \mathrm{E_K})^2/W^2 + (\mathrm{h}\nu - \mathrm{E_K})/W \right] P_K \\
& + \left[ (\mathrm{E_K} - \mathrm{E_L})^2/W^2 + (\mathrm{E_K} - \mathrm{E_L})/W \right] f_{KL}\,\omega_{KL}\,\xi_{KL}P_K \\
& + \left[ (\mathrm{E_L} - \mathrm{E_M})^2/W^2 + (\mathrm{E_L} - \mathrm{E_M})/W \right] f_{LM}\,\omega_{LM}\,\omega_{KL}\,\xi_{KL} \\
& + (\mathrm{E_L^2}/W^2 + \mathrm{E_L}/W)(1 - \omega_{LM})\omega_{KL}\,\xi_{KL}P_K \\
& + \left[ (\mathrm{E_K} - 2\mathrm{E_L})^2/W^2 + (\mathrm{E_K} - 2\mathrm{E_L})/W \right] a_L(1 - \omega_{KL})\xi_{KL}P \\
& + 2\left[ (\mathrm{E_L} - \mathrm{E_M})^2/W^2 + (\mathrm{E_L} - \mathrm{E_M})/W \right] f_{LM}\,\omega_{LM}\,a_L(1 - \omega \\
& + 2(\mathrm{E_L^2}/W^2 + \mathrm{E_L}/W)(1 - \omega_{LM})a_L(1 - \omega_{KL})\xi_{KL}P_K \\
& + \left[ (\mathrm{E_K} - \mathrm{E_L})^2/W^2 + (\mathrm{E_K} - \mathrm{E_L})/W \right](1 - a_L)(1 - \omega_{KL})\xi_{K} \\
& + \left[ (\mathrm{E_L} - \mathrm{E_M})^2/W^2 + (\mathrm{E_L} - \mathrm{E_M})/W \right] f_{LM}\,\omega_{LM}(1 - a_L)(1 \\
& + (\mathrm{E_L^2}/W^2 + \mathrm{E_L}/W)(1 - \omega_{LM})(1 - a_L)(1 - \omega_{KL})\xi_{KL}P_K \\
& + \left[ (\mathrm{E_K} - \mathrm{E_M})^2/W^2 + (\mathrm{E_K} - \mathrm{E_M})/W \right] f_{KM}\,\omega_{KM}(1 - \xi_{KL} \\
& + (\mathrm{E_K^2}/W^2 + \mathrm{E_K}/W)(1 - \omega_{KM})(1 - \xi_{KL})P_K \\
& + \left[ (\mathrm{h}\nu - \mathrm{E_L})^2/W^2 + (\mathrm{h}\nu - \mathrm{E_L})/W \right] P_L'(1 - P_K) \\
& + \left[ (\mathrm{E_L} - \mathrm{E_M})^2/W^2 + (\mathrm{E_L} - \mathrm{E_M})/W \right] f_{LM}\,\omega_{LM}P_L'(1 - P \\
& + (\mathrm{E_L^2}/W^2 + \mathrm{E_L}/W)(1 - \omega_{LM})P_L'(1 - P_K) \\
& + (\mathrm{h}\nu^2/W^2 + \mathrm{h}\nu/W)(1 - P_L')(1 - P_K) \\
& + 2(\mathrm{h}\nu - \mathrm{E_K})/W(\mathrm{E_K} - \mathrm{E_L})/W f_{KL}\,\omega_{KL}\,\xi_{KL}P_K\,\mathrm{RTF}_{KL}(\nu) \\
& + 2(\mathrm{h}\nu - \mathrm{E_K})/W(\mathrm{E_L} - \mathrm{E_M})/W f_{LM}\,\omega_{LM}\,\omega_{KL}\,\xi_{KL}P_K\,\mathrm{RTF} \\
& + 2(\mathrm{h}\nu - \mathrm{E_K})/W(\mathrm{E_L}/W)(1 - \omega_{LM})\omega_{KL}\,\xi_{KL}P_K \\
& + 2(\mathrm{h}\nu - \mathrm{E_K})/W(\mathrm{E_K} - 2\mathrm{E_L})/W a_L(1 - \omega_{KL})\xi_{KL}P_K \\
& + 4(\mathrm{h}\nu - \mathrm{E_K})/W(\mathrm{E_L} - \mathrm{E_M})/W f_{LM}\,\omega_{LM}\,a_L(1 - \omega_{KL})\xi_{KL}P \\
& + 4(\mathrm{h}\nu - \mathrm{E_K})/W(\mathrm{E_L}/W)(1 - \omega_{LM})a_L(1 - \omega_{KL})\xi_{KL}P_K \\
& + 2(\mathrm{h}\nu - \mathrm{E_K})/W(\mathrm{E_K} - \mathrm{E_L})/W(1 - a_L)(1 - \omega_{KL})\xi_{KL}P_K \\
& + 2(\mathrm{h}\nu - \mathrm{E_K})/W(\mathrm{E_L} - \mathrm{E_M})/W f_{LM}\,\omega_{LM}(1 - a_L)(1 - \omega_{KL})\xi \\
& + 2(\mathrm{h}\nu - \mathrm{E_K})/W(\mathrm{E_L}/W)(1 - \omega_{LM})(1 - a_L)(1 - \omega_{KL})\xi_{KL}P_K \\
& + 2(\mathrm{h}\nu - \mathrm{E_K})/W(\mathrm{E_K} - \mathrm{E_M})/W f_{KM}\,\omega_{KM}(1 - \xi_{KL})P_K\,\mathrm{RTF}
\end{aligned}
$$

$$
\begin{aligned}
\mathrm{MTF}_{\mathrm{pc}}(\nu) = \frac{1}{\bar{G}_{\mathrm{pc}}} \Big\{ & P_K(\mathrm{h}\nu - \mathrm{E_K})/W + P_K\xi_{KL}\,\omega_{KL}f_{KL}\,\mathrm{RTF}_{KL}(\nu)(\mathrm{E_K} - \mathrm{E_L})/W \\
& + P_K\xi_{KL}\,\omega_{KL}\,\omega_{LM}f_{LM}\,\mathrm{RTF}_{LM}(\nu)(\mathrm{E_L} - \mathrm{E_M})/W + P_K\xi_{KL}\,\omega_{KL}(1 - \omega_{LM})\mathrm{E_L}/W \\
& + P_K\xi_{KL}(1 - \omega_{KL})a_L(\mathrm{E_K} - 2\mathrm{E_L})/W \\
& + 2P_K\xi_{KL}(1 - \omega_{KL})a_L\,\omega_{LM}f_{LM}\,\mathrm{RTF}_{LM}(\nu)(\mathrm{E_L} - \mathrm{E_M})/W \\
& + 2P_K\xi_{KL}(1 - \omega_{KL})a_L(1 - \omega_{LM})\mathrm{E_L}/W + P_K\xi_{KL}(1 - \omega_{KL})(1 - a_L)(\mathrm{E_K} - \mathrm{E_L})/W \\
& + P_K\xi_{KL}(1 - \omega_{KL})(1 - a_L)\omega_{LM}f_{LM}\,\mathrm{RTF}_{LM}(\nu)(\mathrm{E_L} - \mathrm{E_M})/W \\
& + P_K\xi_{KL}(1 - \omega_{KL})(1 - a_L)(1 - \omega_{LM})\mathrm{E_L}/W \\
& + P_K(1 - \xi_{KL})\omega_{KM}f_{KM}\,\mathrm{RTF}_{KM}(\nu)(\mathrm{E_K} - \mathrm{E_M})/W \\
& + P_K(1 - \xi_{KL})(1 - \omega_{KM})\mathrm{E_K}/W + (1 - P_K)P_L'(\mathrm{h}\nu - \mathrm{E_L})/W \\
& + (1 - P_K)P_L'\,\omega_{LM}f_{LM}\,\mathrm{RTF}_{LM}(\nu)(\mathrm{E_L} - \mathrm{E_M})/W \\
& + (1 - P_K)P_L'(1 - \omega_{LM})\mathrm{E_L}/W + (1 - P_K)(1 - P_L')\,\mathrm{h}\nu/W \Big\}
\end{aligned}
$$

$$
\begin{aligned}
\bar{G}_{\mathrm{pc}} = & P_K(\mathrm{h}\nu - \mathrm{E_K})/W + P_K\xi_{KL}\,\omega_{KL}f_{KL}(\mathrm{E_K} - \mathrm{E_L})/W \\
& + P_K\xi_{KL}\,\omega_{KL}\,\omega_{LM}f_{LM}(\mathrm{E_L} - \mathrm{E_M})/W + P_K\xi_{KL}\,\omega_{KL}(1 - \omega_{LM})\mathrm{E_L}/W \\
& + P_K\xi_{KL}(1 - \omega_{KL})a_L(\mathrm{E_K} - 2\mathrm{E_L})/W + 2P_K\xi_{KL}(1 - \omega_{KL})a_L\,\omega_{LM}f_{LM}(\mathrm{E_L} - \mathrm{E_M})/W \\
& + 2P_K\xi_{KL}(1 - \omega_{KL})a_L(1 - \omega_{LM})\mathrm{E_L}/W + P_K\xi_{KL}(1 - \omega_{KL})(1 - a_L)(\mathrm{E_K} - \mathrm{E_L})/W \\
& + P_K\xi_{KL}(1 - \omega_{KL})(1 - a_L)\omega_{LM}f_{LM}(\mathrm{E_L} - \mathrm{E_M})/W \\
& + P_K\xi_{KL}(1 - \omega_{KL})(1 - a_L)(1 - \omega_{LM})\mathrm{E_L}/W + P_K(1 - \xi_{KL})\omega_{KM}f_{KM}(\mathrm{E_K} - \mathrm{E_M})/W \\
& + P_K(1 - \xi_{KL})(1 - \omega_{KM})\mathrm{E_K}/W + (1 - P_K)P_L'(\mathrm{h}\nu - \mathrm{E_L})/W \\
& + (1 - P_K)P_L'\,\omega_{LM}f_{LM}(\mathrm{E_L} - \mathrm{E_M})/W \\
& + (1 - P_K)P_L'(1 - \omega_{LM})\mathrm{E_L}/W + (1 - P_K)(1 - P_L')\,\mathrm{h}\nu/W \qquad \text{(A2)}
\end{aligned}
$$

$$+2(h\nu-E_K)/W(E_K/W)(1-\omega_{KM})(1-\xi_{KL})P_K$$
$$+2(E_K-E_L)/Wf_{KL}(E_L-E_M)/Wf_{LM}\,\omega_{LM}\,\omega_{KL}\xi_{KL}P_K\,\mathrm{RTF}_{KL}(\nu)\mathrm{RTF}_{LM}(\nu)$$
$$+2(E_K-E_L)/Wf_{KL}(E_L/W)(1-\omega_{LM})\omega_{KL}\,\xi_{KL}P_K\,\mathrm{RTF}_{KL}(\nu)$$
$$+2(E_K-2E_L)/W(E_L-E_M)/Wf_{LM}\,\omega_{LM}\,a_L(1-\omega_{KL})\xi_{KL}P_K\,\mathrm{RTF}_{LM}(\nu)$$
$$+2(E_K-2E_L)/W(E_L/W)(1-\omega_{LM})a_L(1-\omega_{KL})\xi_{KL}P_K$$
$$+2(E_K-2E_L)/W(E_L-E_M)/Wf_{LM}\,\omega_{LM}\,a_L(1-\omega_{KL})\xi_{KL}P_K\,\mathrm{RTF}_{LM}(\nu)$$
$$+2(E_K-2E_L)/W(E_L/W)(1-\omega_{LM})a_L(1-\omega_{KL})\xi_{KL}P_K$$
$$+2\left[(E_L-E_M)/Wf_{LM}\,\omega_{LM}\,\mathrm{RTF}_{LM}(\nu)\right]^2 a_L(1-\omega_{KL})\xi_{KL}P_K$$
$$+4(E_L-E_M)/W(E_L/W)f_{LM}\,\omega_{LM}(1-\omega_{LM})a_L(1-\omega_{KL})\xi_{KL}P_K\,\mathrm{RTF}_{LM}(\nu)$$
$$+\,2(E_L/W)^2(1-\omega_{LM})^2 a_L(1-\omega_{KL})\xi_{KL}P_K$$
$$+2(E_K-E_L)/W(E_L-E_M)/Wf_{LM}\,\omega_{LM}(1-a_L)(1-\omega_{KL})\xi_{KL}P_K\,\mathrm{RTF}_{LM}(\nu)$$
$$+2(E_K-E_L)/W(E_L/W)(1-\omega_{LM})(1-a_L)(1-\omega_{KL})\xi_{KL}P_K$$
$$+2(h\nu-E_L)/W(E_L-E_M)/Wf_{LM}\,\omega_{LM}P_L'(1-P_K)\mathrm{RTF}_{LM}(\nu)$$
$$+2(h\nu-E_L)/W(E_L/W)(1-\omega_{LM})P_L'(1-P_K)\Big\}$$

$$(\mathrm{A3})$$

---

* Electronic mail: jyao@imaging.robarts.ca

[1] J. J. Heine and P. Malhotra, "Mammographic tissue, breast cancer risk, serial image analysis, and digital mammography. Part 1. Tissue and related risk factors," Acad. Radiol. **9**, 298–316 (2002).

[2] J. J. Heine and P. Malhotra, "Mammographic tissue, breast cancer risk, serial image analysis, and digital mammography. Part 2. Serial breast tissue change and related temporal influences," Acad. Radiol. **9**, 317–335 (2002).

[3] P. Van Landeghem, L. Bleyen, and G. De Backer, "Age-specific accuracy of initial versus subsequent mammography screening: Results from the Ghent breast cancer-screening programme," Eur. J. Cancer Prev. **11**, 147–151 (2002).

[4] L. Tabar, G. Fagerberg, H. H. Chen, S. W. Duffy, C. R. Smart, A. Gad, and R. A. Smith, "Efficacy of breast cancer screening by age. New results from the Swedish Two-County Trial," Cancer **75**, 2507–2517 (1995).

[5] C. R. Smart, R. E. Hendrick, J. H. III Rutledge, and R. A. Smith, "Benefit of mammography screening in women ages 40 to 49 years. Current evidence from randomized controlled trials," Cancer **75**, 1619–1626 (1995).

[6] R. E. Hendrick, R. A. Smith, J. H. III Rutledge, and C. R. Smart, "Benefit of screening mammography in women aged 40-49: A new meta-analysis of randomized controlled trials," J. Natl. Cancer Inst. Monogr **22**, 87–92 (1997).

[7] X. Zhou and R. Gordon, "Detection of early breast cancer: An overview and future prospects," Crit. Rev. Biomed. Eng. **17**, 203–255 (1989).

[8] S. F. Hurley and J. M. Kaldor, "The benefits and risks of mammographic screening for breast cancer," Epidemiol Rev. **14**, 101–130 (1992).

[9] S. A. Feig and M. J. Yaffe, "Digital mammography," Radiographics **18**, 893–901 (1998).

[10] M. J. Yaffe, "Digital mammography," in *Handbook of Medical Imaging, Vol. 1. Physics and Psychophysics*, edited by J. Beutel, H. L. Kundel, and R. L. Van Metter (SPIE Press, Bellingham, WA, 2000), pp. 329–372.

[11] C. J. Baines, A. B. Miller, D. B. Kopans, M. Moskowitz, D. E. Sanders, E. A. Sickles, T. To, and C. Wall, "Canadian national breast screening study: Assessment of technical quality by external review," Am. J. Roentgenol. **155**, 743–747 (1990).

[12] N. F. Boyd, H. M. Jensen, G. Cooke, H. L. Han, G. A. Lockwood, and A. B. Miller, "Mammographic densities and the prevalence and incidence of histological types of benign breast disease. Reference Pathologists of the Canadian National Breast Screening Study," Eur. J. Cancer Prev. **9**, 15–24 (2000).

[13] K. Kerlikowske, D. Grady, J. Barclay, E. A. Sickles, and V. Ernster, "Effect of age, breast density, and family history on the sensitivity of first screening mammography," JAMA **276**, 33–38 (1996).

[14] K. Kerlikowske, D. Grady, J. Barclay, E. A. Sickles, and V. Ernster, "Likelihood ratios for modern screening mammography. Risk of breast cancer based on age and mammographic interpretation," JAMA **276**, 39–43 (1996).

[15] S. A. Feig, "Estimation of currently attainable benefit from mammographic screening of women aged 40-49 years," Cancer **75**, 2412–2419 (1995).

[16] K. Rossmann, "Measurement of the modulation transfer function of radiographic systems containing fluoroscent screens," Phys. Med. Biol. **9**, 551–557 (1964).

[17] K. Rossmann, "The spatial frequency spectrum: A means for studying the quality of radiographic imaging systems," Radiology **90**, 1–13 (1968).

[18] J. C. Dainty and R. Shaw, *Image Science* (Academic Press, New York, 1974).

[19] C. E. Metz and K. Doi, "Transfer function analysis of radiographic imaging systems," Phys. Med. Biol. **24**, 1079–1106 (1979).

[20] "Medical imaging—the assessment of image quality," ICRU Report No. 54 (International Commission of Radiation Units and Measurements, MD, 1995).

[21] I. A. Cunningham and R. Shaw, "Signal-to-noise optimization of medical imaging systems," J. Opt. Soc. Am. A **16**, 621–632 (1999).

[22] H. H. Barrett and K. Meyers, *Image Science: Mathematical and Statistical Foundations* (Wiley, New York, 2003).

[23] I. A. Cunningham, "Applied linear-systems theory," in *Handbook of Medical Imaging, Vol. 1. Physics and Psychophysics*, edited by J. Beutel, H. L. Kundel, and R. L. Van Metter (SPIE Press, Bellingham, WA, 2000), pp. 79–159.

[24] H. H. Barrett, "Objective assessment of image quality: Effects of quantum noise and object variability," J. Opt. Soc. Am. A **7**, 1266–1278 (1990).

[25] A. E. Burgess, "The rose model, revisited," J. Opt. Soc. Am. A **16**, 633–646 (1999).

[26] C. S. Chen, K. Doi, C. Vyborny, H. P. Chan, and G. Holje, "Monte carlo simulation studies of detectors used in the measurement of diagnostic x-ray spectra," Med Phys **7** (1980).

[27] H. P. Chan and K. Doi, "Energy and angular dependence of x-ray absorption and its effect on radiographic response in screen-film systems," Phys Med Biol **28** (1983).

[28] H. P. Chan and K. Doi, "Studies of x-ray energy absorption and quantum noise properties of x-ray screens by use of Monte Carlo simulation," Med. Phys. **11**, 37–46 (1984).

[29] Y. Kodera, K. Doi, and H. P. Chan, "Absolute speeds of screen-film systems and their absorbed-energy constants," Radiology **151**, 229–36 (1984).

[30] J. M. Boone, J. A. Seibert, J. M. Sabol, and M. Tecotzky, "A monte carlo study of x-ray fluorescence in x-ray detectors," Med. Phys. **26**, 905–916 (1999).

[31] W. Zhao, W. G. Ji, and J. A. Rowlands, "Effects of characteristic x rays on the noise power spectra and detective quantum efficiency of photoconductive x-ray detectors," Med. Phys. **28**, 2039–2049 (2001).

[32] C. E. Metz and C. J. Vyborny, "Wiener spectral effects of spatial correlation between the sites of characteristic x-ray emission and reabsorption in radiographic screen-film systems," Phys. Med. Biol. **28**, 547–564 (1983).

[33] I. Kawrakow and D. W. O. Rogers, "The EGSnrc code system: Monte Carlo simulation of electron and photon transport," Technical Report PIRS-701 (National Research Council of Canada, Ottawa, 2000).

[34] I. Kawrakow, "Accurate condensed history Monte Carlo simulation of electron transport. I: EGSnrc, the new EGS4 version," Med. Phys. **27**, 485–498 (2000).

[35] B. R. B. Walters and D. W. O. Rogers, "DOSXYZnrc users manual," Technical Report PIRS-794 (National Research Council of Canada, Ottawa, 2002).

[36] R. L. Morin, *Monte Carlo Simulation in the Radiological Sciences* (CRC Press, Boca Raton, FL, 1988).

[37] T. T. Monajemi, S. Steciw, B. G. Fallone, and S. Rathee, "Modeling scintillator-photodiodes as detectors for megavoltage CT," Med. Phys. **31**, 1225–1234 (2004).

[38] Y. El-Mohri, K. W. Jee, L. E. Antonuk, M. Maolinbay, and Q. Zhao, "Determination of the detective quantum efficiency of a prototype, megavoltage indirect detection, active matrix flat-panel imager," Med. Phys. **28**, 2538–2580 (2001).

[39] M. Z. Kabir and S. O. Kasap, "Dependence of the DQE of photoconductive x-ray detectors on charge transport and trapping," Proc. SPIE **4682**, 42–52 (2002).

[40] J. Yao and I. A. Cunningham, "Parallel cascades: New ways to describe noise transfer in medical imaging systems," Med. Phys. **28**, 2020–2038 (2001).

[41] F. H. Attix, *Introduction to Radiological Physics and Radiation Dosimetry* (Wiley, New York, 1986).

[42] H. E. Johns and J. R. Cunningham, *The Physics of Radiology*, 4th ed. (Charles C Thomas, Springfield IL, 1983).

[43] H. H. Barrett, R. F. Wagner, and K. J. Myers, "Correlated point processes in radiological imaging," Proc SPIE **3032** (1997).

[44] J. A. Rowlands and J. Yorkston, "Flat panel detectors for digital radiography," in *Handbook of Medical Imaging, Vol. 1. Physics and Psychophysics*, edited by J. Beutel, H. L. Kundel, and R. L. Van Metter (SPIE Press, Bellingham, WA, 2000), pp. 223 – 328.

[45] S. T. Perkins, D. E. Cullen, M. H. Chen, J. H. Hubbell, J. A. Rathkopt, and J. H. Scofield, "Tables and graphs of atomic subshell and relaxation data derived from the LLNL evaluated atomic data library (EAOL), Z=1-100," Technical Report UCRL - 50400, Vol. 30 (Lawrence Livermore National Laboratory, Livermore, California, 1991).

[46] W. Que and J. A. Rowlands, "X-ray imaging using amorphous selenium: Inherent spatial resolution," Med. Phys. **22**, 365–374 (1995).

[47] H.-P. Chan and K. Doi, "Monte carlo simulation in diagnostic radiology," in *Monte Carlo Simulation in the Radiological Sciences*, edited by R. L. Morin (CRC Press, Boca Raton, FL, 1988), pp. 103–191.

[48] R. N. Bracewell, *The Fourier Transform and Its Applications*, 3rd ed. (McGraw Hill, New York, 2000).

[49] H. H. Barrett and W. Swindell, *Radiological Imaging* (Academic Press, New York, 1981).

[50] M. Sattarivand and I. A. Cunningham, "Computational engine for development of complex cascaded models of signal and noise in x-ray imaging systems," IEEE Trans. Med. Imag. **24**, 211–222 (2005).

[51] K. J. Myers, "Ideal observer models of visual signal detection," in *Handbook of Medical Imaging, Vol. 1. Physics and Psychophysics*, edited by J. Beutel, H. L. Kundel, and R. L. Van Metter (SPIE Press, Bellingham, WA, 2000), pp. 559–592.

[52] R. Shaw, "The equivalent quantum efficiency of the photographic process," J. Photogr. Sci. **11**, 199–204 (1963).

[53] "Matlab," tech. rep. (The MathWorks, Inc., ).

[54] J. H. Siewerdsen, I. A. Cunningham, and D. A. Jaffray, "A framework for noise-power spectrum analysis of multidimensional images," Med. Phys. **29**, 2655–2671 (2002).